V_{oc} from a morphology point of view: On the open circuit voltage of polycrystalline organic heterojunction solar cells

Dissertation

zur Erlangung des
Doktorgrades der Naturwissenschaften
(Dr. rer. nat.)

eingereicht an der
Mathematisch-Naturwissenschaftlich-Technischen Fakultät
der Universität Augsburg

vorgelegt von

Ulrich Hörmann

2014

Universität Augsburg
Mathematisch-Naturwissenschaftlich-
Technische Fakultät

1. Gutachter:	Prof. Dr. Wolfgang Brütting
2. Gutachterin:	Prof. Dr. Ellen Moons
Tag der mündlichen Prüfung:	23.02.2015

Contents

Chapter 1

Introduction

175 petawatts power continuously arrive at our planet in form of solar radiation.[1] An enormous energy source of which about one half reaches the surface of the earth as utilizable energy.[2] Despite the invention of the first p-n junction solar cell in 1954 by Chapin *et al.*[3] the main energy source of the modern human civilization still is the combustion of fossil fuels.[4,5]

In 2010 the total worldwide energy consumption was roughly 150 PWh and it is projected to rise to about 240 PWh in 2040. This is accompanied by a projected increase of the annual CO_2 emission from 31 gigatons to almost 46 gigatons.[4] Even though a major part of this increase is expected to be caused by emerging countries such as India and China as well as Central and South America,[4,5] the emission of greenhouse gases poses a global problem that needs to be tackled on an international scale and foremost by the leading industrialized countries.

In the aftermath of the Fukushima nuclear disaster in March 2011, the government of the federal republic of Germany announced a nuclear phase-out until 2022.[6,7] This leaves a transition to renewable energy sources as the only reasonable option in order to achieve a reduction of greenhouse gas emission. While most of the renewables essentially rely on the power of the sun, photovoltaic (PV) cells provide a direct way of solar energy conversion into electricity. Despite the fact that the sun delivers the energy needed during a whole year within hours, less than 0.1 % of the global energy demand is actually covered by directly harvesting solar energy. Typical, commercially available, silicon based PV modules have an average power conversion efficiency of about 16 %.[8] Record efficiencies of lab scale cells reach 20 % to almost 26 % for multi- and single crystalline silicon, respectively.[9] Still, photovoltaic energy is not yet truly competitive with fossil and nuclear energy sources.[4]

As a promising complement technology to conventional photovoltaics, organic solar cells have received increasing attention in the last 20 years. Instead of differently doped inorganic semiconductors, organic compounds are employed as the photo-active materi-

als in this device class. Both polymers and low molecular weight materials are typically used in these cells. The key design to achieve efficient charge generation was already found in 1986 by Tang, who combined two sequential layers of energetically different materials, denoted as the electron donor and the electron acceptor, to form a heterojunction, similar to a conventional p-n junction but yet fundamentally different.[10] In the 1990s, this concept was successfully transferred to so-called bulk heterojunctions, i.e. intimate blends of the donor and the acceptor material.[11–13]

The high absorption coefficients of organic semiconductors allow for active layers typically significantly thinner than 1 µm. These extremely thin films combined with low processing temperatures and the endless variety of organic chemistry enables totally new device categories regarding shape and color and allow flexible or even transparent solar cells.[14] Hence, building integration and design aspects open a completely new market for organic photovoltaic cells.[15] Yet, economic considerations predict that roll-to-roll produced organic solar cells can already compete with silicon if module efficiencies of 7 % and life times of at least 5 years can be achieved.[16*]

Recently, the power conversion efficiency of organic solar cells has hurdled the 10 % threshold and today the certified record efficiency reached by laboratory scale cells is 11.1 % – a power conversion efficiency of 6.9 % is reported for sub-modules.[9] This is an achievement of intense research of chemists, physicists, engineers and materials scientists around the world during the last two decades focused on understanding the elementary processes in organic solar cells and refining materials, interfaces and device architecture. One of the key parameters has been found to be the morphology of the active layer, regardless of the specific materials employed.[18–21] This includes the topographical microstructure as well as the absolute and mutual orientation of the molecules.

The present work contributes with a distinct focus on the open circuit voltage of simple planar heterojunctions, i.e. pure layers of the donor and the acceptor with a nominally sharp, flat interface. This deliberate reduction of the complexity of the morphology compared to blend films enables a more specific concentration on the impact of molecular orientation. For this purpose diindenoperylene (DIP) is introduced as an acceptor molecule. Not only does this yield remarkably high open circuit voltages in combination with α-sexithiophene (6T) or poly(3-hexylthiophene) (P3HT) as donor materials: Its rod-shaped molecular structure and comparison to cells with the spherical fullerene C_{60} also provides additional insight on the effects caused by mutual orientation at the donor/acceptor interface.

Depending on the growth conditions, 6T based solar cells with both acceptors show distinct changes of the open circuit voltages which can clearly be correlated with a changed morphology and are in opposite direction for the two different acceptors. While increased recombination of charge carriers is found to reduce the open circuit voltage

*In spite of the generally encouraging development it must be mentioned that it is still questionable if organic photovoltaic cells will eventually make it into broad commercialization. In particular the striking, recent advances of perovskite solar cells left the solar cell community flabbergasted by certified record efficiencies of 17.9 %, virtually reached within 5 years.[9,17] At the moment their main drawback seems to be potential toxicity resulting from the lead contained in these devices.

for cells comprising C_{60}, a fundamental change of the recombination mechanism is proposed for cells where DIP is employed as the acceptor. This is backed by theoretical considerations which predict the activation of singlet emission from DIP as an additional recombination channel.

Furthermore, the energy loss at open circuit is quantified for a variety of donor/acceptor combinations and film morphologies. For most devices the absolute loss observed is in agreement with the widely found value of approximately half an electron volt compared to the energy of the intermolecular donor/acceptor energy gap. However, an attempt to quantify the loss intrinsic to the device and not compensated by the photocurrent illustrates that this intrinsic loss is significantly different for the investigated devices. Ideality factors strongly deviating from unity identify increasing amounts of trap assisted recombination as the main cause of the increased losses.

Finally, the behavior of ternary solar cells is studied where a DIP interlayer is introduced between the 6T donor and the C_{60} acceptor films. The open circuit voltage is found to increase with the interlayer thickness, which is partly ascribed to reduced recombination losses.

Chapter 2

Device Physics of Organic Solar Cells

The following Sections 2.1 - 2.4 have been taken literally from earlier work "Characterization of planar and diffuse heterojunction solar cells based on poly(3-hexylthiophene)" (Ref. 22) and have been extended or updated where appropriate.

2.1 Organic semiconductors

Organic semiconductors are materials that feature a conjugated π-electron system. This class of materials splits up into two major groups: low-molecular weight materials (also referred to as *molecular* semiconductors or *small molecules*) and polymers. In both cases the molecular backbone is made up by the so called σ-bonds between sp^2-hybridized carbon atoms. Atop this backbone the conjugated π-system is formed by overlapping p_z orbitals of neighbouring carbon atoms. This is illustrated at the example of ethene in Figure 2.1. As π-bonding is significantly weaker than σ-bonding, electronic transitions from bonding π-orbitals to antibonding π^*-orbitals are possible by optical excitation without breaking the molecule (Figure 2.2).[23] In contrast to inorganic semiconductors, where the band gap is a property of the crystal, the energy gap of organic semiconductors is an intrinsic property of the molecule (apart from a slight shift). It originates from the energy difference between the *highest occupied molecular orbital* (HOMO) and the *lowest unoccupied molecular orbital* (LUMO) and depends on the size of the conjugated system as well as on the influence of functional groups. Thus the literally infinite variety of organic chemistry opens the possibility to tailor the optical and electronic properties of semiconducting materials to meet specific needs. The energy gap is typically in the range of 1.5 to 3 eV and thus in the range of visible light, rendering organic semiconductors applicable for optoelectronic devices.[24] On the other hand, thermal excitation of charge carriers from the HOMO into the LUMO is not possible and intrinsic carriers are virtually not present in organic semiconductors. This means that charge carriers

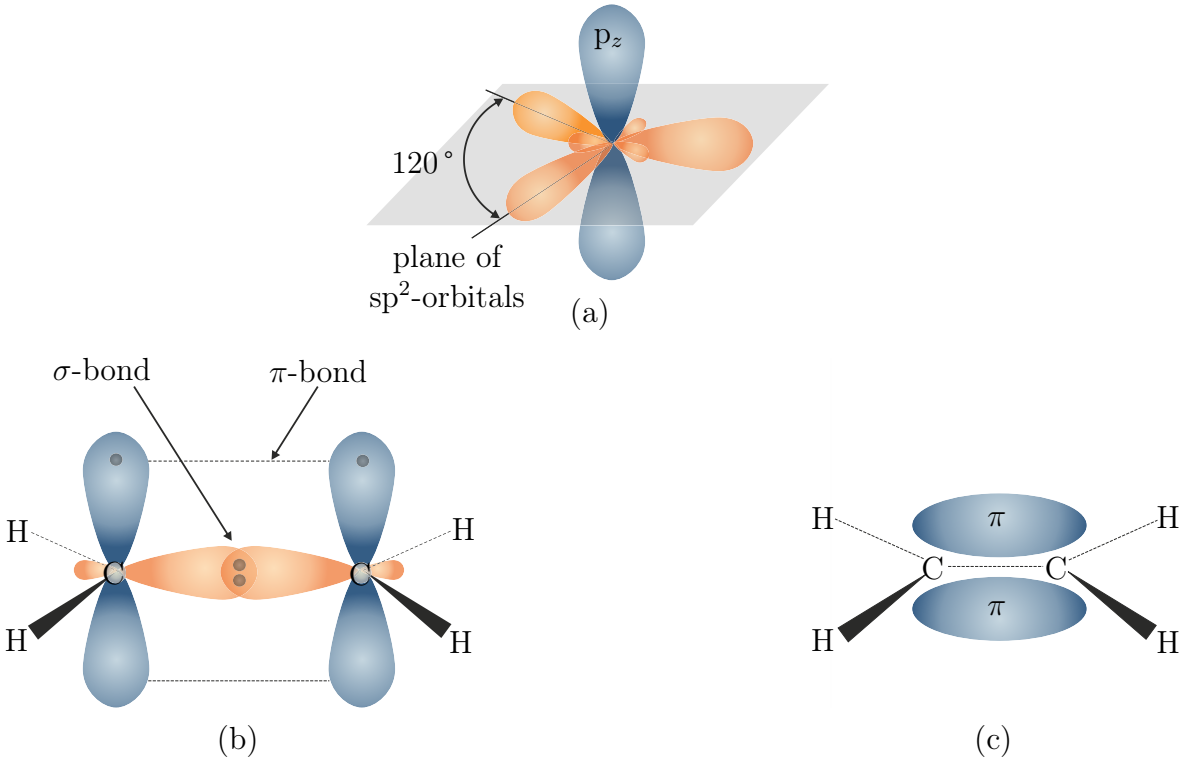

Figure 2.1: Schematic drawings of σ- and π-bonds in ethene.

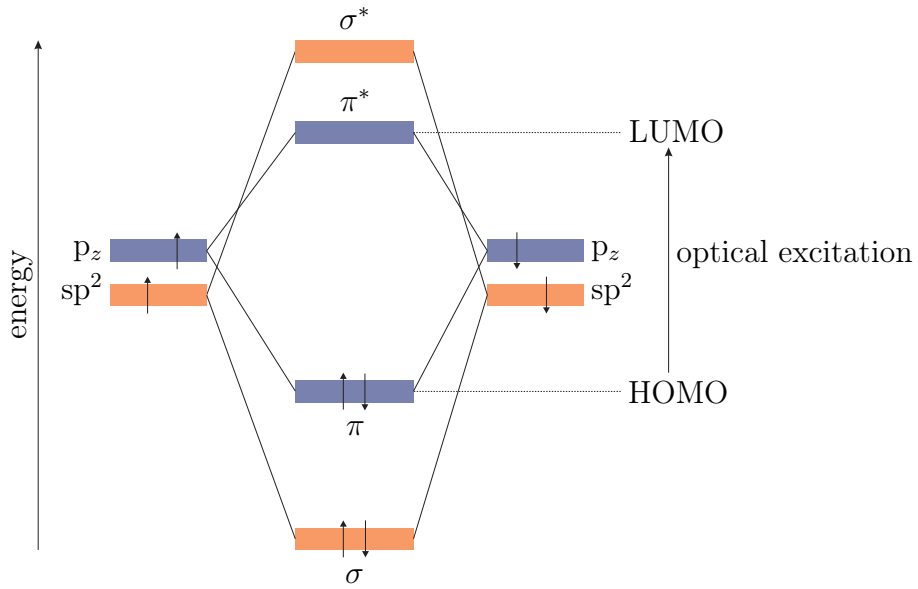

Figure 2.2: Energy diagram of σ- and π-bonding of sp^2-hybridized atoms. The lowest electronic excitation is indicated from the bonding π- to the antibonding π^*-orbital.

have to be generated by doping, optical excitation, field effect accumulation or injection from the contacts.[24] Thin films of organic materials typically used in devices are polycrystalline or even amorphous to a very large extent. This disordered structure together with the comparatively weak van-der-Waals forces that bind the molecules prevents the formation of broad energy bands as known from inorganic crystals. Instead it leads to a localization of the charges to single molecules which is accompanied by electronic polarization of their surrounding in an organic solid. Even though in analogy to inorganic semiconductors the charge carriers in organic semiconductors are frequently simply referred to as electrons and holes a more correct term for the charge and the polarization it induces would be negative and positive polarons, respectively.[25]

The mechanism underlying charge carrier transport in disordered organic films is a thermally assisted hopping transport from one localized state to the other in a Gaussian density of states.[26,27] Being a random process hopping transport yields very low charge carrier mobilities ($\mu \ll 1\,\mathrm{cm^2/Vs}$) when compared to band transport mobilities in inorganic semiconductors ($\mu \approx 100 - 10000\,\mathrm{cm^2/Vs}$).[23]

Another property directly related to the absence of broad bands is the large binding energy of electron-hole pairs, so called Frenkel-excitons. Once created, the electron and the hole are typically located on the same molecule and thus within the range of their Coulomb potentials. Assuming a typical molecular diameter of $r = 1\,\mathrm{nm}$ and a dielectric constant of $\varepsilon_\mathrm{r} = 3$ the exciton binding energy can be estimated to about 0.5 eV, which is significantly larger than the thermal energy at room temperature of about 25 meV. As many organic semiconductors are dyes, they feature high absorption coefficients of around $10^5\,\mathrm{cm^{-1}}$, which enables organic films of less than 100 nm thickness to absorb a major fraction of incident light.[28] For organic photovoltaic cells, however, it is crucial to efficiently dissociate the excitons created upon absorption in order to generate free charge carriers. Here the so-called heterojunction concept has proved itself successful.

2.2 Physical principles of organic heterojunction solar cells

Solar cells are devices that directly transform light into electrical energy. In organic solar cells a photoactive layer of one or more organic materials is sandwiched between two electrodes which form the terminals for an external electric circuit. One electrode – typically the anode – is transparent allowing light to enter the device. A widely spread transparent conductive material used in solar cells is indium tin oxide (ITO), for the cathode a low work function metal such as aluminum (Al) is used. In contrast to conventional inorganic solar cells, the binding energy of excitons created in organic solar cells cannot be overcome thermally. Therefore so called *homojunction* solar cells (i.e. cells based on a single semiconductor) are very inefficient in this case. An approach to drastically increase the efficiency is the concept of organic *heterojunction* solar cells, first realized by Tang.[10] Here the photoactive layer consists of two different organic semiconductor materials, one acting as an electron *donor*, the other as an *acceptor*. At

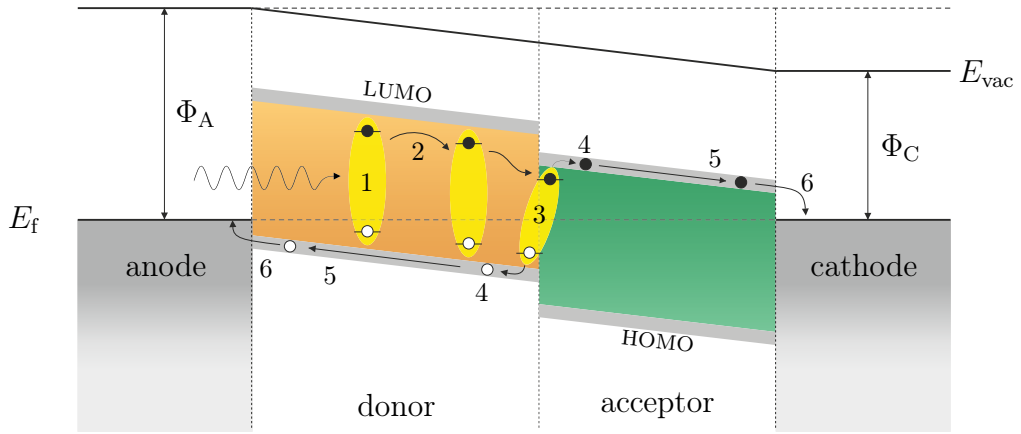

Figure 2.3: Energy diagram of an organic solar cell under short circuit conditions and basic steps of charge generation: (1) light absorption and exciton creation, (2) exciton diffusion to and (3) dissociation at the donor/acceptor interface, (4) charge carrier separation and (5) transport to the electrodes, (6) charge extraction. Φ_A and Φ_C denote the work functions of the anode and cathode, respectively, causing an internal field throughout the device that assists charge separation. Note that even though the formation of a relaxed charge transfer state is illustrated here, the exact nature of steps three and four is a matter of current debate.[32–34]

the donor-acceptor interface exciton dissociation is energetically favored and achieved by charge transfer of the electron into the LUMO of the acceptor or the hole into the HOMO of the donor molecules, respectively (cf. Figure 2.3). In order for this transfer to take place, however, the material combination needs to be suitable to form a staggered or *type-II* heterojunction:[29] the HOMO and LUMO energy levels of the donor have to be higher than those of the acceptor. For efficient charge transfer this energy offset should be in the range of a few 100 meV.[30] Additionally the *charge transfer exciton*, i.e. excitation of an electron from the HOMO of the donor into the LUMO of the acceptor, has to be the lowest excited state when compared to intra molecular excitation of both the donor and the acceptor materials.[31] The generation of electric current in organic solar cells can be divided into six steps at a microscopic level:[28]

1. Light absorption and exciton creation
2. Exciton diffusion
3. Exciton dissociation
4. Charge separation
5. Charge transport
6. Charge extraction

Upon the absorption of light strongly bound excitons are created within the organic semiconductor. As these excitons are neutral in charge their movement is not influenced by the electric field but solely governed by the laws of diffusion. Due to their large binding energy, however, the excitons are likely to decay and thus get lost for the external circuit. While the heterojunction architecture enables efficient exciton dissociation, the amount of excitons which can contribute to the photocurrent is limited to the fraction that reaches the donor-acceptor interface. This requires that the exciton is created within a range from the interface that does not exceed the exciton diffusion length, which typically is on the scale of a few 10 nm.[35] Once the exciton is successfully dissociated, the generated charges can be separated and transported to the electrodes by the internal field that is caused by the difference in work function of the anode and cathode material. Finally the charges can be extracted and drive an electric circuit.

Unfortunately, the steps of charge generation are countered by charge recombination processes that pose loss channels in solar cells. These processes are typically categorized as geminate and non-geminate recombination. The former refers to recombination of geminate (electron-hole) pairs, essentially stemming from the same photon, before they have been fully separated. Non-geminate recombination, on the other hand, denotes the recombination of formerly separated charge carriers.[36] Several recombination mechanisms are distinguished within this category. Most importantly direct recombination of two free and mobile charges and trap assisted recombination of a mobile carrier with an immobile charge trapped in a localized, energetically deep state. Other non-geminate recombination processes include Auger recombination, where the energy released by the recombination of two charges is transfered to a third charge carrier, and surface recombination of minority carriers at the electrodes.[37,38]

2.3 Donor/acceptor heterojunction architectures

An efficient organic solar cell depends on the efficiency of each of the steps mentioned above, thus that the overall efficiency can be expressed as follows:

$$\eta_{\text{total}} = \eta_{\text{absorption}} \times \eta_{\text{diffusion}} \times \eta_{\text{dissociation}} \times \eta_{\text{separation}} \times \eta_{\text{transport}} \times \eta_{\text{extraction}}$$

While of course all of these efficiencies depend on the choice of material, only the last three depend on the internal electric field,[28] namely charge separation, transport and extraction. Additionally the overall efficiency depends on the thin film morphology of the active layer which has a major impact on the exciton diffusion and dissociation as well as charge separation and charge transport. Only excitons that reach the donor/acceptor interface will be dissociated, while on the other hand, charges can only be separated, if continuous paths of one material to the corresponding electrode exist. These different effects lead to a trade off between charge transport in *planar heterojunctions* (Figure 2.4 (a)) and exciton dissociation in well dispersed *bulk heterojunctions* (Figure 2.4 (b)).[39] The first is formed by depositing a film of one semiconducting material on top of the other layer resulting in a strict, two dimensional donor/acceptor interface. This planar heterojunction architecture limits dissociation to the fraction of excitons created

close to the donor/acceptor interface but ensures closed paths to the electrodes. The bulk heterojunction emerges from depositing one layer from a mixed solution of both semiconductors, thus a more or less dispersed blend film is formed, with donor and acceptor domains in close vicinity. The latter yields a very large donor/acceptor interface distributed across the whole film, providing close to 100 % exciton quenching efficiency*.[40] This, however, is concurring with the lack of percolation paths to the electrodes and shunts by closed paths of one material from one electrode to the other. A third architecture, the so called *planar-mixed heterojunction*, features an extended donor/acceptor interface (as compared to the planar heterojunction) at the same time as it prevents shunts and offers homogeneous layers of the appropriate material at each electrode. This architecture is illustrated in Figure 2.4 (c) and can be considered as a bulk heterojunction sandwiched between two layers of the neat donor and acceptor materials respectively.[41]

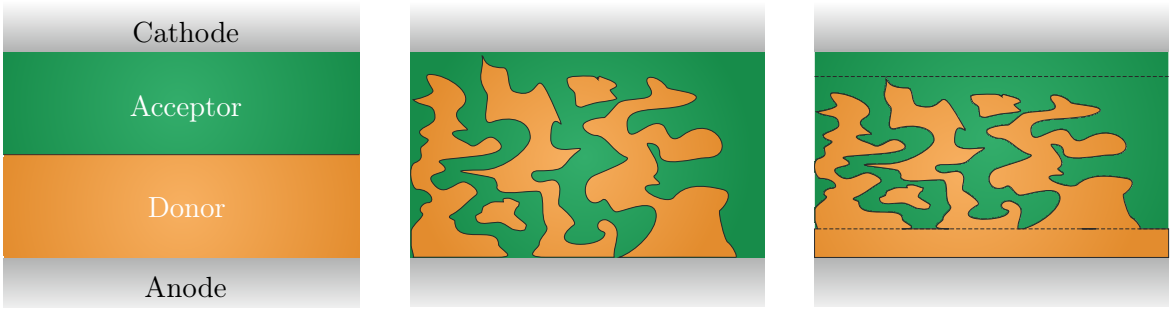

(a) Planar heterojunction (b) Bulk heterojunction (c) Planar-mixed

Figure 2.4: Different types of donor/acceptor heterojunction architectures in organic solar cells. (a) Planar heterojunction with defined, two dimensional donor/acceptor interface. (b) Bulk heterojunction with increased interface resulting from a blend of both materials. (c) Planar-mixed heterojunction with a donor/acceptor blend sandwiched between thin films of the respective neat material.

Organic photovoltaic cells commonly have a thickness of some hundred nanometers, matching the wavelength region from ultraviolet to infrared light. As a consequence interference effects of incident and reflected light by the electrodes cannot be neglected and lead to the formation of standing waves inside the device.[35] It is therefore crucial for the efficiency of the device, that the heterojunction resides at the maximum photon flux. While this is a minor problem for bulk and planar-mixed heterojunction cells, planar layouts have to be designed more carefully as the position of the junction – as well as the maximum photon flux – is shifted according to the thicknesses of the single layers. Since the optimum layer stack depends on the employed materials, the devices studied in the present work have not been optimized. Instead, a common thickness was chosen where all investigated devices work well, regardless of the material properties.

*$\eta_{\text{quenching}} = \eta_{\text{diffusion}} \times \eta_{\text{dissociation}}$

2.4 Solar cell device characteristics

A solar cell as an electronic device may be considered as a diode in parallel with a current source supplying the photocurrent density j_{ph}. In order to account for leakage currents through the real device, a shunt resistance R_{p} in parallel circuit to the diode is assumed. Finally all contact resistances are summarized in a series resistance R_{s}. This equivalent circuit is depicted in Figure 2.5, its current-voltage characteristics is described by the Shockley equation for diodes, extended by terms accounting for the parasitic resistances and the photocurrent[37]

$$j = j_0 \cdot \left[\exp\left(\frac{q(V - jR_{\mathrm{s}})}{nk_{\mathrm{B}}T}\right) - 1\right] + \frac{V - jR_{\mathrm{s}}}{R_{\mathrm{p}}} - j_{\mathrm{ph}} \quad , \tag{2.1}$$

where j_0 is the saturation current of the diode, q the elementary charge and k_{B} the Boltzmann constant. V represents the applied voltage, T the temperature and n denotes the so called ideality factor which is related to the prevailing recombination mechanism and takes typical values between 1 (direct recombination of free carriers) and 2 (trap assisted recombination).[42] Even though equation 2.1 was originally derived for inorgainc solar cells it was successfully used to describe the current-voltage characteristics of organic solar cells.[43] While the j-V curve measured without illumination (dark curve)

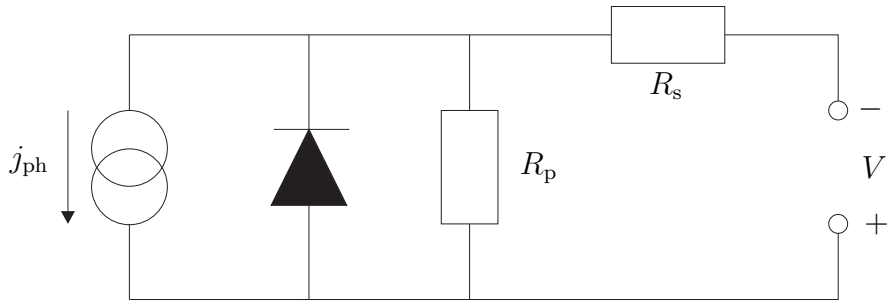

Figure 2.5: Equivalent circuit of a solar cell. j_{ph} is the generated photocurrent density, while R_{p} and R_{s} denote the shunt and series resistances, respectively.

resembles a typical diode curve as expressed by the Shockley equation, the characteristics measured under illumination (light curve) is shifted towards the negative current regime.

Figure 2.6 shows the corresponding curves calculated from Eq. 2.1. If no voltage is applied to the diode ($V = 0$), the solar cell is under short circuit conditions and the current flowing at this state is the so-called *short circuit current*. For convenience, however, it is more common to refer to the short circuit current density j_{sc} which is independent of the area of the solar cell and therefore more comparable. Strictly speaking, the measured short circuit current does not exactly equal the maximum photocurrent j_{ph}, which is only reached in reverse bias in most organic solar cells. The assumption of a constant photocurrent is also why Eq. 2.1 cannot predict the frequently observed

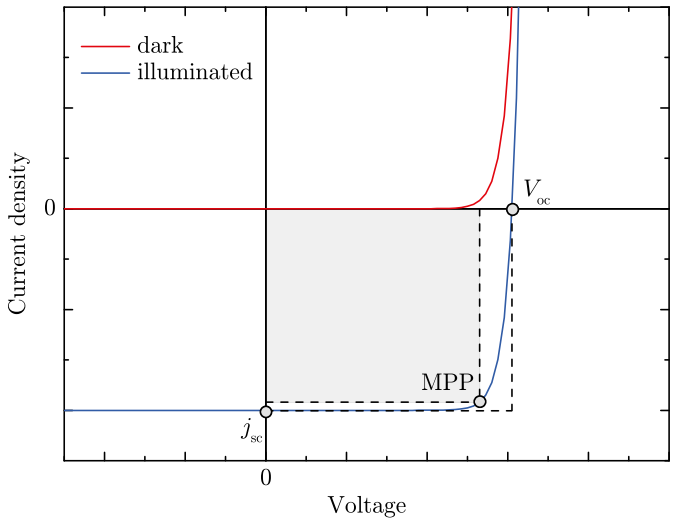

Figure 2.6: Solar cell current-voltage characteristics in the dark and under illumination for an ideal solar cell ($n = 1, R_s = 0, R_p \to \infty$). The characteristic quantities have been marked. The ratio between the gray rectangle and $j_{sc} \cdot V_{oc}$ defines the fill factor.

intersection of dark and light j-V curves of organic solar cells at the so-called compensation voltage. Yet, $j_{sc} \approx j_{ph}$ is typically assumed even for organic cells and often is a good approximation.

The voltage at which the photocurrent exactly compensates the dark current, thus that the net current vanishes ($j = 0$) is called *open circuit voltage* V_{oc}. This quantity is set by the splitting of the quasi-Fermi levels of electrons and holes generated by the incident light.[29,37] V_{oc} is hence related to the respective energies of electrons and holes and in principle determined by the donor HOMO and the acceptor LUMO, i.e. by the intermolecular energy gap. A detailed consideration of this relation is presented in Section 2.5.

In the range between the short circuit current and the open circuit voltage (i.e. where the $j \cdot V$ is negative) the device generates power and operates as a solar cell. The point of maximum power output is called *maximum power point* MPP and determines the operating point of the solar cell. At negative bias or at voltages above V_{oc} the device consumes power. An overview of the band conditions in the device at different bias voltages is given in Figure 2.7.

An important quantity to characterize a solar cell is the so-called fill factor FF. It is defined as the ratio between the maximum power output ($j_{MPP} \cdot V_{MPP}$) and the product of the short circuit current and the open circuit voltage ($j_{sc} \cdot V_{oc}$) and is a measure for the "squareness" of the curve. The *power conversion efficiency* (PCE) of a solar cell is defined as the ratio between the electrical power density generated by the solar cell and the intensity (i.e. power per unit area) of the incident light P_{in}. It can be expressed as follows:

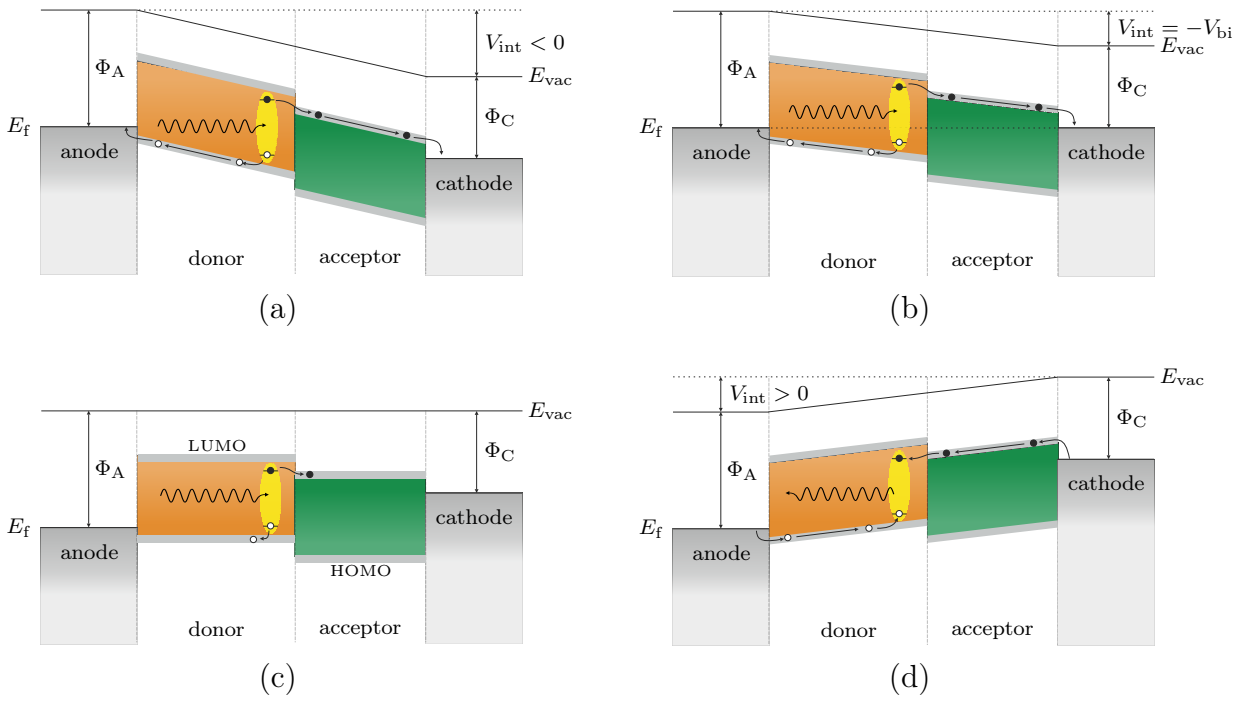

Figure 2.7: Band conditions of an organic solar cell. (a) Under reverse bias generated charge carriers are subjected to a strong electric field, the device operates as a photodetector. (b) In short circuit conditions the bands are tilted by the internal electric field caused by Fermi level alignment of electrode materials with different work functions. (c) Under flat band conditions the photocurrent is purely diffusion governed due to the absence of an internal electric field. (d) In forward bias charge carriers are injected from the electrodes: in principle the device works like a light emitting diode (LED). Note that the band conditions at V_{oc} are not *a priori* clear. In particular the open circuit voltage of planar heterojunctions may even exceed the built in potential V_{bi}, i.e. the difference of the electrode work functions.[44]

$$\mathrm{PCE} = \frac{P_{max}}{P_{in}} = \frac{j_{MPP} \cdot V_{MPP}}{P_{in}} = \frac{\mathrm{FF} \cdot j_{sc} \cdot V_{oc}}{P_{in}} \tag{2.2}$$

Thus for an efficient solar cell the values for the fill factor, the short circuit current and the open circuit voltage simultaneously need to be as large as possible.

A second measure for the performance of a photovoltaic cell is its *external quantum efficiency* (EQE) or *incident photon to current efficiency* (IPCE). While the power conversion efficiency is a measure for the overall efficiency under illumination with a certain spectrum of light, the external quantum efficiency accounts for the wavelength of the incident light. It is defined as

$$\mathrm{EQE}(\lambda) = \frac{hc}{q\lambda} \cdot S(\lambda) \tag{2.3}$$

where

$$S(\lambda) = \frac{j_{\mathrm{sc}}(\lambda)}{P_{\mathrm{in}}(\lambda)} \quad . \tag{2.4}$$

Here h is Planck's constant, c the speed of light and q the elementary charge. $j_{\mathrm{sc}}(\lambda)$ denotes the short circuit current density and $P_{\mathrm{in}}(\lambda)$ the intensity of the incoming light at the wavelength λ. S is called *spectral sensitivity* or *spectral response* and gives the current output to power input ratio at a certain wavelength in terms of unit current per unit power. By dividing j_{sc} by the elementary charge q and P_{in} by the energy of a single photon at wavelength λ ($\frac{hc}{\lambda}$) one gets the ratio of the number of output electrons to the number of incident photons at wavelength λ. This ratio is called the external quantum efficiency. Since the external quantum efficiency is essentially a quantum yield for a specific wavelength, it is a property of the device and independent of the light source used for the measurement. This renders the external quantum efficiency suitable for comparison of cells measured at different setups.

Even though the external quantum efficiency is of course related to the absorption spectra of the organic semiconductors building up the photoactive layer of the cell, they do not necessarily have to match: if, e.g. in planar heterojunction cells, the thickness of the donor layer is a lot larger than the exciton diffusion length, the photons of a wavelength where the donor absorbs well create excitons far away from the junction which therefore do not contribute to the photocurrent. At the same time only a very small amount of photons is left near the junction. This is called *inner filter effect* and leads to *antibatic* behavior of the device,[45] i.e. low efficiency where the device absorbs most light and higher efficiency where the absorption is less. This effect is, however, not expected for bulk heterojunction devices. As excitons can be separated throughout the whole device *symbatic* behavior is anticipated, which means that the external quantum efficiency matches the absorption spectra.

Due to the spectral sensitivity of a solar cell the power conversion efficiency is strongly dependent on the spectrum of the light source. In consequence intercomparison of power conversion efficiencies has to be treated with caution even if the overall illumination intensities are equal. For this reason standard testing conditions for rating the solar cell performance have been defined as follows: 25 °C device temperature, 100 mW/cm^2 irradiance and an air mass (AM) 1.5 global reference spectrum.[46] This is a simulated spectrum of the solar radiation reaching the surface of the earth under a solar zenith angle of 48.19° (corresponding to an air mass of 1.5) as defined in the International Electrotechnical Commission (IEC) Standard 60904-3[47] and the American Society for Testing and Materials (ASTM) Standard G173 (cf. Figure 2.8).

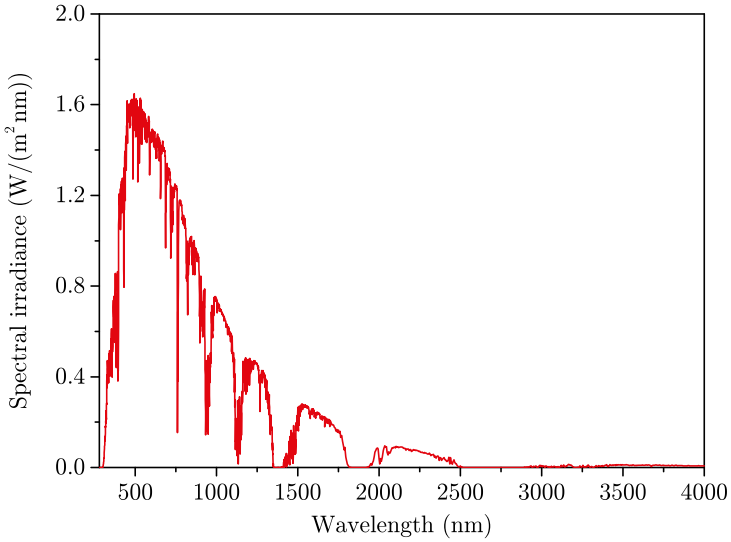

Figure 2.8: AM 1.5 global reference spectrum as defined by the IEC Standard 60904-3.[47]

2.5 The detailed balance limit

The detailed balance limit of a solar cell is a thermodynamic efficiency limit and has first been considered by Shockley and Queisser in 1961.[48] They predicted the thermodynamically possible efficiency of a single pn-(homo)junction to about 33 %. Recently, their model has been extended to describe organic solar cells, where the introduction of an energy offset at the heterojunction poses an intrinsic energy loss that further reduces the maximum possible efficiency.[49–53] In the following, these considerations are recapitulated with the focus on the open circuit voltage and how it is affected by the cell temperature.

2.5.1 The heterojunction as black body radiator

In this approach, both the sun and the solar cell are regarded as black body radiators at their specific temperatures ($T_s \approx 5778\,\mathrm{K}$ and $T \approx 300\,\mathrm{K}$). In accordance with Planck's law of radiation, the photon flux, i.e. the number of photons per unit area and per unit time, emitted by a black body at temperature T is given by the integral of the black body spectrum over all energies E. To account for the fraction of photons relevant for the photo-active material, the black body spectrum is additionally weighted by the absorption profile of the solar cell, yielding the photon flux that is absorbed by the cell:

$$\begin{aligned} N(T) &= \int_0^\infty \alpha(E) \times n(E,T) dE \\ &= \int_0^\infty \alpha(E) \times \frac{1}{4\pi^2\hbar^3c^2} \left(\exp\left(\frac{E}{k_\mathrm{B}T}\right) - 1 \right)^{-1} E^2 dE \end{aligned} \tag{2.5}$$

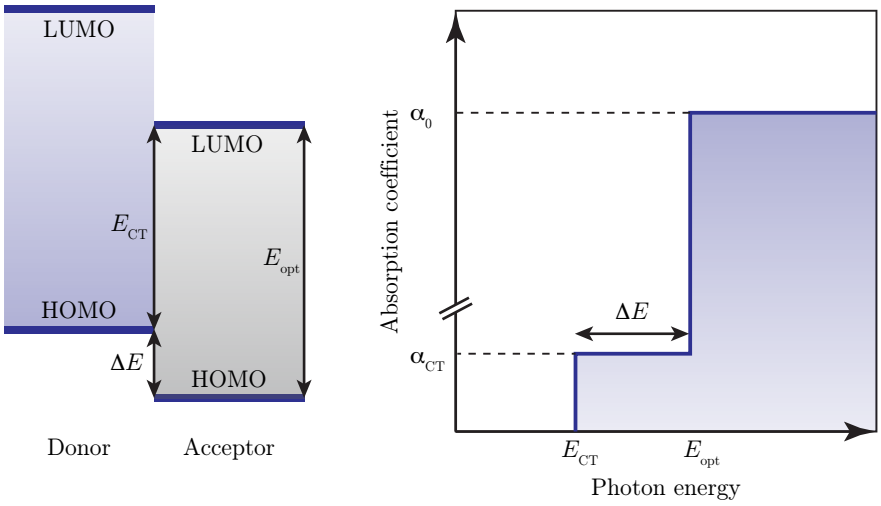

Figure 2.9: Schematic illustration of the idealized step absorption profile, resulting from the E_{CT} and E_{opt} energy steps of the donor/acceptor heterojunction.

Here $\hbar$ is the reduced Planck constant, c the speed of light and k_B is the Boltzmann constant. For a conventional pn-junction, α equals 0 for photon energies below the band gap and 1 for photon energies above the band gap of the semiconductor, if a step function is assumed in the limit of full absorption above the band gap.

The situation changes slightly for a heterojunction of two different (not necessarily organic) semiconductors: The absorption onset is no longer given by the optical gap of either of the semiconductors in this case. Instead, a charge transfer (CT) process, where an electron is excited from an occupied state of one semiconductor to an unoccupied state of the other semiconductor, enables additional absorption at photon energies below the smallest individual band gap (cf. Figure 2.9). Thus the absorption profile contains two steps and is given by:[51]

$$\alpha(E) = \begin{cases} 0 & : E < E_{CT} \\ \alpha_{CT} & : E_{CT} < E < E_{opt} \\ \alpha_0 \equiv 1 & : E > E_{opt} \end{cases}, \tag{2.6}$$

where E_{opt} denotes the smaller optical gap of both semiconductors and E_{CT} the charge transfer energy. α_{CT} denotes the absorption strength of the CT transition relative to α_0.

The short circuit current j_{sc} in the radiative limit can now be calculated by Eq. 2.5 from the number of photons emitted by the sun (approximated as black body radiator at 5778 K) and absorbed by the solar cell. Note that since the sun isotropically emits its radiation into all space, only a fraction of $s = 2.18 \times 10^{-5}$ of the photons reach the surface of the earth.[53] If every absorbed photon generates one electron-hole pair, the short circuit current is given by $j_{sc} = q \cdot sN(T = 5778\,\mathrm{K})$, where q is the elementary charge.

On the other hand, Eq. 2.5 can be used to calculate the photon flux emitted by the

solar cell as required by Kirchhoff's law of radiation.[54] The origin of the generation of photons is the recombination of electrons and holes. This may be expressed as a recombination current for a solar cell at a temperature of 300 K:

$$j_{0,\mathrm{rad}} = q \cdot N(T = 300\,\mathrm{K}) \tag{2.7}$$

This quantity can be extracted as the reverse saturation current j_0 from an ideal device, if radiative recombination, i.e. emission of photons, is the only allowed recombination mechanism. Then, the detailed balance also requires that in equilibrium the amount of absorbed photons equals the amount of emitted photons, if no net current flows. The latter is fulfilled under open circuit conditions. An expression for V_{oc} can be derived from the Shockley equation (2.1) for an ideal ($n = 1, R_{\mathrm{s}} = 0, R_{\mathrm{p}} \to \infty$) solar cell under illumination:

$$V_{\mathrm{oc}} = \frac{k_{\mathrm{B}}T}{q} \ln\left(\frac{j_{\mathrm{sc}}}{j_0} + 1\right) \tag{2.8}$$

This expression shows that V_{oc} is reduced by the reverse saturation current. Note that j_0 is not generally limited to (thermodynamically inevitable) radiative recombination but contains an additional contribution from non-radiative processes, thus that the reverse saturation current is given by

$$j_0 = j_{0,\mathrm{rad}} + j_{0,\mathrm{non}} \tag{2.9}$$

As a direct consequence, the open circuit voltage of a solar cell is maximal in the radiative limit, i.e. if $j_{0,\mathrm{non}} = 0$. This also implies that an ideal solar cell simultaneously is an ideal light emitting diode, from a photonic point of view. Note, however, that even in the thermodynamically ideal case entropic losses are present caused by the difference of the solid angle under which the sun appears on earth and the solid angle into which emission from the solar cell occurs.[55] In terms of V_{oc} this amounts to an intrinsic loss of about 300 mV compared to the photovoltaic gap.[17]

2.5.2 The coupling factor

Equation 2.8 relates the open circuit voltage to the short circuit current and the dark saturation current. This can be extended to relate V_{oc} to the photovoltaic gap E_{PVG} of the solar cell by inserting the following expression into Eq. 2.8:[29]

$$j_0 = j_{00} \cdot \exp\left(\frac{-E_{\mathrm{PVG}}}{k_{\mathrm{B}}T}\right) \tag{2.10}$$

Here j_{00} denotes the coupling factor that is generally assumed to be a constant accounting for the electronic coupling strength of the material system.[56–59] Under the assumption $j_{\mathrm{sc}}/j_0 \gg 1$, Eq.2.8 and Eq.2.10 yield the commonly found relation

$$qV_{\mathrm{oc}} \approx E_{\mathrm{PVG}} - k_{\mathrm{B}}T \cdot \ln\left(\frac{j_{00}}{j_{\mathrm{sc}}}\right). \tag{2.11}$$

Equation 2.11 implies a linear temperature dependence of the V_{oc}, which approaches a value of E_{PVG}/q at absolute zero. A linear extrapolation to 0 K of the V_{oc} measured at a series of temperatures is thus widely used in order to experimentally determine E_{PVG}.[53,59–61] In the context of organic heterojunction solar cells E_{PVG} is oftentimes identified with the energy of the charge transfer state E_{CT}, even if various terms for slightly different experimental conditions are used.[53,56,57,59,61–63] It is important to note that this identification is *not a priori* made here.

Simulated temperature dependences of the open circuit voltage (calculated by Eq. 2.8) for a broad range of α_{CT} are shown in Figure 2.10 (a). Similar to Ref. 53, values of $E_{opt} = 1.9\,\text{eV}$ and $E_{CT} = 1.4\,\text{eV}$ have been chosen, corresponding to a heterojunction of diindenoperylene (DIP) and the C_{60} fullerene. As was already shown by Gruber *et al.*, the V_{oc} indeed shows an almost perfectly linear temperature dependence down to 0 K for α_{CT} values relevant for the DIP/C_{60} solar cell, while for very low α_{CT} the open circuit voltage at finite temperature may exceed E_{CT}/q. In the extreme case of $\alpha_{CT} = 0$ (dashed line Figure 2.10 (a)) the device behaves like a classical homojunction with a band gap of 1.9 eV.[53]

In order to understand the occurrence of the kink of V_{oc} observed for low α_{CT} values, we have to take a closer look into Eq. 2.7 and Eq. 2.5. For a bi-step function as given by Eq. 2.6 the integral can be solved analytically and yields:

$$N(T) = Ak_BT\left[\alpha_{CT}\gamma_{CT}(T)\exp\left(\frac{-E_{CT}}{k_BT}\right) + (\alpha_0 - \alpha_{CT})\gamma_{opt}(T)\exp\left(\frac{-E_{opt}}{k_BT}\right)\right] \quad (2.12)$$

where $A = 1/(4\pi^2\hbar^3c^2)$ and the parameters γ_{CT} and γ_{opt} are given by:

$$\begin{aligned}\gamma_{CT}(T) &= E_{CT}^2 + 2k_BTE_{CT} + 2k_B^2T^2\\ \gamma_{opt}(T) &= E_{opt}^2 + 2k_BTE_{opt} + 2k_B^2T^2\end{aligned} \quad (2.13)$$

And thus:

$$j_0 = \underbrace{qAk_BT\left[\alpha_{CT}\gamma_{CT}(T) + (\alpha_0 - \alpha_{CT})\gamma_{opt}(T)\exp\left(\frac{E_{CT} - E_{opt}}{k_BT}\right)\right]}_{j_{00}}\exp\left(\frac{-E_{CT}}{k_BT}\right) \quad (2.14)$$

This expression has the structure of Eq. 2.10, where E_{PVG} formally is identified with E_{CT}. Be aware that the factoring in Eq. 2.14 was an arbitrary choice. A similar expression can be derived that formally identifies E_{PVG} with E_{opt}. This does, however, not affect the general message of the following consideration.

Sticking to this choice, Eq. 2.14 yields an expression for j_{00}:

$$j_{00} = qAk_BT\Bigg[\underbrace{\alpha_{CT}\gamma_{CT}(T)}_{\text{emission via } E_{CT}} + \underbrace{(\alpha_0 - \alpha_{CT})\gamma_{opt}(T)\exp\left(\frac{E_{CT} - E_{opt}}{k_BT}\right)}_{\text{emission via } E_{opt}}\Bigg] \quad (2.15)$$

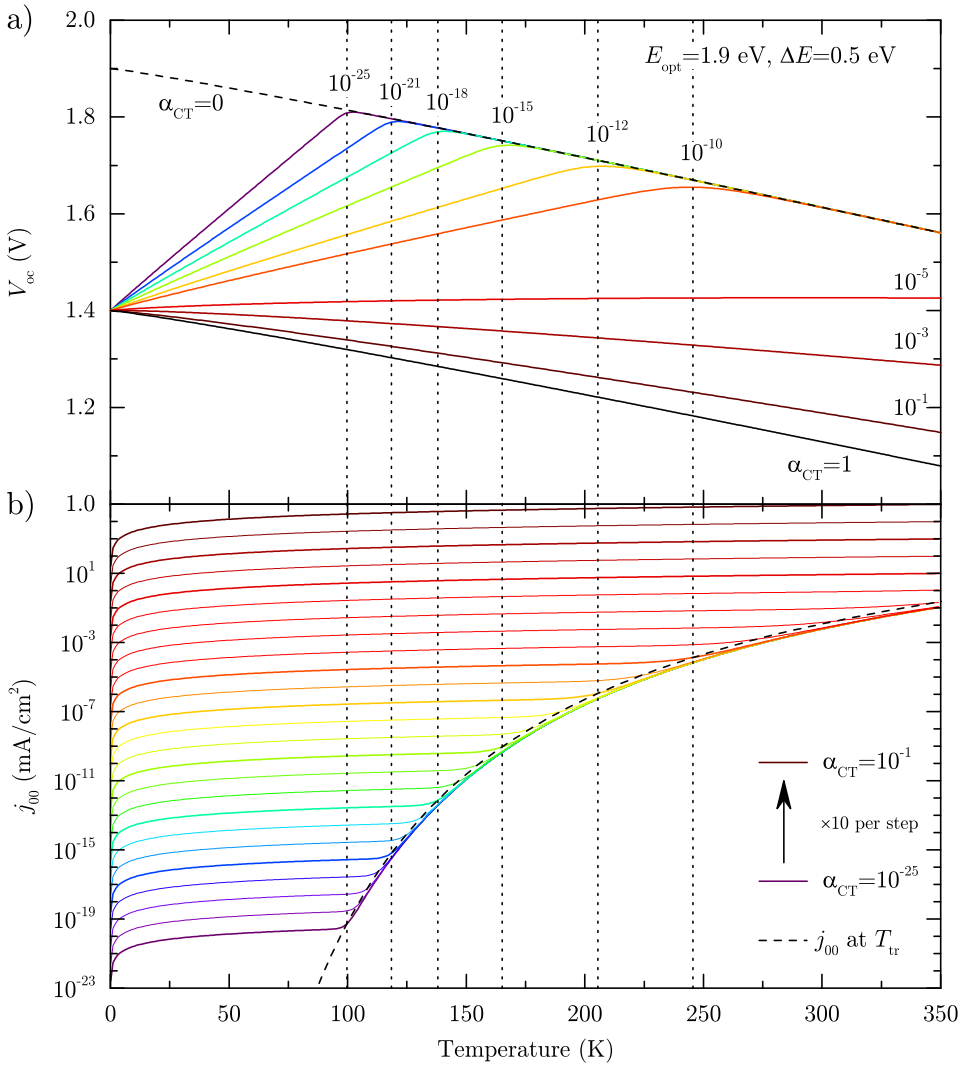

Figure 2.10: Simulation of the temperature dependence of the open circuit voltage (a) and the coupling factor (b) of an ideal solar cell for a variation of α_{CT}. E_{opt} and ΔE have been chosen to match the material system DIP/C_{60}. For calculation of V_{oc} from Eq. 2.8, the short circuit current was calculated from the spectrum of a black body at the temperature of the sun. For clarity, only a subset of the α_{CT} values is shown in (a). The transition temperature for this subset is indicated by the vertical, dashed lines.

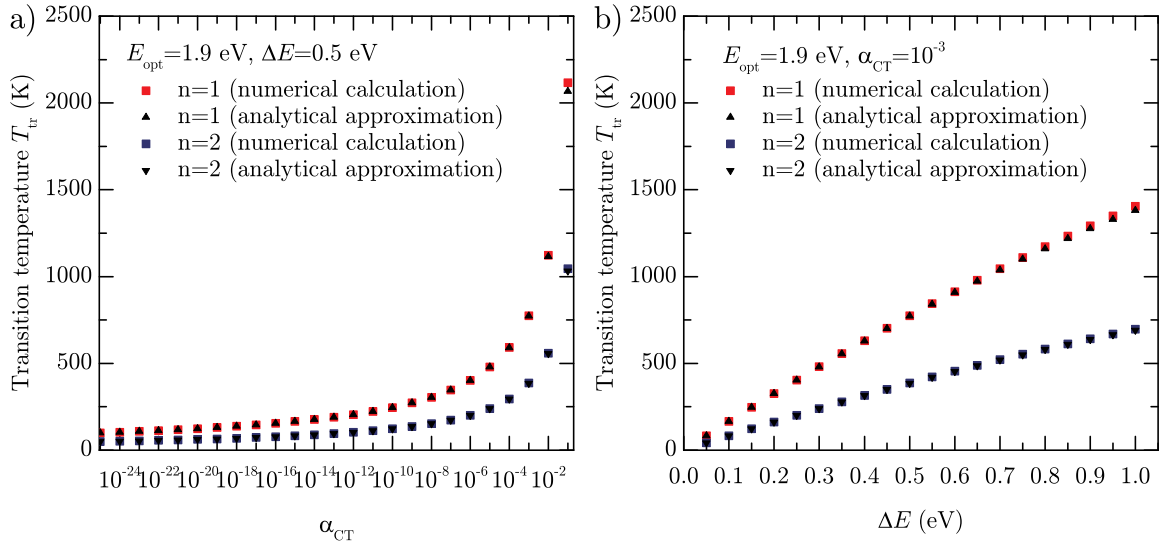

Figure 2.11: Dependence of the transition temperature on α_{CT} (a) and ΔE (b). The blue curves have been calculated under the assumption $n = n_{CT} = n_{opt} = 2$ (see section 2.5.3).

In contrast to the common treatment (i.e. exploiting Eq. 2.10), this is utterly dependent on temperature as illustrated in Figure 2.10 (b). In particular, two terms with different temperature dependence can be identified. The first term is responsible for emission via the CT state, the second describes emission via the optical gap of the system. Depending on the temperature, one of the two terms is dominant, thus that a *transition temperature* T_{tr} can be defined as the temperature where both contributions are equal:

$$\alpha_{CT}\gamma_{CT}(T_{tr}) \stackrel{!}{=} (\alpha_0 - \alpha_{CT})\gamma_{opt}(T_{tr})\exp\left(\frac{E_{CT} - E_{opt}}{k_B T_{tr}}\right) \tag{2.16}$$

This equation can only be solved numerically. However, for sufficiently low temperatures (typically below 2000 K) the parameters γ reduce to $\gamma_{CT}(T) \approx E_{CT}^2$ and $\gamma_{opt}(T) \approx E_{opt}^2$ and an analytical approximation of T_{tr} is possible:

$$T_{tr} \approx \frac{\Delta E}{k_B\left[\ln\left(\alpha_{CT}E_{CT}^2\right) - \ln\left((\alpha_0 - \alpha_{CT})E_{opt}^2\right)\right]} \tag{2.17}$$

where $\Delta E = E_{CT} - E_{opt}$ denotes the energy difference between the optical gap of the absorber and the CT energy. It is worth noting that the transition temperature does not depend on the choice of factoring in Eq. 2.14. It does, however, clearly depend on α_{CT} and ΔE. Figure 2.11 shows this dependency and additionally illustrates that the analytical approximation almost perfectly matches the numerical calculation of T_{tr} for practically relevant temperatures. In principal T_{tr} not only depends on ΔE but also on the absolute values of E_{opt} and E_{CT}, yet their influence is small. (Note that Figure 2.11 also shows T_{tr} calculated with an ideality factor of $n = 2$. The introduction of n is not quite straight forward and will be discussed separately.)

The transition temperature for the corresponding α_{CT} values is indicated as the vertical, dashed lines in Figure 2.10. It is clearly visible that T_{tr} marks the kink in both the V_{oc} and the j_{00} curves. The value of j_{00} at the respective transition temperature is indicated by the dashed curve in Figure 2.10 (b). The curve shapes are distinctly different left and right of the transition temperature and, except for a small transition region, the coupling is clearly dominated by the contribution of recombination either via the CT ($T < T_{\mathrm{tr}}$) or via the optical ($T > T_{\mathrm{tr}}$) gap. From Figure 2.10 (a) it becomes now obvious that a linear extrapolation of the V_{oc} at temperatures larger than T_{tr} will result in a photovoltaic gap that is close to E_{opt}. If V_{oc} values below T_{tr} are extrapolated, a value of $E_{\mathrm{PVG}} \approx E_{\mathrm{CT}}$ will be extracted.

Mathematically, this can be derived if Eq. 2.14 is considered in the respective temperature regime:

$$j_0 \approx \begin{cases} qAk_{\mathrm{B}}T \cdot \alpha_{\mathrm{CT}}\gamma_{\mathrm{CT}}(T) \cdot \exp\left(\frac{-E_{\mathrm{CT}}}{k_{\mathrm{B}}T}\right) & : T < T_{\mathrm{tr}} \\ qAk_{\mathrm{B}}T \cdot (\alpha_0 - \alpha_{\mathrm{CT}})\gamma_{\mathrm{opt}}(T) \cdot \exp\left(\frac{-E_{\mathrm{opt}}}{k_{\mathrm{B}}T}\right) & : T > T_{\mathrm{tr}} \end{cases} \tag{2.18}$$

Together with Eq. 2.8, this yields:

$$qV_{\mathrm{oc}} \approx \begin{cases} E_{\mathrm{CT}} - k_{\mathrm{B}}T \cdot \ln\left(\frac{j_{00}}{j_{\mathrm{sc}}}\right) & : T < T_{\mathrm{tr}} \\ E_{\mathrm{opt}} - k_{\mathrm{B}}T \cdot \ln\left(\frac{j_{00}}{j_{\mathrm{sc}}}\right) & : T > T_{\mathrm{tr}} \end{cases} \tag{2.19}$$

Thus, comparison to Eq. 2.11 shows that the identification of E_{PVG} with either E_{CT} or E_{opt}, cannot generally be made but depends on the temperature regime the solar cell is operated in. Please note that j_{00} as used in Eqs. 2.19 and 2.18 still contains a slight temperature dependence, which leads to a minor overestimation of E_{PVG} if the temperature dependence of V_{oc} is extrapolated to 0,K, as shown by Gruber *et al.*.[53]

A second method to experimentally determine the value of E_{PVG} from the actual device is analyzing the behavior of the dark saturation current with temperature. According to Eq. 2.10 the following relation can be used to extract E_{PVG} from the slope of $\ln(j_0)$ plotted against $1/k_{\mathrm{B}}T$:

$$\ln(j_0) = \frac{-E_{\mathrm{PVG}}}{k_{\mathrm{B}}T} + \ln(j_{00}) \tag{2.20}$$

This is demonstrated in Figure 2.12 for a DIP/C_{60} solar cell with a hypothetical α_{CT} of 1×10^{-10} in the radiative limit. As expected from Eq. 2.18, the slope of the curve changes (more or less abruptly) at the transition temperature and E_{CT} and E_{opt} are extracted for temperatures below and above T_{tr}, respectively.

Recent publications experimentally identify E_{PVG} with E_{CT} for a broad range of material systems.[57,59–64] This implies that the transition temperature is above the typical operating temperature for a lot of real solar cell devices. Still, this is not necessarily the case for all solar cells and we will later see a material system where the transition temperature appears to be below room temperature.

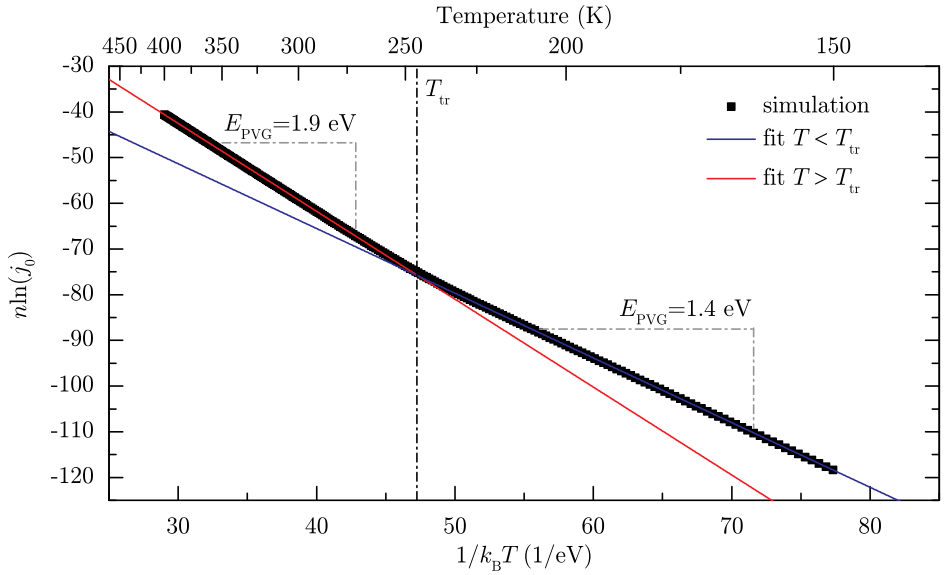

Figure 2.12: Extraction of the photovoltaic gap from the dark saturation current. Different values are found in the regimes above and below the transition temperature. For temperatures above T_{tr}, $E_{PVG} = E_{opt}$ is extracted, for temperatures below T_{tr}, $E_{PVG} = E_{CT}$ is found.

2.5.3 Non-radiative recombination

So far, only ideal solar cells in the radiative limit have been discussed. Recombination in real devices, however, can usually not simply be described by radiative recombination of two free charge carriers any more. Instead, non-radiative recombination processes play an important or even dominant role. In the simulations by Gruber *et al.* this was successfully accounted for by the introduction of a constant $\beta = j_{0,non}/j_{0,rad}$ that linearly connects the non-radiative recombination to the radiative recombination current, thus that the total dark saturation current is given by:[53]

$$j_0 = (1 + \beta) j_{0,rad} \tag{2.21}$$

From an electrical characterization perspective, a more common approach is the introduction of so called *ideality factors* that enable description of non-ideal solar cells to the Shockley equation (n in Eq. 2.1) and to Eq. 2.10, which then reads

$$j_0 = j_{00} \cdot \exp\left(\frac{-E_{PVG}}{n' k_B T}\right) \tag{2.22}$$

Note that, following the notation of Potscavage *et. al.*,[56] two *a priori* different ideality factors n and n' have been introduced. Consequently, the open circuit voltage is then expressed by:

$$qV_{oc} \approx \frac{n}{n'} E_{PVG} - n k_B T \cdot \ln\left(\frac{j_{00}}{j_{sc}}\right) \tag{2.23}$$

In accordance with the common practice to regard n and n' as identical parameters, Potscavage *et al.* have noted that their difference is expected to be small.[56] This is

also in agreement with the above mentioned fact that (now) $\frac{n}{n'}E_{\mathrm{PVG}}$ has been found to be identical with the energy of the CT state for a lot of heterojunctions. Hence, in the following $n = n'$ is assumed. While there is an ongoing discussion on the physical interpretation of the ideality factor, n is typically expected to range from 1 to 2, where $n = 1$ is expected to describe simple direct recombination of free charge carriers (see Section 5.3.1).[65]

Eq. 2.23 demonstrates the implicitly assumed but practically relevant fact that V_{oc} scales linearly with temperature as long as the ideality factor is constant. This implies that E_{PVG} can still be extracted from temperature dependent V_{oc} measurements by linear extrapolation to 0 K regardless of the value of n. As an interesting consequence, an approximation of measured $V_{\mathrm{oc}}(T)$ data can be modeled with different ideality factors, if the parameter β is adjusted, accordingly. This is demonstrated in Figure 2.13 for a DIP/C_{60} solar cell. While simulations with both values of n describe the temperature dependence of V_{oc} equally well, the values of j_0 are closer to those retrieved from a fit to the solar cell characteristics, if n is set to values larger than one. As expected, the results appear thus more realistic if n is close to values determined from a fit to real data. Note that in this type of simulation, the parameters α_{CT} and β have the same effect. However, α_{CT} for this solar cell has been estimated experimentally to 1.5×10^{-4}.[53] If this value is used, β is reduced from about 10^7 to 9×10^4, if n is set to 1.3. The fact that β is still non-zero suggests that the introduction of the ideality factor only accounts for a part of the non-radiative recombination. In particular, direct recombination of free charge carriers with one another occurs not only radiatively and by far not all generated photons are also emitted from the solar cell device. Despite the ongoing discussion on the exact meaning of the ideality factor, n should at least not account for the latter.

Impact of the ideality factor on the transition temperature

As suggested from Eq. 2.18, it cannot generally be assumed that the ideality factors are identical for recombination via E_{CT} and E_{opt}. Two different ideality factors n_{CT} and n_{opt} are thus introduced for the respective temperature regimes. This has severe effects on the transition temperature T_{tr} as Eq. 2.16 transforms to:

$$\alpha_{\mathrm{CT}}\gamma_{\mathrm{CT}}(T_{\mathrm{tr}}) \stackrel{!}{=} (\alpha_0 - \alpha_{\mathrm{CT}})\gamma_{\mathrm{opt}}(T_{\mathrm{tr}})\exp\left(\frac{\frac{1}{n_{\mathrm{CT}}}E_{\mathrm{CT}} - \frac{1}{n_{\mathrm{opt}}}E_{\mathrm{opt}}}{k_{\mathrm{B}}T_{\mathrm{tr}}}\right) \tag{2.24}$$

The analytical approximation then reads:

$$T_{\mathrm{tr}} \approx \frac{\frac{1}{n_{\mathrm{CT}}}E_{\mathrm{CT}} - \frac{1}{n_{\mathrm{opt}}}E_{\mathrm{opt}}}{k_{\mathrm{B}}\left[\ln\left(\alpha_{\mathrm{CT}}E_{\mathrm{CT}}^2\right) - \ln\left((\alpha_0 - \alpha_{\mathrm{CT}})E_{\mathrm{opt}}^2\right)\right]} \tag{2.25}$$

With respect to the ideal case, the transition temperature is hence changed by a factor:

$$\frac{T_{\mathrm{tr}}}{T_{\mathrm{tr,ideal}}} \approx \frac{1}{n_{\mathrm{CT}}} + \left(\frac{1}{n_{\mathrm{CT}}} - \frac{1}{n_{\mathrm{opt}}}\right)\frac{E_{\mathrm{opt}}}{\Delta E} \stackrel{\Delta E<0}{=} \frac{1}{n_{\mathrm{CT}}} + \left(\frac{1}{n_{\mathrm{opt}}} - \frac{1}{n_{\mathrm{CT}}}\right)\frac{E_{\mathrm{opt}}}{|\Delta E|} \tag{2.26}$$

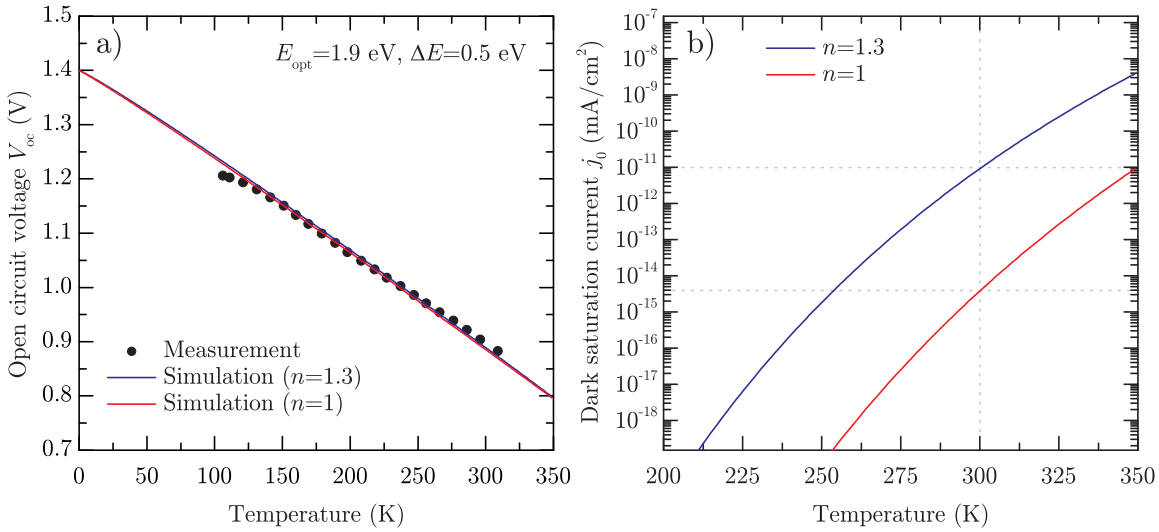

Figure 2.13: Demonstration of the possibility to model the temperature dependence of V_{oc} with different ideality factors. Here, for both $n = 1$ and $n = 1.3$ the V_{oc} data of a DIP/C_{60} junction are modeled equally well (a). The corresponding calculated dark saturation currents are shown in (b).

The dependence of the transition temperature on n_{CT} and n_{opt} is shown in Figure 2.14. The simulations have been performed by solving Eq. 2.24 for different configurations of E_{CT} and E_{opt} that match the material systems α-sexithiophene (6T)/C_{60} (a), DIP/C_{60} (b), and 6T/DIP (c) and a hypothetic α_{CT} of 1×10^{-3}. The values of ΔE of these systems are 0.95 eV, 0.5 eV and 0.3 eV, respectively. In accordance with Figure 2.11 T_{tr} is generally lower for smaller values of ΔE, that is if E_{CT} and E_{opt} are closer to each other. Moreover, the transition temperature shifts in favor of the recombination process with the larger ideality factor, i.e. for otherwise identical conditions, T_{tr} is lower if $n_{opt} > n_{CT}$ and vice versa. More importantly, the white areas in Figure 2.14 (b) and (c) mark n_{CT}, n_{opt} combinations, where the transition temperature would be negative. The border of this area is marked by a line, where Eq. 2.26 becomes 0. This implies that for some material systems, certain conditions may exist, where no transition occurs at finite temperatures. Strikingly, the CT energy would be expected to be practically irrelevant for such a heterojunction.

To illustrate the effect of α_{CT} on the transition temperature, Figure 2.14 (d) shows the DIP/C_{60} system with a hypothetic α_{CT} of 1×10^{-10}. As expected from Figure 2.11 (a) the overall value of T_{tr} is reduced.

These considerations show that depending on the combination of the ideality factors the transition temperature can shift by over 2000 K for common material systems. The idealtiy factor is usually only known in one of the two regimes and even there, different analysis methods can sometimes yield different results. It is thus utterly difficult to predict T_{tr}. If the optical gap of the absorber or the CT energy is known, however, the two methods to extract E_{PVG} from the device characteristics described above can be

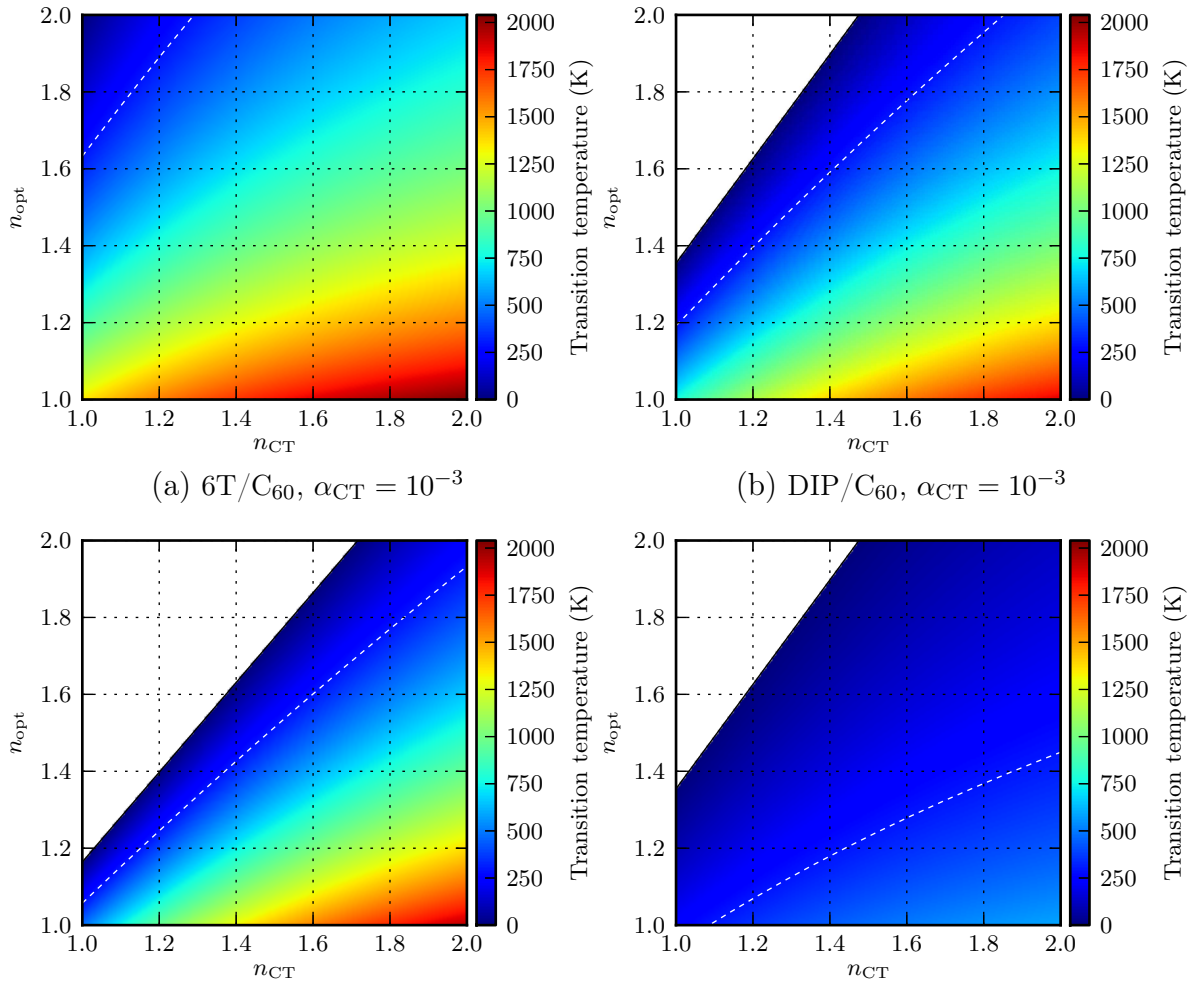

(a) 6T/C_{60}, $\alpha_{\mathrm{CT}} = 10^{-3}$

(b) DIP/C_{60}, $\alpha_{\mathrm{CT}} = 10^{-3}$

(c) 6T/DIP, $\alpha_{\mathrm{CT}} = 10^{-3}$

(d) DIP/C_{60}, $\alpha_{\mathrm{CT}} = 10^{-10}$

Figure 2.14: Influence of the introduction of ideality factors n_{CT} and n_{opt} on the transition temperature. The energies E_{opt} and E_{CT} have been chosen to correspond to three different material systems in (a), (b) and (c). The white areas in (b) and (c) show that under certain conditions, a finite transition temperature does not exist. To demonstrate the influence of α_{CT}, the DIP/C_{60} system was simulated with two different values of α_{CT} in (b) and (d). The white, dashed line marks $T_{\mathrm{tr}} = 300\,K$.

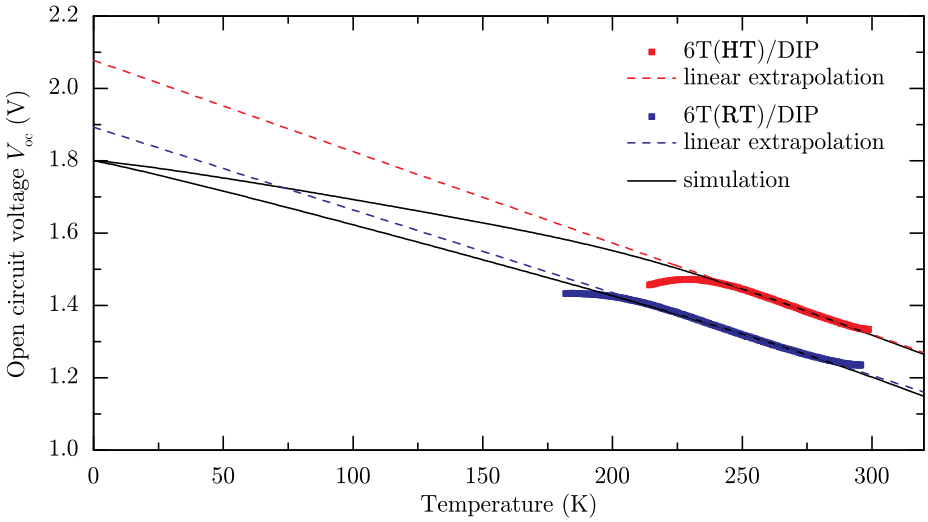

Figure 2.15: Comparison of the V_{oc} of two differently prepared 6T/DIP heterojunctions. If the 6T film is grown at 100 °C, the linear extrapolation identifies E_{PVG} with the optical gap of DIP. If 6T is grown at room temperature, a value close to the CT gap is extracted. The black lines show that both solar cells can be modeled with the same values $E_{opt} = 2.1$ and $E_{CT} = 1.8$. The parameters used for the 6T(HT)/DIP device are $\alpha_{CT} = 6.5 \times 10^{-4}$, $n = 2$ and $\beta = 0.5$. For the 6T(RT)/DIP device $\alpha_{CT} = 1 \times 10^{-3}$, $n = 1.55$ and $\beta = 2 \times 10^{3}$.

used to identify the temperature regime the cell is operated in.

In the case of the DIP/C_{60} solar cell demonstrated above, the extracted value for E_{PVG} is 1.4 eV and matches perfectly with the intermolecular HOMO-LUMO offset determined by photoelectron spectroscopy.[63] As for many other material system, it can thus be concluded that recombination via the CT energy is the dominating process at the operating temperature. Hence, the transition temperature has to be above 300 K.

Still, this is not necessarily the case for all solar cells. Specifically, the open circuit voltage of solar cells based on the donor 6T and DIP as acceptor has been shown to depend on the preparation conditions of the device.[66] Temperature dependent electrical device characterization shows that this is caused by a change of the photovoltaic gap. As shown in Figure 2.15 values of qV_{oc} of 1.9 eV and 2.1 eV are extracted from a linear extrapolation of V_{oc} to 0 K, depending on the preparation condition.

The CT gap of this system was determined to 1.8 ± 0.15 eV by UPS.[63] This is in good agreement with the 1.9 eV extracted from devices where the 6T film is grown at room temperature. The optical gap of DIP is estimated to 2.1 eV,[53] which perfectly matches the photovoltaic gap extracted for 6T/DIP solar cells where the 6T film was grown at 100 °C. The morphological changes induced by the preparation conditions thus appear to drastically reduce the transition temperature and thus shift the operating regime above T_{tr}.

The black lines in Figure 2.15 are simulated curves that illustrate that both cells can be modeled with the same values of E_{CT} and E_{opt}. Note that the device with the 6T layer grown at 100 °C was modeled with a single value for n_{opt} and n_{CT}, since no

experimental information about n_{CT} is available. In this case, however, setting n_{CT} to the experimental value of $n \approx 2$ provides an upper limit for the transition temperature (cf. Figure 2.14 (c)). Yet, additional uncertainty is added by the parameter β, which may shift T_{tr} in a manner similar to the ideality factor. Since no information on the value of β in either regime is available, the introduction of two additional parameters is not useful. Hence, a possible mismatch of β for recombination via the CT gap and the optical gap has been disregarded in the simulation. These problems do not occur for the simulation of the room temperature prepared device, as only one regime is modeled in this case.

The dark saturation current of this system has previously been analyzed by Dr. Julia Kraus. In accordance with the extrapolation of V_{oc} a photovoltaic gap of 2.1 eV was found for the case where 6T was grown at 100 °C. For the room temperature prepared device, however, the extracted value is about 2.0 eV and thus too large.[67] This might be an indication that the measured temperature range is close to T_{tr} and might possibly overlap with part of the transition regime. As can be seen from Figure 2.12, a linear fit across the transition regime would result in an E_{PVG} value between E_{CT} and E_{opt}. A detailed discussion of these particular photovoltaic cells is presented in Section 5.2.3.

Note that a possible way to experimentally access the value of β could be the operation of the solar cell as an LED. A correspondence $EQE_{EL} = \frac{1}{1+\beta}$ between β, as defined in Eq. 2.21, and the electroluminescence external quantum efficiency is expected for $n = 1$.[55,68] If the ideality factor is included a similar relation is expected as $EQE_{EL} = \frac{1}{(1+\beta)^n}$. It is important to note that EQE_{EL} is generally voltage dependent thus that an experimental value would have to be determined as close to V_{oc} as possible. An alternative way by calculation from the solar cell IPCE has been reported in the literature.[69]

If EQE_{EL} can be measured spectrally resolved, a separation of the emission via the CT state and the optical gap of the absorber might be possible. This might then allow the calculation of the transition temperature based on experimentally determined quantities.

Chapter 3

Materials and Sample Preparation

The contents of this chapter have been taken literally from earlier work "Characterization of planar and diffuse heterojunction solar cells based on poly(3-hexylthiophene)" (Ref. 22) and have been extended or updated where appropriate.

3.1 Organic materials

In the following the organic materials used and studied in this work are briefly introduced. Their respective structural formulae and an overview of their energy levels in thin films are shown in Figure 3.1. Note that the given energy values are collected from a broad range of literature sources and should be regarded as a rough guide for identification of possible donor/acceptor combinations. The exact energy level alignment can only be determined by direct measurement in the respective layer stack.[70,71]

3.1.1 α-sexithiophene

α-sexithiophene (6T) is a rod shaped oligothiophene with a molecule length of about 2.7 nm built-up by six thiophene rings.[76] It has served as a prototypical material for the study of basic organic semiconductor properties and especially as a controllable model system for the important polymer class of polythiophenes. 6T has intensively been studied since the late 1980s.[77] It forms a herring bone structure in single crystals, whereas different polymorphs have been found in thin films.[78,79] Additionally, the orientation of the 6T molecules in thin films has been reported to depend strongly on growth conditions such as the deposition rate, substrate temperature and the substrate itself.[79–82] An immediate consequence is that the properties of 6T films directly relevant for electronic devices, such as optical properties or charge carrier mobilities, depend critically on the growth conditions.[79,81,83] In particular a difference in the bulk mobility of almost three

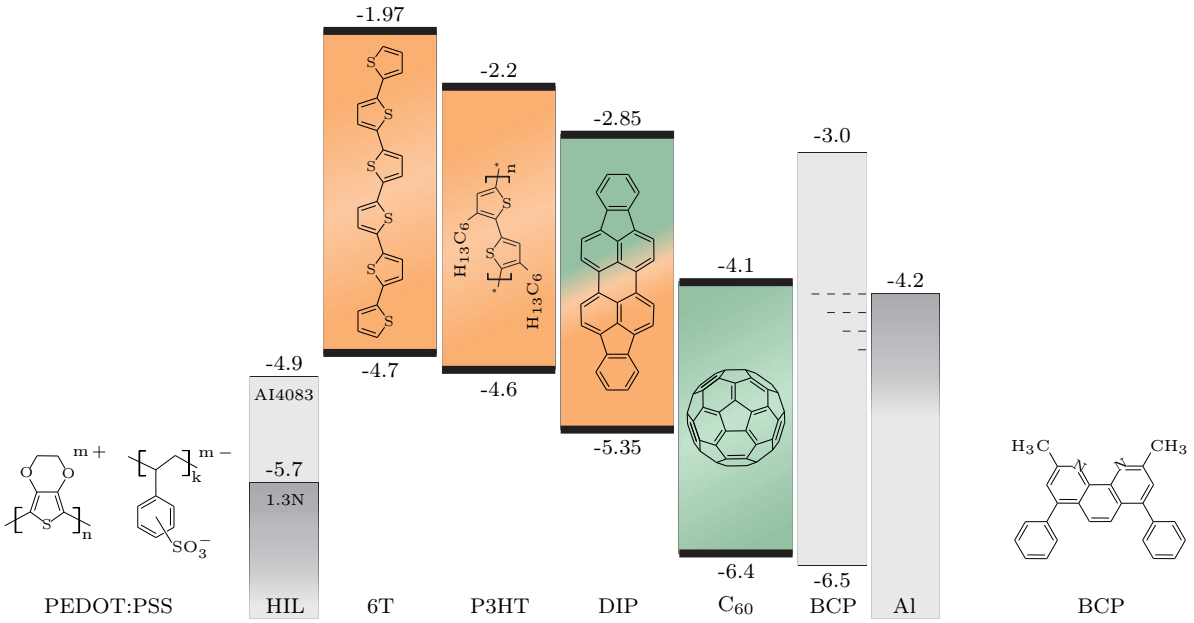

Figure 3.1: Schematic drawing of molecular formulae and energy levels (in eV) of 6T, DIP and C_{60}. Energy values of organic materials are taken from,[63,72–74] 6T LUMO is estimated by adding the transport gap[75] to the HOMO. The P3HT LUMO was estimated by adding the optical gap $E_{opt} + 0.5\,eV$ to the HOMO. Defect states enabling electron transport through BCP are sketched.[74] Note that the stated energies are literature values and may shift relative to other materials in an actual device stack. This diagram should merely be regarded as an estimate of possible donor/acceptor combinations.

orders of magnitude has been reported for 6T films grown on single crystalline substrates at room temperature ($5\times10^{-2}\,cm^2/Vs$) and at 100 °C ($\sim5\times10^{-5}\,cm^2/Vs$).[81] The ionization potential of 6T is known to change with the molecular orientation and has been reported to 5.0 eV for purely standing and 5.4 eV for purely lying molecules.[84] 6T was purchased from Sigma Aldrich and purfied twice by temperature gradient sublimation.

3.1.2 Poly(3-hexylthiophene)

Poly(3-hexylthiophene) (P3HT) is a hole conducting polymer and probably still the most widespread donor polymer available. Its monomer unit consists of a thiophene ring with a hexyl side chain grafted at position three. This geometry leaves different possible configurations for the polymer chain: head to tail, tail to head, head to head and tail to tail. Head to tail regio-regular poly(3-hexylthiophene) (rr-P3HT) is commonly used in electronic devices as it shows the highest mobilities when compared to other conformations. Field effect mobilities of $0.1\,cm^2/Vs$ have been shown.[85] Its structure yields a planar polymer chain with a large conjugated system, which enables π-stacking of the polymer chains in coplanar segments,[86] thus spin cast rr-P3HT films are semi crystalline. It has been shown, that the degree of crystallinity can be influenced by the choice of solvent or by annealing the film.[87] An amazingly wide range of values for the

HOMO level of P3HT can be found in the literature, depending on the measurement technique. For example −5.2 eV have been found from cyclic voltammetry,[88] while around −4.6 eV have been found by photoelectron spectroscopy on thin films.[63,73] P3HT was purchased from BASF as Sepiolid P200.

3.1.3 Diindenoperylene

Diindenoperylene (DIP) is a rod shaped molecule with a length of approximately 1.8 nm.[89] Structural investigations have revealed that DIP grows in a herringbone structure but undergoes a phase transition at 403 K in single crystals. In a low temperature phase the molecules are slightly bent and exhibit a triclinic crystal structure. Above 403 K a monoclinic high temperature phase is formed and the molecules are fully stretched (i.e. flat).[90,91] This high temperature phase is stabilized in thin films and hence the relevant phase in thin films even at low temperatures.[92] However, two orientations of crystallites in this phase have been found in thin films. In the so-called σ-orientation the molecules are standing upright with respect to the substrate plane, while in the λ-orientation the molecules are lying.[92,93] DIP was introduced as a donor in organic solar cells by Wagner *et al.* in 2010 and found to be growing in σ-orientation on typical OPV substrates.[72] Later, DIP was found to exhibit ambipolar transport, where the extraordinarily high electron mobility of $1\times10^{-1}\,\mathrm{cm^2/Vs}$ even outranges the already high hole mobility by about a factor of 2.[94] This potentially qualifies DIP for the application as electron acceptor in solar cells.[66] DIP has an optical gap of 2.1 eV, a transport gap of 2.55 eV and an ionization potential of 5.35 eV.[63,95] The material used in this work was purchased pre-purified by two temperature gradient sublimation steps from Stephan Hirschmann, 3. Physikalisches Institut, University of Stuttgart.

3.1.4 Buckminsterfullerene

Besides graphite and diamond, fullerenes are the third modification of carbon. The buckminsterfullerene (C_{60}) consists of 60 carbon atoms, arranged in a soccer ball like structure built up by 20 hexagonal and 12 pentagonal rings. Its molecule diameter is 7.1 Å and it forms a face-centered cubic structure with a lattice constant of 14.2 Å at room temperature.[96] C_{60} shows an optical bandgap of 1.9 eV,[97] the reported transport bandgap is spread between 2.2 eV and 2.5 eV.[63,88,98] Its LUMO level of about −3.9 eV[63] (cf. Figure 3.1) makes C_{60} suitable as an acceptor species in combination with common donor materials and ultrafast charge transfer between several polymers and the fullerene have been observed at a sub-picosecond time scale.[99] Its comparatively large dielectric constant of $\varepsilon = 4.4$[100] stabilizes the charge separated state upon exciton dissociation.[101] While commonly regarded insoluble a solubility of C_{60} in chloronaphthalene as high as 56 mg/ml has been reported.[102] C_{60} was purchased pre-purified by gradient sublimation from CreaPhys and used as received.

3.1.5 Bathocuproine

Bathocuproine (BCP) is a wide-gap organic semiconductor that may be introduced into the device as a thin film of 5 nm-10 nm between the acceptor and the cathode. Its function is generally regarded to be two-fold. On the one hand it serves as an exciton blocking layer in fullerene cells because of its HOMO located slightly below that of C_{60} and its wide energy gap of about 3.5 eV.[74,103] On the other hand it protects the organic layers that may otherwise become damaged by metal penetration during the deposition of the cathode.[74,104] As positive side effect metal penetration into the BCP layer enables efficient electron transport through the BCP film via defect states and hence counteracts the negative effects expected from injection barriers at the BCP/cathode interface. The optimum BCP thickness is directly determined by the penetration depth of the metal into the organics and varies for different metals and preparation parameters.[74,103] Note that different values for the gap of BCP exist in the literature.[105] It is therefore unclear whether BCP functions as an exciton blocking layer for DIP or if it simply has to be regarded as a sacrificial layer during metal deposition. BCP was purchased from Sigma Aldrich and used as received.

3.1.6 Poly(3,4-ethylenedioxythiophene):poly(styrenesulfonate)

Poly-3,4-ethylenedioxythiophene (PEDOT) is an intrinsically conducting polymer. By aqueous oxidative polymerization of the EDOT monomer in the presence of polystyrene sulfonic acid (PSS) a dispersion of the PEDOT:PSS complex is formed, where PSS acts as a polymeric counter anion to the PEDOT cation. PEDOT:PSS is sold under the trade name CLEVIOS P (formerly Baytron P) and is widely used for example in antistatic coatings. In organic solar cells layers of PEDOT:PSS are used to smoothen the ITO surface and to enhance the hole extraction from the device.[106] This is achieved by the relatively high work function of PEDOT:PSS, whose exact value, however, depends on parameters such as the PEDOT and PSS ratio or on the presence of residual water in the film.[107] Especially the latter is important since residual water may be removed to a certain degree by thermal annealing in vacuum. This is illustrated in Figure 3.2. A common type is CLEVIOS P AI4083, which is used throughout this work unless otherwise stated. This material has been reported to increase its workfunction from 4.75 eV to 5.1 eV by heating in vacuum.[108] A different PEDOT:PSS formulation used occasionally in this work is HIL1.3N which has a workfunction of 5.7 eV even without annealing.[72] Both AI4083 and HIL1.3N were used as received from Heraeus Clevios.

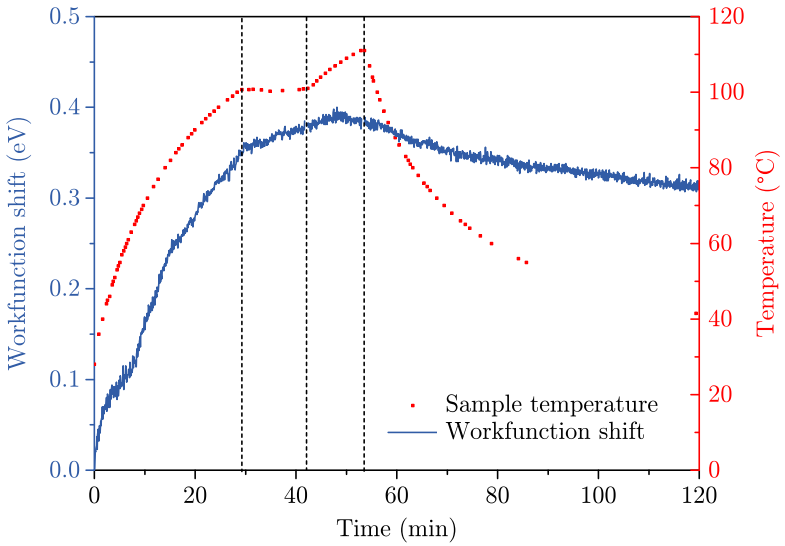

Figure 3.2: Increasing workfunction of AI4083 over time while heating the sample in vacuum, measured *in situ* with a Kelvin probe. A significantly increased workfunction remains even if the sample is cooled down again. This is ascribed to removal of residual water from the PEDOT:PSS film.

3.2 Preparation methods

3.2.1 Spin coating

Spin coating or *spin casting* is a standard method for the preparation of thin solid films of solution processable materials. Starting from a small amount of solution, which is dispensed onto the surface of a flat substrate, a thin film of the coating material is formed by rotating the sample at large spin speeds typically around 1000 to 6000 rpm. During the rotation the solution is equally spread across the sample surface and as the solvent evaporates a uniform coating is left on the surface. The process of spin coating can be separated into four phases as illustrated by Figure 3.3:[109]

1. dispensing
2. acceleration
3. film thinning
4. film drying

During the acceleration step the excess liquid is thrown off the sample until the remaining film is thin enough to follow the rotation of the substrate. The amount of excess solution initially dispensed as well as the acceleration rate do not influence the resulting film thickness (unless the solution is very dilute or has a low viscosity[110]). The acceleration rate does, however, influence the radial uniformity of the film, where faster

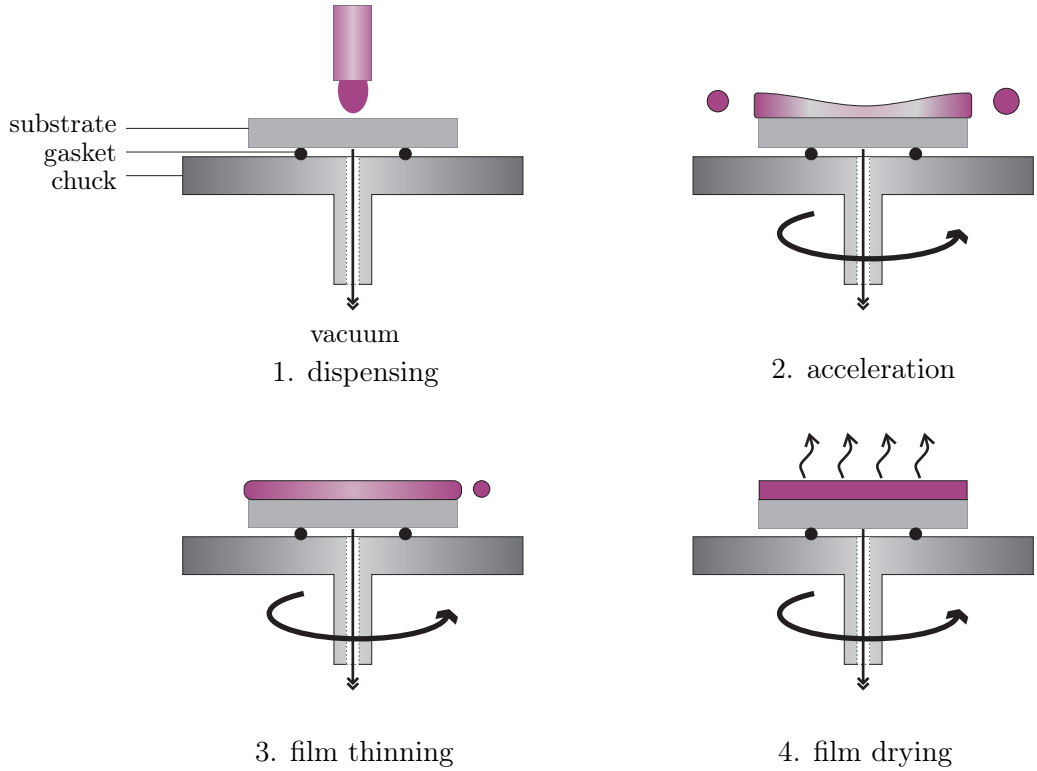

Figure 3.3: Schematic drawing of the phases of spin coating: (1) dispensing the solution, (2) acceleration to the desired spin speed, (3) film thinning by radial flow of the solution and solvent evaporation and (4) film drying by further evaporation. During the whole process the sample is held on the chuck by vacuum.

acceleration yields more uniform layers.[111] Once the film is co-rotating with the substrate the third stage begins and viscous forces start to play the dominant role as they balance the centrifugal forces caused by the rotation. The resulting net fluid flow is the main mechanism of film thinning. Since the viscosity of the solution is strongly depending on its concentration, the fluid flow depends heavily on the concentration of solute in the solvent. As the film thinning is accompanied by evaporation of the solvent at the same time as the solute stays in the fluid, the concentration of the solution and thus its viscosity is increased - finally the flow starts to cease. This determines the final film thickness.[109] A direct consequence of this effect is a thickness dependence on the initial concentration: starting from a more viscous solution the centrifugal forces will be compensated earlier and the film gets thicker. On the other hand, higher spin speeds will lead to larger centrifugal forces and thus generate thinner films. The fourth phase starts when solvent evaporation becomes the major mechanism of fluid loss and the film is fixed by strong viscous forces. The film is then drying until only little residual solvent is left in the coating.

The final thickness h_f of a polymer film produced by spin coating is described by the following relation:

$$h_\mathrm{f} = k x_{1,0} \omega^{-\beta} \tag{3.1}$$

where ω denotes the spin speed and $x_{1,0}$ the initial polymer weight fraction. k is a constant which depends on the properties of the polymer and the solvent. The exponent β is typically close to 0.5 for most materials.[110]

The spin coater used for thin film preparation in this work is a Delta 6 by Süss MicroTec.

3.2.2 Vacuum thermal evaporation

A common way to produce thin films of organic materials of low molecular weight is *vacuum thermal evaporation*. This technique, also referred to as *organic molecular beam deposition* (OMBD), is especially suitable for insoluble materials that cannot be processed from solution. Inside a vacuum chamber the organic material resides in a crucible (usually quartz glass) inserted into an effusion cell. By heating the effusion cell to an appropriate temperature (typically between 200 and 400 °C depending on the material), the organic material starts to evaporate, where the evaporation rate can be adjusted by variation of the material temperature. Once the desired rate is reached, the temperature is held constant. The evaporation rate is measured by means of a quartz microbalance, which consists of a driven quartz resonator that is exposed to the vapor beam inside the vacuum chamber. An additional mass will then strongly decrease the crystal's resonance frequency. This frequency shift is related to the density of the material and its acoustic impedance[112] and can be utilized to monitor the growth of the film. The substrate, on which the film is grown, is usually placed some 10 cm above the effusion cell and can be shielded from the beam by a shutter which allows for the preparation of layers of well-defined thickness. If more than one effusion cell (with its own quartz balance) is present in the chamber, blend layers of different materials can be formed. Typical evaporation rates for organic materials range from 0.1 to 1 Å/s, which is significantly slower than film preparation by spin coating. A photograph as well as a schematic drawing of a vacuum system used for thermal evaporation of organic compounds is shown in Figure 3.4.

Vacuum thermal evaporation is also applied for the deposition of metal films. In this case, however, a variety of boats and crucibles, heated by a constant current flow, are used as evaporation sources instead of temperature controlled effusion cells.

Independent of the type of material evaporated, the base pressure inside the vacuum chamber should be in the low 10^{-7} mbar range to avoid doping with ambient gas molecules and to provide a directed vapor beam.

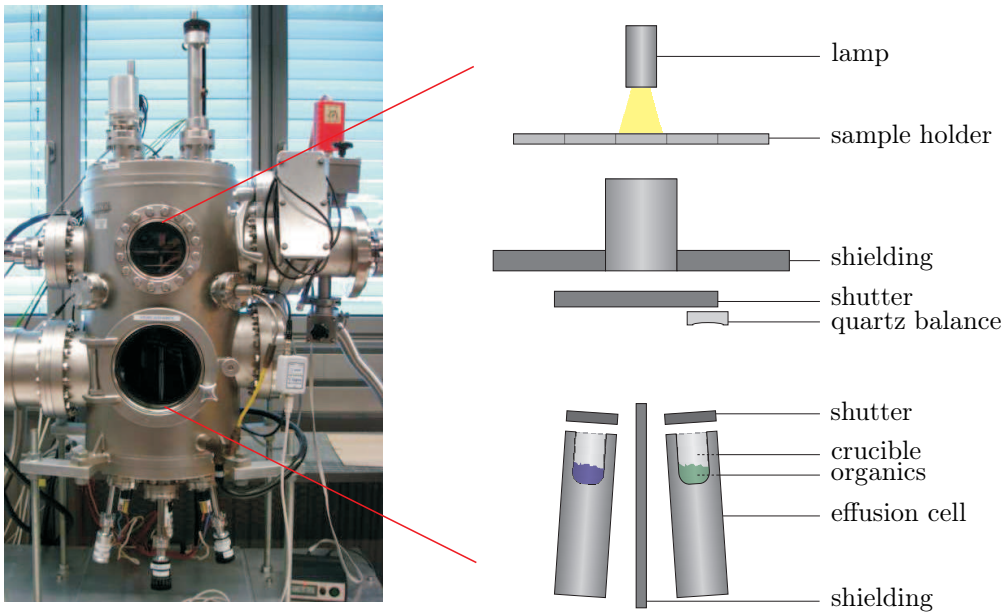

Figure 3.4: Picture of a vacuum chamber used for thermal evaporation of organics (left) and schematic drawing of its inside (right). For simplicity only two of four effusion cells have been drawn. The sample holder can hold up to five samples which can be selected for processing by a linear transfer mechanism. As a special option, the lamp can be used to heat the sample during the evaporation process.

3.3 Sample preparation

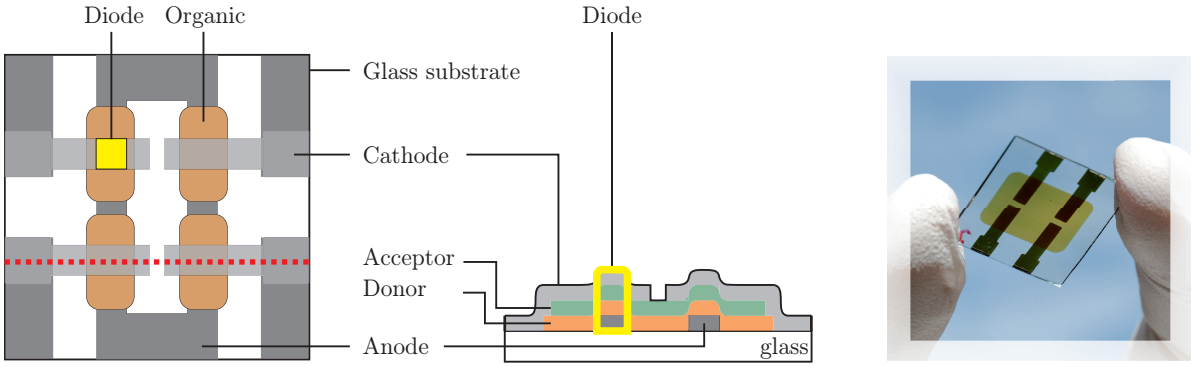

Figure 3.5: Schematic drawing of the sample geometry. The left hand picture shows the topview onto the device: the four metal "fingers" define four solar cell pixels where they intersect with the ITO pattern. The size of each device is $2\times2\,\mathrm{mm}^2$. The center drawing shows the cross section through the sample along the dashed red line. The different organic and electrode layers building up the diode are shown. A photograph of an actual sample is shown on the right.

All samples presented in this work have been prepared on indium tin oxide (ITO) covered glass slides, unless otherwise noted. ITO is a transparent conducting oxide and commonly used as the anode material in organic photovoltaic cells. For structural investigation ITO coated glass sheets purchased from Merck were used. Solar cell devices have been prepared on pre-patterned ITO received from Thin Film Devices with a thickness of 145 nm and sheet resistance of $20\,\Omega/\square$. The device layout is depicted in Figure 3.5.

For all samples the substrates have been sonicated in technical grade isopropanol, UV/IR grade acetone and UV/IR grade isopropanol for seven minutes each. After blow-drying with nitrogen the samples have been exposed to a UV/Ozone treatment for 15 min to 30 min to remove residual organic contaminants from the surface and to increase the wettability for aqueous solutions.

To increase the workfunction, a layer of PEDOT:PSS was then spin cast onto the ITO surface at 5000 rpm for 30 s with a 5 s acceleration ramp. The water based PEDOT:PSS dispersion has been deposited from a syringe through a 0.45 µm hydrophilic nylon filter. After the spin coating process the samples have been dried on the hot plate for 30 minutes at 150 °C to remove the residual water. This yields a PEDOT:PSS layer of approximately 30 nm thickness. All wet-processing has been carried out in ambient air in the clean room.

Deposition of the molecular donor and acceptor layers was carried out by organic molecular beam deposition in a vacuum chamber at a base pressure of 2×10^{-7} mbar. 6T films were deposited at a rate of 0.3 Å/s, DIP and C_{60} were evaporated at 0.5 Å/s. For contact deposition, solar cell devices have subsequently been transferred to a second vacuum chamber (2×10^{-7} mbar) through a nitrogen atmosphere but without exposure to air. A 5 nm BCP blocking layer was deposited at a rate between 0.1 Å/s and 0.5 Å/s. The devices were then finalized by depositing an aluminum cathode of 100 nm thickness through a shadow mask. The initial Al deposition rate during the first 10 nm was 0.5 Å/s and then increased to 1 Å/s. The resulting cross-bar structure yields four solar cells per sample, each with an active area of 0.04 cm^2 as illustrated in Figure 3.5.

Chapter 4

Characterization Techniques

4.1 X-ray scattering

X-ray scattering summarizes a number of techniques that apply X-ray radiation to analyze the structure of crystalline materials. In the present work X-ray reflectivity (XRR) and grazing incidence X-ray diffraction (GIXD) are used to investigate organic thin films. The basic principles of these techniques can be found in References 113, 114 and many other physics textbooks.

The conditions for Bragg reflection are schematically illustrated in Figure 4.1: The incident beam of monochromatic X-rays hits the periodic lattice planes of a crystallite under an angle θ. This angle is equal to the angle of reflection and hence the angle between the incident and reflected X-ray equals 2θ. Since only a fraction of the beam is reflected at each lattice plane, the photons reflected at different planes interfere. A net reflection is thus only observed if the condition for constructive interference is fulfilled, i.e. if the angle is such that the path difference of the photons reflected at two neighboring planes equals an integer multiple of the wavelength:

$$2d\sin(\theta) = n\lambda, \tag{4.1}$$

where d is the lattice spacing, θ the angle of incidence w.r.t. the surface plane, n is an integer and λ the wavelength of the X-rays.

As illustrated in Figure 4.1, the scattering process can also be described by the change of the wave vector of the incident X-ray $\boldsymbol{k}_\mathrm{i}$ to $\boldsymbol{k}_\mathrm{f}$ by a scattering vector $\boldsymbol{q}$:

$$\boldsymbol{k}_\mathrm{i} + \boldsymbol{q} = \boldsymbol{k}_\mathrm{f} \tag{4.2}$$

For elastic scattering, the photon energy is conserved and the magnitude of the wave vectors of the incident and reflected photons are equal $|\boldsymbol{k}_\mathrm{i}| = |\boldsymbol{k}_\mathrm{f}| = \frac{2\pi}{\lambda}$, where λ is the wave length of the X-rays. In this case it can be shown that the Bragg condition is

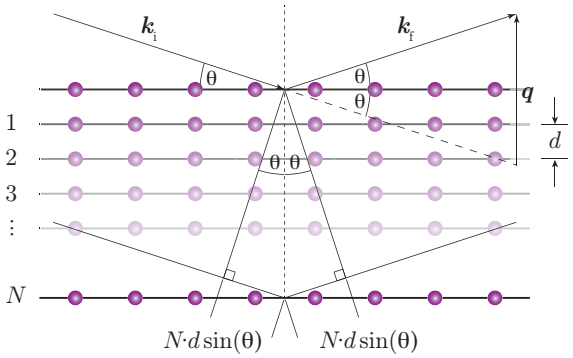

Figure 4.1: Schematic drawing of the Bragg reflection at lattice planes of a crystal with spacing d.

fulfilled if the scattering vector equals a reciprocal lattice vector.[114] The magnitude of the scattering vector is then given by

$$q = 2|\boldsymbol{k}_\mathrm{i}| \sin(\theta) = \frac{4\pi}{\lambda} \sin(\theta) \tag{4.3}$$

Note that since the momentum of a photon is given by $\boldsymbol{p} = \hbar\boldsymbol{k}$ and because of the definition of $\boldsymbol{q} = \boldsymbol{k}_\mathrm{f} - \boldsymbol{k}_\mathrm{i}$ in Eq. 4.2, $\boldsymbol{q}$ is typically also called the momentum transfer vector.

Bragg's law (4.1) is exploited for a typical X-ray reflectivity measurement (illustrated in Figure 4.2). With the sample substrate aligned parallel to the xy-plane, the X-ray source is directed at the sample under an angle θ. The detector is positioned at an angle 2θ, with respect to the incident X-ray beam, where the reflection is expected. During the XRR scan the source and detector angles θ and 2θ are changed synchronously thus that reflections caused by lattice planes aligned parallel to the substrate are detected (Figure 4.2 (a)). Because of the geometric configuration of such a θ-2θ scan, reflections at lattice planes tilted from the substrate plane are not recorded (c.f. Figure 4.2 (b)). The latter is equivalent with the presence of a non-zero in-plain component $\boldsymbol{q}_{xy}$ of the momentum transfer vector. This method thus probes the so called out-of-plane (i.e. perpendicular to the substrate) crystallinity of the film.

In a very similar manner, grazing incidence X-ray diffraction probes the lateral, in-plane structure of the sample. In contrast to XRR, however, the out-of-plane angle of incidence (and reflectivity), i.e. the angles with respect to the sample surface, are kept constant and small (grazing incidence). Instead the in-plane angle of the source (ϕ) and the detector (2ϕ) are changed during the scan. Ideally, this corresponds to a configuration where the $\boldsymbol{q}_z$ component of the momentum transfer vanishes, thus that only information on lattice planes perpendicular to the substrate is collected.

In order to detect signals where neither of the components of the momentum transfer vector $\boldsymbol{q}$ vanishes, reciprocal space maps may be recorded. The indexing of the features in XRR and GIXD spectra as well as the reciprocal space maps is achieved by calculating the expected peaks from the lattice spacing of given unit cell parameters. For details see

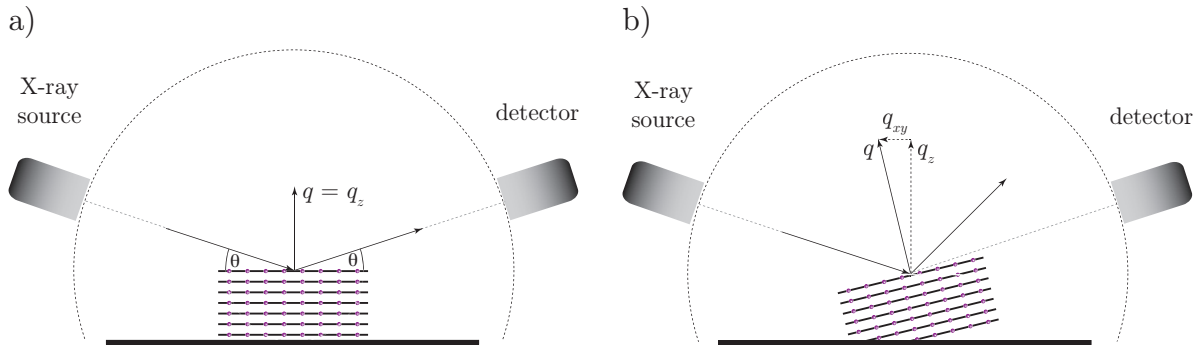

Figure 4.2: Schematic drawing of the geometrical configuration of a typical θ-2θ X-ray reflectivity measurement. Only reflections at planes perpendicular to the z direction are detected. This equals orientations where the in-plane component of the momentum transfer q_{xy} vanishes. Samples are typically oriented with the substrate in the xy-plane hence, lattice planes parallel to the substrate cause features in the diffraction pattern.

Appendix A.1. A Matlab script that calculates the momentum transfer for a range lattice planes (h,k,l) has kindly been provided by Christopher Lorch, University of Tübingen.

Apart from the qualitative information on the crystallinity obtained from the occurrence of certain peaks in the X-ray scattering data, quantitative information on the size of the crystallites can be extracted from the width of the peaks in the XRR and GIXD data. The full width at half maximum (FWHM) can be determined by fitting a pseudo Voigt function to the respective peak and the coherent crystallite size D is then obtained from the Scherrer formula:[115]

$$D = \frac{2\pi K_{\mathrm{s}}}{\mathrm{FWHM}}, \tag{4.4}$$

where $K_{\mathrm{s}} = 0.94$ is the Scherrer factor for spherical domains. Note that the coherent crystallite size yields merely a lower limit of the actual grain size which might be larger but not perfectly crystalline. Because of the nature of the experiment, the out-of-plane crystallite size is extracted from XRR measurements, the in-plane crystallite size from GIXD measurements.

If not otherwise stated, X-ray scattering measurements have been carried out by our collaboration partners at the University of Tübingen in the group of Prof. Dr. Frank Schreiber. X-ray reflectivity was measured ex-situ with a GE/Seifert X-ray diffractometer using Cu $K_{\alpha 1}$ X-ray radiation. Grazing incidence X-ray diffraction and reciprocal space maps were recorded at the ID10B (ESRF) beamline using a wavelength of 0.925 Å. A MarCCD area detector was used to acquire the reciprocal space maps.

4.2 Near Edge X-ray Absorption Fine Structure Spectroscopy

While X-ray scattering techniques are suitable for crystallographic analysis of bulk materials, Near Edge X-ray Absorption Fine Structure (NEXAFS) spectroscopy is a versatile, surface sensitive method that is based on resonant absorption of linearly polarized X-ray radiation. Soft X-rays excite core level electrons (typically) from the K-shell initial state (1s electrons) to a final, bound state within unoccupied molecular orbitals or to the continuum and generate core holes.[116,117] Relaxation of the excited state then either occurs via the re-emission of a photon (fluorescence) or via an Auger process under the emission of an electron (cf. Figure 4.3). A sweep of the photon energy across a certain absorption edge then results in a spectrum with sharp peaks near the edge stemming from 1s $\longrightarrow \pi^*$ resonances and more and more broadened features further away from the edge resulting from 1s $\longrightarrow \sigma^*$ transitions.[116] A suitable energy region is typically about 30 eV to 40 eV around the binding energy of the respective 1s electron. By picking the energy range, the initial state can be chosen to correspond to the K-shell of a certain element, which makes NEXAFS spectroscopy an element selective technique. For organic molecules typically the C1s-edge (285 eV) is investigated but K-edges of other elements such as oxygen, nitrogen or fluorine can also be accessed.[117]

In general, direct measurement of the absorption in transmission mode and indirect detection via the fluorescence yield are possible. Yet, for thin films the emission of Auger electrons provides a convenient measure for the X-ray absorption strength, essentially measuring the re-filling of the generated core holes.[116,117] Different ways of determining the number of ejected electrons exist with varying depth sensitivity. If an energy selective detector is used, the Auger electron yield (AEY) may directly be detected. In this case all inelastically scattered electrons stemming from deeper layers in the film are rejected and only electrons stemming from the surface are regarded. Hence this method is utterly surface sensitive. Instead of selecting a specific energy, in partial electron yield (PEY) mode the ejected electrons are detected after passing a retarding field. Hence only

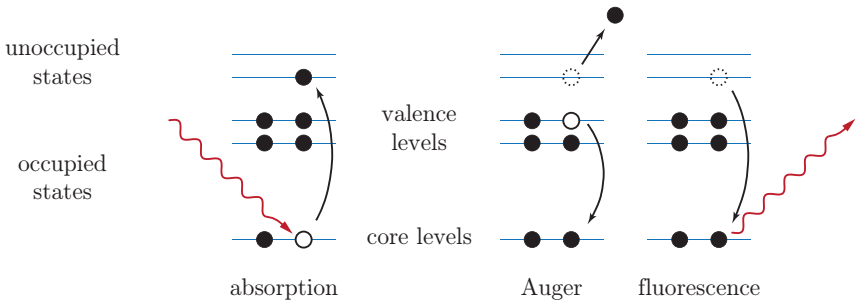

Figure 4.3: Schematic illustration of the internal processes during the NEXAFS experiment: A core level electron is excited to an unoccupied molecular orbital upon the absorption of an X-ray photon. Relaxation can happen via an Auger processes or via fluorescence under the re-emission of an X-ray photon. (after Ref. 118)

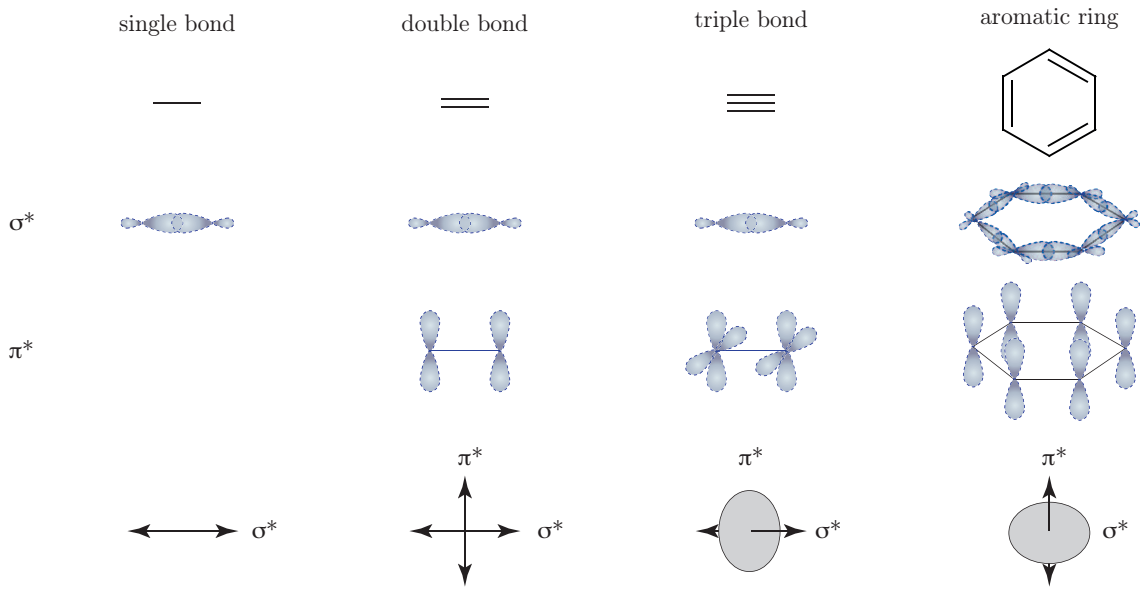

Figure 4.4: Schematic illustration of the orientation of $\pi*$ and $\sigma*$ orbitals in single, double, and triple bonds as well as aromatic systems. Depending on the symmetry, the orbital direction may be treated as a plane or as a vector. Note that for simplicity the shape of the atomic orbitals instead of anti-bonding molecular orbitals has been drawn. Adapted from References 119 and 117.

electrons with an energy above a certain pass energy are detected while low energy electrons are suppressed. This allows an adjustment of the information depth between approximately two and ten nanometers by adjusting the retarding field.[117] Finally, instead of directly detecting the electrons ejected into vacuum, the total electron yield (TEY) mode uses the current from the sample holder onto the sample as a measurement signal and thus detects all electrons, including secondary electrons stemming from deeper layers within the film. Measurements in the TEY mode are therefore slightly less surface sensitive compared to the PEY mode. This is feasible for the investigation of buried interfaces e.g. in bilayer structures and a general advantage for ex-situ prepared samples, as the TEY signal is less sensitive to potential surface contaminants.

Angular resolved NEXAFS can be applied to determine the orientation of the molecule on the substrate surface. Because of the spherical symmetry of the 1s initial state, the direction of the transition dipole moment in K-edge absorption is determined by the final state. For the investigated 1s $\longrightarrow \pi^*$ and 1s $\longrightarrow \sigma^*$ resonances the final states are closely related to chemical bonds. The transition dipole moment is thus highly oriented either parallel (σ^*) or perpendicular (π^*) to the bond, which can be denoted by a vector pointing from the center of the excited atom to the spatial maximum of the respective anti-bonding orbital.[116,117,119] This is schematically illustrated in Figure 4.4. In the case of triple bonds two perpendicular orientations for 1s $\longrightarrow \pi^*$ resonances exist which may be considered to span a plane of π^* orbitals. Similarly, in aromatic rings, such as benzene, the σ^* orbitals may be regarded as a plane rather than a vector (cf.

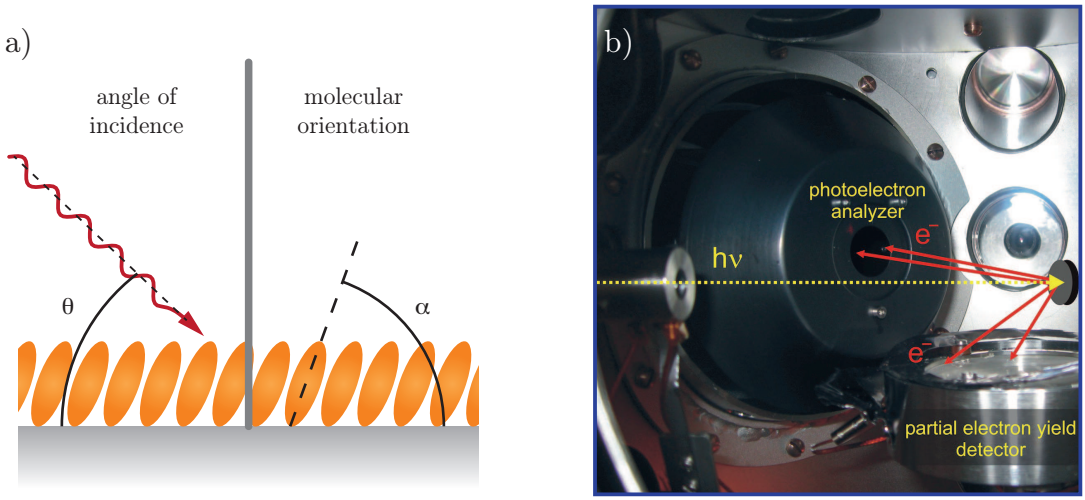

Figure 4.5: Illustration of the NEXAFS setup. (a) Schematic drawing of the angle of incident X-rays and the molecular orientation. (b) Picture of the analysis chamber of beamline D1011 at MAX-lab in Lund, Sweden. The image in (b) is taken from the MAX-lab web site.[120]

Figure 4.4).[119] Even if the examples illustrated in Figure 4.4 are simplified, they form the building blocks of many organic semiconductor materials. This is especially true for the double bond and the aromatic ring. Hence, with the orientation of the π^* orbitals represented as a vector (identical to the orientation of the transition dipole moment), the absorption intensity of 1s $\longrightarrow$ π^* transitions depends by a $\cos^2\delta$ behavior on the angle δ between the electric field vector $\boldsymbol{E}$ and the orientation of the final state orbital, i.e. the absorption is maximal if the electric field is parallel to the final state orbital and vanishes if $\delta = 90$.[117]

Because of the dependence of the intensity of the π^* resonances on the orientation of the electric field, the absorption strength of organic molecules usually shows a dependence on the angle of incidence θ of the polarized X-ray beam with respect to the substrate plane (dichroism) (cf. 4.5 (a)). As an example the NEXAFS spectra of DIP recorded under 30°, 55° and 90° (i.e. normal incidence) are shown in Figure 4.6 (a). The dichroism is clearly visible. Furthermore the intensity dependence of the π^* resonances is opposite to that of the σ^* features, nicely demonstrating the orthogonal orientation of the respective orbitals as illustrated in the inset cartoon.[121,122] However, not all molecules are dichroic. A highly relevant example is the spherically symmetric C_{60} fullerene. It is clearly visible from the spectra presented in Figure 4.6 (b) that there is virtually no angular dependence of the resonance intensities.

The increasing intensity of the π^* resonances observed in the DIP example (cf. Figure 4.6 (a)) with increasing θ – from close to grazing incidence to normal incidence – already indicates that the molecules are preferentially upright standing (the π^* orbitals are (by trend) perpendicular to the surface normal). In addition to this qualitative result, dichroism can be exploited to quantitatively extract the molecular orientation angle α (w.r.t the substrate plane, cf. 4.5 (a)) from a series of NEXAFS spectra recorded under different angles of incidence. For organic thin films without in-plane preferential

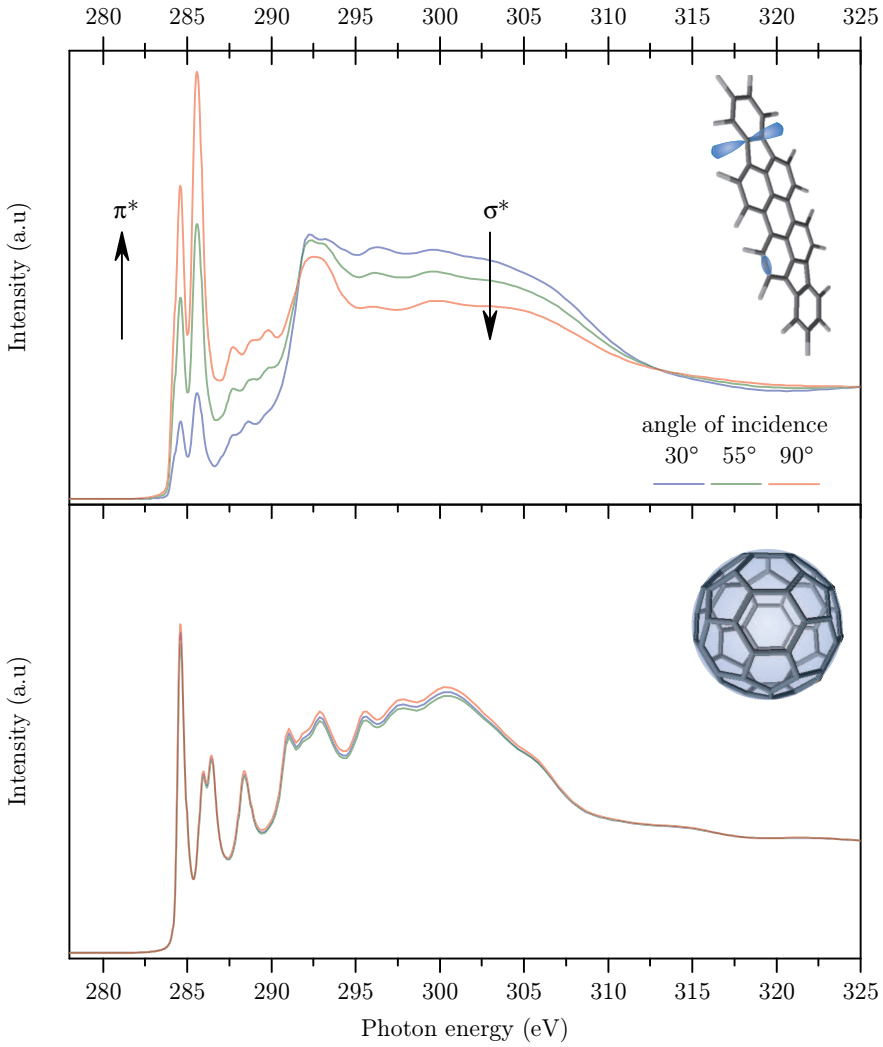

Figure 4.6: NEXAFS spectra of DIP (a) and C_{60} (b) at 30°, 55°, and 90° angle of incidence of the X-ray photons recorded in TEY mode. A distinct dichroism is visible for DIP because of the planar shape of the molecule, which results in a perpendicular orientation of the σ and π orbitals (cf. cartoon in (a)). Owing to its spherical symmetry no dichroism is observable for C_{60}.

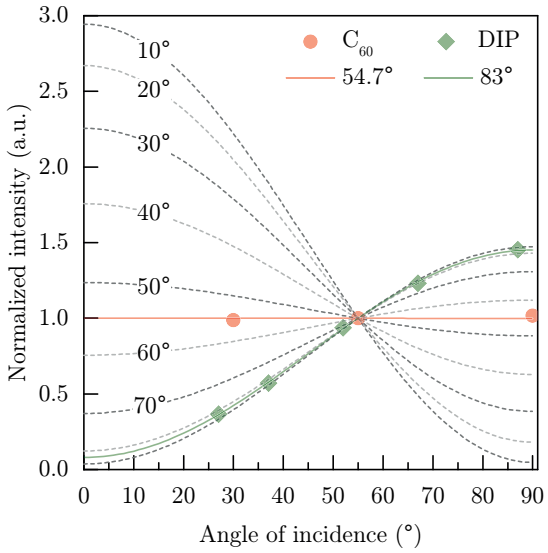

Figure 4.7: Angular dependence of the NEXAFS intensity extracted from the example spectra shown in Figure 4.6. Fits to the data (solid lines) yield a molecular orientation angle of $\alpha = 83$ for DIP and the magic angle for the isotropic absorption of C_{60}. The dashed lines show the predicted dependencies for molecular orientations from 10° to 90°, calculated for a polarization factor of $P = 0.975$. The data have been corrected for angle misalignment and normalized to 55° angle of incidence. An integral over an energy range from 284.5 eV to 286.5 eV was used to yield an average intensity from the measured data.

orientation the absorption intensity I is given by[119]

$$I = A\left[\frac{P}{3}\left(1 + \frac{1}{2}\left(3\cos^2\theta - 1\right)\left(3\cos^2\alpha - 1\right)\right) + \frac{1-P}{2}\sin^2\alpha\right], \tag{4.5}$$

where P is the polarization factor and the pre-factor A is an angle independent normalization constant and comparable to the extinction coefficient of conventional optical spectroscopy.[117] During the experiment I is measured as a function of θ, P is usually known for the beam line. Since the intensities of the π^* resonance at different θ are usually considered relative to each other and normalized to a certain angle, A cancels and the molecular orientation angle α can be determined by a least squares fit of the measured angular dependence with Eq. (4.5).

The calculated behavior for different molecular orientations is illustrated in Figure 4.7 together with measured relative intensities extracted from the two examples DIP and C_{60} presented above. For DIP the fit yields a tilt angle of $\alpha \approx 83$, confirming the qualitatively found tendency of standing molecules. It is important to note that NEXAFS cannot discriminate different orientations present in the probed volume and rather yields an average orientation angle. Moreover, strictly speaking, this procedure yields the orientation of the final state orbital. Hence, for rod-shaped molecules like DIP this method cannot distinguish between molecules standing on the short edge and molecules standing on the long edge.

The isotropic absorption of C_{60} data yields a constant intensity and thus matches well with the curve calculated for $\alpha = 54.7$. At this angle the term $(3\cos^2\alpha - 1)$ in Eq. 4.5 becomes zero and thus the dependence of the absorption on the incident angle vanishes, i.e. the absorption becomes isotropic. Inversely, an isotropic absorption of the film will result in an angle of 54.7° independent whether the isotropy is an intrinsic property of the molecule (as for C_{60}) or if the molecules are isotropically oriented in the probed volume or if the molecules are actually oriented at an angle of 54.7° to the substrate. Similarly, if angle of incidence is set to $\theta = 54.7$, the absorption does not depend on the orientation of the molecules (since P is usually close to unity). This angle is therefore commonly denoted as the "magic angle".

The methods presented so far make NEXAFS a powerful tool for the investigation of organic surfaces. However, it is also possible to probe buried interfaces in bilayer structures of different materials, if the top layer is thin enough. In that case the resulting NEXAFS spectrum is a superposition of the individual spectra of the two components and has to be deconvoluted before further analysis can be carried out. This is achieved by modeling the π^* resonance region of the measured spectra by a linear combination of the neat component spectra, preferably recorded at 55° angle of incidence, which is close to the magic angle. For an angular resolved series of NEXAFS spectra the relative contribution of the individual components at different incident angles yields information about the molecular orientation of the respective molecules directly at the interface. Note that the same deconvolution procedure has previously been applied for compositional analysis of blend films in order to investigate enrichment of one material at the surface of the film.[123,124]

All NEXAFS measurements have been carried out at beamline D1011 at the MAX-lab synchrotron facility in Lund, Sweden. Both PEY and TEY spectra were recoded simultaneously. For PEY detection a multichannel plate (MCP) detector was used with a retarding field of −150 V, which corresponds to an information depth of about two to three nanometers.[125] The TEY was recorded by measuring the sample current. For angular resolved measurements spectra were recorded at 90°, 70°, 55°, 40° and 30°. The 90° spectrum was always recorded again at the end of each sequence to cross check for possible beam damage of the film. Energy calibration was performed by measuring the energy difference between the first and second harmonic of the C1s X-ray photoelectron spectroscopy (XPS) peak and comparison to the nominally preset energy. Note that an accurate energy calibration is crucial for the deconvolution of composed spectra but is non-trivial to achieve and has to be repeated at least once after each injection into the storage ring. This was not always done during early beam times and recalibration of the affected spectra was achieved by careful comparison to neat material spectra accurately calibrated by the XPS procedure.

For data evaluation the recorded raw data was normalized by the ring current and divided by a reference spectrum – recorded on in-situ sputtered gold on mica – to account for potentially present absorption inside the system (e.g. by carbon contamination). Subsequently, a linear background was subtracted to yield zero average intensity at energies below the absorption edge. The spectra were finally normalized to one in the

continuum (high energy end of the spectrum).[118]

The custom software qiXAS was written to automate the data correction and normalization procedure. Furthermore qiXAS enables a graphical analysis of the spectra including deconvolution of compositional spectra and extraction of the molecular orientation (cf. Figure 4.8). qiXAS is cross-platform and available on request, including the python source code.

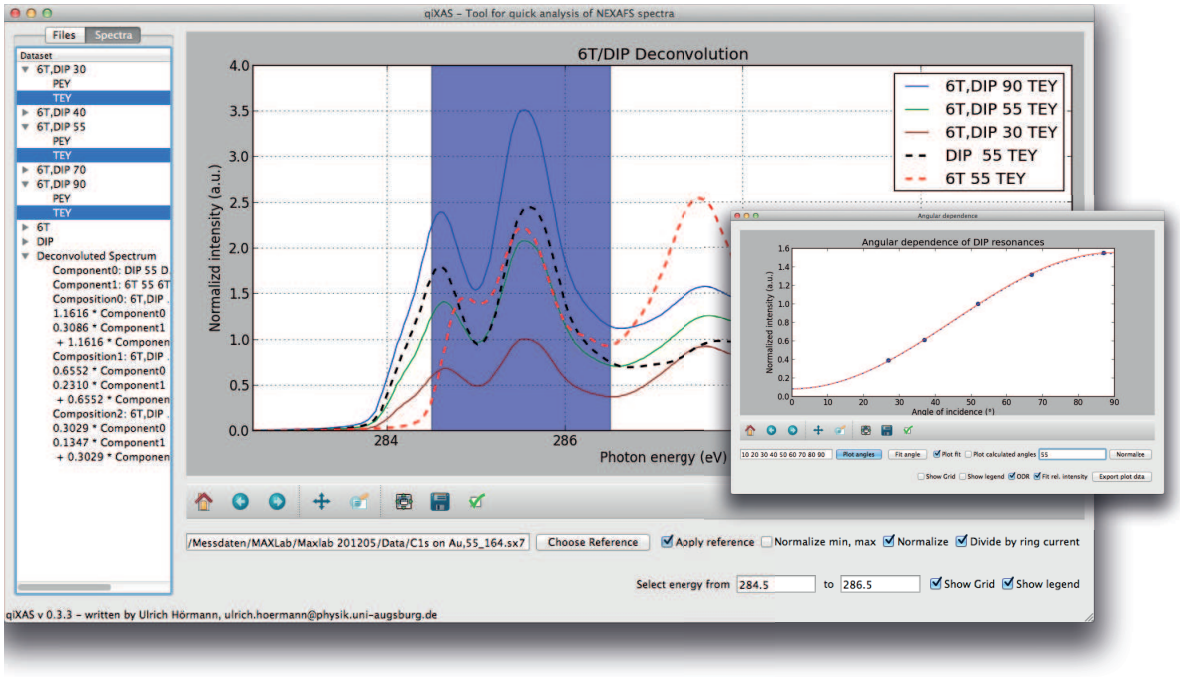

Figure 4.8: Screenshot of qiXAS running on Mac OSX.

4.3 Ultraviolet Photoelectron Spectroscopy

Photoelectron spectroscopy (PES) methods are based on the photoelectric effect, i.e. the emission of an electron upon the absorption a photon. A monochromatic beam of light is applied to excite electrons from bound states within a sample into the vacuum.[126] The kinetic energy of the electrons is then spectrographically analyzed by sweeping the pass energy of the detector. Ultraviolet Photoelectron Spectroscopy (UPS) utilizes a photon energy in the ultraviolet regime which is suitable for the emission of electrons in the valence band or, in the case of organic materials, from the frontier occupied molecular orbitals.

In order to eject an electron into vacuum, the photon energy $h\nu$ needs to be sufficiently large to overcome both the binding energy E_B and the work function ϕ, which in sum yield the ionization energy (IE).[126,127] The excess energy is the kinetic energy of the electron at the sample surface $E_\mathrm{kin} = h\nu - E_\mathrm{B} - \phi$. However, since the sample and the detector are electrically connected the electrons are additionally accelerated (or retarded) by the contact potential difference generated by the alignment of the detector and sample Fermi-levels (cf. Figure 4.9). The kinetic energy at the detector is thus given by $E'_\mathrm{kin} = E_\mathrm{kin} + (\phi - \phi_\mathrm{Detector})$, where ϕ_Detector denotes the work function of the detector. Note that the measured quantity is the kinetic energy at the detector E'_kin rather than initial kinetic energy at the sample surface.

Typically, the interesting value is not the kinetic energy but binding energy. If the detector work function is known, the binding energy can thus be calculated by:

$$E_\mathrm{B} = h\nu - E'_\mathrm{kin} - \phi + (\phi - \phi_\mathrm{Detector}) = h\nu - E'_\mathrm{kin} - \phi_\mathrm{Detector} \tag{4.6}$$

Noteworthy, this expression does not depend on the sample work function but on the work function of the detector. Unfortunately, ϕ_Detector is not always known. Yet, it can be determined by a reference measurement of the valence band spectrum of a clean metal surface, e.g. *in situ* deposited gold. Since the electrons directly at the Fermi-level have zero binding energy by definition, the detector work function can be derived with the help of Eq. 4.6 from the measured kinetic energy at the Fermi-edge of the metal and the selected photon energy.

Once calibrated for ϕ_Detector, the binding energy of the valence band electrons can be determined even for semiconductors without occupied sates at the Fermi-level. For organic semiconductors the intensity onset of the valence region marks the energy of the HOMO-level with respect to the Fermi-level.[128] If the investigated sample is a thin film on top of an electrode material, this energy is typically regarded as the hole injection barrier (HIB).[129]

A second important quantity that can be determined by UPS is the work function of the sample which is extracted from the secondary electron cutoff (SECO). These secondary electrons have lost kinetic energy before they left the sample, e.g. because of inelastic scattering processes. The cutoff electrons have lost all excess energy and posses zero kinetic energy when they reach the sample surface ($E_\mathrm{kin} = 0$). Because of the contact potential difference, they are accelerated and arrive at the detector with a

kinetic energy of $E'_{\mathrm{kin}} = \phi - \phi_{\mathrm{Detector}}$. If the detector work function is known (see above), the work function of the sample can be derived from the measured kinetic energy at which the secondary electron cutoff is observed as $\phi = E'_{\mathrm{kin}} + \phi_{\mathrm{Detector}}$. As seen from Eq. 4.6 on a binding energy scale the SECO would be located at $E_{\mathrm{B}} = h\nu - \phi$ and thus also yield the sample work function.

Since the electrons hitting the detector will in turn generate additional secondary electrons stemming from the detector itself, a bias voltage is usually applied between the sample and the detector to separate the sample electrons from the detector electrons. This bias voltage needs to be accounted for when E_{B} or ϕ is calculated.

The UPS measurements presented in this work have been carried out at beam line BL8B at the Ultraviolet Synchrotron Orbital Radiation (UVSOR) facility at the Institute for Molecular Science in Okazaki, Japan. The incident angle of the X-ray beam was set to 45° and the emission angle to 0° from the surface normal (i.e. normal emission). A photon energy of 30 eV was used for all measurements. A bias of -13 V was applied to the sample for SECO measurements, a sample bias of +5 V was used for valence region measurements to reduce charging effects. The detector work function was calibrated by measurement of a gold reference sample and a best fit of the Fermi-edge. HOMO-level onset and SECO positions have been determined as the intersection of a linear extrapolation of the baseline and the tangent to the slope of the signal.[128]

Organic thin films for UPS analysis were deposited in-situ on PEDOT:PSS (AI4083) covered ITO substrates. 6T was deposited at a rate of 0.3 Å/s - 0.8 Å/s and a pressure of approximately 9×10^{-7} mbar. DIP and C_{60} were evaporated at 0.3 Å/s - 0.5 Å/s in the low 10^{-5} mbar pressure regime.

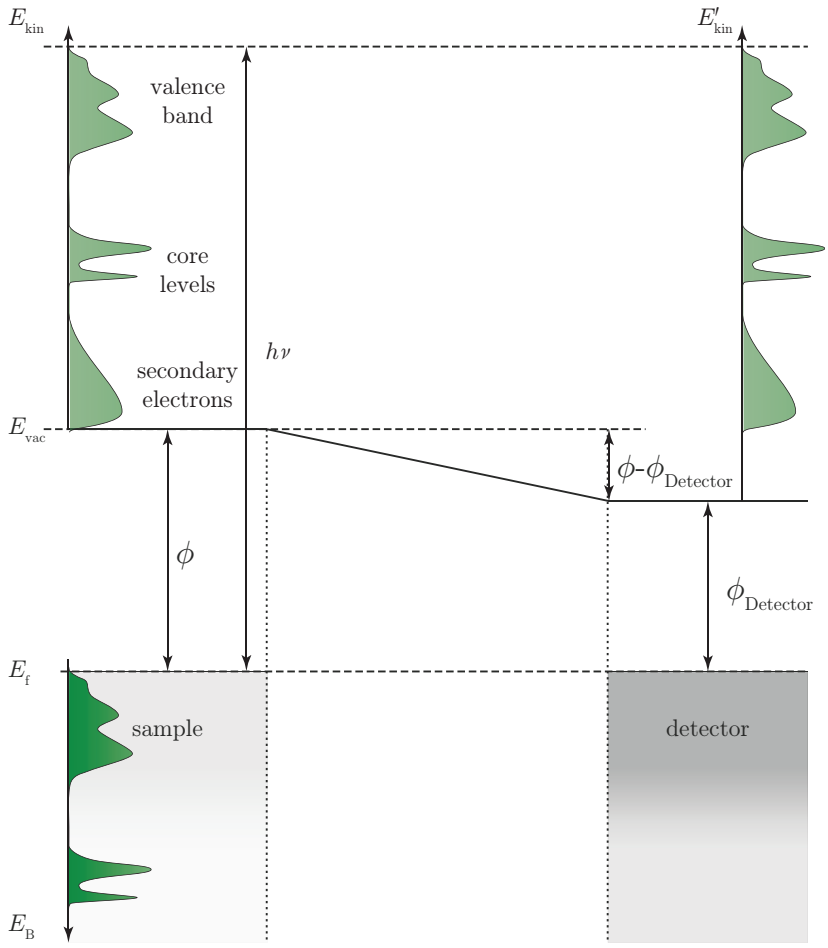

Figure 4.9: Schematic drawing of the different energy scales of the UPS measurement at the example of a metal sample. The binding energy E_B is the energetic position of the electron density of states with respect to the Fermi-level. E_{kin} denotes the excess energy of a photo electron directly after leaving the sample and surpassing both the binding energy and the work function. The kinetic energy E'_{kin} is the measured energy at the detector. Adapted from Ref. 127.

4.4 Scanning Force Microscopy

This section has been taken literally from earlier work "Characterization of planar and diffuse heterojunction solar cells based on poly(3-hexylthiophene)" (Ref. 22). *Scanning force microscopy* (SFM or more commonly AFM) is a form of scanning probe microscopy (SPM) originally introduced by Binnig in 1986[130] as a complementary method to scanning tunnelling microscopy. Based on mechanical forces between the sample surface and a tip SFM is suitable for (but not limited to) investigation of insulating surfaces. Since the strength of this interaction depends on the distance between the specimen and the tip, a height profile of the surface can be created by scanning the tip over the sample surface. This is achieved by moving either sample or tip in x-, y- and z-direction by a piezo crystal (see Figure 4.10).

The SFM tip is attached to the end of a cantilever which is deflected by the forces on the tip. This deflection can be determined by detecting the reflection of a laser beam pointed onto the cantilever and directly serves as the measured signal in the so called *contact mode*, which is a static mode where the tip is in contact with the sample. By controlling the z-position, i.e. the distance between the surface and the scanner head, the deflection can be kept at a constant value ("constant force mode"). Contact mode SFM allows for high scan rates but can harm the sample as well as the tip. To avoid these negative side effects different dynamic modes have been developed, where the cantilever is oscillated at or slightly off its resonance frequency. Any interaction between sample and tip will then change the resonance frequency and thus the amplitude and phase of the oscillation. While in frequency modulation (FM) the driving frequency is adjusted and the frequency shift yields information about the surface, the driving frequency is kept constant in amplitude modulation (AM) where the change in amplitude is used as control signal. In order to examine the comparatively soft organic surfaces the SFM is commonly operated in *tapping mode*, where the surface damaging is significantly reduced[131] as the oscillating cantilever is in intermittent contact with the sample surface. In this AM mode the cantilever is oscillated close to its resonance frequency. As the surface interacts with the tip, the resonance frequency is shifted further away from the driving frequency and the amplitude A is decreased as compared to the amplitude A_0 of the free cantilever. By adjusting the distance between sample and tip the oscillation amplitude can be controlled to a certain relative set point, being the ratio A/A_0. Both in contact mode as well as in tapping mode the z-voltage applied to the piezo yields a measure of surface height and serves as the acquired signal for topography images, which give information on the lateral structure and the roughness of the surface. The roughness is usually stated in terms of the root mean square roughness (R_{rms}), which is the standard deviation of the average surface height:

$$R_{\mathrm{rms}} = \sqrt{\frac{1}{MN}\sum_{m=1}^{M}\sum_{n=1}^{N}\left(z(x_m, y_n) - \overline{z}\right)^2}$$

where

$$\overline{z} = \frac{1}{MN} \sum_{m=1}^{M} \sum_{n=1}^{N} z(x_m, y_n) \quad .$$

M is the number of lines, N the number of rows of the acquired image. $z(x_m, y_n)$ is the height at point (x_m, y_n).

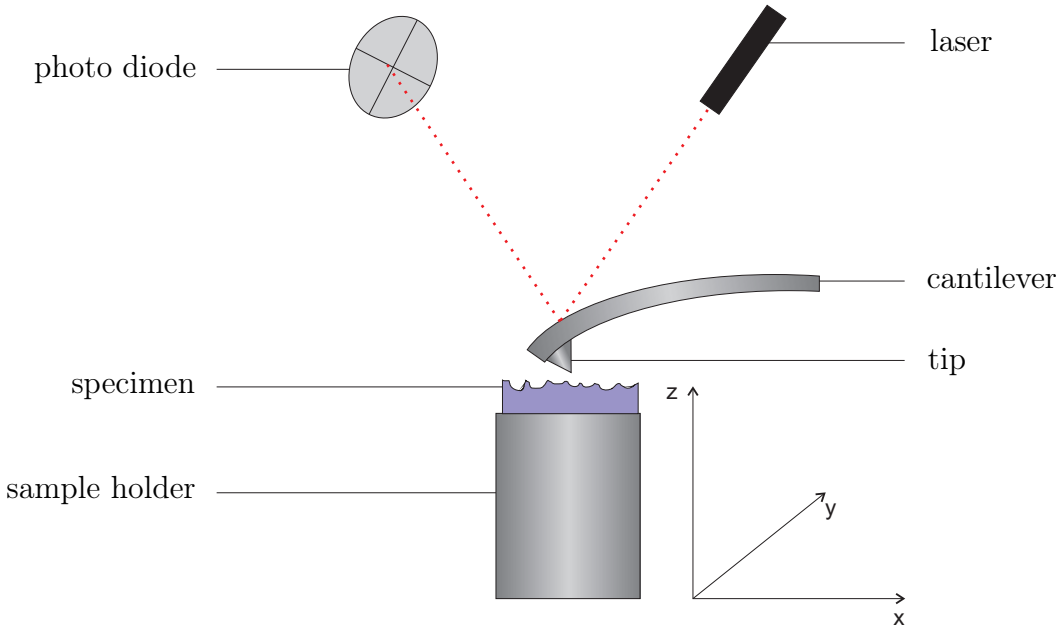

Figure 4.10: Schematic drawing of a scanning force microscope. In tapping mode the amplitude of the oscillating cantilever is measured by the laser signal detected by the photo diode. Scanning in x-, y- and z-direction is provided by a piezo crystal in the sample holder.

In addition to topography information gained from the tapping mode amplitude, the phase of the oscillation is influenced by certain properties of the surface material such as its stiffness. Lateral tapping mode phase images can thus - to some extend - yield information on the surface composition.[132]

All scanning force microscopy images were recorded in air with a Thermo Microscopes Autoprobe CP-Reserach device in tapping mode.

4.5 Reflectometry

Reflectometry is a method that allows optical characterization of thin films by simultaneously measuring the transmission and reflection of white light impinging almost perpendicularly to the sample surface. If the optical properties of the materials in the investigated layer stack are known, a reflectometer can be used to quickly determine the corresponding film thicknesses, which makes this technique interesting for in-line quality control in industrial scale thin film production.[133] In research it primarily serves as tool to determine the optical constants of thin films of known thickness and hence also the absorption coefficient of the investigated materials. The full advantage of this method can only be exploited by modeling the complete layer stack. This was done with the commercially available simulation software SCOUT.[134] Yet, this can be a tedious task and good fits are not always achieved.

Especially for simple stacks, e.g. a single organic layer on top of a glass substrate, it is often sufficient to apply a simplified analysis of the measured data, in particular if a full set of refractive indices is not the goal. In fact a good approximation for the absorptance A is already obtained by

$$A = 1 - T - R, \tag{4.7}$$

where T is the transmittance and R is the reflectance. While this seem like a crude estimate, it is expected to be superior to typical UV/Vis analysis since the reflectance is usually ignored in these measurement systems.

A refined approximation of the absorption coefficient α is obtained via the Beer-Lambert law if the reflected intensity I_R is accounted for:

$$\frac{I_\mathrm{T}}{I_0 - I_\mathrm{R}} = \frac{I_0 T}{I_0 - I_0 R} = \frac{T}{1 - R} = e^{-\alpha d} \tag{4.8}$$

and hence

$$\alpha = \frac{1}{d} \left(\ln(1 - R) - \ln(T) \right), \tag{4.9}$$

where d is the thickness of the film and I_0 the initial light intensity arriving at the surface of the film before reflexion.

Again it is important to note that these approximations are only useful for very simple stacks since they do not account for reflexion at buried interfaces or for interference effects. Further more the substrate absorption has to be taken into account by a separate measurement.

All absolute absorption coefficients shown in this work have been extracted from the measured data by optical modeling of the layer stack using the SCOUT software. The modeling was done by Dr. Andreas Opitz. An OMT Instruments reflectometer setup was used for the measurements.

4.6 Electrical and photovoltaic characterization

As mentioned before, two different types of electrical and photovoltaic characterization of solar cells are typically performed. One is the recording of j-V curves by a sweep of the bias voltage in the dark and under illumination while measuring the current response of the device. The other is the measurement of the incident photon to current efficiency by sweeping the illumination wavelength while recording the short circuit current. Three different setups have been used for these measurements with different configuration. At an early stage of this work j-V curves have been recorded in a nitrogen filled glove box under non-standardized white light illumination using an LED (Luxeon LXHL-NWE8) and a stabilized current source. A Keithley 2400 Source Meter was used for these measurements.

Later, a solar simulator was integrated into the glove box system and measurements under simulated sun light (100 mW/cm^2) were possible by a xenon arc lamp (LOT Oriel) equipped with an AM 1.5G filter set. The resulting spectrum of such a system is shown in Figure 4.11 in comparison to the calculated standard spectrum and to the previously used LED. Measurements at lower intensity are enabled by a computer controlled filter wheel containing neutral density filters. The absolute intensities have been monitored by a Si reference photodiode built into the sample holder of the setup. Additionally, rough IPCE measurements in 20 nm steps are possible by color filters of 10 nm bandwidth. A Keithley 236 source measure unit (SMU) has been used for measurements with this setup.

A second setup outside the glovebox is built around a continuous flow liquid nitrogen cryostat (CryoVac). To protect the sample, the transfer from the glove box system is possible without exposure to ambient air. During the measurement the sample chamber is either evacuated or filled with 300 mbar nitrogen contact gas for temperature dependent measurements. This setup is equipped with a white light source and a Keithley 237 SMU for current-voltage measurements. Both a solar simulator (LOT Oriel with xenon arc lamp and AM1.5G filter set) and a white LED with stabilized current source have been used for illumination of the solar cell at different stages of this work. The equivalent light intensity for cryostat measurements is estimated by comparison of the short circuit current at room temperature with the value obtained at one sun in the calibrated setup in the glove box. Again neutral density filters allow intensity dependent measurements.

A monochromator (LOT Oriel Omni-λ300) and an additional xenon arc lamp (Müller Elektronik-Optik) allow wavelength dependent measurements of the short circuit current in steps of 1 nm. The monochromatic beam is coupled into an optical fiber which incorporates a beam splitter. One beam is thus directed onto a Si reference diode with known IPCE spectrum. The other beam is chopped and focused onto the device. The modulated current signal is then detected by a Stanford Research Systems SR830 lock-in amplifier synchronized to the chopper frequency. The current generated by the reference diode is measured by the SMU. From time to time the setup has to be calibrated by the measurement of a second Si diode, identical to the reference diode. For these identical

cells a factor can be determined that relates the intensity at the sample position to the intensity at the reference diode:

$$C = \frac{P_{\mathrm{meas}}}{P_{\mathrm{ref}}} = \frac{j_{\mathrm{sc,meas}}}{j_{\mathrm{sc,ref}}} \tag{4.10}$$

With this calibration and the known IPCE of the reference diode the light intensity at the sample position can be determined. The IPCE of a probed sample can hence be calculated from the ratio between the measured j_{sc} and the current of the reference diode according to Eq. (2.3) and Eq. (2.4) directly within the measurement software:

$$\mathrm{IPCE}_{\mathrm{sample}} = \frac{j_{\mathrm{sc,sample}}}{j_{\mathrm{sc,ref}}} \frac{1}{C \cdot \mathrm{IPCE}_{\mathrm{ref}}} \tag{4.11}$$

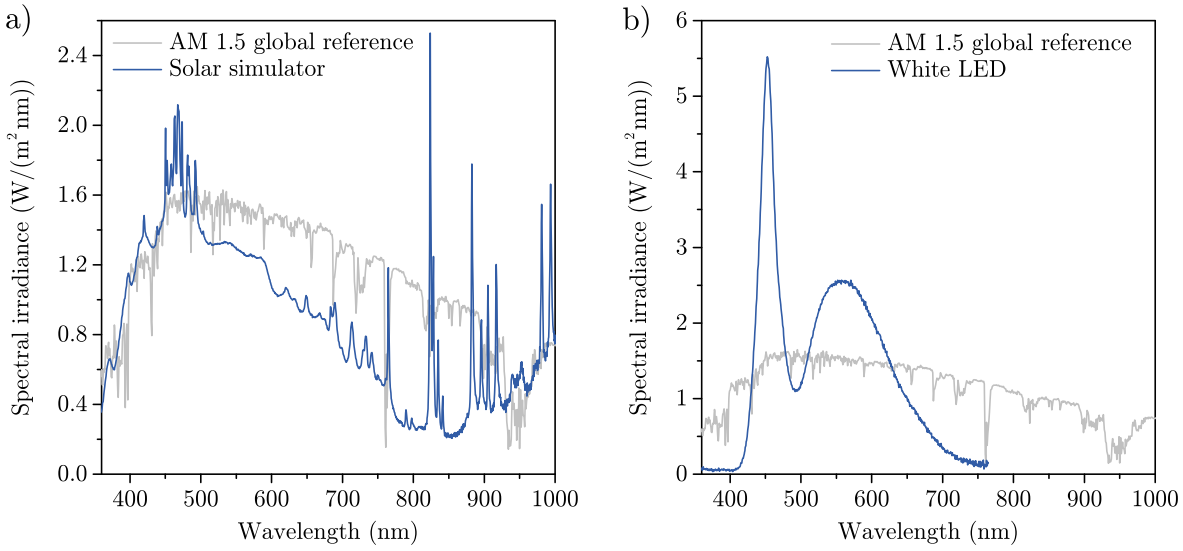

Figure 4.11: Spectra of the used white light sources and the AM 1.5G reference spectrum in comparison. The spectrum of a xenon arc lamp equipped with an AM 1.5G filter set is shown in (a), the spectrum of white Luxeon LXHL-NWE8 LED is shown in (b).

Chapter 5

Results and Discussion

5.1 Introducing DIP as acceptor

The results of this section have been published in Ref. 66.

During the intense research on organic photovoltaic cells in the last 20 years a countless number of compounds has been developed for application in the photo-active layer. The vast majority is, however, typically used as donor. Since the discovery of ultra-fast photo-induced charge transfer from polymers to C_{60} in the early/mid 1990s[12] acceptor materials have been largely dominated by fullerenes and their derivatives. Yet, the first organic heterojunction solar cell, introduced by Tang in 1986, consisted of a bilayer of copper-phthalocyanine (CuPc) and a perylene derivative and already reached decent device performance compared to CuPc/C_{60} bilayer cells.[10,135] Perylene derivatives have thus previously been shown to potentially be a suitable material class for electron acceptors. Diindenoperylene has been introduced as a solar cell donor material by Wagner *et al.* in 2010 and since been heavily investigated morphologically and electrically in solar cells and organic field effect transistors.[21,72,94,136] Despite the fact that it performs well in solar cells as an electron donor for fullerenes[72] it was also found to posses an electron mobility that even exceeds the already good hole mobility in thin film transistors and single crystals.[90,136] This potentially enables the application of DIP as electron acceptor in solar cells if an energetically suitable material is found to form a type-II heterojunction. 6T has been shown to meet these requirements[66] and an intermolecular gap of 1.8 eV has been found for the 6T/DIP interface.[63] For comparison, the intermolecular gaps found for the 6T/C_{60} and DIP/C_{60} heterojunctions are 0.95 eV and 1.4 eV, respectively.[63*] A schematic drawing of the energetic landscape is shown in Figure 5.1.

Figure 5.2 (a) shows j-V characteristics of planar heterojunction solar cells of the

*Note that these values are measured directly at the respective interfaces and thus deviate from the numbers found in Rev. 66, which had been estimated from literature values of different sources.

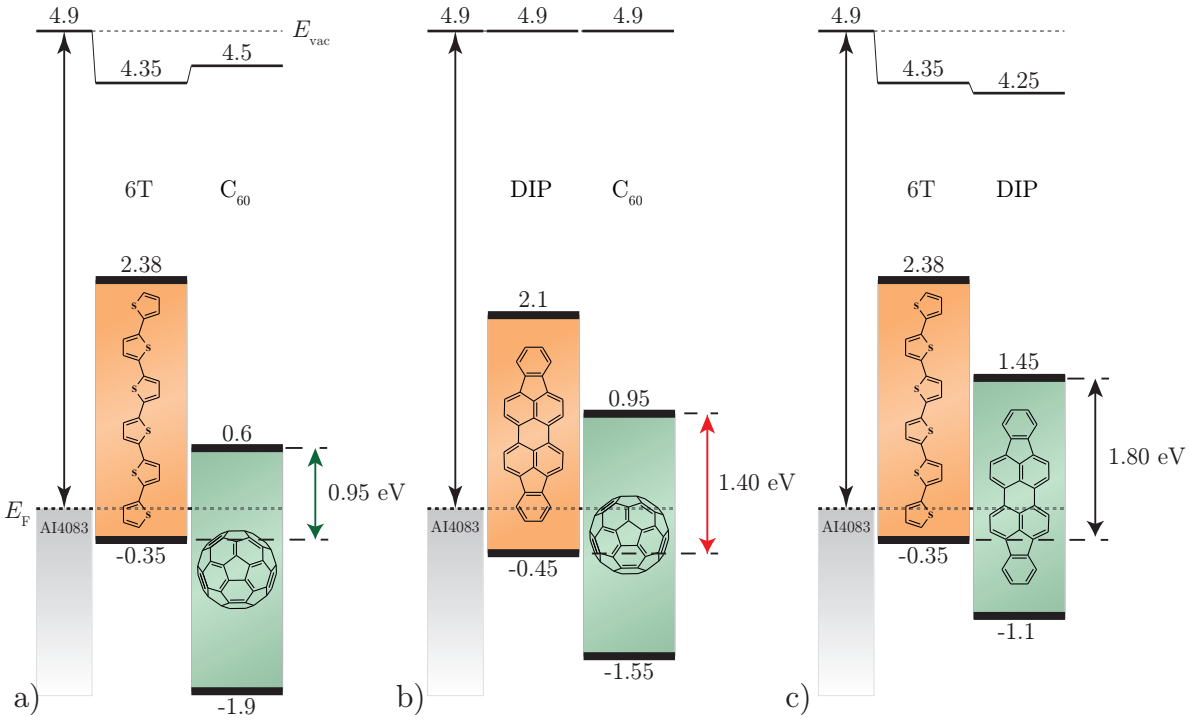

Figure 5.1: Band diagrams of the interface energetics of 6T/C_{60} (a), DIP/C_{60} (b), and 6T/DIP (c) heterojunctions. The workfunction of AI4083 and the AI4083/DIP hole injection barrier are taken from Ref. 72. The LUMO of 6T is estimated by adding the transport gap to the HOMO energy.[75] All other values have been published by Wilke *et al.*.[63]

three possible combinations 6T/C_{60}, DIP/C_{60} and 6T/DIP under white LED illumination. Note that because of the non-standardized illumination conditions, which are in favor of the absorption spectra of the used materials, the photocurrent is slightly overestimated compared to 1 sun. The alternative PEDOT formulation HIL1.3N was used as hole injection layer for these devices. Its larger workfunction avoids the hole injection barrier at the anode/DIP interface present for the standard AI4083 PEDOT:PSS.[108] The observed V_{oc} increases in accordance with the general understanding that the intermolecular gap determines the open circuit voltage in planar heterojunction cells. Opposed to this, the two devices comprising C_{60} have more or less identical short circuit currents, in spite of the different absorption spectra of the donors 6T and DIP (cf. Figure 5.3). This is a strong hint that a significant part of the excitons actually leading to charges stem from the C_{60} rather than from the donor. This is emphasized by the reduced j_{sc} seen for the fullerene-free 6T/DIP solar cell. Still, this j-V curve illustrates that 6T and DIP are a suitable material combination for a heterojunction where DIP acts as the acceptor and yields a reasonable photovoltaic cell.

Even though the wet processing of polymers and the vacuum deposition of small molecules are rarely combined, DIP can also be used as an acceptor for poly(3-hexylthiophene) (P3HT), which probably is the most widely investigated donor polymer and typically used in polymer/fullerene solar cells. The P3HT (Sepiolid P200, purchased

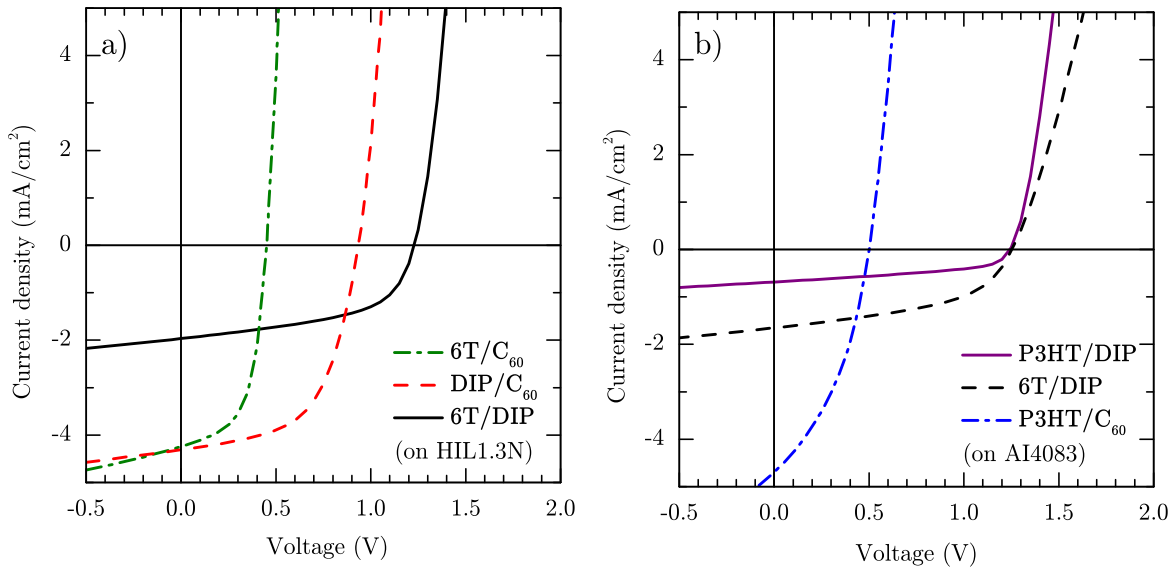

Figure 5.2: DIP can take the role of the acceptor. (a) Comparison or the three possible heterjunction combinations of the materials 6T, DIP and C_{60}. (b) DIP as acceptor can not only be used with 6T but also with P3HT. For comparison, a P3HT/C_{60} planar heterojunction solar cell is shown. (Taken from Ref. 22. Note that the C_{60} thickness is 80 nm in this case and be aware of the reproducibility issues of P3HT/C_{60} heterojunctions.[22])

from BASF) was spin cast on top of PEDOT:PSS (AI4083) from a chloroform solution (12 mg/ml) at a spin speed of 3000 rpm for 80 s. This results in an 80 nm thick film that was annealed in air (but in the absence of UV light) at 75 °C for two hours before further processing. The j-V characteristics of the P3HT/DIP cell are shown as the purple curve in Figure 5.2 (b). The achieved open circuit voltage is 1.24 V and practically identical to that of the 6T/DIP cell and drastically larger than the 0.5 V found for P3HT/C_{60}.[22] This corresponds well with the observed intermolecular HOMO-LUMO gaps of 1.0 eV (P3HT/C_{60}) and 1.65 (P3HT/DIP).[63] Considering the fact that this is less than the gap of 6T/DIP, the energy loss seems to be lower in the P3HT/DIP device than in its 6T counterpart. Furthermore, qV_{oc} of the P3HT/DIP device is less than 0.7 eV below the optical gap $E_{opt} = 1.9$ eV of pristine P3HT. Keeping in mind that the ultimate V_{oc} attainable with any given solar cell material at room temperature is expected to be set by $qV_{oc} = E_{opt} - 0.6$ eV,[64] DIP closely approaches the limit of what is possible with P3HT in terms of open circuit voltage. The short circuit current is obviously even lower than in the 6T/DIP case. This can most likely be attributed to the short exciton diffusion length of only 8.5 nm in P3HT.[137] Despite the strong absorption of P3HT, the majority of the generated excitons is thus expected to be lost before they can reach the junction and contribute to the current.

The introduction of DIP as an electron acceptor in combination with 6T is the basis of the following chapters. The possibility to combine 6T with the spheric standard acceptor C_{60} as well as the rod shaped DIP molecule enables a unique possibility to investigate the impact of mutual molecular orientation at the donor/acceptor heterojunction. As

a start, we investigate the morphology of the underlying 6T film, the growth of the acceptor layers and the orientation directly at the interface.

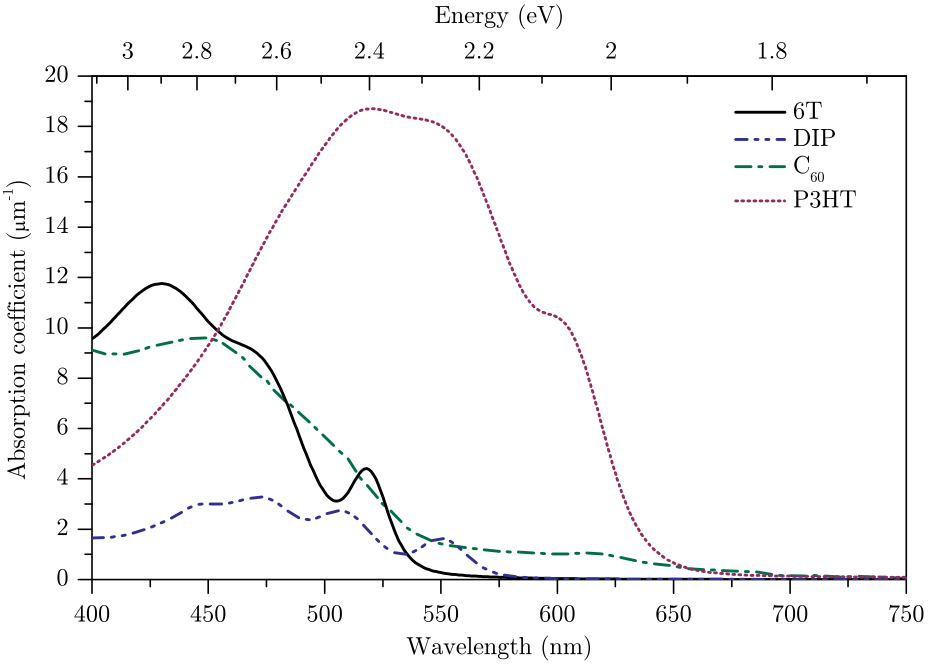

Figure 5.3: Absorption spectra of the organic semiconductors used for the devices shown in Figure 5.2. C_{60} and P3HT are taken from Ref. 138

5.2 6T based planar heterojunction solar cells

5.2.1 Morphology of 6T thin films and 6T/acceptor bilayers

The data of this section have been acquired in close collaboration with the groups of Prof. Dr. Frank Schreiber (University of Tübingen), Prof. Dr. Ellen Moons (Karlstad University, Sweden) and PD. Dr. Andreas Opitz (Humboldt University of Berlin) and are published in Ref. 139.

The morphology of 6T thin films has previously been shown to depend on the growth conditions such as the substrate type, substrate temperature and the deposition rate.[78–81,140,141] In the following the growth of 6T on PEDOT:PSS is investigated as well as the impact of the thiophene structure on subsequent acceptor layers. The substrate temperature during the growth of 6T was either kept at room temperature (RT), i.e. typical lab temperatures between 20 °C and 30 °C, or heated to 100 °C referred to as high temperature (HT). Note that the sample was always cooled down to room temperature in vacuum before further deposition of subsequent layers, thus that throughout this work RT or HT always denotes the growth condition of the 6T film and only the 6T film. If not stated otherwise, the deposition rate of 6T was always set to 0.3 Å/s and the acceptor layers have been deposited at a rate of 0.5 Å/s. The thickness of each layer is 60 nm. The morphological investigation is presented in three different steps. First the bulk morphology is investigated by means of X-ray scattering techniques. Then the molecular orientation at the free surface of 6T and directly at the donor/acceptor interface is analyzed by means of X-ray absorption. Finally, the surface topography is studied by tapping mode scanning force microscopy.

Bulk morphology

X-ray reflectivity spectra of 6T grown at room temperature (blue) and 100 °C (red) as well as 6T/DIP and 6T/C_{60} bilayers are shown in Figure 5.4 (a). Both the RT and HT neat 6T films (lower data in Figure 5.4(a)) exhibit distinct features stemming from the (200) lattice plane and its higher orders and belong to a low temperate phase of upright standing 6T molecules.[78] The (10,00) peak of the RT film is, however, broadened by an additional contribution from the (41-1) reflection. This broadening is illustrated more clearly by the magnification of the (10,00) peak shown in Figure 5.4 (b) and can be attributed to a lying 6T phase. For the heated 6T film the broadening of the (10,00) peak vanishes and only upright standing 6T is present in the film with an angle of approximately 70° between the long molecular axis and the substrate plane, as extracted from the crystal data found by Horowitz *et al.*[78] The respective orientation is a result of differently tilted 6T unit cells as illustrated in Figure 5.5. The 6T molecules are standing on the (200) plane and are lying almost flat within the (41-1) plane with an angle of only 3° to the long molecular axis.

If DIP is deposited onto these films (middle lines in Figure 5.4 (a)), (001) and (002) features of DIP are visible for both the RT and the HT samples. These peaks belong to an upright standing orientation of DIP molecules, the so called σ-orientation.[89] Ad-

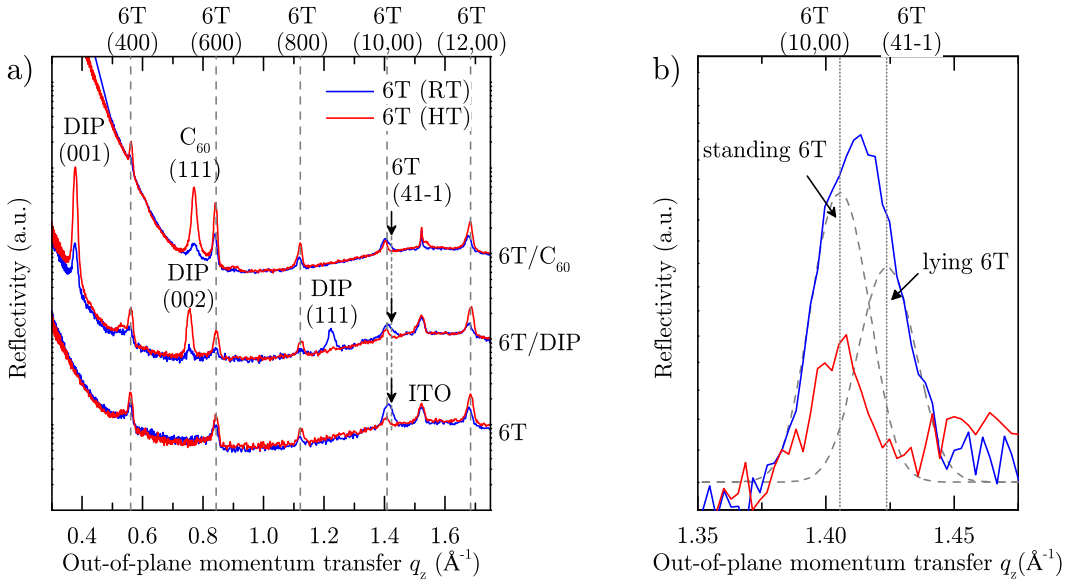

Figure 5.4: (a) X-ray reflectivity spectra of neat 6T and bilayers of 6T/DIP as well as 6T/C_{60} with 6T grown at room temperature (blue lines) and at 100 °C (red lines) substrate temperature. (b) Zoom in on the 6T (10,00) for neat 6T. At room temperature this peak is a superposition of the (10,00) and the (41-1) reflexes indicated by the dashed gray curves.

ditionally, for the 6T(RT)/DIP bilayer the DIP (111) reflection, stemming from the λ-orientation of lying molecules, is clearly visible.[91,143] When DIP is grown on HT 6T, the (111) peak of DIP vanishes at the same time as the DIP (001) and (002) strongly increase. This shows that the DIP growth is templated by the 6T morphology. Only upright standing DIP grows on purely upright standing 6T, while a mixture of standing and lying DIP domains is present if standing and lying 6T crystallites coexist in the bottom layer.

Finally, C_{60} grown on top of sexithiophene (upper data in Figure 5.4 (a)) exhibits a peak of the (111) reflection of the C_{60} fcc phase.[144] This feature is small for the room temperature case but becomes drastically stronger when the fullerene is grown on the HT 6T film. Apparently, a templating effect is present also for this system resulting in remarkably high crystallinity of the C_{60} compared to the room temperature case and to what is typically found for C_{60} thin films in similar systems.[72,135] Presumably, the observed increase of the peak intensity is due to a changed overall crystallite orientation of C_{60}, where the (111) lattice planes align parallel to the substrate, similar to what was shown for C_{60} thin films grown on DIP.[145] The intensity gain of the C_{60} (111) reflection is accompanied by the occurrence of significantly sharper 6T features for the 6T(HT)/C_{60} bilayer compared to the neat HT 6T film. This indicates increased crystallinity of the underlying 6T film and suggests that C_{60} induces a ripening of the 6T crystallites, an effect that is not observed for 6T/DIP bilayers.

The out-of-plane coherent crystallite sizes have been extracted from the X-ray reflectivity data and are summarized in Table 5.1. For both 6T preparation conditions

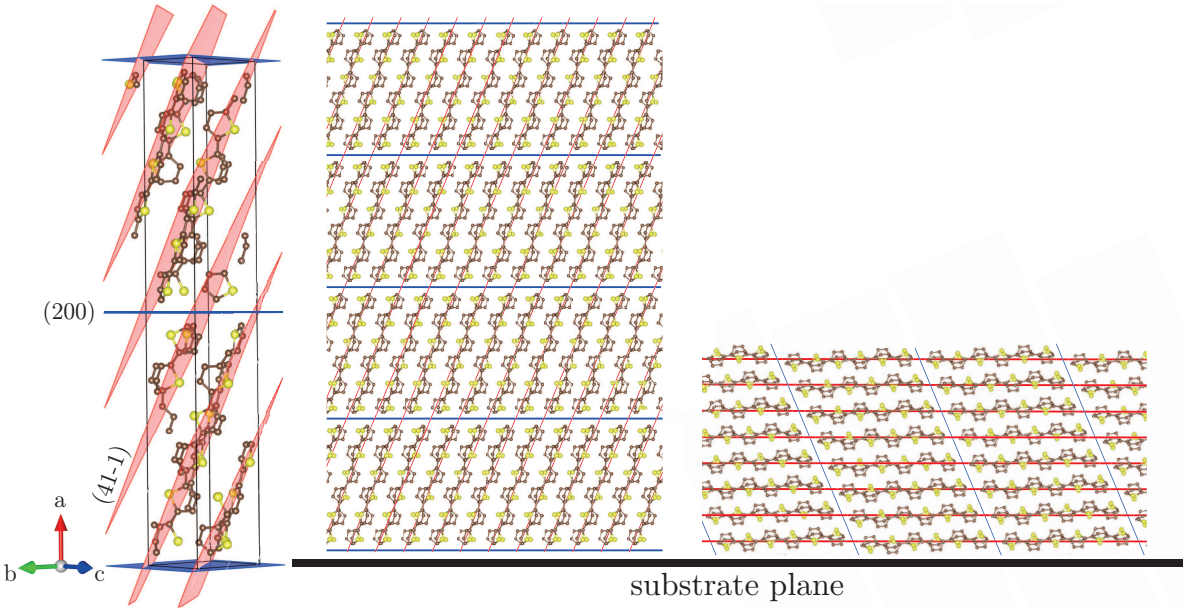

Figure 5.5: Unit cell of α-sexithiophene according to the crystal data found by Horowitz *et al.*[78] The reflections at the (200) (blue) and the (41-1) (red) planes observed in the XRR measurement correspond to crystallites of standing and lying molecules, respectively. The pictures have been created with the free software VESTA.[142]

the extracted sizes are approximately one half of the total 6T film thickness of 60 nm. Yet, as a general trend, 6T grown at 100 °C shows slightly larger crystallites than 6T grown at room temperature. The same holds for the donor films grown on top of the differently prepared 6T layers. The vertical size of crystallites of standing DIP tends to be slightly larger than that of 6T which remains virtually unchanged by the DIP. On the other hand, when C_{60} is deposited the 6T crystallite size increases. This effect is slightly stronger for the HT sample. The crystallite sizes of lying 6T and DIP are similar to that of standing 6T. Note, however, that the (41-1) feature of lying 6T is screened by the overlapping (10,00) peak and has thus to be treated as a rough estimate.

In addition to the X-reflectivity measurements probing the out-of-plane order of the sample, reciprocal space maps of room temperature and high temperature grown 6T films and the respective 6T/DIP bilayers are shown in Figure 5.6. The co-existence of domains of lying 6T molecules (marked in red) and domains of standing 6T (yellow) in films grown at room temperature is nicely illustrated in Figure 5.6 (a). Comparison of the RT and HT reciprocal space maps (Figure 5.6 (a) and (b)) shows that the crystallites with a lying orientation of 6T vanish if the film is grown at 100 °C. This confirms the findings of the XRR measurements.

Similarly, the reciprocal space map in Figure 5.6 (c) confirms that standing and lying DIP domains co-exist if both orientations are already present in the 6T film. If DIP is grown on top of purely upright standing 6T (Figure 5.6), the features of lying DIP vanish except for a small contribution from the DIP (001) peak, visible even in the high temperature case. However, domains of lying DIP molecules have previously been

Table 5.1: Coherent crystallite sizes extracted from the X-ray reflectivity (out-of-plane) and grazing incidence X-ray diffraction measurements (in-plane). The values in parentheses are extracted from the 6T (41-1) feature that overlaps with the (10,00) peak and thus has to be regarded as a rough estimate. All values are given in nm.

	w/o acceptor		DIP				C_{60}			
	6T		RT		HT		RT		HT	
	RT	HT	6T	DIP	6T	DIP	6T	C_{60}	6T	C_{60}
out-of-plane	26	31	25	37	33	44	35	25	46	39
out-of-plane (lying)	(28)			26						
in-plane (standing)	20	19	16	16	19	19				
in-plane (lying)	35		24	32		25				

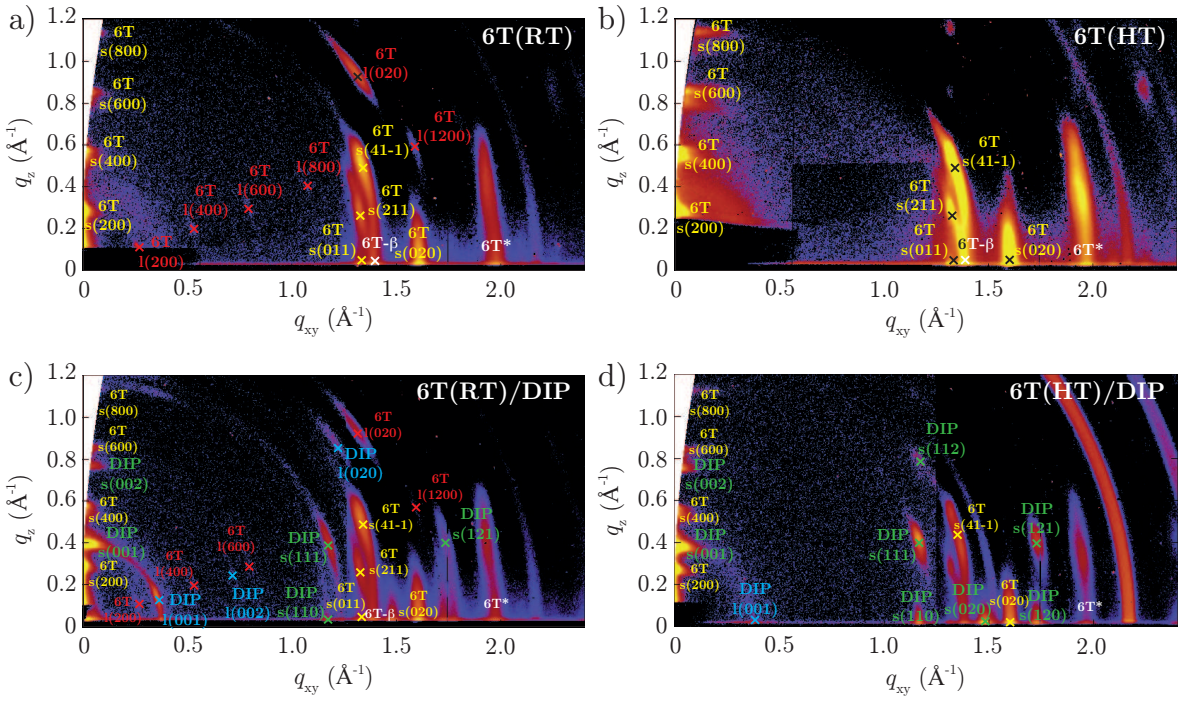

Figure 5.6: Reciprocal space maps of 6T grown at room temperature (a) and at 100 °C (b) and DIP grown on top of such films (c) and (d), respectively. Features stemming from lying 6T (DIP) are marked in red (blue), features caused by standing 6T (DIP) in yellow (green). The reciprocal space maps are background corrected and stitched together from two or more detector images.

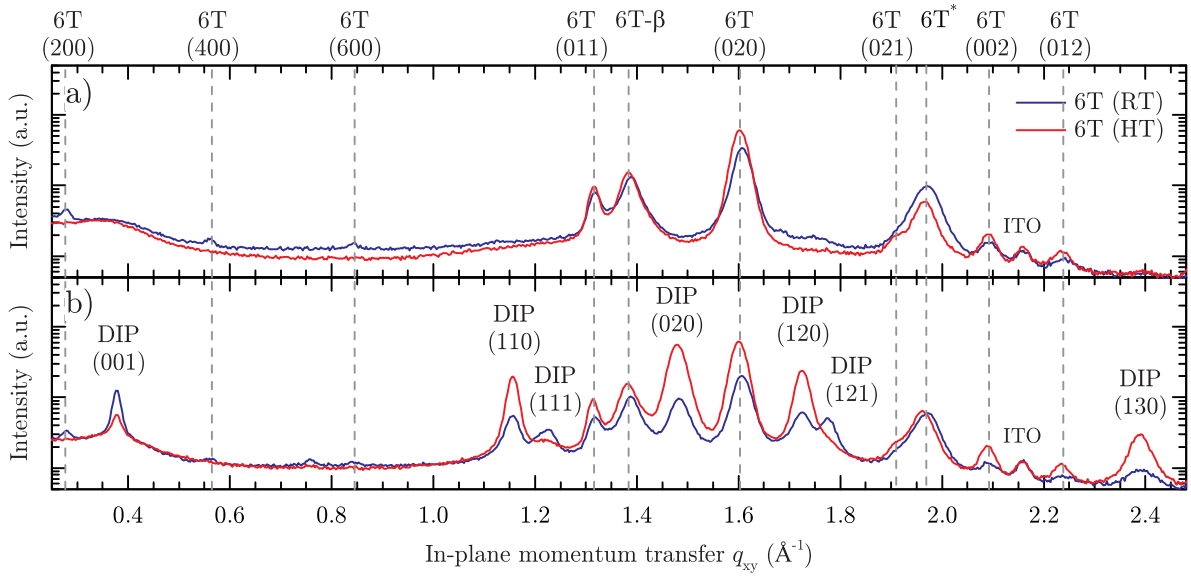

Figure 5.7: Grazing incidence diffraction spectra of 6T (a) grown at room temperature (blue) and 100 °C (red) and DIP grown on top of such 6T films (b).

reported to form with increasing DIP layer thickness.[93,143,146] The formation of lying DIP is hence expected to occur in the upper part of the film only, whereas the 6T/DIP interface is expected to consist solely of upright standing molecules in the HT case.

Finally, grazing incidence diffraction spectra of neat 6T and 6T/DIP bilayers are shown in Figure 5.7. The presence of lying 6T molecules in the RT films is indicated by the occurrence of tiny (200), (400) and (600) in-plane features, which vanish for the HT grown films where only upright standing molecules are present. Besides the peaks identified with 6T lattice planes an additional peak is visible in Fig 5.7 and marked with 6T-β. This feature presumably stems from a different polymorph of upright standing 6T, previously found in literature and referred to as the 6T β-phase.[79,80] Additionally, there is a peak marked 6T*. This peak is difficult to assign and is most likely a superposition of the (32-1) peak and a contribution stemming from the β-phase of 6T. Note that since the (32-1) lattice plane is more or less parallel to the long molecular axis of 6T, it cannot be clearly derived if the (32-1) contribution originates from standing or lying molecules. Its presence in the RT as well as in the HT data, however, is a very strong hint that the 6T*-peak stems primarily from upright standing molecules.

In accordance with the reciprocal space maps, the DIP (001) feature is present in the GIXD data of both the RT and the HT bilayer in Figure 5.7 (b). This confirms the presence of lying DIP even when it is grown on purely upright standing 6T. Again, it is assumed that domains of lying DIP are only present in the upper part of thick DIP layers in this case. The lateral coherent crystallite sizes can be extracted from grazing incidence X-ray diffraction patterns by fitting the peaks and applying the Scherrer equation (4.4). The results are again summarized in Table 5.1. The lateral sizes of crystallites of standing molecules are 20 nm and below and thus slightly smaller than the vertical

dimensions. The values for 6T and DIP extracted from the bilayer samples match well for both preparation conditions, which is in agreement with the expected templating effect. The lateral coherent size of the crystallites consisting of lying molecules appears to be significantly larger compared to the respective upright standing species for both materials. This is even the case for the lying DIP present in the upper part of the film grown on HT 6T despite the absence of lying molecules in the bottom 6T film. The lateral coherent crystallite size of the 6T β-phase domains is 15 nm in both the RT and the HT films.

Interface morphology

While the bulk morphology has been probed by means of the X-ray scattering technologies presented above, the molecular orientation at the free 6T surface and directly at the donor/acceptor interface can be probed by Near Edge X-ray Absorption Fine Structure spectroscopy. Since the sample current is used as the measurement signal in TEY mode, Silicon/PEDOT:PSS was used as substrate instead of ITO/PEDOT:PSS. The thickness of the 6T films was 40 nm for NEXAFS samples. Since NEXAFS is a surface sensitive technique, only 5 nm of the donor materials were used for investigation of the interface in bilayer structures.

The carbon K-edge NEXAFS TEY spectra of the neat materials are shown in Figure 5.8. The corresponding spectra of 6T/DIP and 6T/C_{60} bilayers as well as their deconvolution into component spectra are presented in Figure 5.9 and Figure 5.10, respectively. For clarity only spectra recorded at 30°, 55° and 90° angle of incidence w.r.t. the substrate plane are shown. With the exception of neat C_{60}, additional spectra at 40° and 70° angle of incidence have been recorded and were regarded for the extraction of the molecular orientation.

The neat 6T spectra show a clear dependence of the intensity on the angle of the incident X-rays. Similar to the DIP example discussed in Section 4.2, the intensity of the π^* resonances increases with the angle of incidence, indicating a preferentially upright orientation of the molecules.[119,147,148] The dichroism becomes even more pronounced for 6T grown at a substrate temperature of 100 °C and indicates a larger average molecular tilt angle. This is in agreement with the vanishing of lying 6T molecules observed by X-ray scattering, bearing in mind that NEXAFS averages over all molecular orientations present in the probed volume.

DIP and C_{60} have already been discussed in Section 4.2 and an orientation angle of 83° was found for DIP while, expectedly, C_{60} does not show a preferential orientation. Note that the presented DIP NEXAFS spectra are recorded on DIP grown at 100 °C. Yet, there is virtually no difference to films grown at room temperature and both yield the same orientation. This is in accordance with the absence of lying molecules in neat DIP grown on PEDOT:PSS regardless of the growth temperature (for temperatures above 20 °C).[72]

Even though the bilayer spectra on the far left in Figure 5.9 and Figure 5.10 show a dependence on the incident angle, the signal is a superposition of the individual component spectra. This is nicely visible in the seemingly reduced dichroism of the HT 6T/C_{60}

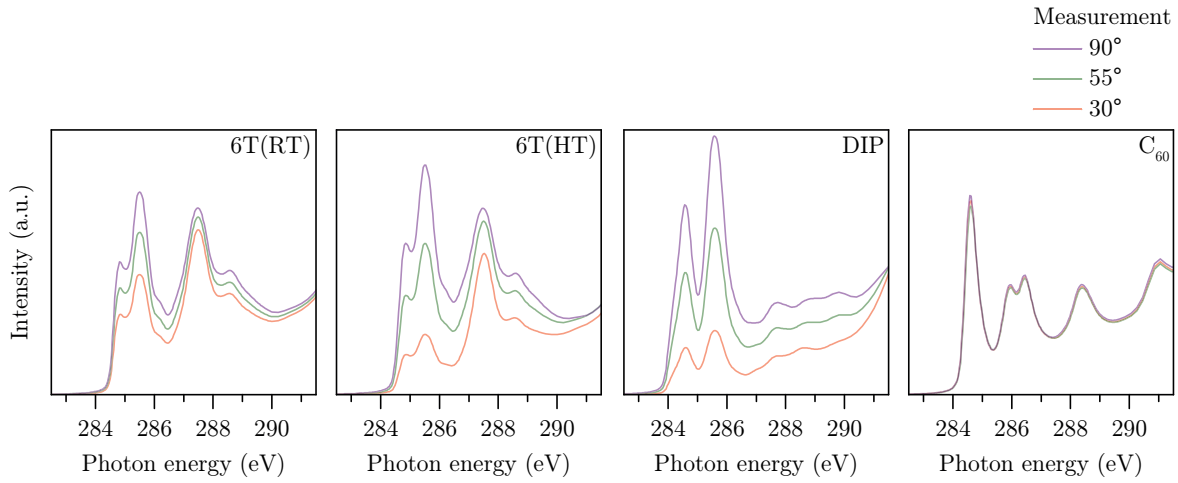

Figure 5.8: C1s NEXAFS spectra of neat films of 6T(RT), 6T(HT), DIP and C_{60}. For clarity only 30°, 55°, and 90° angle of incidence are shown. All spectra are recorded in TEY mode, all films have been prepared ex-situ.

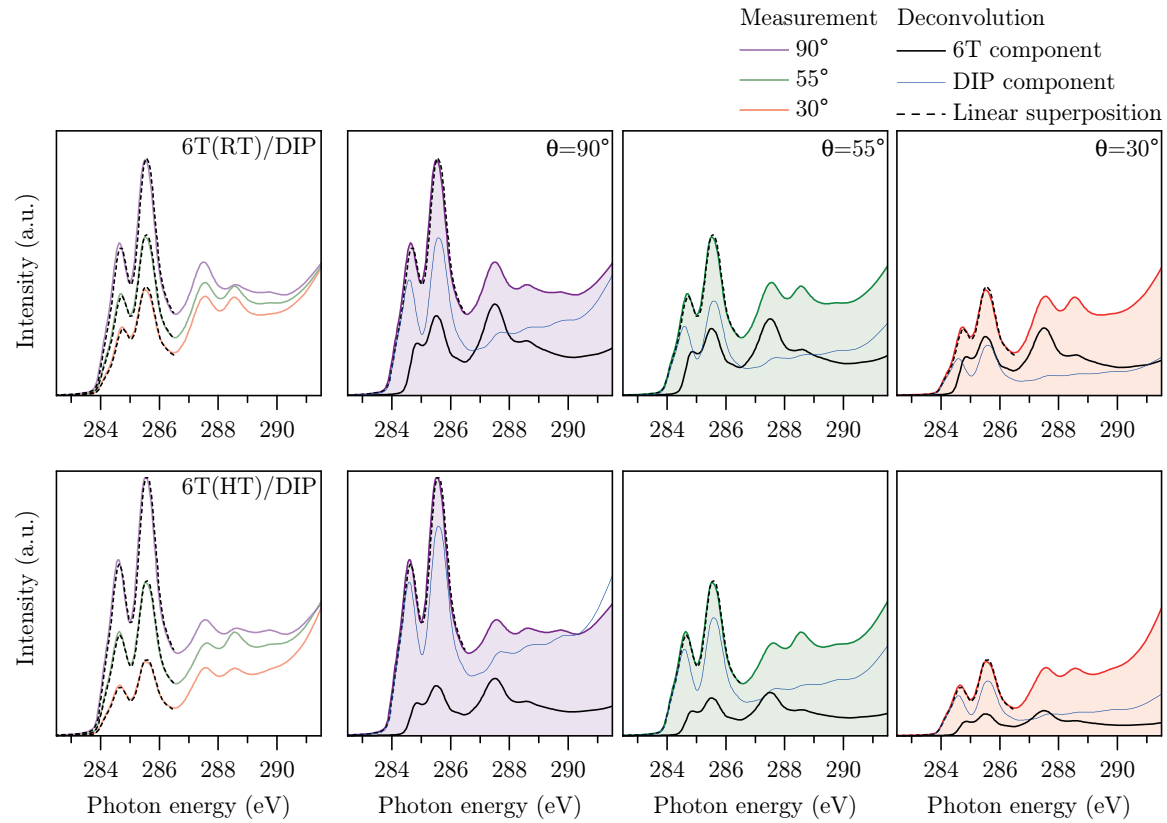

Figure 5.9: C1s NEXAFS spectra of 6T/DIP bilayers (left) and deconvolution into component spectra. The compositional fit has been performed for an energy range from 284.5 eV to 286.5 eV and the result is shown as the black dashed lines. For clarity only 30°, 55°, and 90° angle of incidence are shown. All spectra are recorded in TEY mode, all films have been prepared ex-situ.

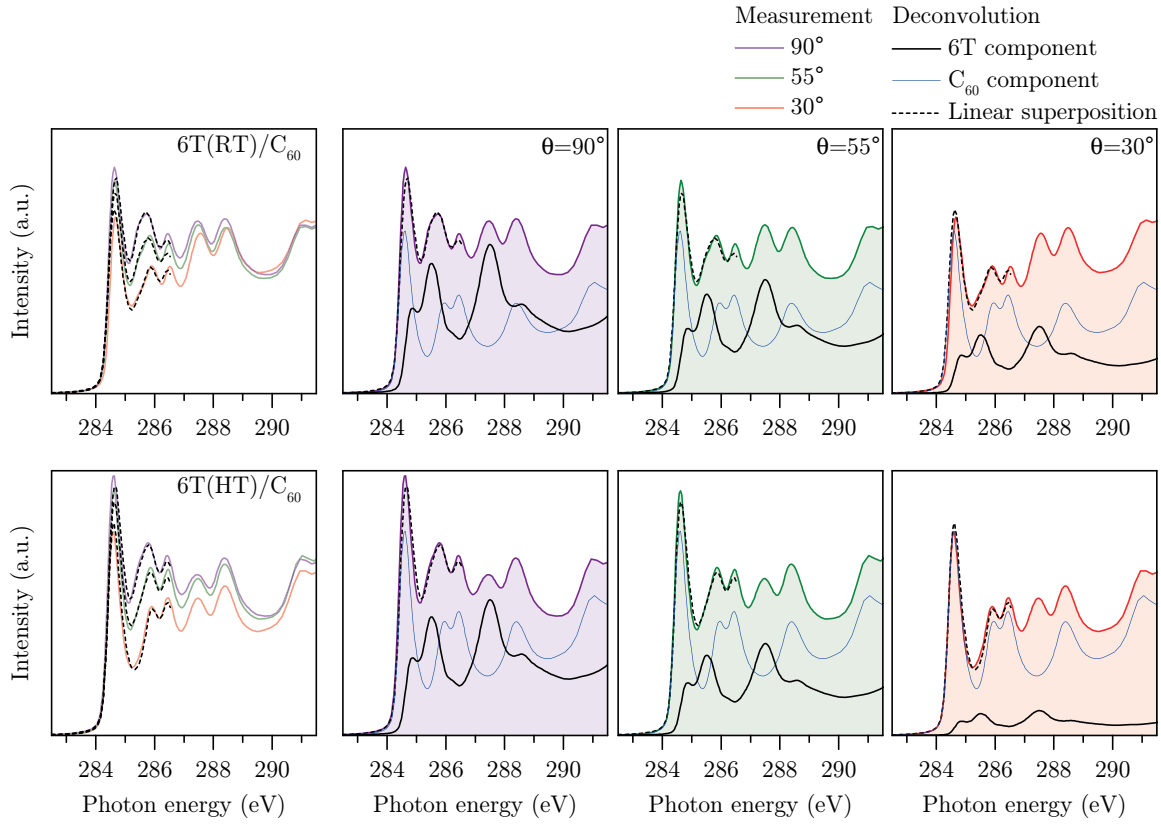

Figure 5.10: C1s NEXAFS spectra of 6T/C_{60} bilayers (left) and deconvolution into component spectra. The compositional fit has been performed for an energy range from 284.5 eV to 286.5 eV and the result is shown as the black dashed lines. For clarity only 30°, 55°, and 90° angle of incidence are shown. All spectra are recorded in TEY mode, all films have been prepared ex-situ.

spectra compared to the neat 6T(HT) spectra that become damped by the isotropic absorption of C_{60}. These spectra were thus deconvoluted by a best fit of the common π^* region with a linear combination of the individual component spectra in an energy range of 284.5 eV - 286.5 eV. The fit results are shown as the black dashed lines in Figure 5.9 and Figure 5.10. Additionally, the deconvoluted components are shown under the measured curves in the three graphs on the right. Their relative contributions at different angles then provide information on the molecular orientation directly at the interface. Note that a common contribution of C_{60} was used for all angles in the deconvolution process of the 6T/C_{60}, since no angular dependence is expected for the C_{60} component.

The angular dependence of 6T in the neat films and its contribution to the bilayer spectra are presented in Figure 5.11. As an overall trend for all configurations, larger angles are found for 6T grown at 100 °C (more upright standing molecules) than for RT grown films. This is in agreement with the X-ray scattering results and confirms the presence of lying 6T molecules at the surface of RT films that vanish if the 6T is grown at 100 °C substrate temperature. The data points of neat 6T(HT) and the 6T(HT) at the interface to C_{60} are very close to each other and a common fit yields a molecular tilt angle of 84°. This is slightly larger than the 6T angle of 72° extracted for the interface to DIP. The expected average angle between the plane of the 6T backbone, containing the thiophene rings, and the substrate plane is approximately 78°, as extracted from the crystal structure.[78] This angle is essentially the quantity determined by NEXAFS. Compared to the bulk, the measurements thus suggest slightly more upright standing molecules at the free surface and at the interface to C_{60} but slightly more tilted 6T at the 6T/DIP interface. Note, however, that apart from the experimental error of ±3 additional uncertainties are introduced by the deconvolution procedure and the fit itself. The latter is estimated to about ±5 for extreme angles but expected to strongly reduce for angles close to the magic angle. Further uncertainty is added to the deconvolution by the dichroism of DIP which adds an additional free parameter to the linear combination.

In the room temperature case, a similar trend is visible, with a slightly larger angle for C_{60} covered 6T. Yet, the differences between the free surface of 6T and the interfaces to the two acceptors are within the error. A common fit of all three datasets yields an average angle of 64°. Because of the herring-bone structure, the average angle between the molecule planes and the (41-1) plane, i.e. the average angle of lying molecules, as extracted from the crystal structure is approximately 56°.[78] With the theoretical angle of 78° of standing molecules, this allows a (perhaps oversimplified) estimation of the ratio between standing and lying 6T and yields approximately 43 % standing and 57 % lying molecules. It thus appears that more lying than standing molecules are present at the 6T(RT) donor/acceptor interface.

Bear in mind that because of the relatively large errors the extracted values have to be handled with care and should be regarded as trends rather than absolute angles. Nevertheless the differences between RT and HT films are clear and confirm the bulk findings of the X-ray scattering analysis.

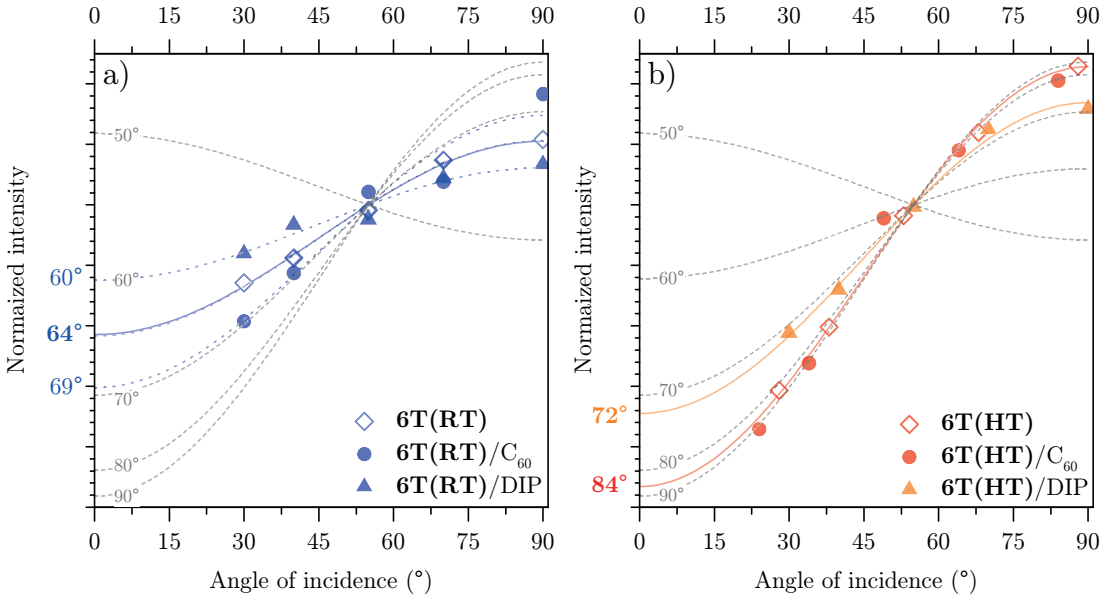

Figure 5.11: Dependence of the 6T C1s $\longrightarrow \pi^*$ resonances on the angle of incidence of the X-ray beam. An energy range from 284.4 eV to 286.5 eV was taken into account for the extraction of the relative intensities. Colored, dashed lines indicate fit results to individual datasets, solid lines show the result of a common fit to the respective datasets. The gray, dashed lines illustrate the calculated behavior for orientation angles from 50° to 90° and are provided as a guide to the eye. The data have been corrected for angle misalignment and normalized to 55° angle of incidence.

Surface topography

The surface topography corresponding to the bulk and interface morphology investigated above is shown in the AFM images in Figure 5.12. The surface of neat 6T grown at room temperature as well as DIP and C_{60} grown on top of RT 6T are shown in Figure 5.12 (a) above the height scale bar. The maximal height differences are approximately 70 nm at nominal thicknesses of 60 nm (6T) and 120 nm (6T/DIP and 6T/C_{60}). Yet, they appear relatively smooth compared to the HT films shown in Figure 5.12 (b) below the height scale bar. The neat 6T(HT) film (left in Figure 5.12 (b)) exhibits a terrace like structure of smooth islands with a diameter of about 400 nm, which is about 4 times the size of the grains in the RT film. However, the otherwise smooth film is disturbed by large pillars as high as 250 nm, as indicated by the inset height profile in the AFM image.

DIP grown on such a film more or less preserves the underlying 6T structure and forms small grains that slightly smooth the surface (cf. center image in Figure 5.12 (b)). C_{60} on the other hand, seems to induce a ripening of the 6T(HT) bottom layer that increases the number and size of the pillars (right image in Figure 5.12 (b)). The area between the pillars resembles the island structure observed for the 6T film covered by smaller grains of C_{60} with a size of ~65 nm.

Note that the topography of a neat 6T film grown at a nominal temperature of

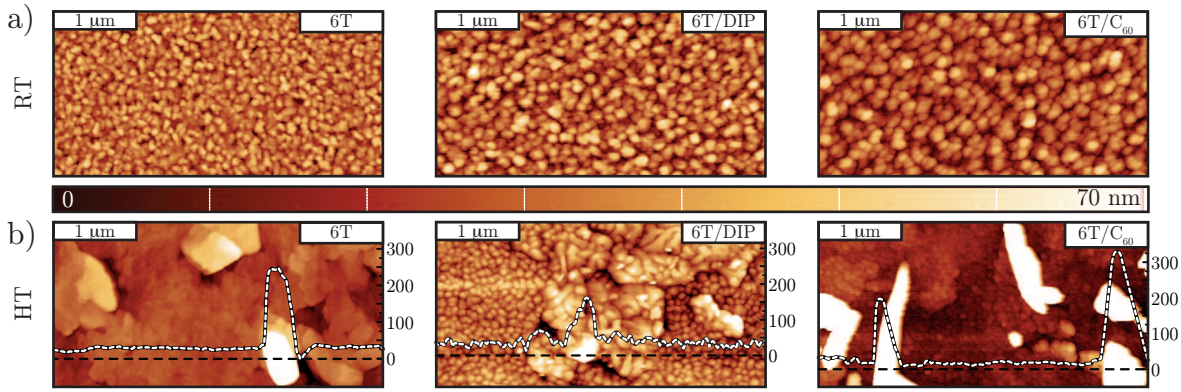

Figure 5.12: Scanning force microscopy topography images of neat 6T (left) grown at room temperature (a) and at 100 °C (b) as well as DIP (center) and C_{60} (right) grown on such films. The black and white dashed lines set in into (b) are height profiles taken at the black dashed lines with the scale given in nanometers at the right side of the respective image. Taken from Ref. 139.

100 °C is not quite straightforward to retrieve. Instead the number and size of the observed pillars varies for different samples thus that the surface topography seems to be very sensitive to slight variations in the preparation process, presumably to deviations of the actual substrate temperature or possibly minimal variations of the deposition rate. It appears, however, that a smooth structure with the absence of pillars are fragile and ripened by C_{60}. This possibly correlates with the increased intensity of the 6T peaks observed in the X-ray reflectivity if C_{60} is deposited on HT grown C_{60} (cf. Figure 5.4). Surprisingly, these topographical differences seem to be largely independent of the molecular orientation present in the 6T film, which always has been found to be upright standing. Also the device characteristics of solar cells seem to be unaffected by potential variations in the topography of the initial, neat 6T layer.

The results of the morphological investigations of the growth of 6T on PEDOT:PSS and of subsequent acceptor films presented above are graphically summarized as the cartoons shown in Figure 5.13. Note that it cannot be excluded that the C_{60} molecules partially roll off of the 6T pillars which leaves the 6T partially uncovered. Furthermore it cannot clearly be distinguished between a scenario, where the ripening of HT grown 6T is induced by C_{60} and a case, where the ripening has to be regarded as a degradation of 6T which is suppressed by DIP but not by C_{60}. The latter would imply that the formation of the pillars observed by AFM and the increased crystallinity caused by C_{60} discovered by X-ray scattering are two, totally independent phenomena.

A direct consequence of the morphological changes of the 6T film accompanied with changing the growth temperature from room temperature to 100 °C is a drastically reduced absorption coefficient of the 6T film. This is illustrated in Figure 5.14 and can be explained by the absence of lying molecules in the HT film. The transition dipole moment for optical absorption is oriented parallel to the long molecular axis of 6T.[149] This is unfavorable for the absorption of photons impinging perpendicularly to

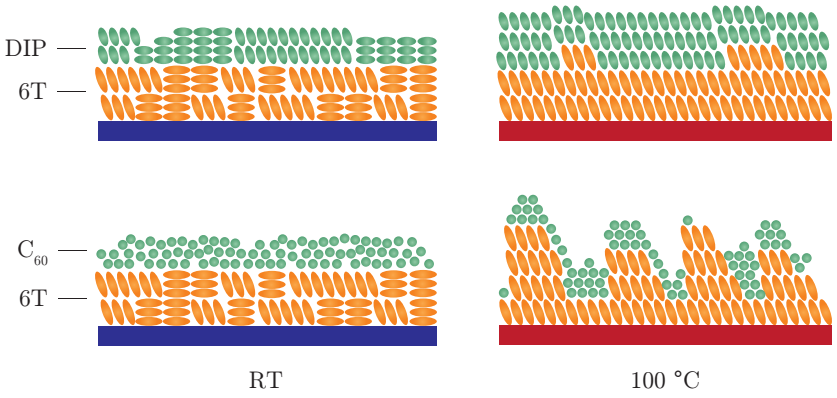

Figure 5.13: Schematic illustration of the morphology of 6T/C_{60} and 6T/DIP bilayers grown on PEDOT:PSS at room temperature (left) and 100 °C (right) substrate temperature. At room temperature domains of lying and standing 6T are present in the film, while a an elevated temperature during the growth process yields to a highly ordered 6T film of solely upright standing molecules. Subsequent acceptor layers are templated by the 6T morphology. Growth of domains of lying and standing DIP is induced by RT grown 6T but mutual overgrowth of the respective domains is expected. An overall increased crystallinity is found for films grown on HT 6T. Taken from Ref. 139

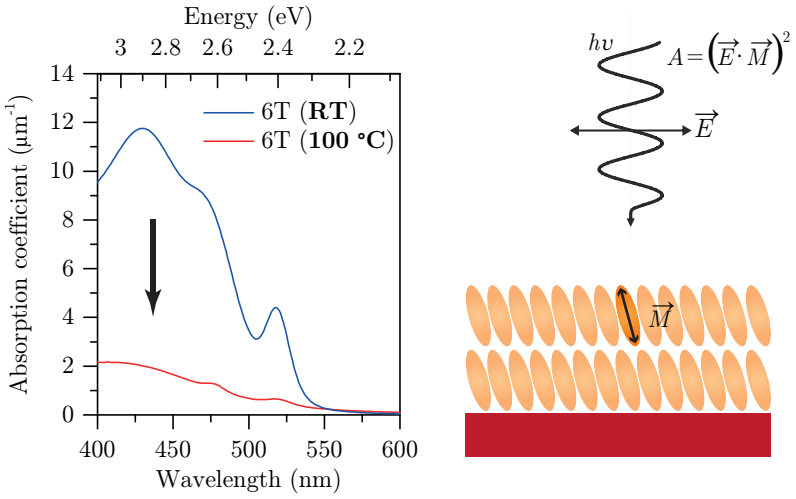

Figure 5.14: Absorption spectra of 6T grown at room temperature (blue) and at 100 °C substrate temperature (red). The absorption coefficient is drastically reduced by the absence of lying molecules in the HT film because of an unfavorable orientation of the transition dipole moment $\boldsymbol{M}$ as illustrated by the cartoon on the right.

the substrate because of reduced coupling to the electric field of the light.

5.2.2 Electronic properties at the 6T/acceptor interface

The interface energetics at the donor/acceptor junction have been shown to be crucial for the device performance of organic photovoltaic cells, most notably for the open circuit voltage.[28,62,63,150] At the same time, it is known that the ionization potential of both 6T and DIP depend on the orientation of their molecules.[84,121,151] Even though the complete film does not change its orientation from solely lying to solely standing molecules when the substrate temperature for the 6T growth is changed from room temperature to 100 °C, the presence of domains of lying molecules in the RT 6T and DIP films might still have an impact on the energetic landscape at the donor/acceptor interface. The HOMO level onsets and SECOs of 6T grown on PEDOT:PSS at 30 °C and 100 °C substrate temperatures as well as stepwise deposited acceptor layers have thus been investigated by ultraviolet photoelectron spectroscopy. The resulting spectra are displayed in Figure 5.15.

The initial work function of the PEDOT:PSS substrates can be extracted from the secondary electron cutoff of the bottom curves in Figure 5.15 (a) and (c) and are marked by vertical bars. The work function of the (*in vacuo*) unheated PEDOT:PSS (blue curve) is determined to almost 5.0 eV and increases to 5.3 eV after the film was heated to 100 °C in vacuum (red curve). The extracted values are well reproduced for the 6T/DIP and the 6T/C_{60} PEDOT:PSS substrates. The relative shift of about 0.3 eV is in good agreement with previously published results on the same PEDOT:PSS formulation and can be attributed to the removal of residual water in the film by heating in vacuum.[107,108]

The SECOs of all measured 6T films (second spectra from the bottom in Figure 5.15 (a) and (c)) reproducibly indicate identical work functions of 4.6 eV independent of the preparation conditions. Independent of the initial substrate work function an interface dipole is formed and the Fermi level gets pinned at the positive polaron level of 6T in both the RT and the HT case.[152] This is in agreement with the reported critical electrode work function of 4.35 eV above which pinning occurs for 6T,[71] and indicates that the minimum possible hole injection barrier is formed at the PEDOT:PSS/6T interface regardless of the preparation conditions.[129] It is thus little surprising that identical HOMO-level onsets, and hence identical hole injection barriers, of approximately 0.25 eV are found for all investigated 6T films. These are indicated by the vertical bars in the valence region spectra shown in Figure 5.15 (b) and Figure 5.15 (d). The resulting ionization energy of 4.85 eV is in between the values found in literature.[63,71,84]

The development of the energetic landscapes at the 6T/DIP interfaces is shown in Figure 5.15 (a) and (b). For the room temperature film (blue), the work function shifts to 4.5 eV if 0.3 nm of DIP are deposited on top of the 6T. The resulting interface dipole of −0.1 eV is in accordance with what was previously reported for this interface and presumably caused by mutual polarization of the molecules.[63] However, unlike to what was observed in Ref. 63, the work function is further shifted to roughly 4.35 eV for 2 nm DIP coverage. At this thickness, the valence region does not include features stemming

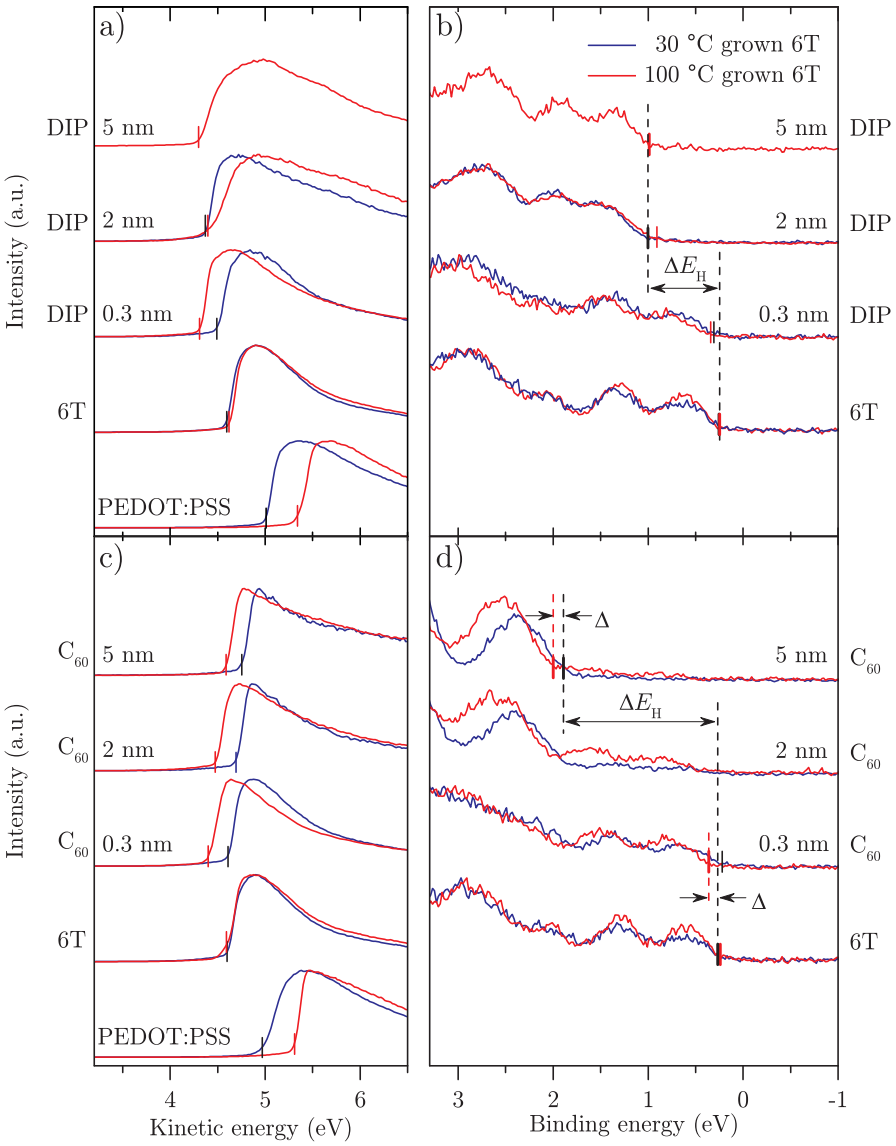

Figure 5.15: UPS SECO ((a) and (c)) and valance region spectra of room temperature (blue) and high temperature (red) grown 6T and DIP (b) or C_{60} (d) grown on top at room temperature. The HOMO level onsets are identical within the experimental error of approximately $\pm 0.05\,\mathrm{eV}$. ΔE_H equals 0.75 eV for 6T/DIP and 1.65 eV for 6T/C_{60}.

from 6T and a HOMO level onset of 1.0 eV is extracted. In good agreement with the findings by Wagner *et al.*, this yields an ionization energy of 5.35 eV.[72]

If DIP is deposited on the 6T film grown at a substrate temperature of 100 °C, the initially formed interface dipole is slightly larger compared to the RT case and a work function of about 4.3 eV is extracted from the SECO. The larger interface dipole might possibly be attributed to orientation dependent polarizability of the rod shaped molecules which is expected to be larger parallel to the long molecular axes.[153] This would be in favor of the upright standing molecules solely present in the HT films. Please note that upon further deposition the work function seems to first relax to the RT value and then back. This appears very unlikely and unfortunately no decent conclusion can be drawn from the recorded SECO data for larger DIP thicknesses. Note that the shape of the 2 nm DIP SECO is broadened and might possibly not be reliable. Furthermore a large jitter was observed for the 5 nm DIP measurement, with a tendency to lower kinetic energies (i.e. higher binding energies) and thus lower work functions. This jitter also affects the valence region measurement of the 5 nm DIP film recorded at different spots on the sample. In this case the presented curve is an average of three measurements recorded at the same spot, rather than an average of different spots (as for the other curves). The shown curve is representative for the *lowest* detected binding energy onsets of the DIP HOMO, which coincides with the value of the RT sample and is the most plausible and conservative interpretation from a device perspective: Even if the acquired data cannot totally exclude a possibly larger binding energy of the DIP HOMO at the heterojunction with HT 6T, the measurements clearly show, that in this case the HOMO-HOMO offset ΔE_{H} is either equal or possibly greater than for the room temperature heterojunction. The latter would, however, strongly contradict the observed solar cell device characteristics of these two heterojunctions (see Section 5.2.3). Noteworthy, the opposite constellation, i.e. a larger HOMO-HOMO offset for the RT sample compared to the 100 °C, is clearly ruled out by the UPS results. In accordance with the findings by Wilke *et al.* identical HOMO-HOMO offsets of 0.75 eV yield identical intermolecular energy gaps of 1.8 eV at the 6T/DIP interface, independent of the preparation condition if a DIP transport gap of 2.55 eV is assumed.[63]

Qualitatively similar results are found for measurements of C_{60} deposited on 6T (Figure 5.15 (c) and (d)). When C_{60} is deposited on top of RT grown 6T the SECO gradually shifts to higher kinetic energies resulting in a positive interface dipole of +0.15 eV, in agreement with previously reported measurements. A HOMO-HOMO offset of 1.65 eV is found for the 6T(RT)/C_{60} heterojunction, which slightly deviates from literature values.[63]

Interestingly, the interface dipole changes its sign when C_{60} is deposited onto HT grown 6T and initially forms an interface dipole of −0.2 eV that relaxes almost completely with increasing C_{60} thickness. With regard to the film morphology, this effect is presumably caused by the permanent quadrupole moment of the 6T molecule which depending on the molecular orientation induces inversely oriented interface dipoles. This would then cause a positive interface dipole at the interface of (41-1) oriented (i.e. lying) 6T and C_{60} and a lower or even negative interface dipole at the interface between

(200) oriented (i.e. standing) 6T and C_{60}.[84,154,155] Orientation dependent signs of the quadrupole induced interface dipole have been observed and theoretically described for pentacene/C_{60} heterojunctions.[154] It is important to note that in this case the positive interface dipole assists charge separation at the donor/acceptor heterojunction, while the negative interface dipole at the interface between standing pentacene and C_{60} enhances the recombination process.[154] The situation is expected to be similar for the 6T/C_{60} system and might be highly relevant for solar cell devices.

The deposition of a sub-monolayer of C_{60} on the 100 °C grown 6T film has a distinct impact on the 6T itself and is accompanied by a shift of the valence region spectrum and thus HOMO onset of the underlying 6T by about 0.1 eV towards higher binding energies. This peculiarity has also been observed when DIP is deposited on high work function C_{60}.[156] The same rigid shift is found for the C_{60} valence spectrum at 5 nm coverage and identical HOMO-HOMO offsets are thus also found for the 6T/C_{60} system irrespectively of the preparation conditions. Note that a small contribution of the 6T valence features is still present in the HT case even for a C_{60} coverage of 5 nm. This probably correlates with the rough surface found for this film. Yet, both the baseline and the slope of the C_{60} HOMO states are clearly visible. The extracted value of the HOMO onset is thus not expected to be severely affected by the remaining 6T signal.

As mentioned above, the inversion of the interface dipole at the 6T/C_{60} interface is a strong hint that the different molecular orientations present in the room temperature grown 6T film affect the interface energetics. Even though ΔE_{H} is not influenced by the morphology, the valence spectrum of a polycrystalline film with different molecular orientations, like the investigated RT 6T and DIP layers, is expected to carry information on both orientations. Indeed, the spectra of the room temperature grown 6T appears slightly broader than that of the 100 °C film, which only contains one 6T orientation. It is hence possible to separate the RT spectrum into two components, one stemming from upright standing, the other stemming from flat lying molecules. The same is possible for DIP grown on top of RT grown 6T and the deconvolution of the UPS valence spectra of 6T and DIP are shown in Figure 5.16.

In both cases the HT spectrum (red) is assumed to only contain information on standing molecules. All input spectra have been smoothed before further processing. RT and HT spectra are then normalized to identical heights of the first peak. Subsequently, the HT spectrum is subtracted from the RT spectrum (blue). The result is expected to be the contribution by the lying molecules of the respective material (green curve).

The spectra clearly support the presence of occupied states stemming from a previously concealed lying phase. Even though the numbers given in Figure 5.16 indicate that a quantitative agreement with literature values for the ionization potential differences of the respective species is found,[84,121,151] the author refrains from extracting absolute energy values because of the additional uncertainty introduced by the deconvolution procedure.

The presence of occupied electronic states stemming from lying molecules, implies the presence of corresponding unoccupied states. These are expected to shift energetically with the occupied states, which has been demonstrated for DIP.[151] In the case of the

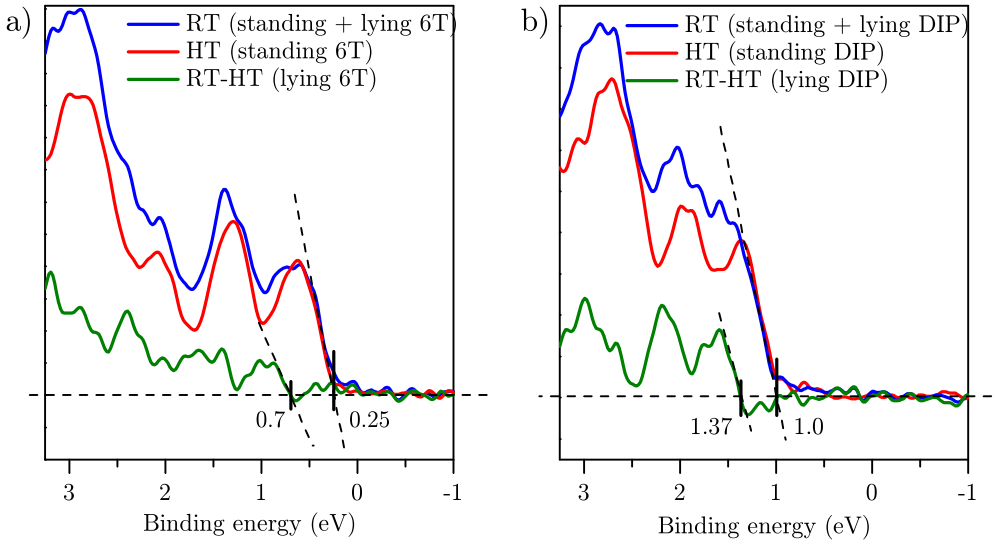

Figure 5.16: Deconvolution of the valence region UPS spectra of RT grown 6T (a) and DIP (b) grown on RT grown 6T (blue) into contributions from standing (red) and lying (green) molecules. The UPS spectrum of the HT film is taken as the reference containing only standing molecules. This contribution is then subtracted from the RT spectrum. The datasets have been smoothed by an FFT filter.

RT 6T/DIP junction this might thus possibly influence the photovoltaic gap depending on the mutual orientation of the molecules at the interface between different grains. This is illustrated in the cartoon in Figure 5.17, where the interface between standing 6T and lying DIP (a) would yield a lower energy gap than expected from the initially determined ΔE_{H} and the transport gap.

Since the energy levels of 6T and DIP are shifted by the same amount, interfaces in lying/lying and standing/standing configuration would yield identical intermolecular gaps (Figure 5.17 (b)). For HT samples this ambiguity does not occur, because of the absence of lying molecules. Please note that despite the presence of lying molecules of both materials in the RT 6T/DIP case, no direct spectroscopic evidence of a reduced donor/acceptor energy gap as predicted from Figure 5.17 (a) could be found. This effect thus seems to be irrelevant for the investigated system but it might be important for other material combinations and should not generally be ignored. In order to unambiguously determine the LUMO onset of the acceptor, however, inverse photo electron spectroscopy directly at the respective heterojunction would be necessary.

Note that even though C_{60} is an isotropic molecule, the presence of lying 6T molecules at the 6T(RT)/C_{60} heterojunction might yield a similar situation as in Figure 5.17 (a). Yet, also in this case no hint for a possibly reduced intermolecular gap was found, neither directly by spectroscopy nor by electrical investigation of solar cell devices.

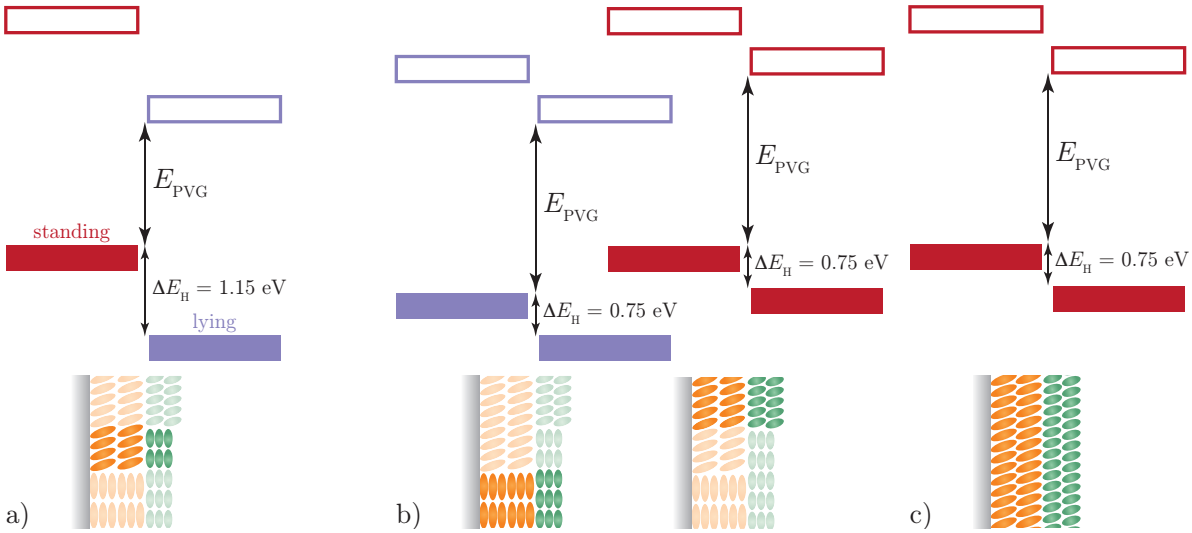

Figure 5.17: Simplified schematic drawings of HOMO and LUMO levels in the investigated films. a) and b) show different interface energetics corresponding to different mutual orientations present in the RT morphology. In a) an interface formed by domains of standing 6T and lying DIP domains is regarded where the energy of the lowest electronic transition is given by the HOMO of standing 6T and the LUMO of lying DIP. b) shows the interface energetics, of domains of lying (standing) DIP on top of lying (standing) 6T. In this case the resulting E_{PVG} of both interfaces is equal. (Note that, since both molecules have identical HOMO level shifts (0.4 eV) between standing and lying orientation,[84,121,151] this is a peculiarity of this material system and not necessarily generally the case.) For the HT grown 6T film only upright standing molecules are present in the film and E_{PVG} is well defined, as shown in c).

5.2.3 Morphological effects on the solar cell performance

The subtle morphological changes induced by changing the film growth conditions strongly affect the solar cell device characteristics of both 6T/C_{60} and 6T/DIP photovoltaic cells. Current-voltage curves of the differently fabricated planar heterojunction cell are presented in Figure 5.18, the characteristic quantities are summarized in Table 5.2. The curves under illumination have been recorded under artificial AM1.5G conditions using a solar simulator. Please note that even though exemplary measurements are shown, they are representative for the respective device type. The extracted V_{oc} values are reproducible within an error bar of 20 meV (30 meV for 6T(HT)/C_{60}) as revealed by statistics over at least five individually prepared samples per cell type, each with two to four working devices per sample. The error of the short circuit current is estimated to 10 % to 12 %. The error sources include unintentional thickness and substrate temperature deviations, batch-to-batch material variations as well as potentially inhomogeneous illumination conditions.

For both acceptors, the short circuit current is reduced for the HT grown 6T film (Figure 5.18 (b)). This is in accordance with the observed drastic reduction of the absorption of upright standing 6T molecules (Figure 5.14) and also reflected by the incident photon to current efficiency (IPCE) presented in Figure 5.19. In the 6T/C_{60}

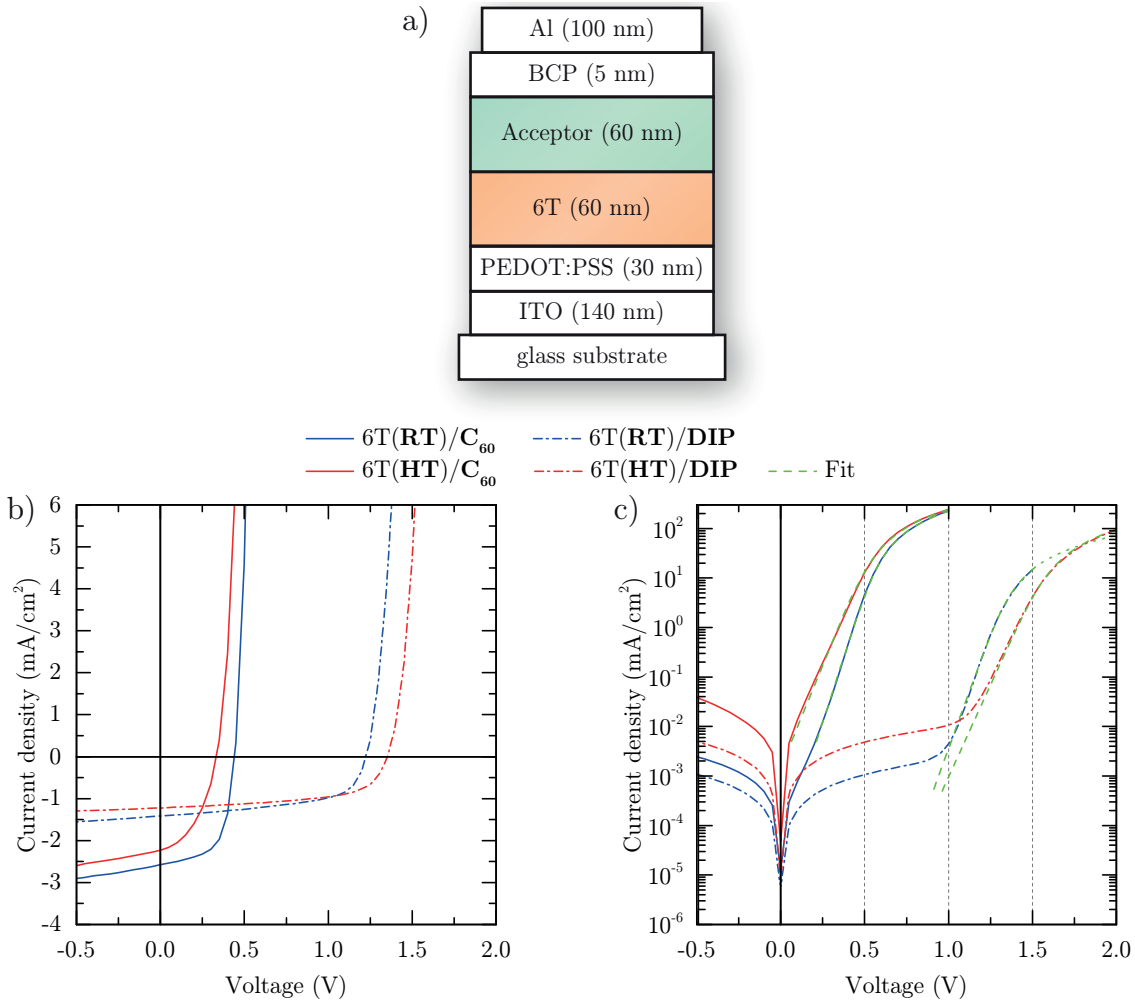

Figure 5.18: (a) Schematic drawing of the device stack of the investigated photovoltaic cells. j-V curves under illumination and in the dark are shown in (b) and (c). The image has been adapted from Ref. 139.

Table 5.2: Characteristic values and fit results of the solar cell devices presented in 5.18. The values of j_{sc}, V_{oc}, the fill factor (FF) and the power conversion efficiency (PCE) are extracted from the j-V characteristics under illumination. Series resistance R_s, ideality factor n and dark saturation current j_0 are extracted by a fit to the dark characteristics with the Shockley equation. V_{oc} (calc) was calculated from j_{sc}, j_0 and n by Eq. 2.8 using $kT = 0.025\,\text{eV}$. Adapted from Ref. 139.

Acceptor	6T growth	j_{sc} (mA/cm^2)	V_{oc} (V)	FF (%)	PCE (%)	R_s (Ωcm^2)	n	j_0 (mA/cm^2)	V_{oc} (calc.) (V)
C_{60}	RT	2.6	0.44	61	0.67	1.5	1.6	3.0×10^{-5}	0.45
C_{60}	HT	2.2	0.33	43	0.31	1.5	2.1	2.2×10^{-3}	0.36
DIP	RT	1.4	1.22	57	0.97	7.5	1.8	1.7×10^{-12}	1.23
DIP	HT	1.2	1.35	59	0.96	3.4	2.3	3.4×10^{-11}	1.40

case (a), the IPCE at wavelength above roughly 550 nm is slightly larger for the device with 6T grown at 100 °C substrate temperature. This regime can solely be attributed to absorption in the C_{60} layer, which might be slightly larger in the HT case as a result of the observed increased crystallinity. With the absorption onset of 6T the RT prepared sample outperforms the HT sample and yields a larger IPCE. For the 6T/DIP system, the RT device yields the larger current through the whole spectral range except for the long-wavelength onset, where both cells yield similar values. This is likely to be caused by the presence of domains of lying molecules in DIP films grown on RT 6T, which, like lying 6T, is expected to be favorable for absorption. As the lying molecules in both the 6T and the DIP layer vanish, the absorption of both is expected to be reduced. Noteworthily, the slight shoulder at the IPCE onset can be assigned to DIP, as shown by the inset in the absorption graph at the bottom of Figure 5.19 (b).

Opposed to the trend of the short circuit current, opposite directions are observed for the open circuit voltage of 6T/C_{60} and 6T/DIP devices. V_{oc} is reduced by roughly 0.1 V for the C_{60} cell if the 6T layer has been grown at 100 °C but increased by 130 mV if DIP is used as the acceptor. Note that Eq. 2.8 indicates that a reduction of the short circuit current will also lead to a lower open circuit voltage. Yet, the effect of the observed j_{sc} decrease can be estimated by $q\Delta V_{oc} \approx nkT \ln\left(\frac{j_{sc,1}}{j_{sc,2}}\right)$ and is on the order of a few mV and thus cannot alone account for the V_{oc} loss of the C_{60} device.

More information on the cause of the V_{oc} changes can be retrieved from the dark characteristics in Figure 5.18 (c). A fit with the Schockley equation is shown as the dashed green lines and the resulting fit parameters are summarized in Table 5.2. Interestingly, for both HT devices the dark saturation current is larger than for their respective room temperature equivalent which implies increased charge carrier recombination for devices comprising a 6T layer grown at 100 °C. This effect is severe in the C_{60} case, where j_0 is about two orders of magnitude larger for the HT device than for the RT device. These drastically increased recombination losses appear to be responsible for the diminished V_{oc} observed for the HT 6T/C_{60} devices.

On the contrary the open circuit voltage gain in 6T/DIP cells is observed despite the increased dark saturation current and despite the lower short circuit current. This is counter-intuitive and recombination seems not to be the cause of the changed open circuit voltage in this system. Note that mathematically Eq. 2.8 still predicts reasonable values for V_{oc} from the otherwise experimentally determined device data because of the impact of the ideality factor.

The open circuit voltage of a planar heterojunction solar cell crucially depends on the photovoltaic energy gap of the donor/acceptor system. As shown in section 2.5.2, E_{PVG} can be extracted from the actual solar cell device by investigating the dependence of V_{oc} on temperature. A linear extrapolation to $T = 0$ K then yields a close approximation of the photovoltaic gap. Figure 5.20 displays the V_{oc} behavior with decreasing temperature for photovoltaic cells prepared identically to those shown in Figure 5.18. After a short, artifactual onset the measured open circuit voltage increases linearly as the sample is cooled down. Below a certain temperature, a deviation form linearity is observed and the open circuit voltage begins to drop for all cells except for the room temperature

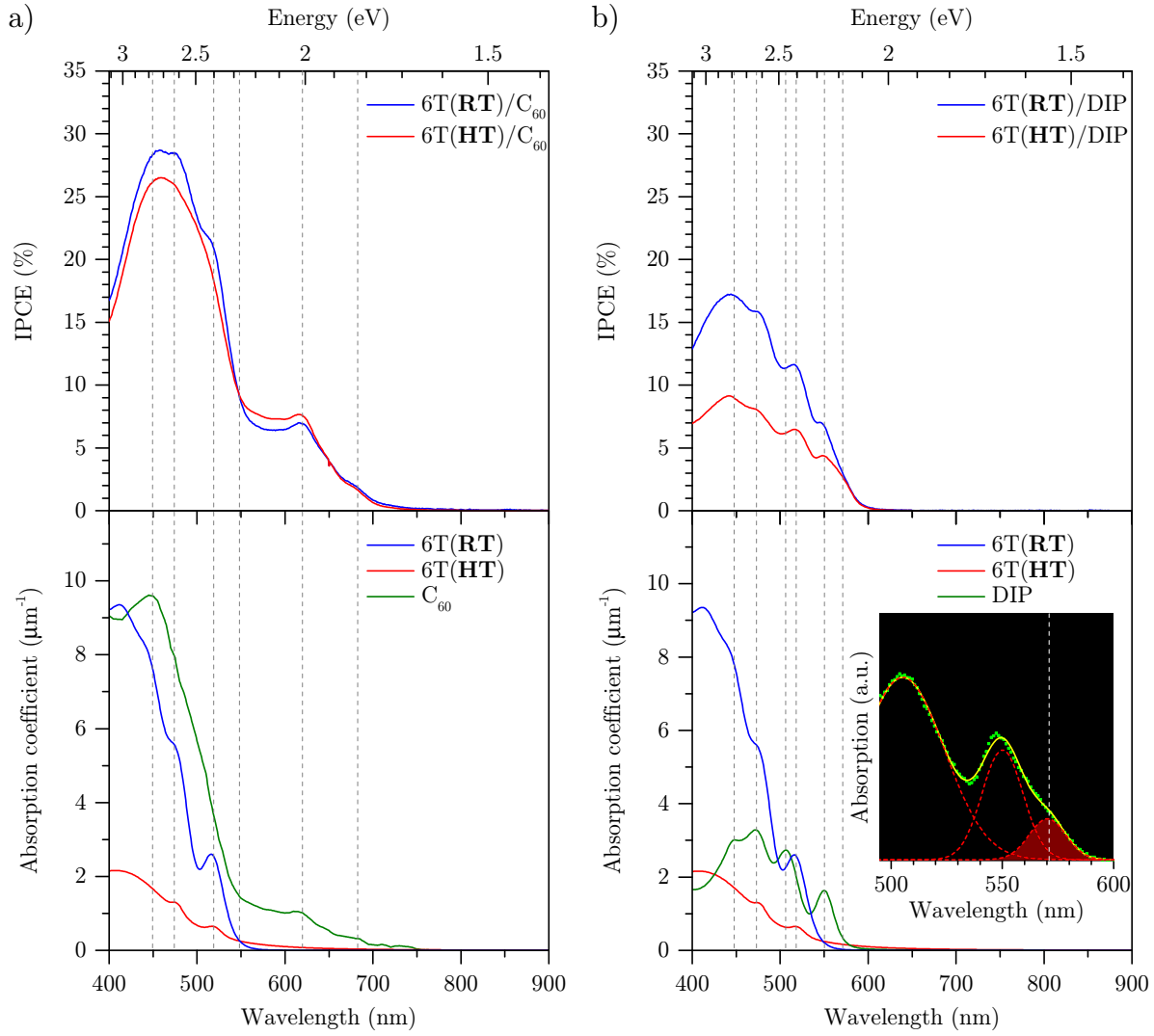

Figure 5.19: IPCE of 6T/C_{60} (a) and 6T/DIP (b) solar cells (top) together with the absorption spectra of the individual components (bottom). The inset in (b) shows a Gaussian deconvolution of the zoomed DIP absorption spectrum at the high wavelength onset. The presence of an additional Gauss peak at roughly 570 nm assigns the corresponding shoulder in the IPCE spectrum to DIP, rather than a CT feature.

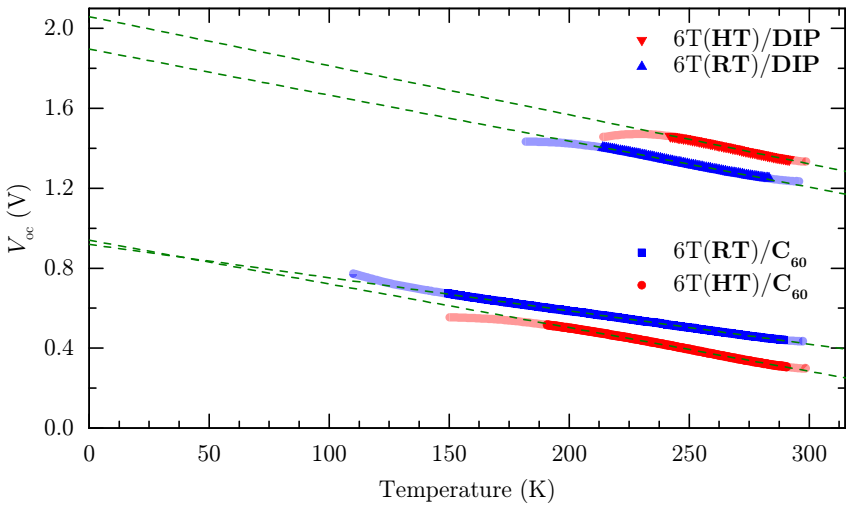

Figure 5.20: Temperature dependence of the open circuit voltage of the investigated 6T/DIP (top) and 6T/C_{60} (bottom) devices. The substrate temperature during 6T deposition was ether 100 °C (red) or room temperature (blue). The extrapolation of the linear dependence regime (opaque) is depicted by the dashed green lines.

prepared 6T/C_{60} device.

A receding open circuit voltage at low temperatures is typically accompanied by severely s-shaped j-V curves.[67,108] For the 6T/DIP devices this can be ascribed to comparatively large electron injection barriers at the contact between DIP and the cathode as indicated by the late onset of the injection current at high bias voltage in the dark as well as comparison of literature values for the energy levels.[28,108] In the 6T/C_{60} case, ohmic contacts caused by Fermi-level pinning and hence minimal injection barriers are expected and indicated by the immediate onset of the injection current in forward bias direction (cf. Figure 5.20).[157] Instead, for this cell the V_{oc} at low temperatures can most likely be attributed to the reduced carrier mobility perpendicular to the substrate reported for 6T thin films only comprising upright standing molecules.[79,158,159] The impact of both, injection barriers and low mobility, become more severe at low temperatures. A combination of the two effects can explain, why the V_{oc} begins to drop earlier for the HT 6T/DIP cell than for its room temperature prepared equivalent. Strikingly, the open circuit voltage of the RT 6T/C_{60} device rises with even steeper slope for temperatures below 130 K. This peculiarity is unexpected and further discussed at the end of this section.

The extraction of E_{PVG} from the linear temperature dependence regime of the open circuit voltage is shown by the dashed green lines in Figure 5.20. Within the uncertainty of the extrapolation, for the 6T/C_{60} system, the photovoltaic gap coincides at approximately 0.93 eV for both preparation conditions and matches well with the intermolecular donor/acceptor energy gap found by photoelectron spectroscopy $E_{D/A} = 0.95$ eV.[63] This clearly shows that the orientation dependent ionization potential of 6T as observed in literature[84] and as seen in the mixture of lying and standing molecules of the RT grown 6T

film (cf. Figure 5.16) does not affect the photovoltaic gap for the investigated 6T/C_{60} devices. Instead, the steeper slope of the HT 6T/C_{60} device confirms the drastically increased recombination losses in this device and thus identifies them as the cause of the reduced open circuit voltage induced by the morphological changes. Unfortunately, the microscopic mechanism that enhances recombination cannot unambiguously be pinpointed and the possible reasons are widespread:

Obviously a larger interfacial area between donor and acceptor will increase the carrier recombination rate.[20] However, considering that the area increase estimated by AFM is well below 20 %, the impact of this simply topographical aspect is too weak to account for the observed V_{oc} loss and several other aspects need to be taken into account. The structural analysis beyond topography by X-ray scattering and X-ray absorption revealed that significant orientational disorder is present in the room temperature grown 6T film, where phases of standing and lying 6T coexist. This is opposed to 6T films that are grown at a substrate temperature of 100 °C and exhibit well-ordered films of standing 6T only. The situation is similar for C_{60} grown on top of the respective films. As stated above and in analogy to pentacene/C_{60}, the positive interface dipole observed in the UPS measurements for the RT sample, where lying 6T is exposed, possibly favors carrier separation while the negative interface dipole found for 100 °C grown 6T favors charge recombination.[154]

It has also been shown that mutual donor/acceptor molecular orientation may have severe impact on the recombination rate. In particular, the group of Brédas have theoretically investigated the impact of molecular orientation on the electronic coupling. For example, Yi *et al.* have shown by simulation that for single pairs of pentacene and C_{60} the recombination process is significantly more efficient in face-on configuration than in edge-on geometry.[160] In further analogy this is likely to be valid also for the 6T/C_{60} system, in particular since 6T and pentacene are similar in the sense that both are rod like molecules, with the π system exposed along their long molecular axis. Yet, a face-on 6T/C_{60} orientation with enhanced electronic coupling is expected to be present independent on the preparation conditions (at the interface to lying 6T in RT devices and at the interface to standing 6T at the edges of the "hills" in 100 °C grown 6T films, cf. Figure 5.13). Since the ratio between face-on and edge-on configuration is difficult to estimate for the respective devices, unfortunately this aspect is ambiguous. This is further complicated by the fact that the lateral position of 6T and C_{60} in face-on geometry as well as the rotational orientation of the C_{60} cage severely change the recombination rate.[161]

Despite the helpful insight provided by these theoretical considerations of single molecule pairs, they are insufficient to explain the processes at a large ensemble of donor and acceptor molecules. Thus extended simulations by Fu, Brédas *et al.* have recently been presented which relate the strength of the electronic coupling at squaraine/C_{60} interfaces to the degree of disorder at the interface and confirm experimental results by Zimmerman *et al.* who suggested that increased disorder reduces the average electronic coupling and thus yields a larger V_{oc}.[162,163] The situation appears to be similar in the case of 6T/C_{60} where the structural investigation suggests increased disorder for the

room temperature prepared device which also yields the higher open circuit voltage.

Even though the morphological investigation revealed a well-ordered film if 6T is grown at an elevated temperature, terraces of upright standing 6T are formed under these conditions that expose the π-system even in this case. For pentacene it has been predicted that under such circumstances intermixing at the interface to C_{60} occurs, which results in a configuration that no longer may be regarded as strict, planar heterojunction of distinctly separated bi-layers.[164,165] Similar observations have been reported for the copper-phthalocyanine (CuPc)/C_{60} system.[166] Hence, in spite of the structural findings we cannot fully exclude that the situation is similar in the investigated HT 6T/C_{60} cells. In such an architecture, the face-on orientation of 6T and C_{60} might play a significantly increased role for recombination. Additionally, the enhanced disorder would then drastically strengthen the impact of trap-assisted recombination which might even become dominant.[167,168]

The situation is fundamentally different for the 6T/DIP devices. As already indicated by the fit to the dark characteristics above (Figure 5.18 (c)), the observed open circuit voltage shift for the different preparation conditions of this system is not caused by a reduction of recombination losses. This is confirmed by the slope of the linear regime of the V_{oc} dependence on temperature, which is slightly steeper for the device with the high temperature grown 6T. Hence, in accordance with the previously extracted dark saturation current (cf. Table 5.2), the slope indicates even slightly larger recombination losses for the HT 6T/DIP cell irrespective of its larger open circuit voltage. Instead, clearly two different values for the photovoltaic gap are extracted by the linear extrapolation of the respective measured V_{oc} data.

For the room temperature prepared device the value of $E_{PVG} = 1.90\,\text{eV}$ is within the error of the intermolecular gap as determined by photoelectron spectroscopy $E_{D/A} = 1.80 \pm 0.15\,\text{eV}$.[63] Consequently, the photovoltaic gap extracted from the actual solar cell matches the donor/acceptor energy gap estimated from the HOMO/HOMO offset determined by UPS. This agreement eliminates the remaining doubt about the validity of the $E_{D/A}$ estimation for the present morphology arising from the mixture of standing and lying molecule domains. As discussed in Section 5.2.2, this might have led to a lower effective donor/acceptor gap compared to the single-phase value (cf. Figure 5.17).

In the case of the HT 6T/DIP device the extracted photovoltaic gap of $E_{PVG} = 2.07\,\text{eV}$ is distinctly larger than the value extracted for the RT prepared device. The UPS measurements, on the other hand, did not indicate that the donor/acceptor gap changes for the different preparation conditions of the 6T layer. However, E_{PVG} is remarkably close to the optical gap of DIP of $E_{opt} = 2.1\,\text{eV}$.[95] Opposed to what is commonly found for organic heterojunctions, the photovoltaic energy gap is thus identified with the optical gap of the absorber $E_{PVG} = E_{opt}$ instead of the intermolecular gap.[57,59–64] In accordance with the theoretical treatment of the detailed balance limit and its extension to account for non-radiative losses (Sections 2.5 and 2.5.3), this indicates that recombination across the optical gap of DIP is a relevant recombination mechanism for 6T/DIP solar cells if 6T was grown at 100 °C substrate temperature.

As briefly discussed in Section 2.5.3, the open circuit voltage dependence on tempera-

ture of both 6T/DIP devices can be simulated with identical optical and intermolecular gaps regardless of the preparation conditions but different parameters n, α_{CT} and β which affect the electronic coupling. Yet, bear in mind that the parameters α_{CT} and β are experimentally unknown and have to be estimated. The resulting calculated curves are displayed in the upper graphs in Figure 5.21. Note that the flattening visible in the simulated V_{oc} is not caused by injection barriers or transport problems but stems from the transition between the dominant part of the competing recombination mechanisms via the optical gap for high temperatures and the CT gap for low temperatures.

Special conditions, under which recombination from the charge transfer state is of minor importance for the operated solar cell, have been predicted even for organic heterojunctions if the energy of the CT sate gets close to the energy of the optical gap of the absorber, or if the absorption strength of the CT state becomes extremely low.[51–53,169] For a systematic variation of $\Delta E = E_{CT} - E_{opt}$ by careful choice of different donor/acceptor combinations, significant contribution of emission from the singlet state of the absorber to electro- and photoluminescence spectra has been observed experimentally for polymer/fullerene bulk heterjunction cells. As reported by Faist *et al.*, activation of the singlet state from the CT state opened an additional recombination channel if ΔE was less than 0.35 eV. With further reduction of ΔE, the recombination via this channel was significantly increased.[170]

Note that in general the presence of an additional recombination pathway is expected to enhance the overall recombination loss and thus reduce V_{oc}. In the present case of the 6T/DIP system, $\Delta E \approx 0.3$ eV and is close to the threshold energy found by Faist *et al.* below which singlet recombination becomes activated. Yet, the open circuit voltage increases for the HT device despite the fact that recombination via the optical gap becomes the dominant mechanism. In these solar cells, however, the situation is somewhat different to the experiments done by Faist *et al.* The materials are not exchanged. Since neither the intermolecular energy gap, as verified by the investigation of the electronic structure at the interface, nor the optical gap of the absorber change, ΔE is expected to remain identical and unchanged for both 6T/DIP cells. It is rather the intermolecular electronic coupling that appears to be reduced by the morphological changes if 6T is grown at 100 °C - most likely because of a reduction of the face-on mutual orientation as a consequence of the absence of the lying/lying configuration. This leads to the situation that, while recombination via the optical gap of DIP is activated in both solar cells as a result of the equally low ΔE, CT recombination is hampered by the reduced intermolecular coupling for the HT device.

The observation that the total recombination seems to be similar for both devices implies that mainly the proportions of the individual contributions get affected by the different morphological structures. This is reproduced in the simulation of the temperature dependent open circuit voltage, where the individual contributions of CT and singlet recombination to the dark saturation current can be regarded separately. As illustrated in Figure 5.21 the total dark saturation current is even slightly larger for the HT 6T/DIP device, which is in accordance with what was extracted from the fit to the dark j-V characteristics (cf. Table 5.2).

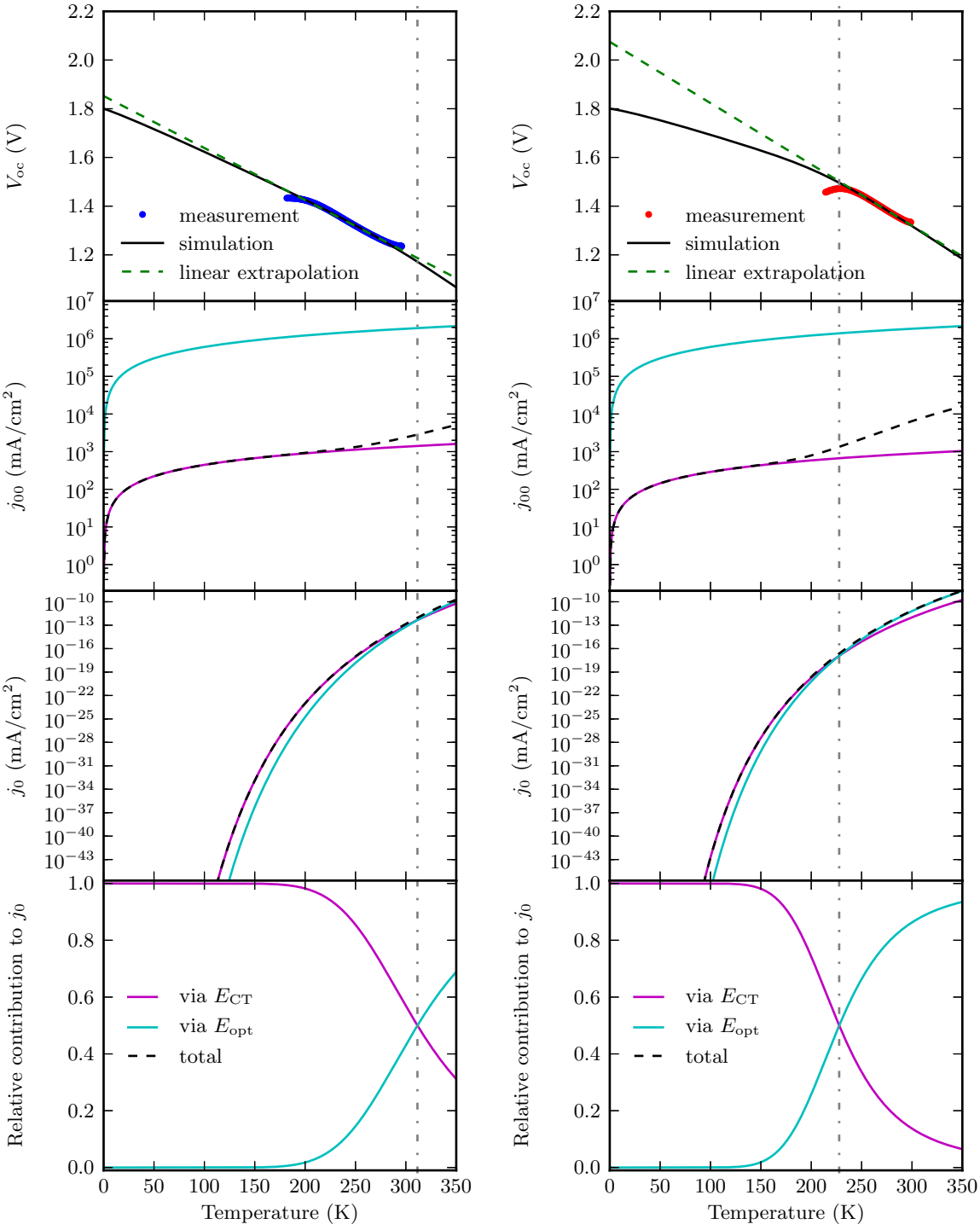

(a) 6T(**RT**)/DIP (b) 6T(**HT**)/DIP

Figure 5.21: Simulation of the temperature dependent open circuit voltage of 6T/DIP solar cells. The room temperature device is shown in (a), the solar cell with 6T grown at a substrate temperature of 100 °C in (b). Parameters used were $E_{opt} = 2.1$, $E_{CT} = 1.8$ for both cells, $\alpha_{CT} = 1 \times 10^{-3}$, $n = 1.55$ and $\beta = 2 \times 10^3$ for the RT case, $\alpha_{CT} = 6.5 \times 10^{-4}$, $n = 2$ and $\beta = 0.5$ for the 6T(RT)/DIP device. The dash-dotted vertical lines mark the respective transition temperatures T_{tr}.

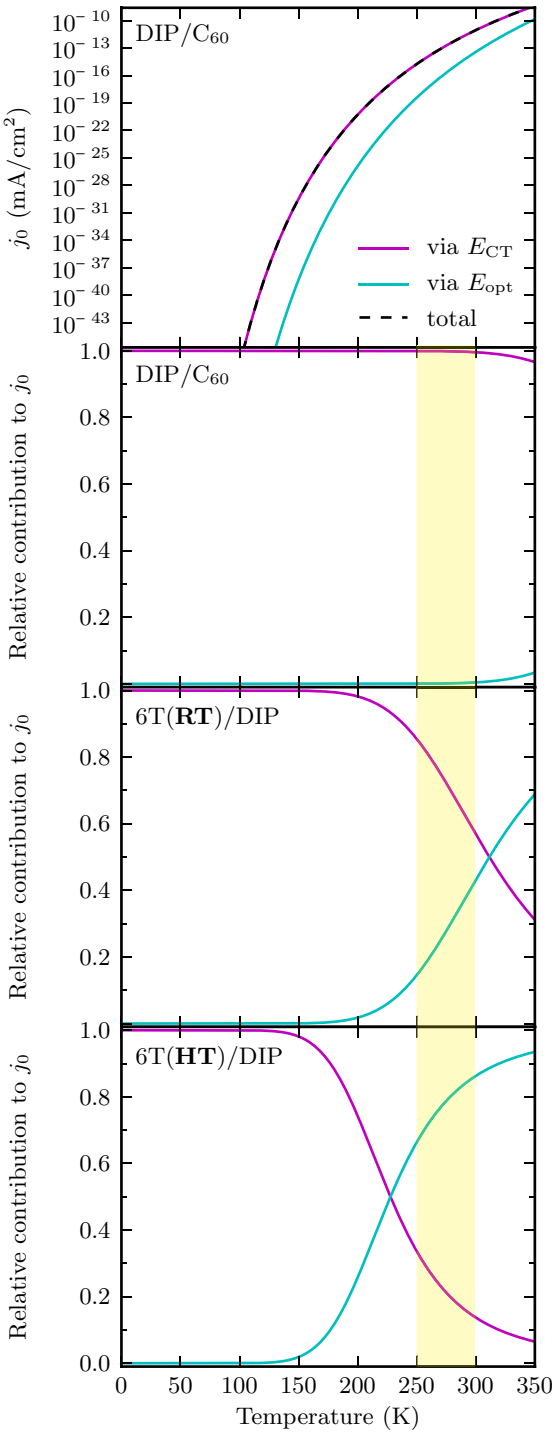

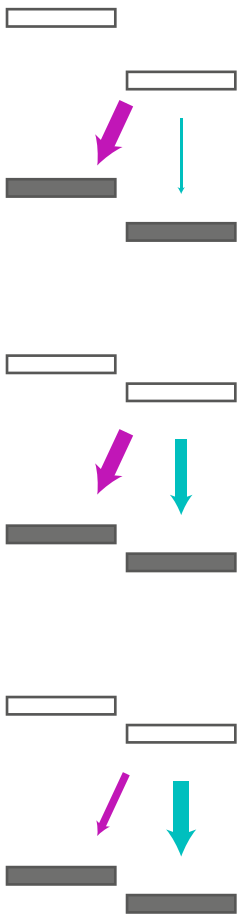

(a) The dark saturation current of a DIP/C_{60} cell is dominated by recombination via the CT state. This is expected to be the case for most organic solar cells reported in literature.

(b) Virtually all recombination occurs via the CT gap (magenta) for a DIP/C_{60} device. Recombination via the optical gap (cyan) is negligible.

(c) The reduced energy offset $\Delta E = E_{opt} - E_{CT}$ activates recombination via the optical gap of DIP as an additional path for 6T/DIP solar cells.[170] The major part remains CT recombination for room temperature prepared cells.

(d) If 6T is grown at 100 °C substrate temperature, reduced intermolecular coupling becomes a "bottle neck" for CT recombination. The standard situation in (b) is inverted to some extent and recombination across the optical gap becomes dominant.

Figure 5.22: Direct comparison of the contribution of recombination via the optical gap of the absorber (cyan) and via the CT gap (magenta) to the dark saturation current j_0 for three different solar cells. Simulation results are shown on the left, the relative strength of the contributions in the operation regime close to room temperature (shaded area) is schematically illustrated by the weight of the respective arrow in the cartoons on the right. Simulations of DIP/C_{60} are shown (a, b) as a prototypical system where virtually all recombination occurs via the donor/acceptor CT gap. In this case the calculated data have been extracted from the simulation of the temperature dependent open circuit voltage of the DIP/C_{60} cell shown in Figure 2.13 ($n = 1.3$, $\alpha_{CT} = 1.5 \times 10^{-4}$, $\beta = 9 \times 10^4$).

Furthermore, the relative strength of the loss channels extracted from the simulations clearly confirms that neither the CT ($j_{0,\mathrm{CT}}$) nor the singlet recombination ($j_{0,\mathrm{opt}}$) component are completely negligible for the dark saturation current of both 6T/DIP devices. Yet, while the CT contribution (magenta) dominates through the whole temperature range for the RT device, singlet recombination (cyan) is predominant for the high temperature prepared solar cell in the relevant operating regime measured. This is also visible in the total dark saturation current which clearly follows the curve of $j_{0,\mathrm{opt}}$ right and $j_{0,\mathrm{CT}}$ left of the transition temperature, indicated by the vertical, dash-dotted line in Figure 5.21. Similarly, this is reflected in the value of the total j_{00} which is strongly enhanced by a contribution of the coupling via the optical gap above the transition temperature.

To visualize, the extent to which the special conditions in the 6T/DIP system affect the dark saturation current, j_0 and its components are considered in relation to the DIP/C_{60} planar heterojunction, previously presented in Section 2.5.3 and discussed in detail in Ref. 53, in Figure 5.22. In this cell virtually all recombination can be attributed to the CT channel, while singlet recombination is basically absent (Figure 5.22 (a, b)). This appears to be the case for the majority of organic solar cells reported today. The reduced energy offset ΔE of the 6T/DIP system activates singlet recombination as a relevant recombination channel and, as a consequence, shifts the transition temperature towards lower temperatures and hence closer to the actual operation temperature (Figure 5.22 (c)). Preparation of the 6T film at an elevated substrate temperature changes the film morphology in such a way that the overall intermolecular coupling at the donor/acceptor interface is reduced while the offset energy ΔE remains constant. This could be a direct consequence of the mutual molecular orientation, that changes to a predominantly edge-on configuration but could also be caused be a general reduction of the interfacial disorder. Either way, the result is a further reduction of the transition temperature *below* the operation temperature of the solar cell. This leads to an inversion of the "normal" conditions (Figure 5.22 (a, b)) to some extent and renders recombination across the optical gap of the absorber the dominant recombination channel (Figure 5.22 (d)).

Please note that while these considerations are self-consistent and explain the observed solar cell behavior well and are supported by the morphological and energetic investigation presented above, direct spectroscopic evidence following the examples of e.g. Faist *et al.*[170] and Ran *et al.*[171] would strongly strengthen the presented picture. A first step is taken in Figure 5.23. A logarithmic plot of the low energy (high wavelength) tail of the IPCE spectra indicates a contribution of the CT state in addition to the absorption of DIP.[68] The extent of the latter is indicated by fits of the respective IPCE data as a sum of Gaussian peaks corresponding to the absorption of DIP. The fit results are shown as the solid lines in Figure 5.23. Since the absorption onset of 6T is expected at higher energies, the low energy tail that does not follow the fit curves is assigned to direct CT absorption. Comparison of the RT and HT datasets and their fits indicates that the relative CT contribution to the overall current is larger for the room temperature prepared device than for the HT cell. This is in agreement with the

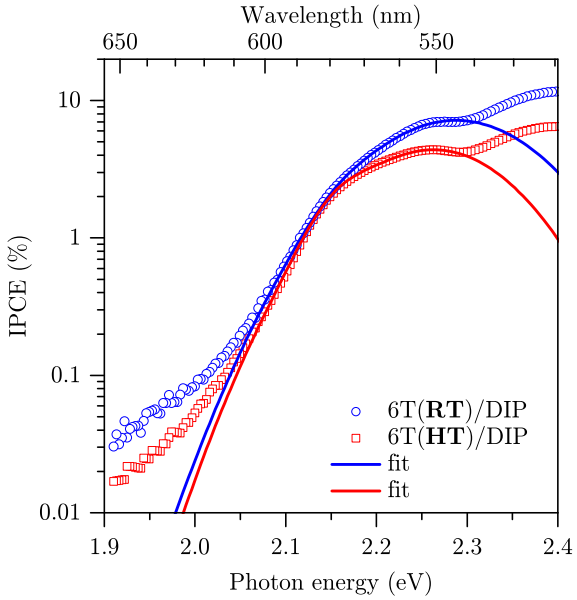

Figure 5.23: Low energy onset of the IPCE of both 6T/DIP devices. The solid lines are fits to the respective IPCE data by two Gaussian peaks, each that correspond to the first two DIP absorption features shown in the inset in Figure 5.19 (b). The presence of an additional shoulder in the IPCE spectrum below the DIP onset is attributed to direct CT absorption.

picture presented above and backs the qualitative result obtained from the simulations. Nevertheless direct evidence from emission spectra is still necessary. This is work in progress and first results are consistent with the presented considerations.[172] Together with more sensitive IPCE measurements this would also enable direct access to the CT energies of the two systems and could completely clear any remaining doubts on the intermolecular gap of the different 6T/DIP interface morphologies.

Quite contrarily to what is typically observed, the open circuit voltage of the room temperature grown 6T/C_{60} device begins to rise more steeply below a temperature of about 130 K. If the region where the new, steeper increase appears to be linear is separately extrapolated to 0 K, a new value of $E'_{\mathrm{PVG}} = 1.12\,\mathrm{eV}$ is obtained. This is shown in Figure 5.24. Following the above reasoning that the extracted value corresponds to an energy gap of the dominant recombination pathway, this would directly imply that a new mechanism outweighs the direct CT recombination. The extracted energy matches neither of the optical gaps nor the triplet states.[173–175] Yet, it would be in good agreement with the energy of the 6T bipolaron, which has been reported to be approx. 1.1 eV and additionally to become more prominent with decreasing temperature.[174,176,177] Apart from this, emission from trap states in 6T thin films has been shown to gain increasing significance with decreasing temperature.[83,178] Because of the good agreement of the energy values, bipolaron recombination is tentatively identified as the possibly predominant recombination path below 130 K in the investigated 6T(RT)/C_{60} solar cell.[179] Note, however, that the measured temperature range in this region is short compared to the extent of the extrapolation. Again, direct spectroscopic investigation of these devices

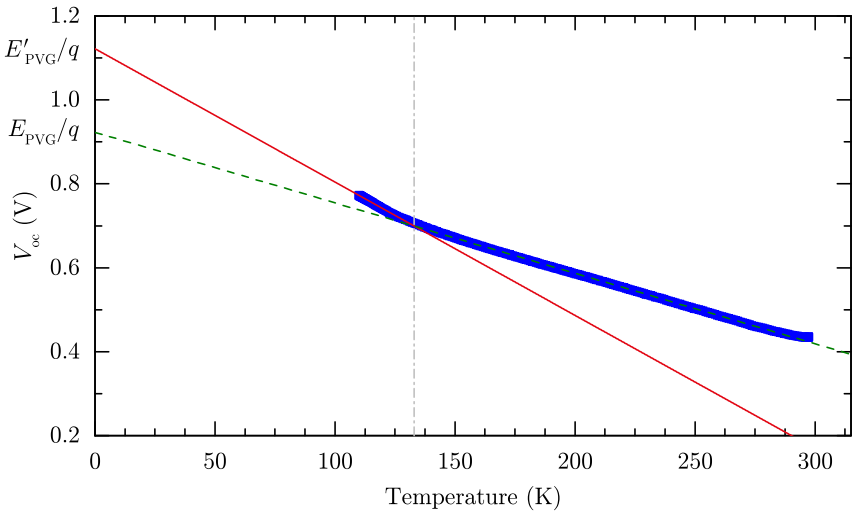

Figure 5.24: Separate extrapolation of the different regimes observed for the temperature dependence of the open circuit voltage of room temperature prepared 6T/C_{60} solar cells. In addition to the range relevant for typical device operation (green, dashed line), a second, steeper linear increase appears for low temperatures, apparently corresponding to a different photovoltaic gap E'_{PVG} (red line). The gray, vertical line marks the intersection of the two extrapolated curves at $T = 133\,K$.

at low temperatures could yield valuable insight and help to identify the cause of this interesting feature.

5.3 Investigation of energy losses in organic solar cells

The following section has in part been published in Ref. 59.

5.3.1 Intensity dependence of the open circuit voltage

Starting from the Shockley equation (2.1), an expression for the open circuit voltage can be derived if the boundary condition $j = 0$ is chosen:

$$V_{\mathrm{oc}} = \frac{nk_{\mathrm{B}}T}{q} \cdot \ln\left(\frac{j_{\mathrm{sc}}}{j_0}\right) \tag{5.1}$$

This expression directly correlates the open circuit voltage with the short circuit current of a given solar cell. Since both quantities are typically measured directly, this leaves the ideality factor n and the the dark saturation current j_0 the only unknown parameters at a given temperature T. An intensity dependent recording of V_{oc} and j_{sc} pairs can thus serve as a tool to determine the ideality factor and the dark saturation current.[180] Due to the linear correlation between j_{sc} and the illumination intensity,[37] this is equivalent to an intensity dependent analysis of the open circuit voltage.[181] An advantage of analyzing V_{oc} in dependence on j_{sc} rather than on the raw light intensity is the that the influence of the illumination spectrum becomes minimized. This enables a more reliable comparison of data recorded at different sites and with different light sources. Furthermore, accurate measurement and calibration of the light intensity is often difficult, whereas the short circuit current can directly be measured.

These effects are illustrated in Figure 5.25 at the example of a 6T/C_{60} solar cell. V_{oc} and j_{sc} value pairs recoded at different illumination intensities using a solar simulator and neutral density filters are shown as the red circles in (a). A fit (solid line) to the data with Eq. 5.1 yields a strikingly good agreement between measurement and theory. The same sample has subsequently been measured under illumination with a white LED at a nominal intensity of about 54 mW/cm^2. The recorded V_{oc}- j_{sc} value pair perfectly coincides with the extrapolation of the fit (blue triangle and dash-dotted line, respectively, in Figure 5.25 (a)); however, it would correspond to a solar simulator intensity of 175 mW/cm^2, i.e. roughly three times the nominal LED intensity. The spectrum of the LED exhibits a broad band between 500 nm and 700 nm wavelength which is accompanied by a distinct peak in the blue (453 nm). Obviously, this is favorable for the spectral sensitivity of the 6T/C_{60} solar cell (cf. Figure 5.19) and thus results in significant spectral mismatch compared to standard illumination conditions.

Figure 5.25 (b) shows a plot of the V_{oc} (blue) and j_{sc} (red) data against the nominal solar simulator intensity. In addition to the measurement (spheres) calculated values are shown as the solid lines. For these calculations, the short circuit current at the highest intensity has been scaled linearly. The V_{oc} curve was then calculated from the scaled j_{sc} values and the parameters obtained previously from the fit. While the linear dependence of j_{sc} on the illumination intensity is clearly confirmed, some data points deviate notably from the calculated line, at the same time as their corresponding V_{oc} data points deviate

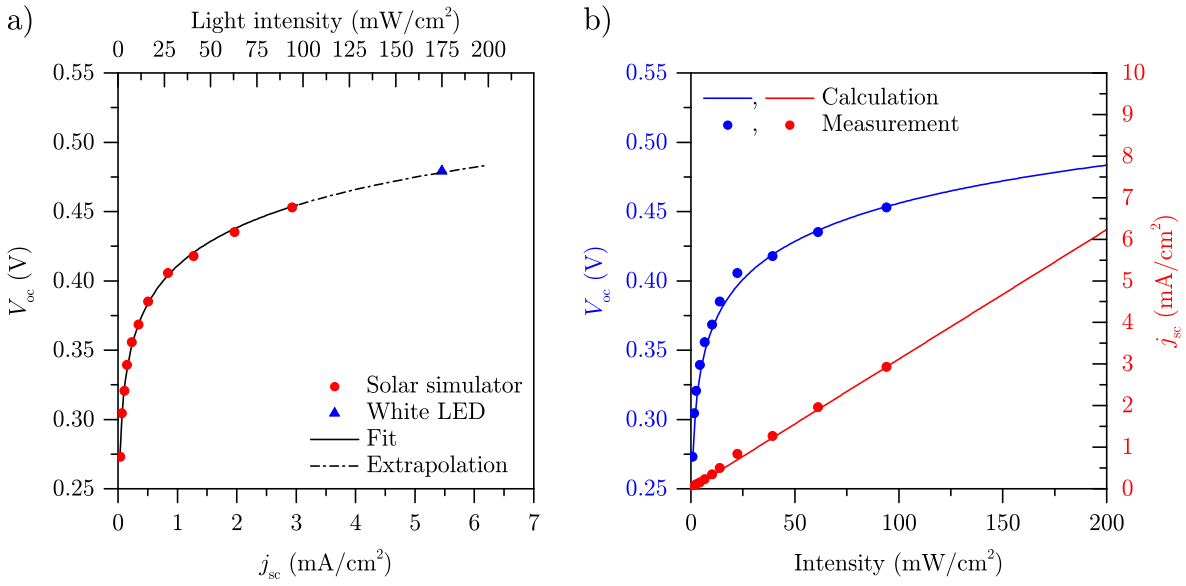

Figure 5.25: Intensity dependent measurement of the open circuit voltage and the short circuit current at the example of a 6T/C_{60} planar heterojunction. (a) Plot of measured V_{oc} vs measured j_{sc} and a corresponding fit with Eq. 5.1. (b) Measured data of V_{oc} and j_{sc} (symbols) plotted against the nominal illumination intensity. The solid lines are calculated values derived from linearly scaling the largest j_{sc} value and Eq. 5.1 using the fit result from (a) as values for the unknown parameters.

from the calculation. This is especially visible at 23 mW/cm^2, roughly, and is a hint that the recorded light intensity might be slightly off.

Note that the parameters n and j_0 may also be extracted from j-V curves measured in the dark. Oftentimes, however, this is complicated by the influence of the parasitic series resistance, which becomes increasingly important at high currents or low temperatures. These undesirable effects are typically less significant under short circuit and open circuit conditions and thus ignored in Eq. 5.1. In particular the open circuit voltage is not sensitive to the series resistance as no net current flows. The short circuit current on the other hand is virtually unaffected by the parallel resistance. This is demonstrated in Figure 5.26, where both j_{sc} and V_{oc} have been calculated from the Shockley equation for a given photo current j_{ph} and under the influence of different combinations of shunt and series resistance. Clearly, the short circuit current becomes limited by the series resistance at high intensities, while the open circuit voltage drops at low intensities because of the shunt resistance. For all investigated solar cells the series resistance, determined from a fit of the dark j-V curve with the Shockley equation under forward bias, is well below 0.025 kΩcm^2 and thus irrelevant for the achieved photo currents. The shunt resistance, as extracted from the reverse bias regime of the dark current, is significantly larger than 20 kΩcm^2 and can be safely ignored for the high range of the measured intensities but may become relevant for low illumination intensities. It is important to note that the impact of the parallel resistance is additionally affected by

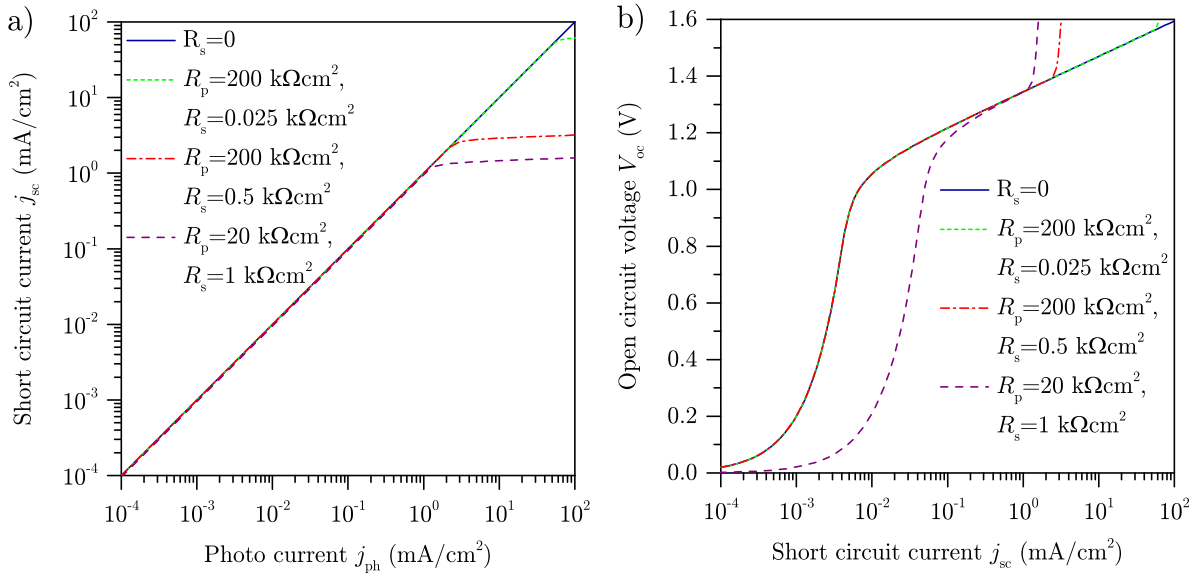

Figure 5.26: Simulation of the short circuit current (a) and open circuit voltage (b) at a given photo current for different combinations of series (R_s) and shunt resistance (R_p). Clearly, j_{sc} is almost independent of the shunt resistance but limited by the series resistance. In contrary, V_{oc} is only influenced by the parallel resistance, whereas its apparent dependence on R_s is caused by the saturation of j_{sc}. The other parameters have been set to $n = 2.05$, $j_0 = 1.7 \times 10^{-11}$ mA/cm^2 and $T = 307$ K which matches the 6T(HT)/DIP cell.

the magnitude of the dark saturation current, where a large j_0 will damp the effect of the shunt. Its impact is thus expected to be stronger for devices with a large photovoltaic gap as indicated by Eq. 2.22.

Compared to the analysis of j-V curves, direct intensity dependent measurement of j_{sc} and V_{oc} avoids unnecessary stressing of the sample, since the measurement process is faster than recording complete j-V characteristics and since no power is dissipated during V_{oc} and j_{sc} measurements. At least for the potentially fragile 6T based solar cells this is an additional advantage of the intensity dependent V_{oc} measurement over the analysis of dark j-V curves, in particular if time consuming temperature dependent measurements are performed. In the following combined temperature and intensity dependent solar cell device properties are analyzed. As a well understood example system, a DIP/C_{60} planar heterojunction solar cell is analyzed, before this method is applied to other material systems.[21,59,72]

5.3.2 The DIP/C_{60} planar heterojunction archetype

The linear extrapolation of the temperature dependent open circuit voltage has already been discussed extensively and been utilized to determine the photovoltaic gap in the previous section. Figure 5.27 (a) shows this analysis for a DIP/C_{60} planar heterojunction solar cell for a broad range of illumination intensities ranging from about 0.5 down to 0.5×10^{-3} suns. The extrapolated curves of all intensities intersect the V_{oc} axis in a narrow range from 1.39 V to 1.40 V, clearly demonstrating the implied assumption that the photovoltaic gap of this solar cell does not depend on the illumination intensity.

The short circuit current corresponding to these intensities and temperatures is shown in Figure 5.27 (b). At high temperatures the short circuit current shows a $\ln(j_{sc}) \propto -1/k_B T$ behavior for all light intensities, which conforms to thermally activated hopping transport of charge carriers.[24] Below approximately 190 K, however, a disproportionate decrease of the short circuit current with temperature occurs, which in turn appears to be following a similar exponential law. This might potentially be an indication of a change of the transport limiting material in the device stack.

The combined dataset of (a) and (b) is displayed in Figure 5.27 (c). Here the intensity dependent V_{oc} data is plotted against the corresponding, measured short circuit current for a series of temperatures. The solid lines are fits to the respective high intensity part of the data with Eq. 5.1, which results in a straight line in the logarithmic j_{sc}-scale and yields a temperature dependent set of fit parameters. Note that the open circuit voltage at the lowest intensities drops below the extrapolated fit curve, as illustrated by the dashed lines. As demonstrated above, a similar effect could be caused by an increasing influence of the shunt resistance. This is exemplary shown for the highest temperature data: The dash-dotted line shows the open circuit voltage calculated from the Shockley equation using the parameters of the fit and accounting for a parallel resistance of $R_p = 510\,\mathrm{k\Omega cm^2}$ as extracted from the reverse bias regime of the dark current. It seems that the influence of the leakage current is to little to account for the measured V_{oc} reduction. Hence, this could be a sign of a severe increase of non-radiative recombination losses at low illumination intensities. Such an effect can possibly be explained by trap assisted recombination, which has been reported to become the dominant loss mechanism at low light intensities and thus low carrier densities.[167,182,183] This interpretation will later be strengthened by simulation of the $V_{oc}(T)$ data.

The individual n and j_0 values extracted from the fits of the V_{oc} vs j_{sc} data at the respective temperatures are shown in Figure 5.28 (a). The diode ideality factor stays at an almost constant value of approximately 1.26 down to a temperature of about 190 K and starts rising rapidly for lower temperatures. At the same time, the extracted dark saturation current, starts to deviate drastically from the previous $\ln(j_0) \propto -1/k_B T$ behavior, expected from Eq. 2.22.

While a temperature dependent ideality factor had been reported in the literature,[181,184] it was later regarded as an experimental artifact caused by increasing influence of leakage current, i.e. shunt resistance, at low temperatures because of the temperature dependent mobility of the hopping transport.[185] In the present case the interpretation of the apparent temperature dependence of the ideality factor as an ar-

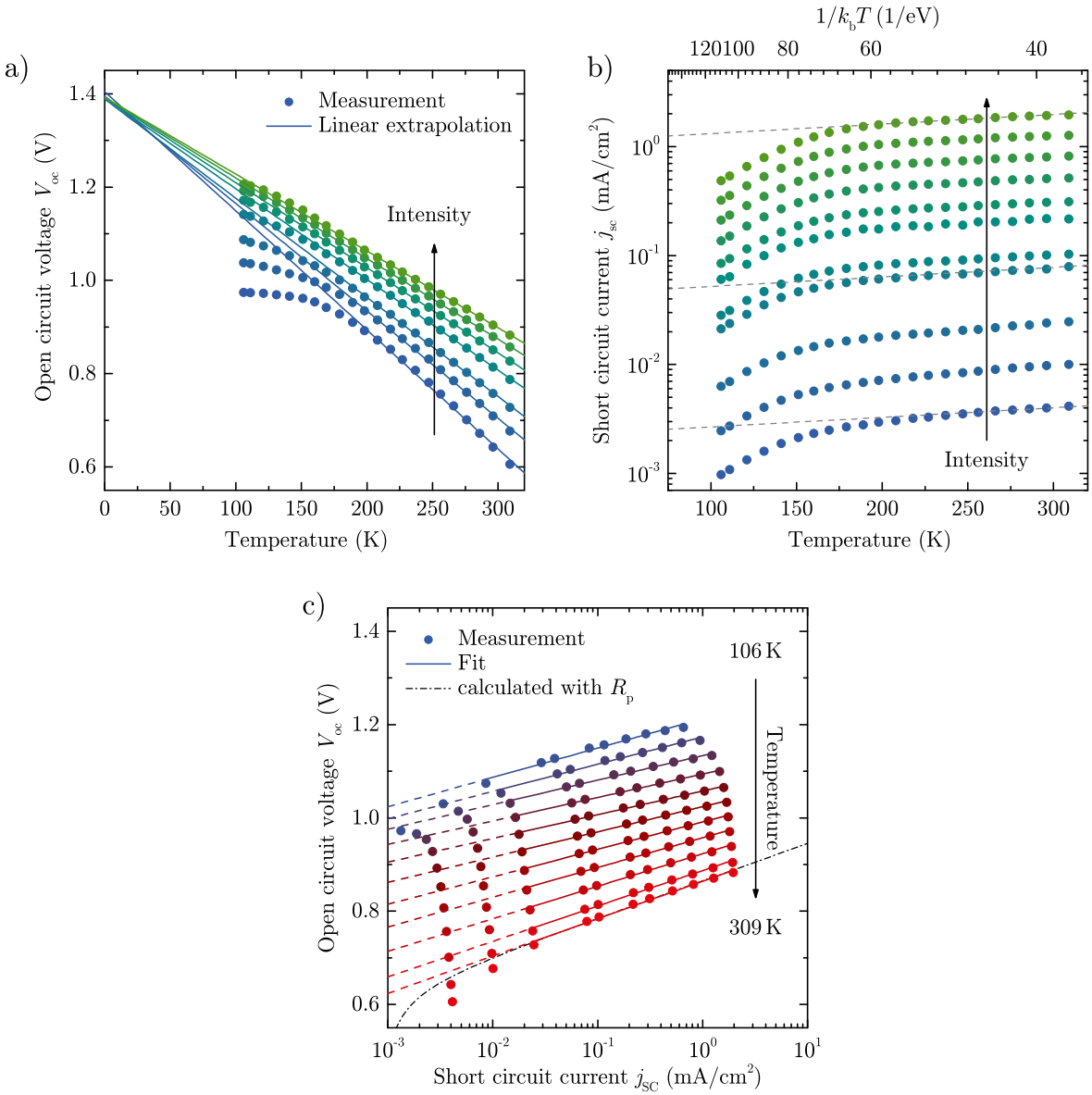

Figure 5.27: Combined intensity and temperature dependent analysis of a DIP/C_{60} planar heterojunction solar cell (layer stack: ITO/PEDOT:PSS/DIP(50 nm)/C_{60}(40 nm)/BCP(5 nm)/Al(100 nm), DIP deposited at 100 °C substrate temperature). (a) Temperature dependence of the open circuit voltage recorded for different illumination intensities. As indicated by the solid lines, the linear extrapolation yields almost perfectly identical intercepts with the V_{oc}-axis for all intensities. (b) Short circuit current in dependence on Temperature at different intensities. The dashed lines are guides to the eye. (c) V_{oc} as a function of j_{sc} measured at the temperatures shown in (a) and (b). The fits indicated by the solid lines allow the extraction of n and j_0 displayed in Figure 5.28. The dash-dotted line in (c) illustrates the impact of R_p as extracted from the reverse bias regime of the j-V curve in the dark. A solar simulator was used as light source, illumination intensities were varied from 0.5 to 0.5×10^{-3} suns by neutral density filters. For clarity only a subset of intensities and temperatures is shown in (a) and (c). Adapted from Ref. 59.

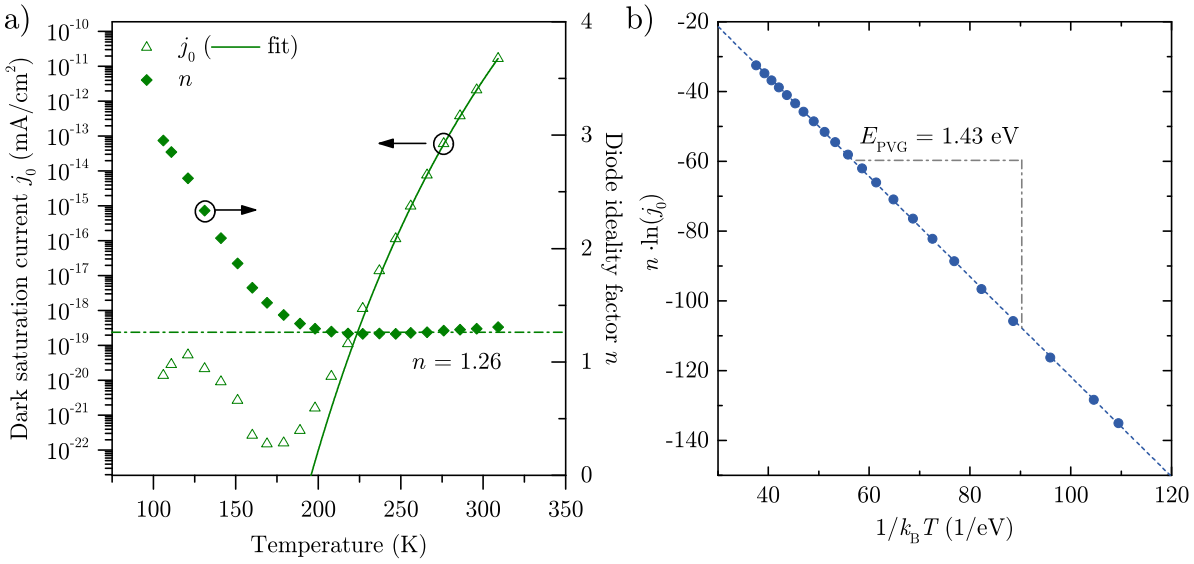

Figure 5.28: Combined intensity and temperature dependent analysis of a DIP/C_{60} planar heterojunction solar cell. (a) Graphical summary of the parameters n and j_0 obtained form the fit results in Figure 5.27 (c). The temperature dependent analysis of these parameters ($n \ln(j_0)$ vs. $1/k_BT$) yields an alternative method to determine the photovoltaic gap as shown in (b). Adapted from Ref. 59.

tifact is indicated by the fact that its onset coincides with the observed change in the dependence of the short circuit current on temperature as illustrated in Figure 5.27.

The possibility, that shunt or series resistances cannot be neglected obviously falsifies the fit result for low temperatures. Nevertheless, this should only be a problem for the separation of the parameters n and $\ln(j_0)$ but not for their product. Since Eq. 5.1 expands to

$$V_{oc} = \frac{k_B T}{q} n \ln(j_{sc}) - \frac{k_B T}{q} n \ln(j_0),$$

the product $n \ln(j_0)$ may be regarded as an individual fit parameter, which is not affected by the j_{sc} drop.

This assumption is confirmed by the perfectly linear correlation of $n \ln(j_0)$ and $1/k_BT$ shown in Figure 5.28 (b). In accordance with Eq. 2.22 a photovoltaic gap of $E_{PVG} = 1.43$ eV is extracted from the slope of a linear fit to the data, which is in perfect agreement with what was found from the linear extrapolation of the open circuit voltage and matches well with the intermolecular gap determined by UPS and IPES.[63] Note that Eq. 2.22 can also be applied to directly fit the j_0 data points in Figure 5.28 (a) (solid, green line). This yields a photovoltaic gap of 1.38 eV, an ideality factor of 1.09 and a prefactor of $j_{00} = 6.9 \times 10^9$ mA/cm^2. However, the fit curve deviates strongly from the data below 230 K.

As stated above, the parameters n and j_0 can also be extracted from the j-V curves recorded in the dark by a fit with the Shockley equation (2.1) extended to account for parasitic resistances. Yet, the exponential current regime is typically narrow, which

complicates a clear separation of the series resistance and the ideality factor in the fit. This effect becomes more severe with decreasing temperature and may quickly render the fit results unreliable. To compare the analysis of the temperature dependence of the product $n \ln(j_0)$ for the two different methods of determining the parameters, i.e. from the intensity dependence of V_{oc} and from the dark j-V characteristics, the analysis of the j-V curves recorded in dark for the same cell as discussed above is performed in Figure 5.29.

For completeness, the j-V curves recorded under illumination are shown in Figure 5.29 (a). Clearly, high fill factors are observed for high temperatures whereas a slight s-shape is formed around 210 K, which rapidly becomes severe for lower temperatures. As mentioned above, this can be attributed to an increased series resistance, probably caused by transport limitations.[108] Note that, while this is the same sample as presented above, j_{sc} and V_{oc} have been measured directly during the cool down process in Figure 5.27 rather than being extracted from the j-V curves, which have been recorded during warming up. This procedure was chosen to avoid stress to the sample and experimental issues.

The corresponding dark curves are depicted in Figure 5.29 (b) in a semi-logarithmic representation. It is clearly visible how the exponential regime in forward bias (apparent as a linear increase in this representation) becomes increasingly narrow with decreasing temperature and thus how the shunt resistance at small bias voltages and the influence of the series resistance at the high bias end become more and more dominant. This strongly affects the fit results shown as the solid lines and makes it near impossible to separate the ohmic resistance from the diode properties at low temperatures.

Figure 5.29 (c) summarizes the fit parameters n and j_0 extracted from the dark curves in (b). Comparison with the parameters extracted from the intensity dependent analysis of the open circuit voltage presented in Figure 5.28 shows that the ideality factor extracted from the dark j-V curves is slightly larger in the plateau region at high temperatures. Such a difference between dark and light ideality factor is reported in literature and has been shown to be caused by the presence of deep traps, which become deactivated under illumination.[180,185] The increasing influence of the parasitic resistances becomes evident through the early onset of a drastic increase of the extracted n value, which happens already at significantly higher temperatures than observed for the light ideality factor, as indicated by the vertical, dashed line. The discrepancy between the two analysis methods strengthens the identification of the temperature dependence of the ideality factor as an experimental artifact. Like in the previous analysis, the trend of the j_0 value with decreasing temperature deviates from the expected behavior as soon as the the ideality factor leaves the plateau value. This is again attributed to the correlation of the fit parameters, which makes a clear separation between the ideality factor, the dark saturation current and the series resistance difficult. Even in the high temperature regime above 240 K the overall value of j_0 is one to three orders of magnitude larger than what was found from the intensity dependent V_{oc} and j_{sc} analysis, where the discrepancy becomes larger for lower temperatures. This could possibly be caused by an increasing impact of the leakage current, which is not included as a separate fit

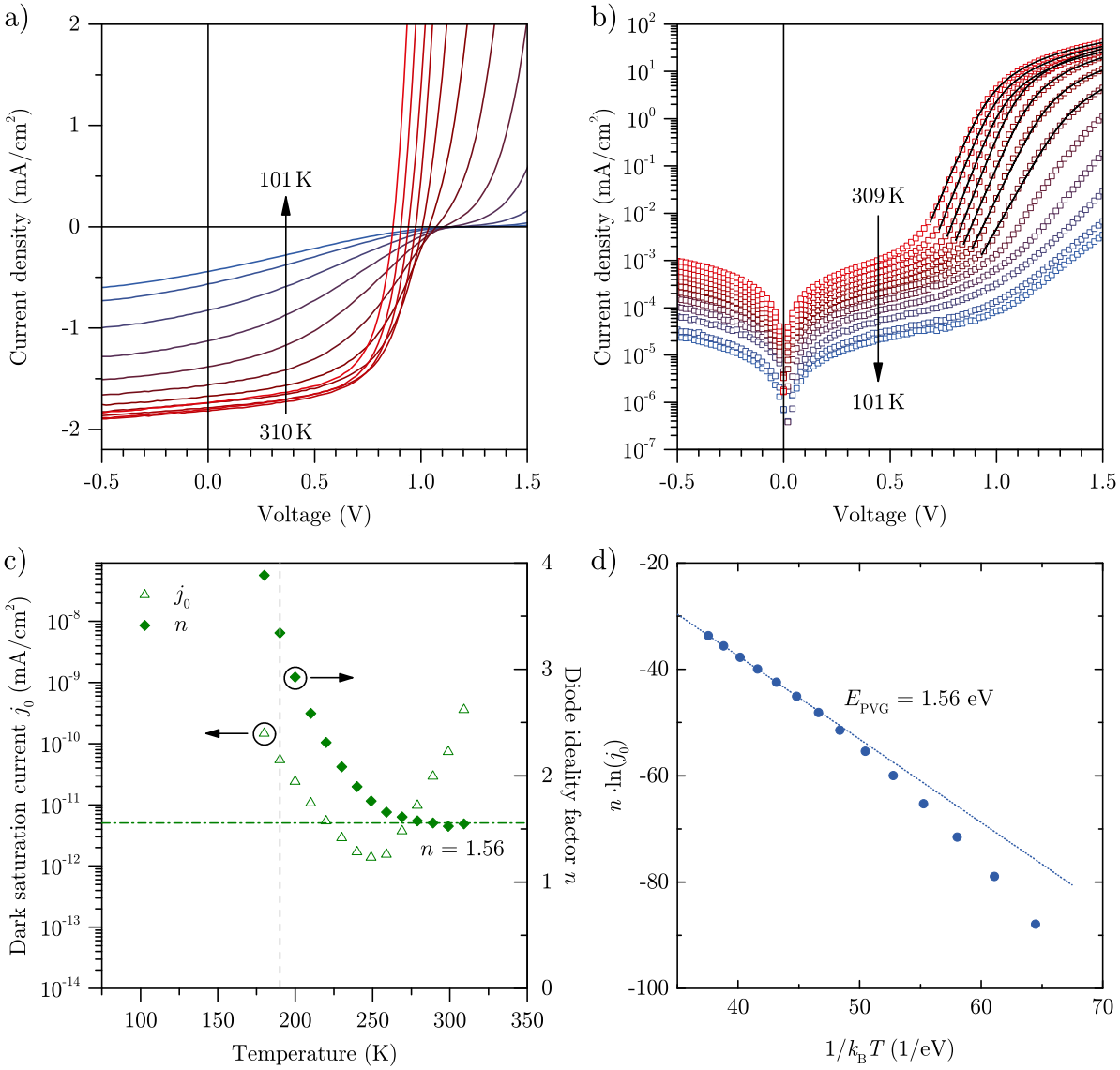

Figure 5.29: Analysis of the dark saturation current of a DIP/C_{60} planar heterojunction extracted from the temperature dependent measurement of the j-V characteristics in the dark.

parameter.

Finally, the photovoltaic gap is extracted from the temperature dependent dark j-V curve parameters in Figure 5.29 (d), where the product $n \ln(j_0)$ is plotted against $1/k_\mathrm{B}T$. Even if only the highest temperatures are included in the linear fit, the extracted value $E_\mathrm{PVG} = 1.56\,\mathrm{eV}$ is larger than what was extracted above and over-estimates the previously found intermolecular energy gap of 1.4 eV.[53,63]

This finding implies that the combined intensity and temperature dependent analysis of the open circuit voltage appears to yield more reliable results than the temperature dependent analysis of the dark j-V characteristics, especially for low temperatures. Nevertheless, it is important to note that a much better agreement between the results of these two methods (and also the linear extrapolation of V_oc to 0 K) has been found in Ref. 59, where the measurement of the dark j-V curves was extended towards higher temperatures. In particular Dr. Julia Kraus has found good agreement of the activation energy of the dark saturation current in Eq. 2.22, derived from the analysis of the dark characteristics and the energy of the charge transfer state, found spectroscopically or by the linear extrapolation of the temperature dependent open circuit voltage, for a broad range of material systems.[67]

5.3.3 The ideality factor

The ideality factor n is generally regarded as an indicator of the prevailing recombination mechanism and is typically expected to take values $1 \leq n \leq 2$. It has been shown by various authors that Langevin type direct recombination of free charge carries yields an ideality factor of $n = 1$.[65,186] Trap assisted recombination, e.g. via tail states, is expected to result in ideality factors larger than one, where the exact value is determined by the respective trap distribution.[65]

Despite the fact, that direct recombination is typically expected to be the dominant recombination mechanism in organic solar cells,[36] the ideality factors reported in the literature are often significantly larger than one. In part, this has recently been attributed to a discrepancy between the conceptual ideality factor usually considered in device models and the experimentally accessible quantity that is considered in the analysis of real world devices.[187] A single ideality factor is typically derived either from a fit of the dark current with the Shockley equation or of the intensity dependent open circuit voltage. These two methods often yield two different values denoted as the dark and light ideality factors, leading to different interpretations of the recombination mechanisms in dark and under illumination. Wetzelaer *et al.* have illustrated that the dark ideality factor is governed by deep traps affecting the carrier transport and may not be directly connected to charge recombination. Instead they consider the light ideality factor suitable to identify the recombination mechanism.[180,185]

Yet, Kirchartz *et al.* pointed out that either of the fit methods averages over a large voltage regime, caused by the applied bias or the open circuit voltage, respectively. Hence, the fits result in values that have to be regarded as average ideality factors. This is particularly problematic for the dark ideality factor because of the influence of series and

shunt resistances but is still an issue for the light ideality factor.[187] It has, for example, been shown that the influence of traps on the carrier recombination becomes more prominent at low intensities, i.e. low open circuit voltages.[167,186] Additionally, Giebink *et al.* introduced two different ideality factors for the donor and for the acceptor in planar heterojunctions, and showed that each of which becomes dominant in a different voltage regime.[186]

In order to prevent the averaging over different recombination mechanisms and to draw reliable conclusions, Kirchartz *et al.* suggest an open circuit voltage and thus intensity dependent consideration of the differentially determined light ideality factor.[187] If again the short circuit current is used as a measure for the light intensity, this can be derived from Eq. 5.1 as:

$$n = \frac{q}{k_\mathrm{B}T}\frac{\partial V_\mathrm{oc}}{\partial \ln(j_\mathrm{sc})} \tag{5.2}$$

Note that similarly the dark ideality factor can be derived differentially from the Shockley equation (2.1):[180,187]

$$n_\mathrm{dark} = \frac{q}{k_\mathrm{B}T}\frac{\partial V}{\partial \ln(j)} \tag{5.3}$$

Yet, the influence of the shunt resistance at low bias and the series resistance at high bias have been shown to make it difficult to correlate the dark ideality factor with physical effects.[187]

Following the example of Kirchartz *et al.*,[187] this is demonstrated in Figure 5.30 (a), where the differentially derived dark and light ideality factors of the DIP/C_{60} solar cell presented above are shown. In the low bias / open circuit voltage regime both ideality factors are in good agreement. As evident from the slope of the solid line, the shunt resistance dominates the dark ideality factor and most likely also the light ideality factor in this range. The solid line then reaches a minimum at $n_\mathrm{dark} = 1.51$, which is slightly lower than what was extracted from the fit of the j-V curve in Figure 5.29. It is, however, highly questionable if the dark ideality factor actually saturates before the series resistance becomes dominant at larger bias.

The light ideality factor on the other hand continuously decreases and reaches a value of $n = 1.06$ at the highest open circuit voltage and thus light intensity. While this is a strong indication that bimolecular recombination of free electrons and holes is the prevailing recombination mechanism, it is less clear, if the light ideality factor between 0.8 V and 0.9 V is still influenced by leakage currents or if a slow trend to trap assisted recombination with decreasing light intensity is present in the device. Note that the average light ideality factor calculated from the differentially obtained values corresponding to the fit range in Figure 5.27 (c) is 1.23 and thus in good agreement with what was found by the fit of the intensity dependent open circuit voltage (cf. Figure 5.28 (a)).

Figure 5.30 (b) depicts the differentially determined light ideality factor for the whole measured temperature range. Clearly, the behavior found from the fits to the intensity

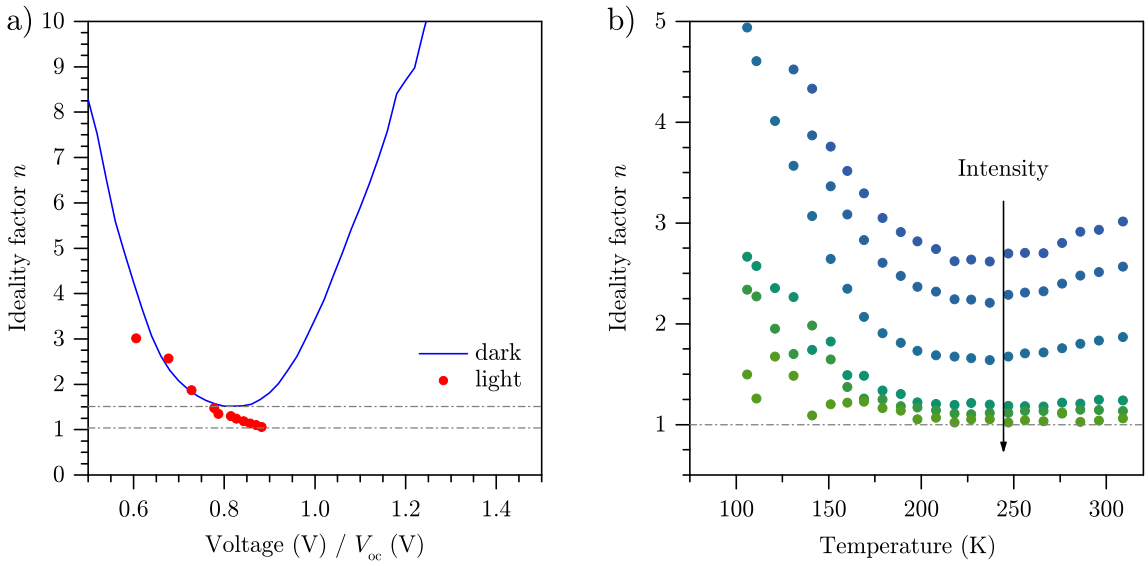

Figure 5.30: Differentially determined ideality factor of a DIP/C_{60} planar heterojunction device. (a) Comparison of dark and light ideality factors derived from the dark j-V curve according to Eq. 5.3 and the intensity dependent V_{oc} measurement (Eq. 5.2), respectively. (b) Temperature dependence of the light ideality factor at different illumination intensities. For clarity only a subset of the recorded intensities is shown.

dependent open circuit voltage (cf. Figure 5.28 (a)) is confirmed and the ideality factor stays more or less constant down to about 190 K. Only for the lowest intensities a slight decrease of the ideality factor with temperature is visible, before the steep increase below $\sim$ 200 K. This might be caused by a reduced leakage current at low temperatures, indicated in reverse bias direction of the dark j-V curves that occurs gradually and already before the drastic decrease of the short circuit current (cf. Figure 5.29).

The confirmed temperature independence encourages an additional approach to refine the ideality factor even closer to an intrinsic value. Starting from the ideality factor differentially determined for the highest light intensity and hence the largest open circuit voltage, the measured temperature dependence of the open circuit voltage is simulated as described in Section 2.5. While keeping the ideality factor fixed at the previously found value, the parameter β, which accounts for the ratio between radiative and non-radiative recombination, is adjusted in such a way that the simulated curve matches the data points recorded for the highest illumination intensity. The result of this step is presented in Figure 5.31 (a). Notably, except for the lowest three intensities all other data are reasonably well described by the same set of parameters, where the changed j_{sc} solely accounts for the reduced open circuit voltage. This is in agreement with what was previously found in Figure 5.27 (c).

In a second step, the linear $V_{oc}(T)$ regime is then fitted by the simulation with the ideality factor as the only free fit parameter; all other parameters are kept at the values found in the first step. As shown in Figure 5.31 (b) the experimental data is now reproduced well for all intensities and the simulation can barely be distinguished from

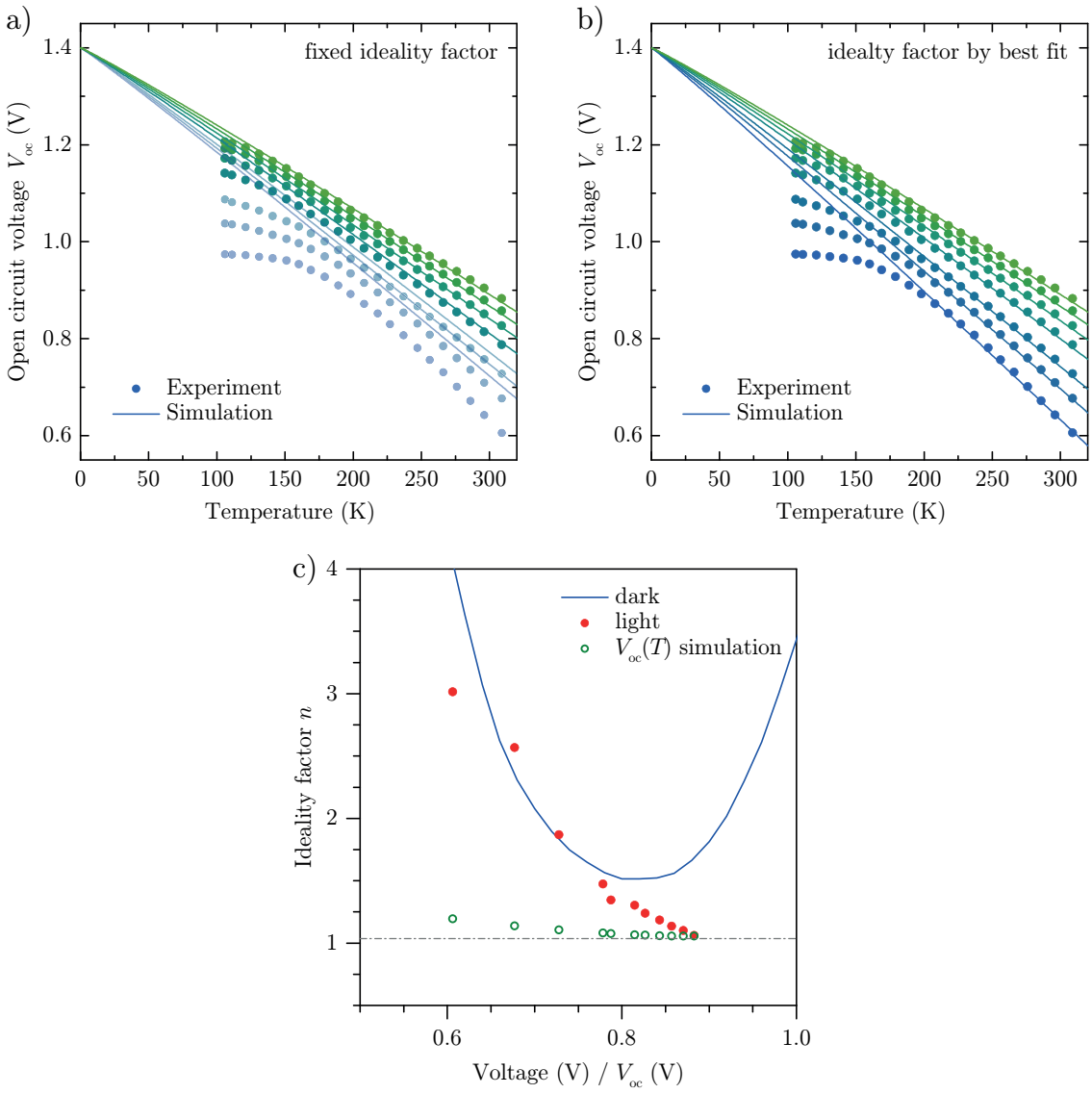

Figure 5.31: Simulation of the temperature and intensity dependent open circuit voltage of a DIP/C_{60} planar heterojunction. At higher intensities the data can be described with a fixed set of parameters, this is not possible for the lowest three intensities (a). Only if the ideality factor is adjusted, all datasets can be simulated (b). The resulting ideality factors are presented as the green circles in (c). Common parameters used for the simulation are $E_{\mathrm{PVG}} = 1.4\,\mathrm{eV}$, $E_{\mathrm{opt}} = 1.9\,\mathrm{eV}$, $\alpha_{\mathrm{CT}} = 1.5 \times 10^{-4}$ and $\beta = 2 \times 10^{6}$. For clarity only subset of intensities is shown in (a) and (b).

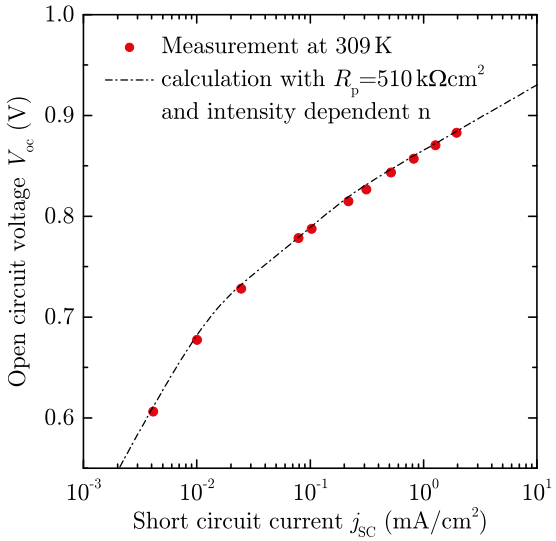

Figure 5.32: Calculation of V_{oc} vs j_{sc} for the DIP/C_{60} planar heterojunction from the Shockley equation using the ideality factor derived from the $V_{oc}(T)$ simulation and the parallel resistance extracted from the reverse bias regime of the j-V curve recorded in the dark. The corresponding value of j_0 was calculated with Eq. 2.22 using $j_{00} = 1.25 \times 10^8$ mA/cm^2 and $E_{PVG} = 1.39$ eV. The intensity dependence of n was approximated with a bi-exponential decay law that well reproduces the refined ideality factor.

a simple linear extrapolation.

The ideality factors obtained by the fitting process are presented in Figure 5.31 (c) as the green circles together with the differentially derived light and dark ideality factors. Overall, the ideality factor obtained from the simulation is significantly closer to one compared to what was found from the derivative of the open circuit voltage (red spheres). This is especially the case for low V_{oc} values, where a maximum ideality factor of $n = 1.20$ is found. At higher open circuit voltage n saturates around 1.06 and remains almost constant. This is a strong hint that the dominant recombination mechanism for this DIP/C_{60} device is indeed direct bimolecular recombination over a large voltage range. Simultaneously, this also implies that the differentially determined light ideality factor is still influenced by the shunt resistance. Only at extremely low intensities the increased ideality factor allows the interpretation that trap assisted recombination might become relevant. Yet, bear in mind that nominally the lowest intensity is three orders of magnitude lower than the highest illumination.

With the refined ideality factor extracted from the simulation procedure combined with the parallel resistance previously retrieved from the dark j-V characteristics, the V_{oc} vs. j_{sc} curve at 309 K can now be closely reproduced as shown in Figure 5.32. This illustrates that the influence of R_p on n was successfully removed. Yet, there might potentially be a remaining contribution from a possibly intensity dependent shunt resistance.[188,189] It is important to note that even though this would further decrease the ideality factor in the low intensity range, the measured data could not successfully

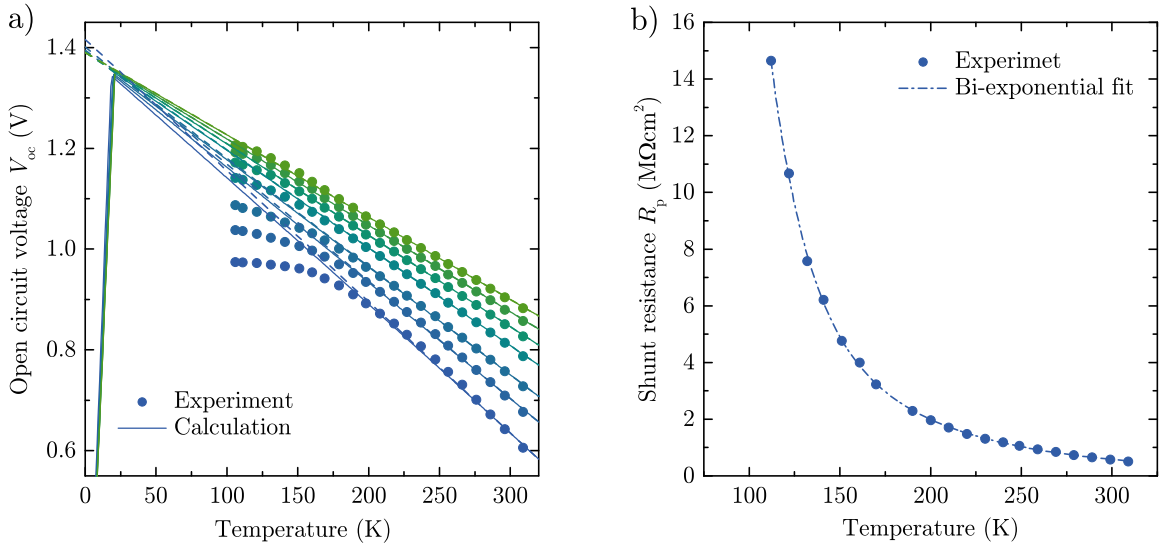

Figure 5.33: (a) Calculation of $V_{oc}(T)$ for the DIP/C_{60} planar heterojunction from the Shockley equation using the ideality factor derived from the simulation of the temperature dependent open circuit voltage in Figure 5.31. (b) The parallel resistance was extracted from the reverse bias regime of the j-V curve recorded in the dark for a series of temperatures. The corresponding value of j_0 was calculated with Eq. 2.22 using $j_{00} = 1.25 \times 10^8\,\mathrm{mA/cm^2}$ and $E_{PVG} = 1.39\,\mathrm{eV}$. The dashed lines in (a) show a linear extrapolation of the calculated curves.

be reproduced with a constant n that is consistent with the differentially determined ideality factor at high intensity.

Also the $V_{oc}(T)$ behavior can now be calculated from the Shockley equation if the temperature dependence of the shunt resistance is extracted from the reverse bias regime of the dark j-V characteristics. This is illustrated in Figure 5.33. Despite the fact that a constant photovoltaic gap of 1.39 eV was used, the slight overestimation of E_{PVG} for the lowest intensity is reproduced by accounting for the shunt resistance. Note that whether the photovoltaic gap will be over or underestimated by a linear extrapolation depends on the specific temperature dependence of the shunt resistance. Importantly, these calculations based on the Shockley equation and macroscopic quantities are not to be confused with the previously presented simulations based on thermodynamic considerations.

Finally, it is worth noting that even though a simulation based approach was chosen above to refine the ideality factor, n can similarly be derived from the slope of the linear extrapolation of the temperature dependent V_{oc} measurement. Based on Eq.(2.23) the slope is given by:

$$m = \frac{\mathrm{d}V_{oc}}{\mathrm{d}T} = -\frac{nk_B}{q} \ln\left(\frac{j_{00}}{j_{sc}}\right) \tag{5.4}$$

and thus

$$n = \frac{qm}{k_B(\ln j_{sc} - \ln j_{00})} \tag{5.5}$$

Note that in Eq. 5.4 it is implicitly assumed that $\ln(j_{sc})$ is constant with respect to T. Obviously, this is not perfectly the case. However, keep in mind that the short circuit current at the *highest temperature* serves as a measure of the temperature independent light intensity and does not directly affect V_{oc}. If like in the simulation example above, the differentially determined ideality factor for the highest V_{oc} is considered the most reliable, this may be used to calculate the corresponding j_{00} value from Eq. 5.4. The intensity dependent ideality factor can then be calculated, under the assumption that j_{00} itself does not change with the illumination intensity. Note that this assumption is a necessary consequence of the detailed balance for ideal solar cells[48,190] and indicated by Eq. 2.15 but has also been found experimentally for a series of polymer/fullerene cells.[191] It is worth noting that as a convenient side effect, this method provides a way to determine j_{00} without prior knowledge of E_{PVG}.

5.3.4 Application to other solar cells

The investigation of energy losses enabled by the combined temperature and intensity dependent analysis of device characteristics shall now be applied to a series of other solar cells. The most important quantities, fit results and derived parameters of all investigated cells, including the DIP/C_{60} cell discussed above, are summarized in Table 5.3 at the end of this section.

DIP:C_{60} planar-mixed heterojunction

Before the focus is turned to different material systems, a change of the cell architecture is considered. At the example of a DIP:C_{60} planar mixed solar cell the effect of intentional intermixing of the donor and acceptor materials is investigated. The mixed layer was deposited in a 1:1 ratio and a total thickness of 50 nm on 5 nm of pristine DIP on ITO/PEDOT:PSS. The substrate was heated to 100 °C during deposition of both the DIP film and the mixed layer. A 15 nm thick C_{60} layer was deposited to conceal the blend before the device was finished by adding the usual BCP(5 nm)/Al electrode.

Figure 5.34 shows the corresponding measurement data for this cell. Quite generally the data look similar to that of the DIP/C_{60} planar heterojunction shown in Figure 5.27, apart from a slightly reduced overall V_{oc} but higher j_{sc} as expected for the architectural change.[72] Interestingly, the linear extrapolation of the temperature dependent V_{oc} results in an increased, seemingly random spread of the photovoltaic gap extracted at different intensities, which ranges from 1.40 eV to 1.45 eV. It thus appears that the structural disorder introduced by the intentional mixture of donor and acceptor is responsible for the increased uncertainty. Yet, the extracted range of about 50 meV is still smaller than the typical PES error[63] and all intensities can be fitted well with a common intercept fixed to the literature value for $E_{D/A} = 1.4$ eV for the DIP/C_{60} system, illustrated in Figure 5.34 (d).

As for the DIP/C_{60} planar heterojunction, the expected dependency of V_{oc} on the illumination intensity according to Eq. 5.1 is well fulfilled as indicated by the fits (solid lines) shown in Figure 5.34 (c). In the present case, the extrapolation of the fit results

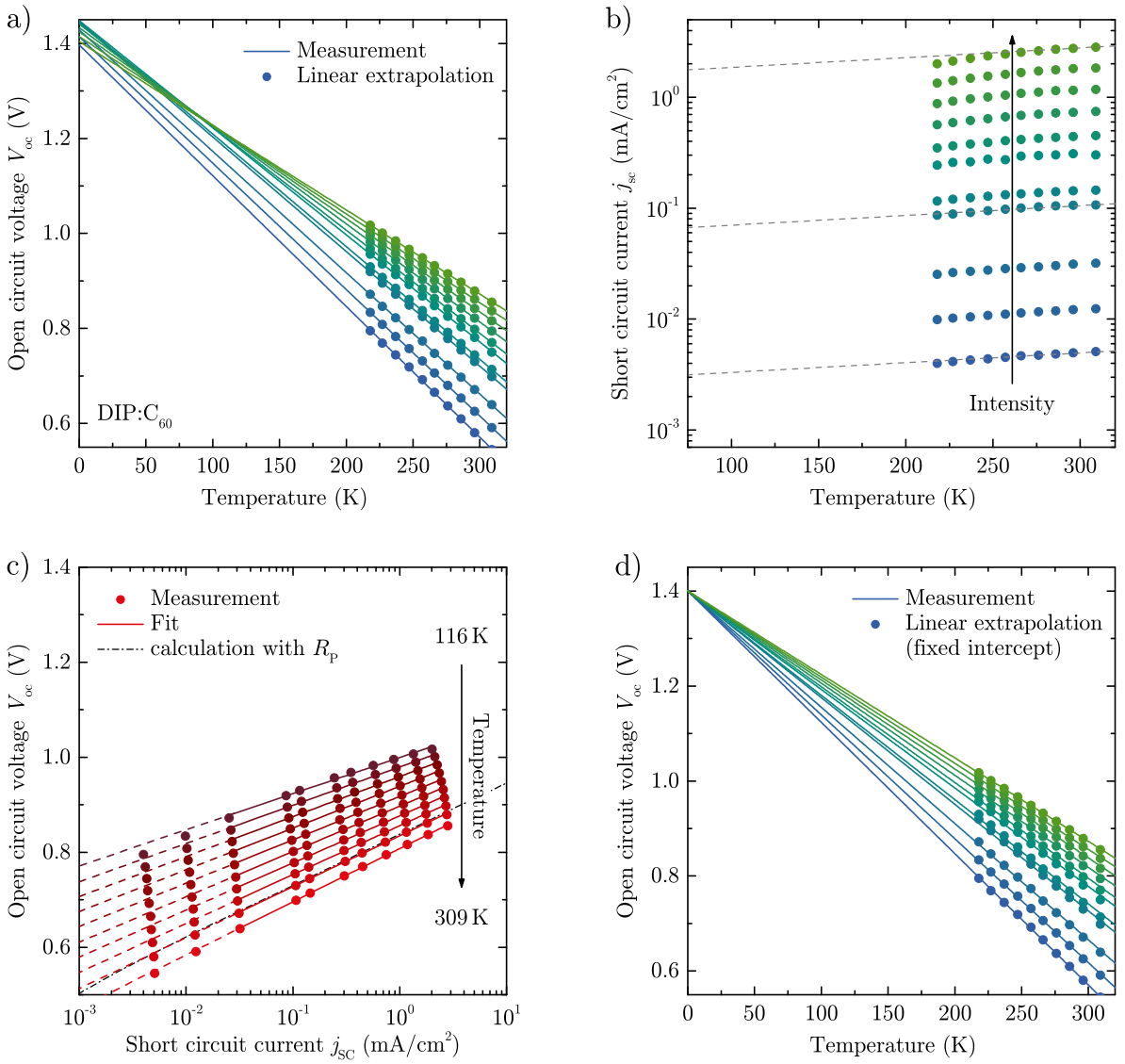

Figure 5.34: Combined intensity and temperature dependent analysis of a DIP:C_{60} planar-mixed heterojunction solar cell. (a) Temperature dependence of the open circuit voltage recorded for different illumination intensities. (b) Short circuit current in dependence on Temperature at different intensities. The dashed lines are guides to the eye. (c) V_{oc} as a function of j_{sc} measured at the temperatures shown in (a) and (b). The fits indicated by the solid lines allow the extraction of n and j_0 displayed in Figure 5.35. The dash-dotted line in (c) illustrates the impact of R_p as extracted from the reverse bias regime of the j-V curve in the dark. As shown in (d) the linear relation of V_{oc} with temperature is well reproduced even if a fixed intercept (i.e. gap energy) is chosen, despite the seemingly random spread of intercepts seen in (a). A solar simulator was used as light source, illumination intensities were varied from 0.5 to 0.5×10^{-3} suns by neutral density filters. For clarity only a subset of intensities and temperatures is shown in (a), (c) and (d).

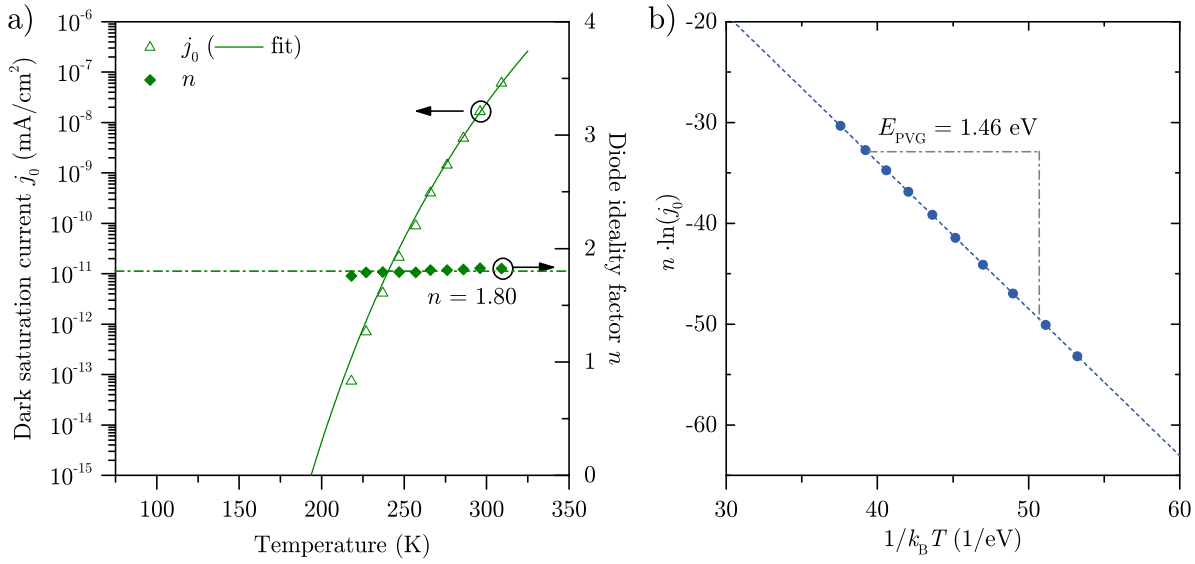

Figure 5.35: Combined intensity and temperature dependent analysis of a DIP:C_{60} planar-mixed heterojunction solar cell. (a) Graphical summary of the parameters n and j_0 obtained form the fit results in Figure 5.34 (c). The temperature dependent analysis of these parameters ($n \ln(j_0)$ vs. $1/k_BT$) yields a photovoltaic gap of 1.46 eV as shown in (b).

towards lower intensities (dashed lines) are closer to the measured data points, especially at high temperatures. This indicates that the loss does not increase severely at low light intensities in this cell architecture. Additionally, the influence of a possible leakage current can clearly be ignored at high temperatures for this device as indicated by the dash-dotted curve, which includes the parallel resistance obtained from the dark j-V curve and was calculated with the corresponding fit parameters. With decreasing temperature, the low intensity data deviate more strongly from the high intensity fit. It cannot clearly be told if this is caused by an increasing effect of the shunt resistance, or by a change of the recombination mechanism. However, judging from what was observed for the DIP/C_{60} planar heterojunction, an at least partial influence of the leakage current could explain the observed scattering of the extracted E_{PVG} values.

The parameters resulting from the fits are again summarized graphically in Figure 5.35. While the ideality factor stays constant at $n = 1.8$ the dark saturation current decreases, nicely obeying Eq. 2.22 as indicated by the fit (solid line) in Figure 5.35 (a). This direct fit of j_0 yields the values $E_{PVG} = 1.42$ eV, $n = 1.77$ and $j_{00} = 6.7 \times 10^5$ mA/cm^2 and is in good agreement with what was obtained from the combined temperature and intensity dependent analysis.

Both n and j_0 are analyzed together in the $n \ln(j_0)$ vs. $1/k_BT$ plot in Figure 5.35 (b). Like for the planar heterojunction, a perfectly linear behavior is observed in the analyzed temperature range. The photovoltaic gap extracted from the linear slope amounts to 1.46 eV and again is in good agreement with the values determined from the temperature dependent V_{oc} and from photoelectron spectroscopy.[63]

The differentially determined light ideality factor is presented in Figure 5.36 (red).

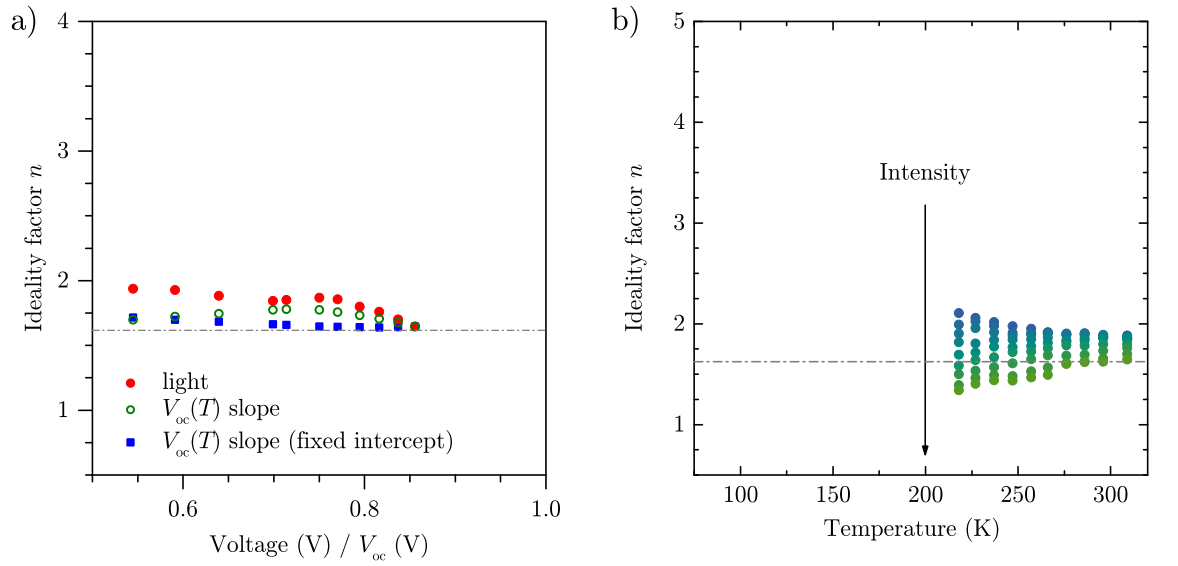

Figure 5.36: (a) Differentially determined ideality factor of a DIP:C_{60} planar-mixed heterojunction device (red) and ideality factors determined from the slope of the temperature dependence of V_{oc} according to Eq. 5.5 for free (green) and fixed intercept (blue). (b) Temperature dependence of the light ideality factor at different illumination intensities. For clarity only a subset of the recorded intensities is shown.

The value of n shows significantly less dependence on the open circuit voltage compared to the planar heterojunction and stays between 1.6 and 2 for all recorded voltages. This is consistent with the reduced discrepancy between the V_{oc} dependence on the short circuit current at high and low intensity and appears to be due to the fact that the dominating loss mechanism is trap assisted recombination throughout the entire, measured intensity range. Qualitatively the same result is found if n is determined from the linear slope of the temperature dependent open circuit voltage.

Figure 5.36 (b) presents the temperature dependence of the differentially determined light ideality factors. For all intensities n stays constant initially but then starts changing with temperature from below about 275 K. Interestingly, the direction depends on the illumination. At low intensities, the apparent ideality factor starts to increase, which might be a sign of the beginning of a slight influence of the leakage current. Oppositely, n reduces with temperature for high light intensities. Such a behavior could potentially be an indication for an increasing role of surface recombination, which would eventually result in ideality factors less than one.[192] Another possibility would be Auger recombination, which would also result in $n < 1$ but is commonly regarded unlikely for organic solar cells.[36,65] Nevertheless, it has been suggested as a possible loss mechanism in polymer:fullerene solar cells and should become more likely at low temperatures and high intensities, especially in the presence of disorder.[36,193]

6T(RT)/C_{60} planar heterojunction

The combined intensity and temperature dependent analysis of a 6T(RT)/C_{60} planar heterojunction cell is shown in Figure 5.37.[†] Like for the device analyzed in Section 5.2.3, the open circuit voltage correlates linearly with temperature for a broad temperature range and, at least for high intensities, even shows a slightly steeper increase at low temperatures Figure 5.37 (a). Similar to the planar-mixed device presented above, the extrapolated fit curves do not converge in a single value at 0 K. This might be an indication of disorder present in the active layer, yet, it seems to be of a different kind compared to the planar mixed DIP:C_{60} device: Instead of a random distribution, the extracted photovoltaic gap clearly increases monotonically with the illumination intensity from about 0.91 eV to just below 0.96 eV. It is important to note that only the data points between 300 K and 190 K have been included in the linear fit thus that the intercept is not influenced by the different behavior below 150 K which would obviously affect the intercept in a similar manner. As shown in Figure 5.37 (d) the data can be fitted with a forced common intercept. However, a slight mismatch is visible for both the highest and the lowest intensities.

The V_{oc} and j_{sc} data from Figure 5.37 (a) and (b) are again condensed into a single plot in (c), illustrating the relationship between the two quantities for the measured temperature range. Similar to the DIP/C_{60} planar heterojunction, the extrapolation (dashed lines) of the high intensity fits (solid lines) towards lower intensities deviates from the measured data at high temperatures. The apparent onset of the deviation shifts to lower short circuit currents and hence light intensities with decreasing temperature before it finally vanishes below ∼150 K. From there on, the extrapolation seems to match the entire intensity range. This observation is consistent with the change in the slope of the temperature dependence of the open circuit voltage discussed previously and could be a hint, that the recombination mechanisms at low temperature and at low intensity are similar. Note, however, that even though the calculated curve (dash-dotted line) in Figure 5.37 (c) indicates that the influence of the shunt resistance, obtained from the reverse bias regime of the dark current, is not large enough to be responsible for the V_{oc} drop, the difference is not as clear as for the DIP/C_{60} device. It is thus difficult to tell for sure if the reduced V_{oc} at the lowest intensities can be attributed to a change in the recombination mechanism. The shunt resistance would have to be a factor of four smaller in order to reproduce the data, which could be the case under illumination.

The parameters n and j_0 extracted from the fits are shown in Figure 5.38 together with the $1/k_BT$ dependence of the product $n\ln(j_0)$. The slope of the latter yields a photovoltaic gap of 0.97 eV for temperatures above 150 K, approximately, but changes more or less abruptly for lower temperatures and corresponds to a different gap of 1.09 eV. Both values are in excellent agreement with what was extracted from the temperature

[†]Note that there is a discrepancy between the values of the characteristic quantities of this cell and the 6T(RT)/C_{60} cell discussed before which exceeds the error stated in Section 5.2.3. This is attributed to a mechanical change inside the deposition chamber that affected the thickness of the active layers and presumably resulted in thinner films. This holds for all 6T based cells presented in this Section but does not affect their general properties.

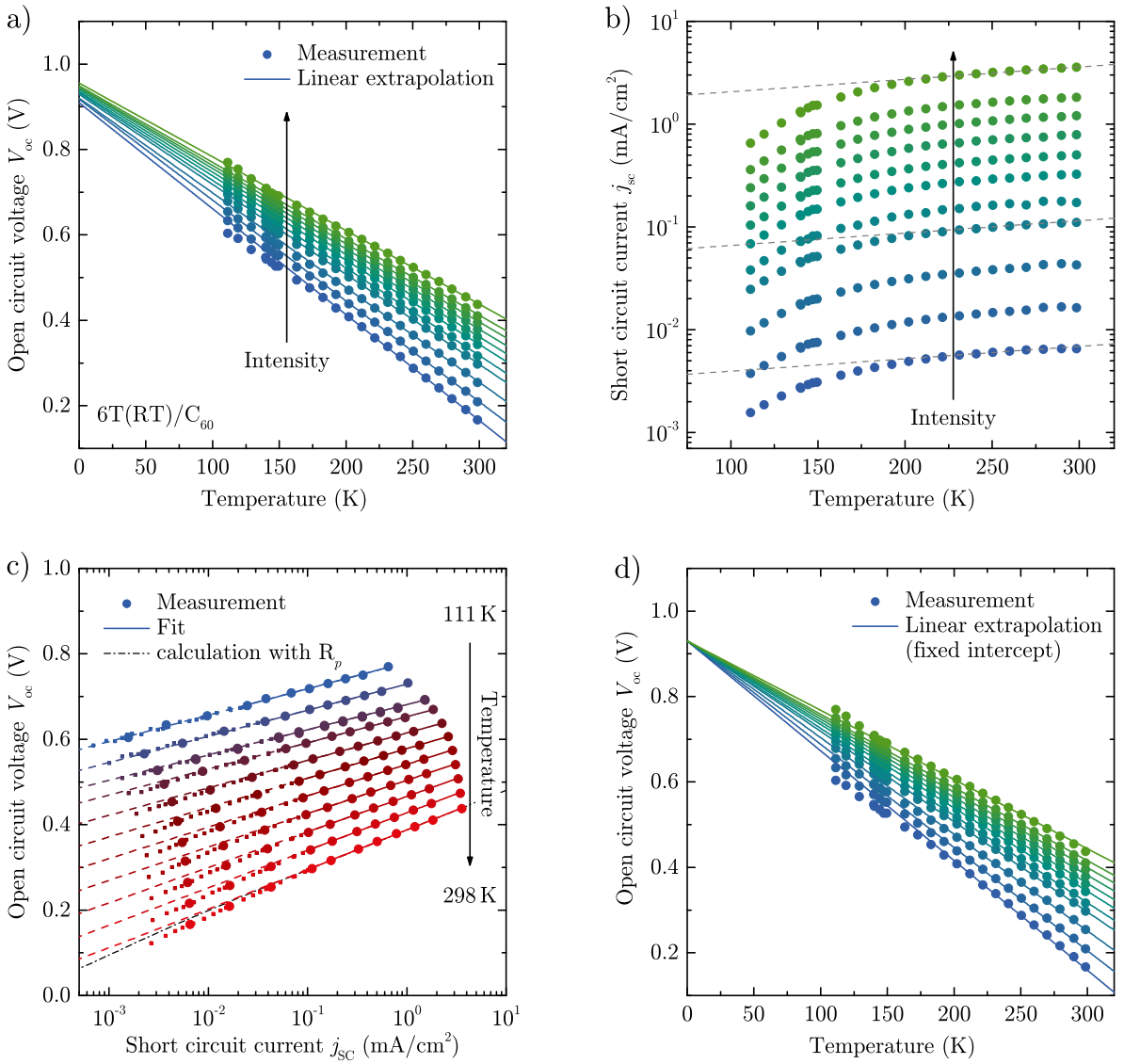

Figure 5.37: Combined intensity and temperature dependent analysis of a 6T(RT)/C_{60} planar heterojunction solar cell. (a) Temperature dependence of the open circuit voltage recorded for different illumination intensities. (b) Short circuit current in dependence on Temperature at different intensities. The dashed lines are guides to the eye. (c) V_{oc} as a function of j_{sc} measured at the temperatures shown in (a) and (b). The fits indicated by the solid lines allow the extraction of n and j_0 displayed in Figure 5.38. The dash-dotted line in (c) illustrates the impact of R_p as extracted from the reverse bias regime of the j-V curve in the dark. As shown in (d) the linear relation of V_{oc} with temperature is not perfectly reproduced if a fixed intercept (i.e. gap energy) is forced. A white LED and a stabilized current source were used as light source. The maximum illumination intensity was equivalent to about 1.4 suns and reduced by neutral density filters (large spheres). Intermediate intensities were achieved by down scaling the LED drive current (small dots). For clarity only a subset of intensities and temperatures is shown

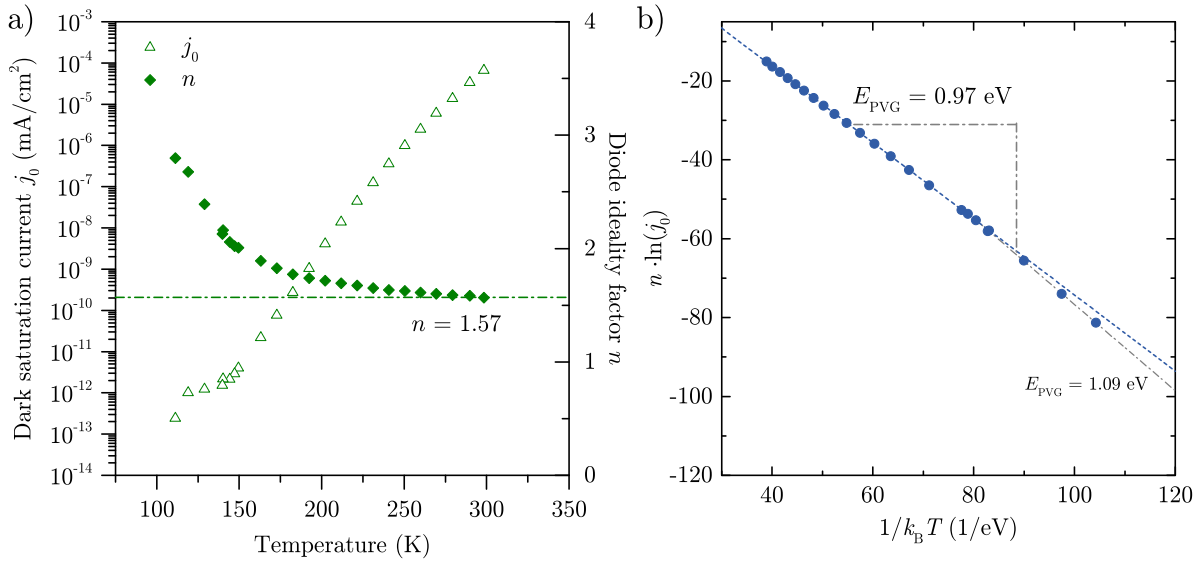

Figure 5.38: Combined intensity and temperature dependent analysis of a 6T(RT)/C_{60} planar heterojunction solar cell. (a) Graphical summary of the parameters n and j_0 obtained form the fit results in Figure 5.37 (c). The temperature dependent analysis of these parameters ($n \ln(j_0)$ vs. $1/k_B T$) yields a photovoltaic gap of 0.97 eV as shown in (b). In accordance with the steeper increase of V_{oc} at low temperatures a value of 1.09 eV is found if the low temperature range is evaluated separately.

dependence of the open circuit voltage (cf. also Figure 5.24 on page 90).

j-V curves under illumination and in the dark have again been recorded during the warming up of the sample after the intensity dependent measurement of V_{oc} and j_{sc} during the cool down process. The necessary parameters have been extracted from the dark j-V characteristics as demonstrated above. Both the j-V curves and the analysis are depicted in Figure 5.39 and an energy of 1.08 eV for the photovoltaic gap is found from the dark characteristics. This is slightly larger than the value obtained from the illuminated device, regardless of the analysis method.

Considering the temperature evolution of the individual parameters n and j_0 separately, the same qualitative behavior is observed in dark and under illumination (Figure 5.38 (a) and Figure 5.39 (c)). Interestingly, the ideality factor shows a slight but continuous increase as the sample is cooled down. Consequently, the dark saturation current cannot be adequately fitted with Eq. 2.22, which would require constant parameters n, j_{00} and E_{PVG}. Such a problem could in principle arise from an inaccurate separation of the ideality factor and the dark saturation current by the respective fit of the measurement. However, this seems unlikely considering the results obtained for other devices. Noteworthy, in Figure 5.38 (a) above 150 K the observed dependence of the ideality factor of this sample on temperature is distinctly different from the abrupt increase that has been seen for the other devices and that has been identified as an experimental artifact. Thus this effect has to be considered to be real and is tentatively attributed to a change in the recombination process.

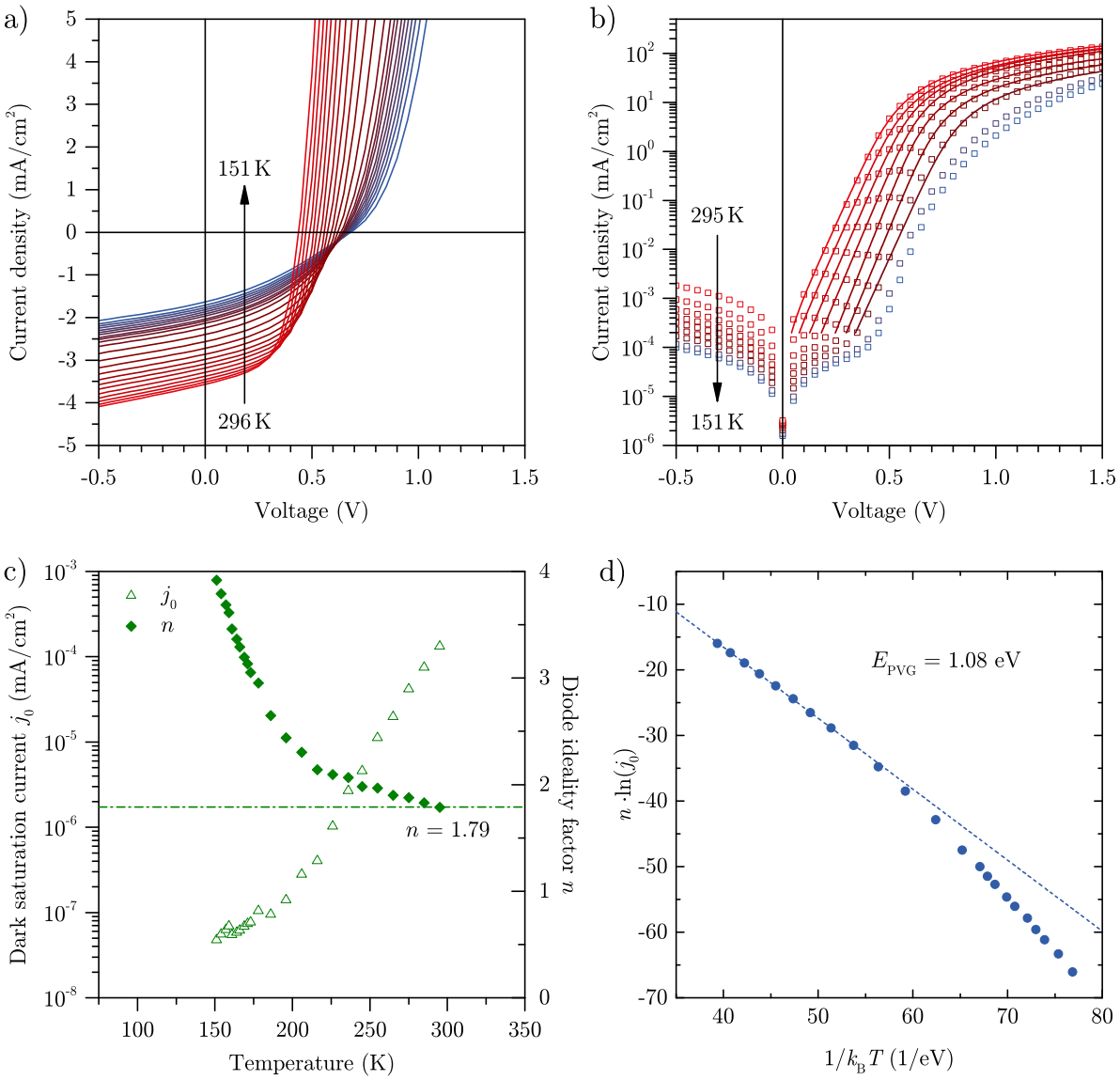

Figure 5.39: Analysis of the dark saturation current of a 6T(RT)/C_{60} planar heterojunction extracted from the temperature dependent measurement of the j-V characteristics in the dark.

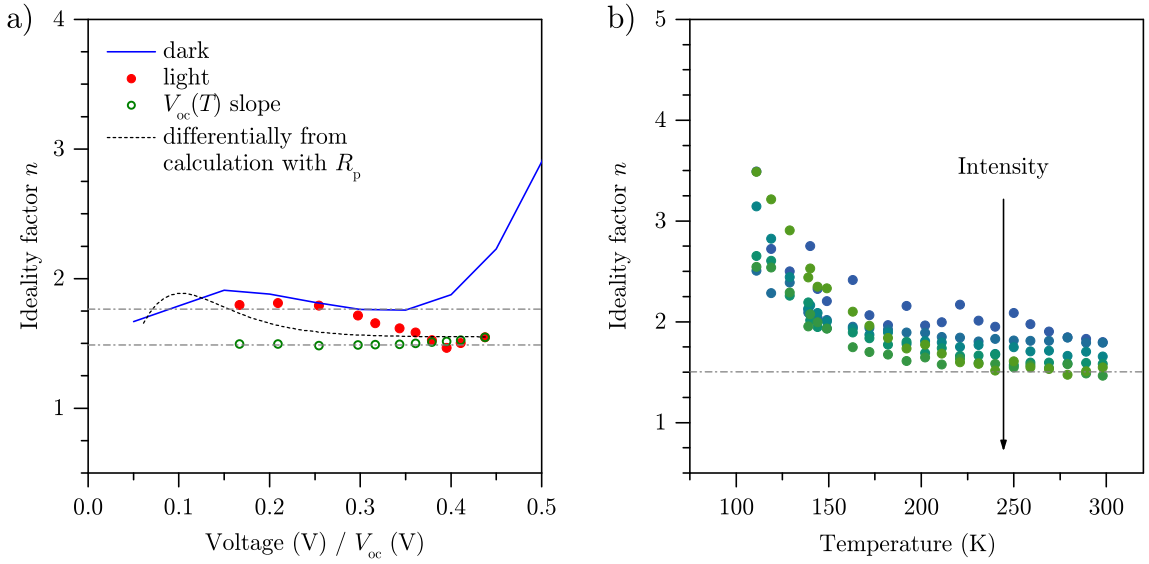

Figure 5.40: Differentially determined ideality factor of a 6T(RT)/C_{60} planar heterojunction device. (a) Comparison of dark and light ideality factors derived for the highest measured temperature from the dark j-V curve according to Eq. 5.3 and the intensity dependent V_{oc} measurement (Eq. 5.2), respectively. Additionally, the ideality factor derived from the slope of the $V_{oc}(T)$ dependence is shown and the expected apparent ideality factor caused by R_p is illustrated. (b) Temperature dependence of the light ideality factor at different illumination intensities.

Similarly, the differentially determined light ideality factor increases with decreasing open circuit voltage, i.e. light intensity, and coincides with the dark ideality factor at low bias voltage (Figure 5.40). This does not seem to be caused by an increasing influence of the shunt resistance: The black dashed curve is the predicted apparent ideality factor caused by the previously determined shunt resistance and derived differentially from the calculated V_{oc} dependence on j_{sc}. Comparison with the data illustrates that the impact of the leakage current is first expected at even lower open circuit voltages. Thus the ideality factor seems to undergo a transition from one plateau at high intensities to a second one at low intensities, which perfectly matches the plateau indicated by the dark ideality factor. The apparent analogy between the temperature and intensity dependence of the ideality factor is in agreement with the above observation that the fit of the V_{oc} vs. j_{sc} data becomes valid for an increasing intensity range at reduced temperature (Figure 5.37 (c)) and the interpretation that low temperature and low intensity similarly affect the recombination process. Note that under such circumstances it is doubtful that deriving the ideality factor from the $V_{oc}(T)$ slope by the procedure described above is actually valid. Nevertheless, for completeness the result is shown in Figure 5.40 but should be treated with care.

Noteworthy, a transition of the ideality factor between two plateaus was also found for the planar-mixed DIP:C_{60} device and thus seems to be a result of structural disorder that is typically accompanied by an energetic disorder.[26] Recently, Blakesley and Neher have

proposed that, amongst other factors, the open circuit voltage of bulk heterojunction cells depends on the degree of energetic disorder in the organic semiconductor and in particular on the presence of tail states.[194]

Similarly, Hawks and Street *et al.* have presented an analytical expression that describes the diode dark current under the premise that exponential tails extend the density of states into the gap and that the tail of either the HOMO or the LUMO is broader than the other. Under these prerequisites it is further assumed that the majority of the carrier type corresponding to the broader density of states, and hence its quasi-Fermi level, (e.g. the holes in the HOMO) resides within the tail while the other carrier type exceeds the transport energy and thus is mobile (e.g. electrons in the LUMO). In such a scenario recombination of free electrons with trapped holes at the hole quasi-Fermi level may be considered the most probable recombination mechanism and the dark current is given by:[195]

$$j_{\mathrm{D}}(V) = \xi q d C_{\mathrm{n}} N_{\mathrm{C}} N_{\mathrm{V}} \exp\left(-\frac{V_{\mathrm{e},0}}{k_{\mathrm{B}}T}\right) \exp\left(-\frac{E_{\mathrm{g}} - V_{\mathrm{e},0}}{E_0}\right) \left[\exp\left(\frac{qV}{E_0}\right) - 1\right], \tag{5.6}$$

where

$$\xi = s\left[1 - \exp\left(-\frac{1}{s}\right)\right] \text{ and } s = \frac{1}{q(V_{\mathrm{bi}} - V)} \frac{E_0 k_{\mathrm{B}} T}{E_0 - k_{\mathrm{B}} T}. \tag{5.7}$$

Here q is the elementary charge and d is the thickness of the active layer. C_{n} is the electron capture rate constant, N_{C} and N_{V} denote the effective density of states at the LUMO and HOMO transport energy (i.e. the threshold energy that separates mobile and trapped charges, also denoted as the mobility edge[192]), respectively. $V_{\mathrm{e},0}$ is the electron injection barrier, E_{g} is the intermolecular HOMO-LUMO energy gap and V_{bi} is the built in potential. E_0 is the slope of the broader band tail, i.e. the HOMO in this case.

Even though Eq. 5.6 has been derived to describe the dark current in dependence on the applied bias voltage it can be extended by a constant term accounting for the photo current generated under illumination. Note that such an extension is naive and not necessarily suitable to describe the complete j-V characteristics under illumination. Yet, it is sufficient to reproduce the temperature dependence of the open circuit voltage measured for the 6T(RT)/C_{60} device. In fact it is possible to mimic the complete intensity range with a common set of parameters where the photo current solely accounts for the observed differences. The calculated V_{oc} is shown as the solid lines in Figure 5.41 (a) and clearly resembles the behavior of the measured open circuit voltage, at least for temperatures above 150 K.

The values of the parameters used in the calculation are summarized in the caption of Figure 5.41. Following the example of Hawks *et al.* the tail slope was determined experimentally from the temperature dependence of $E_0 = nk_{\mathrm{B}}T$ as shown in Figure 5.41 (b).[195] The values determined differentially for the lowest light intensity have been used here and the gap energy E_{g} has been set to $E_{\mathrm{D/A}} = 0.95\,\mathrm{eV}$ determined by PES.[63] The photo

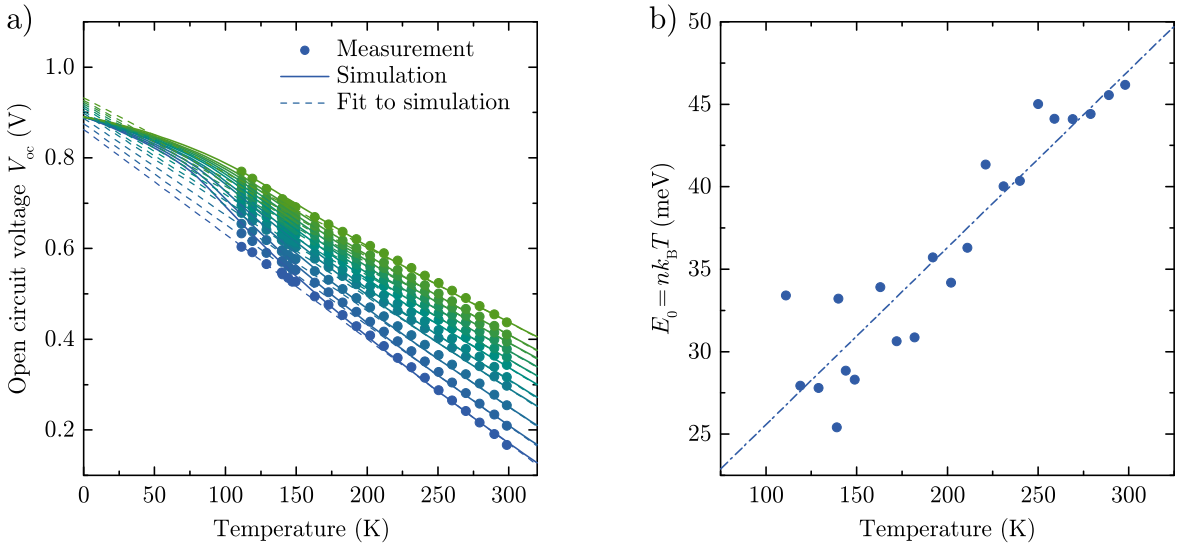

Figure 5.41: (a) Simulation of the temperature dependent V_{oc} of the 6T(RT)/C_{60} cell for different illumination intensities with the analytical model by Hawks *et al.*[195] extended for a constant photo current. The model accounts for recombination via exponential tail states and all curves are simulated with a single set of parameters, except for the photo current, which was set to the respective j_{sc} measured at the highest temperature. (b) The temperature dependence of the tail slope was determined from a linear fit to nk_BT vs temperature for the lowest light intensity; a relation $E_0 \approx 0.1\,\frac{\text{meV}}{\text{K}}\,T + 15\,\text{meV}$ was extracted. The other simulation parameters were $V_{bi} = 0.77\,\text{V}$, $C_n = 1.2 \times 10^{-13}\,\text{cm}^3/\text{s}$, $N_c = N_v = 2 \times 10^{20}\,\text{cm}^{-3}$, $E_g = 0.95\,\text{eV}$ and $V_{e,0} = 0.12\,\text{eV}$.

current has been set to the respective measured short circuit current at the highest temperature. All other parameters are experimentally unknown and have been chosen arbitrarily. However, it is important to note that their values are plausible and characteristic for organic diodes.[195]

Notably, the simulation would even predict a slight increase of the V_{oc} at low temperatures thus that the existence of exponential tail states provides an alternative explanation for this peculiar feature. Like the experimental data themselves, an extrapolation of a linear fit of the high temperature part of the simulation would indicate that the effective energy gap changes with intensity (dashed lines in Figure 5.41 (a)). Such an interpretation would be consistent with the picture of a gradual filling of a broad exponential tail with an accumulating amount of generated charge carriers at increasing illumination intensity. Similar considerations have been presented by Garcia-Belmonte for Gaussian tails.[196]

Note, that since it has been shown above that the influence of the parallel resistance at low photo currents may affect the apparent photovoltaic gap, it is of course imaginable that a combination of n and R_p parameters can be found that would also allow the reconstruction of the measured data. Yet, this could not even closely be achieved with reasonable parameters that are remotely consistent with experimental values.

The observed phenomenon that the photovoltaic gap apparently depends on the

light intensity is thus ascribed to the presence of tail states which in turn implies that significant disorder has to be present in the films, in spite of the crystalline features found during the morphological investigation in Section 5.2.1.

6T(HT)/C_{60} planar heterojunction

The high temperature companion cell of the 6T/C_{60} heterojunction, i.e. with the 6T layer grown at 100 °C substrate temperature, behaves similarly as the room temperature device. As shown in Figure 5.42 (a) the intercept of the linear extrapolation of the temperature dependent open circuit voltage increases slightly with the increasing illumination intensity for the three lowest intensities but then converges in a single spot with a slight jitter between 0.96 V and 0.97 V. It is hence not surprising that all intensities can also be fitted with a $E_{\mathrm{D/A}}/q$ value of 0.95 eV (Figure 5.42 (d)), which again attests excellent agreement with earlier UPS results.[63] The short circuit current (Figure 5.42 (b)) shows the typical behavior observed for the other cells and the V_{oc} data is plotted against the corresponding j_{sc} in Figure 5.42 (c). What is observed looks more similar to the DIP/C_{60} cell than to the room temperature 6T/C_{60} device. The extrapolated high intensity fit towards lower short circuit current increasingly diverges from the measured data with both decreasing intensity and temperature. In contrast to the other solar cells investigated so far, the calculated V_{oc} dependence on j_{sc} in the low intensity region already closely describes the measurement simply by the inclusion of the parallel resistance again obtained from the dark current under reverse bias. It appears thus that, if at all, only a minor reduction of V_{oc} can be assigned to a change in the recombination mechanism.

The plot of the extracted fit parameters presented in Figure 5.43 indicates a slight temperature dependence of the ideality factor which increases initially before it gets lower again. As for the room temperature device, there is no clear evidence that this observation is an experimental artifact, at least down to 150 K; the dark saturation current behaves accordingly. The photovoltaic gap (0.99 eV) extracted from these parameters is again slightly larger than what was found from temperature dependent V_{oc}.

Also for this sample j-V curves under illumination at the highest intensity and in the dark have been recorded while the sample was warmed up after the intensity dependent measurement and the data are shown in Figure 5.44. In accordance with the flattening of the V_{oc} at low temperatures observed in Figure 5.42 (a), the j-V curves under illumination are distinctly s-shaped at low temperatures but recover with increasing temperature. The increase of the parallel resistance with lower temperature is nicely visible from the dark j-V curves in the negative bias regime, while at high voltages the influence of the series resistance becomes increasingly prominent. A fit with the Shockley equation (solid lines in Figure 5.44 (b)) still yields a good description of the measured data at low temperatures but the impact of the parasitic resistances leads to an early overestimation of the ideality factor (Figure 5.44 (c)). The photovoltaic gap extracted from the dark characteristics is once more larger than the values extracted from the illuminated cells and from UPS (Figure 5.44 (d)).[63]

The differentially determined dark and light ideality factors are shown in Figure 5.45.

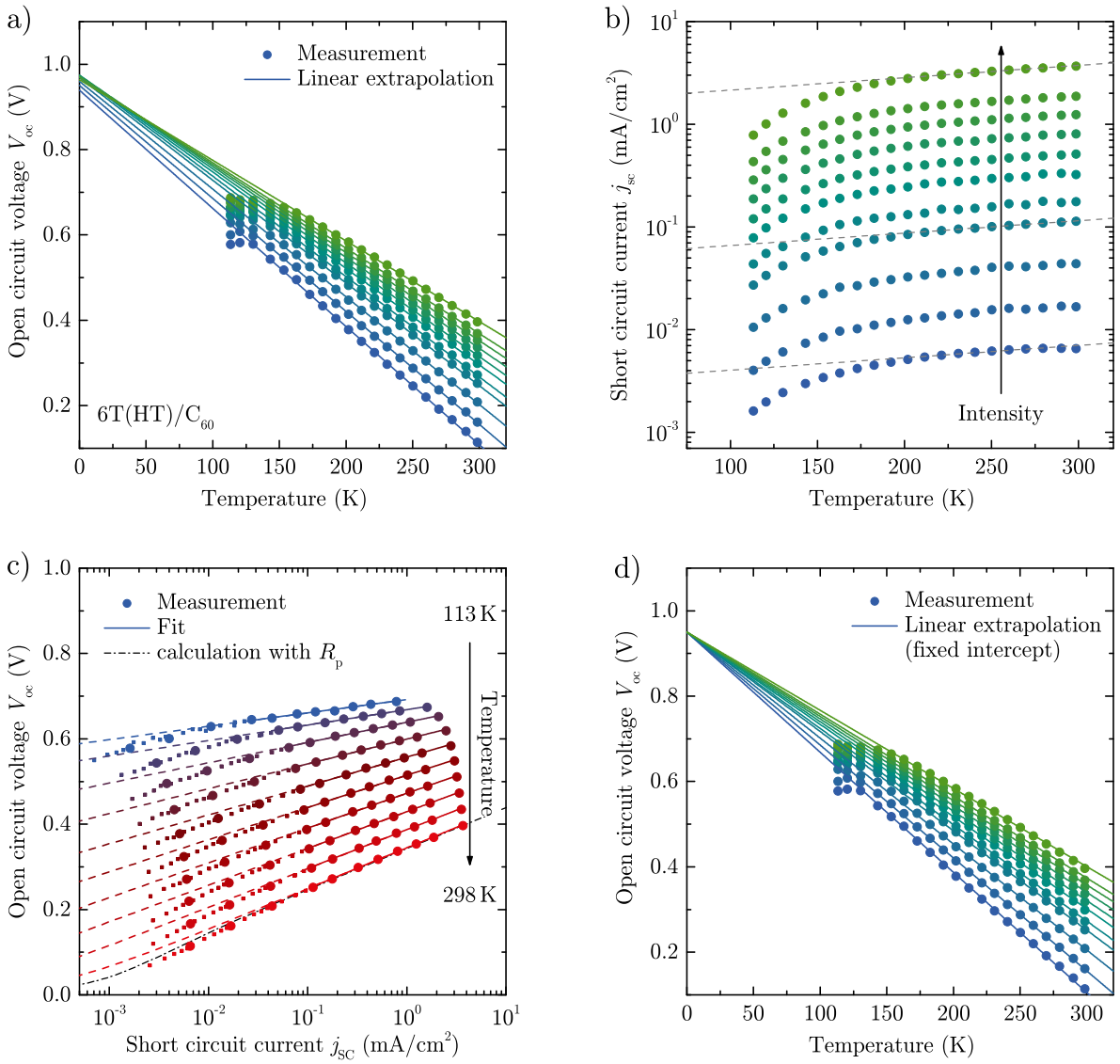

Figure 5.42: Combined intensity and temperature dependent analysis of a 6T(HT)/C_{60} planar heterojunction solar cell. (a) Temperature dependence of the open circuit voltage recorded for different illumination intensities. (b) Short circuit current in dependence on Temperature at different intensities. The dashed lines are guides to the eye. (c) V_{oc} as a function of j_{sc} measured at the temperatures shown in (a) and (b). The fits indicated by the solid lines allow the extraction of n and j_0 displayed in Figure 5.43. The dash-dotted line in (c) illustrates the impact of R_p as extracted from the reverse bias regime of the j-V curve in the dark. As shown in (d) the linear relation of V_{oc} with temperature can also be fitted if a fixed intercept (i.e. gap energy) is forced. A white LED and a stabilized current source were used as light source. The maximum illumination intensity was equivalent to about 1.5 suns and reduced by neutral density filters (large spheres). Intermediate intensities were achieved by down scaling the LED drive current (small dots). For clarity only a subset of intensities and temperatures is shown.

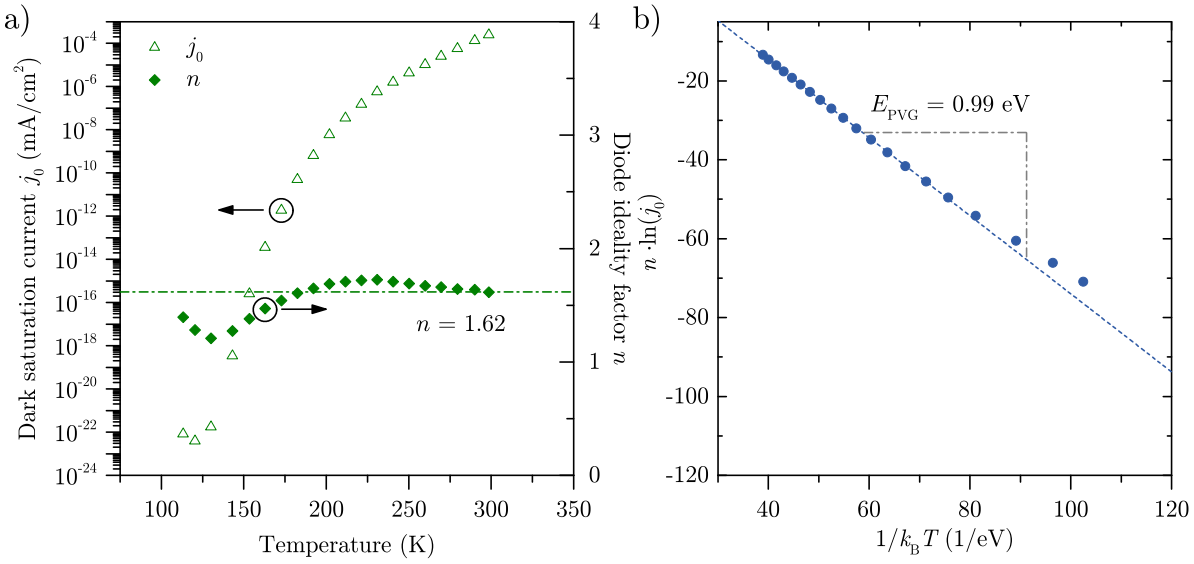

Figure 5.43: Combined intensity and temperature dependent analysis of a 6T(HT)/C_{60} planar heterojunction solar cell. (a) Graphical summary of the parameters n and j_0 obtained form the fit results in Figure 5.42 (c). The temperature dependent analysis of these parameters ($n \ln(j_0)$ vs. $1/k_B T$) yields a photovoltaic gap of 0.99 eV as shown in (b).

Again a good agreement between light and dark ideality factor is evident at low V_{oc} or bias voltage, respectively. Like in the case of the 6T(RT)/C_{60} device, there seems to be a transition between two plateau values. However, this time the light ideality factor does not saturate for low open circuit voltages. This can be attributed to an artifact contribution from the shunt resistance by comparison with the calculated apparent ideality factor caused by R_P (dashed line in Figure 5.45). It thus remains unclear if a partial increase of the ideality factor actually occurs or if it remains more or less constant as indicated by the $V_{oc}(T)$ slope.

Either way the ideality factor remains larger than one in the whole investigated intensity regime and it seems clear that the dominating recombination mechanism is a trap assisted process. Only at low temperatures and at high intensity the ideality factor starts to decrease and eventually even reaches a value below 1. This can possibly be explained with increased surface recombination that becomes relevant but might even be caused by an Auger process.[36,65,192,193]

It is important to note that a (true) transition of the ideality factor may be regarded as a sign of a transition between different dominating recombination mechanisms. In the present case, as well as for the room temperature device and the DIP:C_{60} cell, the ideality factor remains larger than one for the whole range of intensities, which implies that recombination is mainly trap assisted, independent of the illumination intensity. Yet, the exact value of the ideality factor depends on the specific trap distribution. A possible explanation for the observed changes in the ideality factor would, for example, be a transition form recombination via deep trap states within the band gap at low intensities to recombination via tail states at high intensities.[192,197] In the present case,

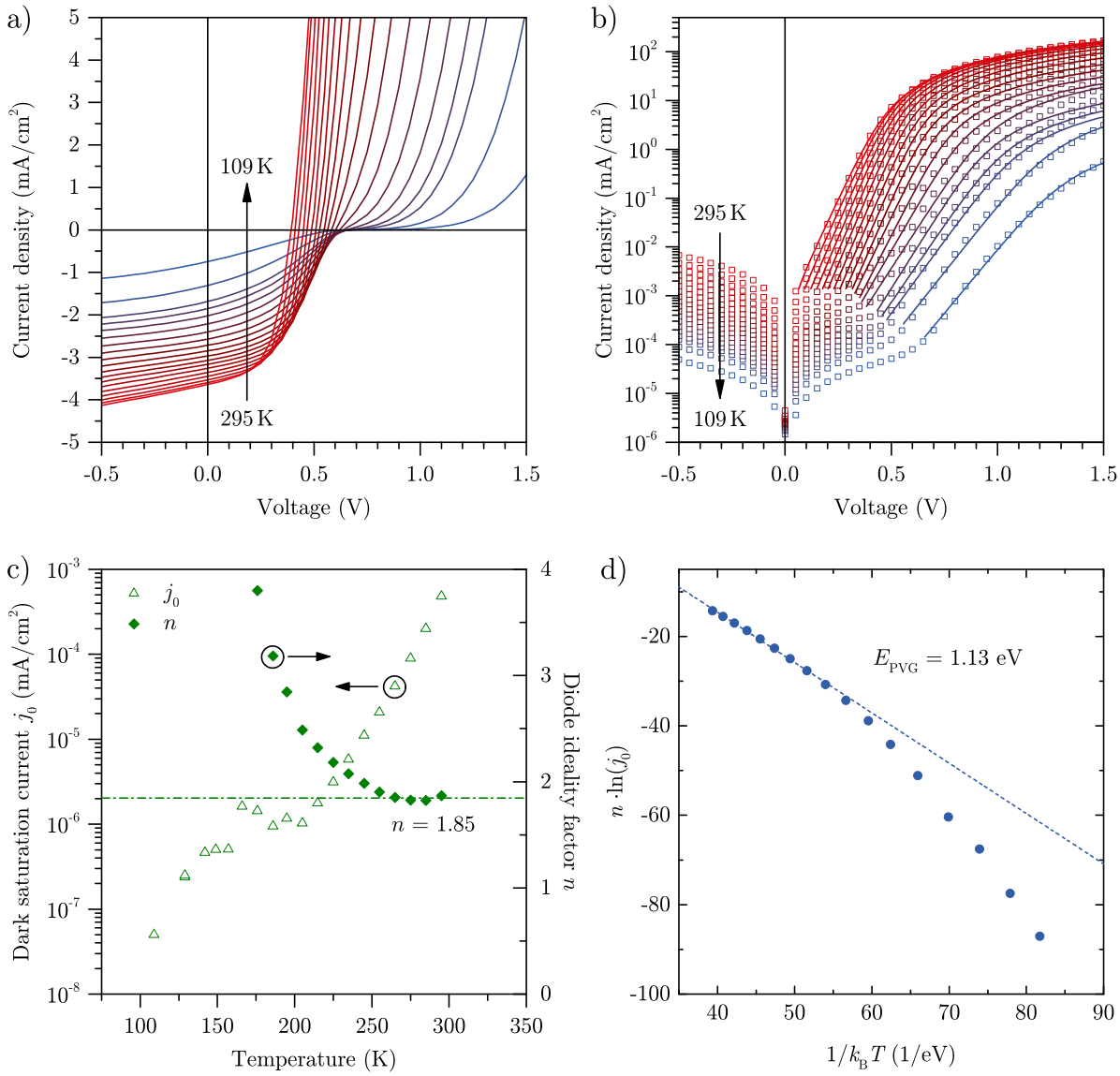

Figure 5.44: Analysis of the dark saturation current of a 6T(HT)/C_{60} planar heterojunction extracted from the temperature dependent measurement of the j-V characteristics in the dark.

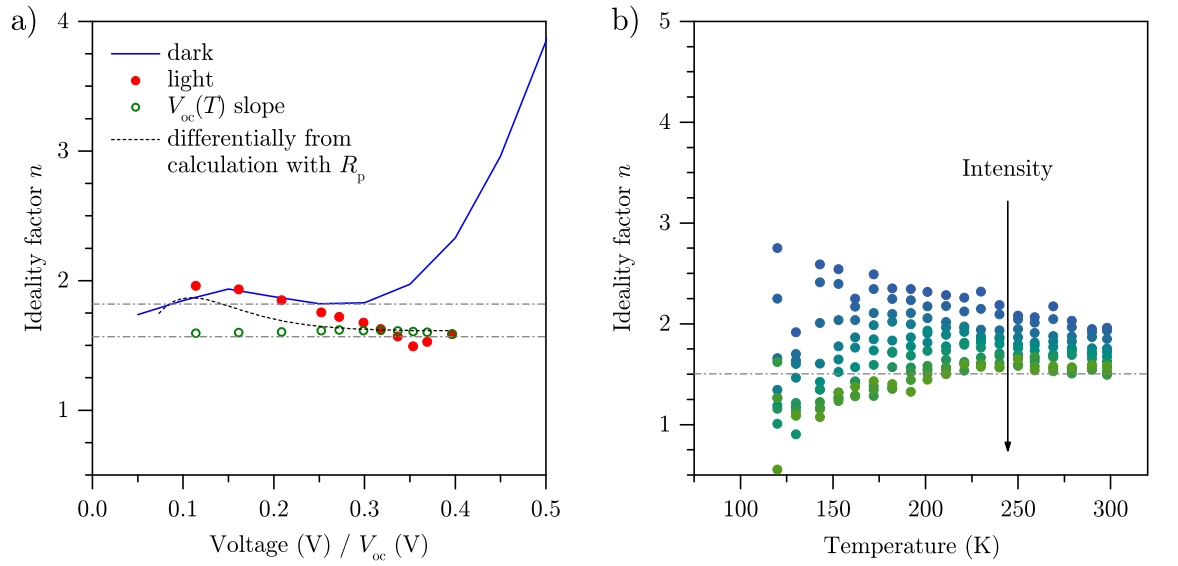

Figure 5.45: Differentially determined ideality factor of a 6T(HT)/C_{60} planar heterojunction device. (a) Comparison of dark and light ideality factors derived for the highest measured temperature from the dark j-V curve according to Eq. 5.3 and the intensity dependent V_{oc} measurement (Eq. 5.2), respectively. Additionally, the ideality factor derived from the slope of the $V_{oc}(T)$ dependence is shown and the expected apparent ideality factor caused by R_p is illustrated. (b) Temperature dependence of the light ideality factor at different illumination intensities.

it seems like the transition of the dominating recombination mechanism is accompanied with a transition of the photovoltaic gap. It has to be pointed out that this is not generally the case and may well be coincidental. While the ideality factor is an indicator for the recombination kinetics, it is independent of the initial and final state energy of the involved particles. The photovoltaic gap on the other hand is determined by the energetic difference of the initial and final state of the majority of the particles but independent of the recombination kinetics in steady state. A good example of this is the DIP/C_{60} cell, where the photovoltaic gap remains perfectly constant for all intensities but the ideality factor indicates a transition of the recombination mechanism from direct recombination of free carriers to trap assisted recombination at low intensities.

6T(RT)/DIP planar heterojunction

The temperature and intensity dependent measurement of the open circuit voltage of a 6T(RT)/DIP planar heterojunction solar cell is shown together with the corresponding short circuit current in Figure 5.46 (a) and (b). The intercept of the extrapolation of the linear temperature dependence regime of the V_{oc} gradually changes from about 1.94 V at low intensities to 1.86 V at high intensities. The direction of this change is opposite to what was observed previously and is probably caused by the influence of the shunt resistance which is not negligible at low intensities for this solar cell. This is clearly illustrated by the dash-dotted line in Figure 5.46 (c) which is calculated from the corresponding V_{oc} vs j_{sc} fit results (solid lines) and the parallel resistance extracted from the dark current j-V curve under reverse bias. Apparently the V_{oc} loss at low intensities can be fully explained by leakage currents whose influence becomes severe at low temperatures. This in turn is markedly visible by the drastic change of the $V_{oc}(j_{sc})$ curve shape which leads to a failure of the fit procedure and additionally manifests itself in the distinct V_{oc} drop at low temperature for the lowest light intensity in Figure 5.46 (a). Hence, in this case, the seeming dependence of E_{PVG} on the intensity has indeed to be regarded as an experimental artifact caused by the shunt resistance.

As shown in Figure 5.46 (d) a good fit is achieved even if the intercept is fixed at 1.9 eV. It is important to note, that the demonstrated influence of the leakage current is not due to an extraordinarily low shunt resistance but a result of a lower overall short circuit current in combination with a very low dark saturation current j_0. In fact, the parallel resistance is comparable with that of the DIP/C_{60} planar heterojunction.

The parameters resulting from the fit of the high intensity regime of the illumination dependent open circuit voltage is shown in Figure 5.47 (a). The ideality factor stays constant initially and starts decreasing continuously for temperatures below 260 K, approximately. The dark saturation current decreases accordingly. The dependence of the product $n \ln(j_0)$ on $1/k_B T$ is plotted in Figure 5.47 (b) and a photovoltaic gap of 1.82 eV is extracted from a linear fit to the data. This is in perfect agreement with the value found from the linear extrapolation of the V_{oc} dependence on temperature at the highest intensity and with the UPS results.[63]

The differentially determined ideality factor is shown in Figure 5.48, in dependence on the open circuit voltage for the highest measured temperature in (a) and on temperature for all intensities in (b). An influence of the shunt resistance with decreasing intensity is clearly present and seems to be successfully removed by determining the ideality factor from the $V_{oc}(T)$ slope. In any case the main recombination mechanism appears to be trap assisted recombination at typical cell operation conditions. At low temperatures the direction of the ideality factor change again depends on the intensity. For low intensities it increases, most likely because of the shunt resistance. For high intensities, the ideality factor becomes lower, before it increases again. As previously noted the decrease could possibly be caused by increasing influence of surface or Auger recombination.

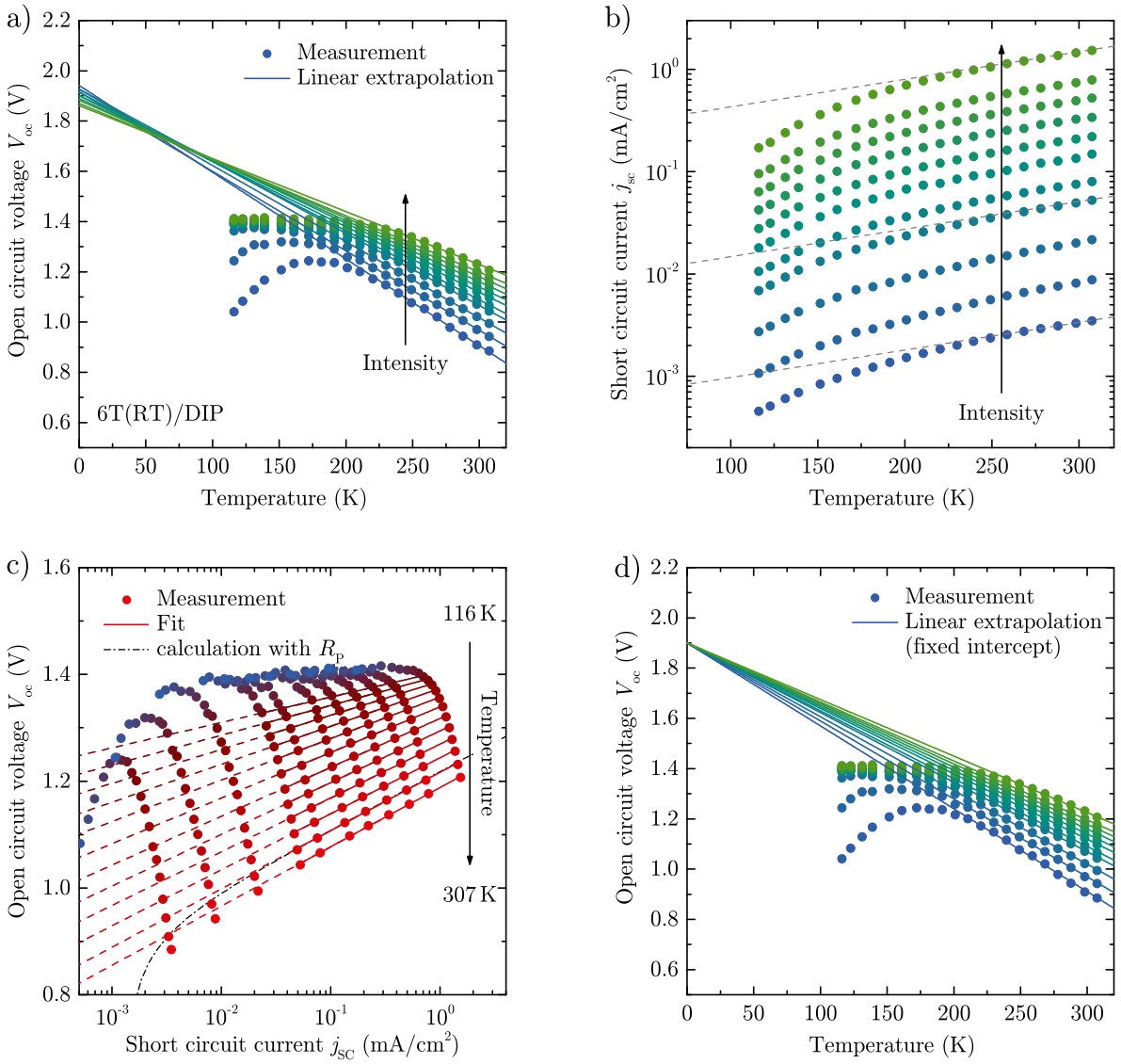

Figure 5.46: Combined intensity and temperature dependent analysis of a 6T(RT)/DIP planar heterojunction solar cell. (a) Temperature dependence of the open circuit voltage recorded for different illumination intensities. (b) Short circuit current in dependence on Temperature at different intensities. The dashed lines are guides to the eye. (c) V_{oc} as a function of j_{sc} measured at the temperatures shown in (a) and (b). The fits indicated by the solid lines allow the extraction of n and j_0 displayed in Figure 5.47. The dash-dotted line in (c) illustrates the impact of R_p as extracted from the reverse bias regime of the j-V curve in the dark. As shown in (d) the linear relation of V_{oc} with temperature is well reproduced if a fixed intercept (i.e. gap energy) is forced. A white LED and a stabilized current source were used as light source. The maximum illumination intensity was equivalent to about 1.1 suns and reduced by neutral density filters. For clarity only a subset of intensities and temperatures is shown.

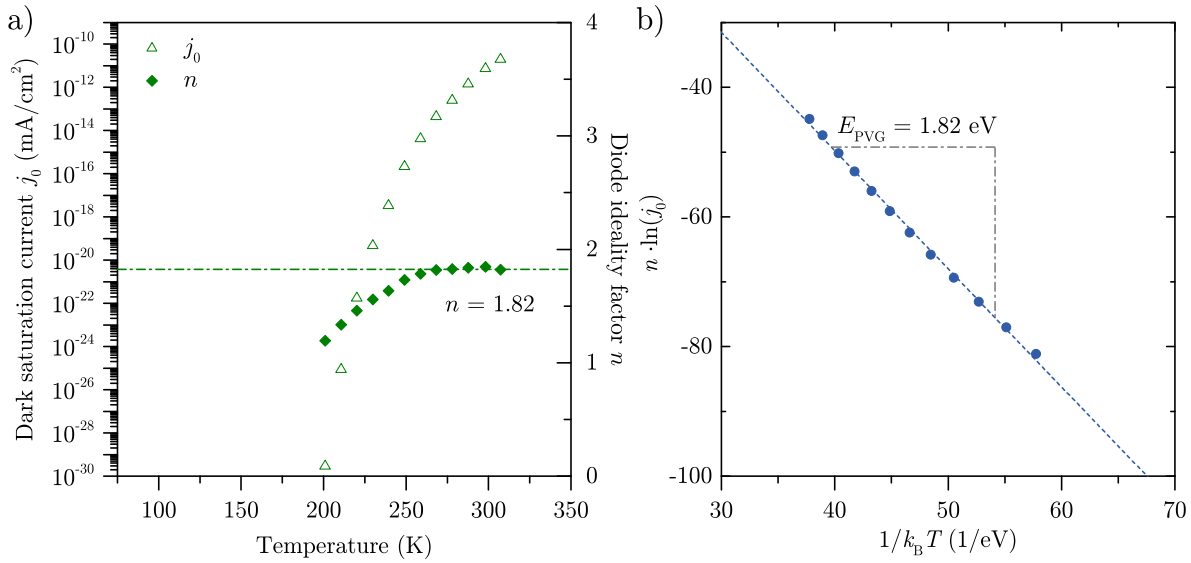

Figure 5.47: Combined intensity and temperature dependent analysis of a 6T(RT)/DIP planar heterojunction solar cell. (a) Graphical summary of the parameters n and j_0 obtained form the fit results in Figure 5.46 (c). The temperature dependent analysis of these parameters ($n \ln(j_0)$ vs. $1/k_B T$) yields a photovoltaic gap of 1.82 eV as shown in (b).

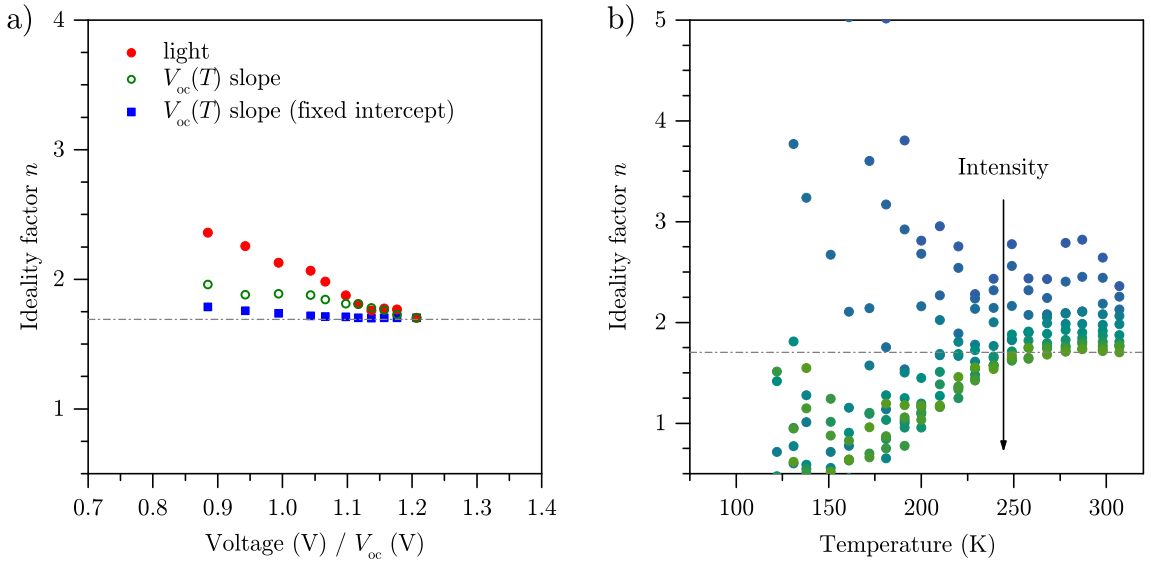

Figure 5.48: (a) Differentially determined ideality factor of a 6T(RT)/DIP planar heterojunction device (red) and ideality factors determined from the slope of the temperature dependence of V_{oc} according to Eq. 5.5 for free (green) and fixed intercept (blue). (b) Temperature dependence of the light ideality factor at different illumination intensities.

6T(HT)/DIP planar heterojunction

Finally the 6T(HT)/DIP planar heterojunction solar cell is analyzed with respect to its temperature and intensity dependent behavior in Figure 5.49. As expected, the open circuit voltage increases as the sample is cooled but begins to flatten out already at about 270 K, except for the lowest intensity. At the same time the short circuit current retains its typical, smooth temperature dependence. The V_{oc} vs j_{sc} plot in Figure 5.49 (c) clearly reveals that the open circuit voltage is severely affected by the shunt resistance both at low intensities and with decreasing temperature. It appears thus that the reason for the early flattening of the V_{oc} with temperature is the influence of the shunt resistance. Likewise, the enormous spread of the extracted intercept or the linear extrapolation is probably mainly caused by the influence of the shunt resistance. While a comparatively low influence yields an overestimation of the photovoltaic gap the massive impact of R_p at very low light intensity yields a heavily underestimated value. Additionally, the linear fit is based on five data points only and there is a significant uncertainty in the extrapolation and thus a wide, random scattering of the intercept. As a consequence, the linear regime of temperature dependence of the open circuit voltage can very well be fitted with a fixed intercept at 2.1 V for all intensities except for the lowest (Figure 5.49 (d)).

Again it is important to note that the parallel resistance is not particularly low for this cell but that its impact is significantly enhanced by an overall low photo current and especially by the extremely low dark saturation current.

Once again, the ideality factor and the dark saturation current obtained by the fit in Figure 5.49 (c) are shown for the different temperatures in Figure 5.50. The overall value of the ideality factor is clearly overestimated and it is difficult to tell if the initial decrease with temperature is actually present. The increase at lower temperatures can clearly be attributed to the influence of the leakage current. In accordance with the observations in Figure 5.49 only the first five temperatures can reliably be used to extract the photovoltaic gap from the $n\ln(j_0)$ vs. $1/k_BT$ plot. This yields a value of 2.14 eV and is in good agreement with what was found from the linear extrapolation of the $V_{oc}(T)$ data at high intensities.

The differentially determined ideality factor for the 6T(HT)/DIP cell at the highest temperature is shown in Figure 5.51 (a). Only for the highest two intensities the ideality factor saturates at 2.05. For all other intensities the influence of the leakage current is clearly visible. The temperature dependence of the differentially determined ideality factor at the highest intensity confirms the slight initial decrease observed above and indicates a change of the recombination mechanism towards a process that appears to be less dominated by deep traps (Figure 5.51 (b)).

Since the change of E_{PVG} with intensity is considered an artifact for this solar cell, the ideality factor was additionally determined from the $V_{oc}(T)$ slope with a forced common intercept (cf. Figure 5.49 (d)). Only with this approach a reasonable ideality factor that does not significantly exceed two could be obtained and its value is more or less constant (blue squares in Figure 5.51 (a)). Indeed the entire intensity range of the V_{oc} vs. j_{sc} curve at the highest temperature can be described with this constant ideality factor as

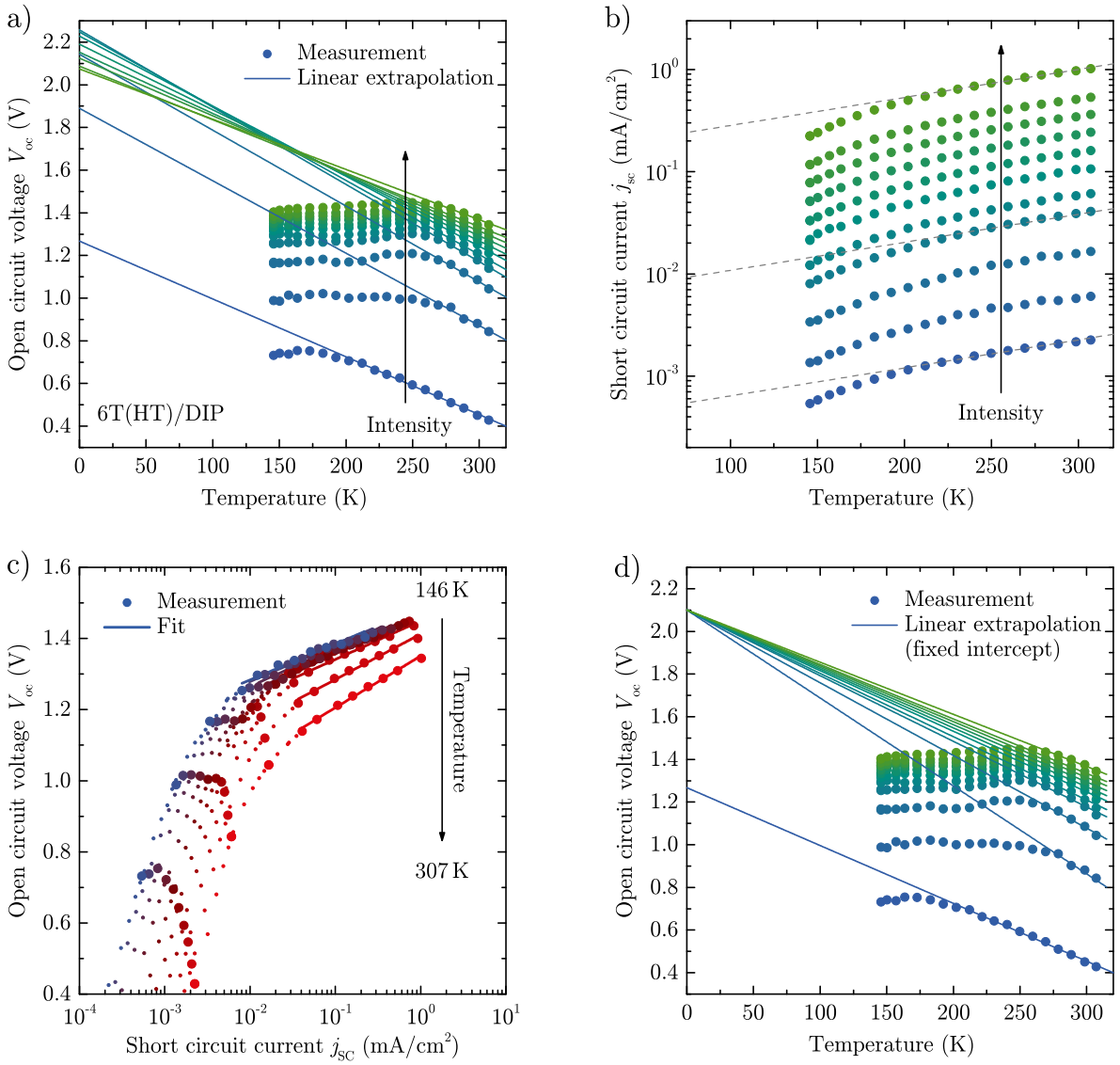

Figure 5.49: Combined intensity and temperature dependent analysis of a 6T(HT)/DIP planar heterojunction solar cell. (a) Temperature dependence of the open circuit voltage recorded for different illumination intensities. (b) Short circuit current in dependence on Temperature at different intensities. The dashed lines are guides to the eye. (c) V_{oc} as a function of j_{sc} measured at the temperatures shown in (a) and (b). The fits indicated by the solid lines allow the extraction of n and j_0 displayed in Figure 5.50. The dash-dotted line in (c) illustrates the impact of R_p as extracted from the reverse bias regime of the j-V curve in the dark. As shown in (d) the linear relation of V_{oc} with temperature is well reproduced if a fixed intercept (i.e. gap energy) is forced, except for the lowest intensity. A white LED and a stabilized current source were used as light source. The maximum illumination intensity was equivalent to about 1.2 suns and reduced by neutral density filters (large spheres). Intermediate intensities were achieved by down scaling the LED drive current (small dots). For clarity only a subset of intensities and temperatures is shown.

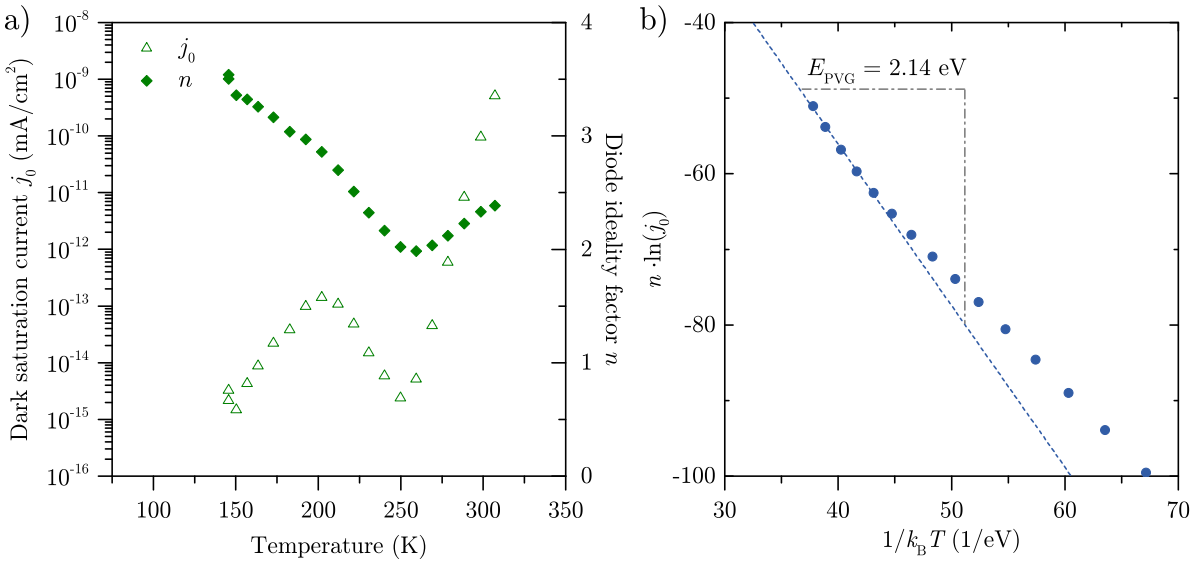

Figure 5.50: Combined intensity and temperature dependent analysis of a 6T(HT)/DIP planar heterojunction solar cell. (a) Graphical summary of the parameters n and j_0 obtained form the fit results in Figure 5.49 (c). The temperature dependent analysis of these parameters ($n \ln(j_0)$ vs. $1/k_B T$) yields a photovoltaic gap of 2.14 eV as shown in (b).

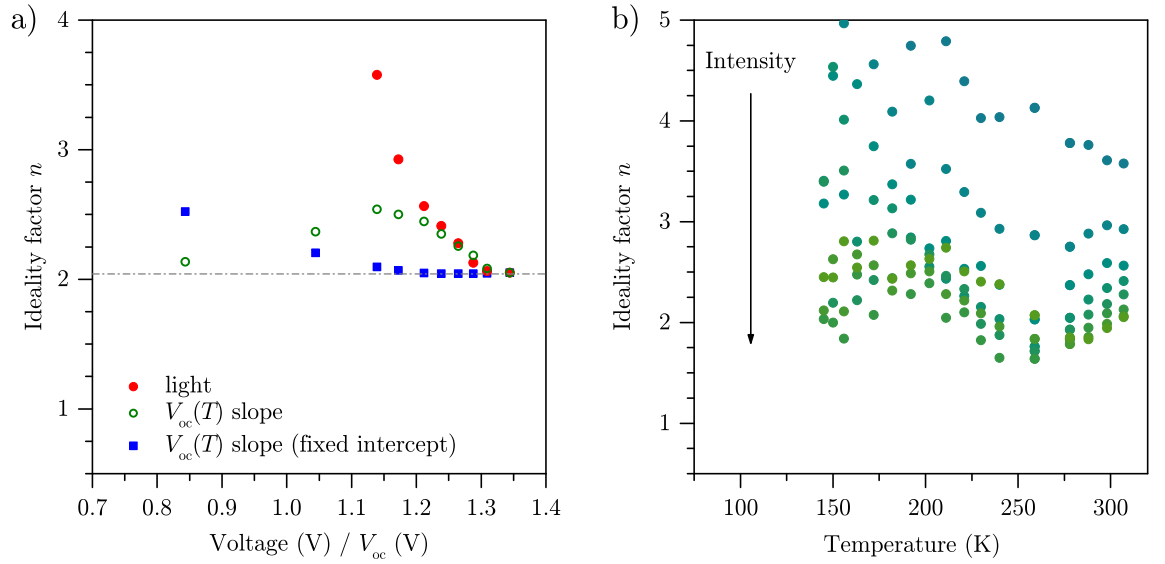

Figure 5.51: (a) Differentially determined ideality factor of a 6T(HT)/DIP planar-mixed heterojunction device (red) and ideality factors determined from the slope of the temperature dependence of V_{oc} according to Eq. 5.5 for free (green) and fixed intercept (blue). (b) Temperature dependence of the light ideality factor at different illumination intensities.

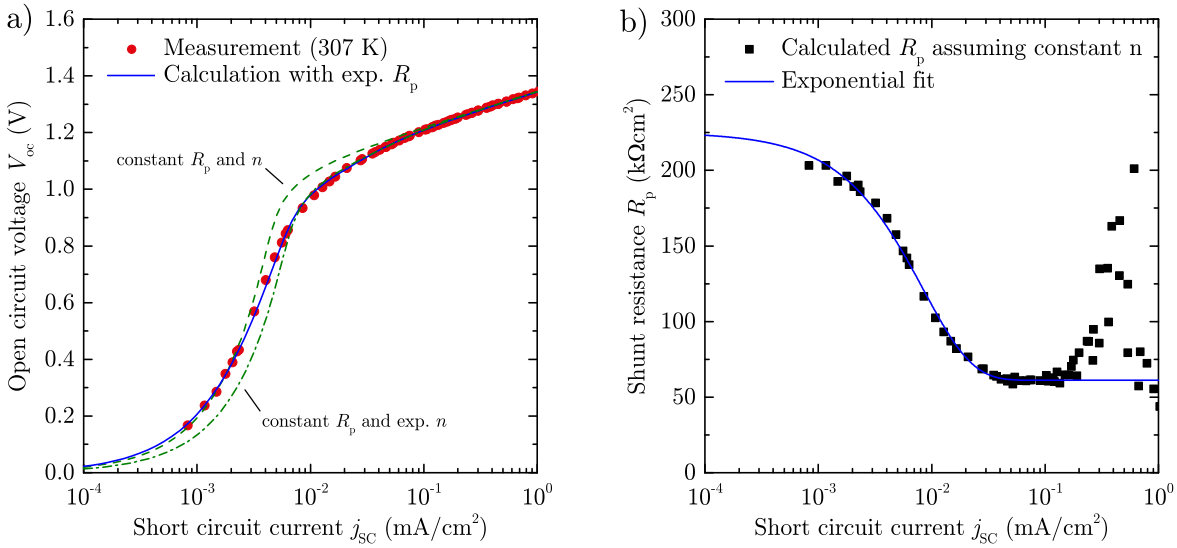

Figure 5.52: Dependence of the open circuit voltage of the 6T(HT)/DIP solar cell on light intensity for the highest measured temperature (a). The complete data set can only be described if an intensity dependent shunt resistance is taken into account following an exponential decay law (b).

illustrated in Figure 5.52. However, for a perfect match an intensity dependent shunt resistance has to be taken into account. This was first calculated from the measured data under the assumption of a constant ideality factor of 2.05 and a negligible series resistance using the Shockley equation. The resulting behavior was extracted by an exponential fit as shown in Figure 5.52 (b) and then used for the calculation of the blue curve in Figure 5.52 (a). It is important to note that a fit of the V_{oc} vs. j_{sc} data could not be achieved with a constant but free parallel resistance even if an intensity dependent ideality factor was used. Further note that regardless of the exact dependence of n on illumination intensity, a description of the data can only be achieved if the ideality factor increases, which would necessarily require values significantly exceeding two. The physical relevance of such values is questionable at best.

It is important to stress, that the saturation of the ideality factor at the two highest light intensities indicates that the influence of R_p is negligible and thus that the extraction of E_{PVG} from the linear extrapolation of the temperature dependent open circuit voltage is reliable. In particular this means that the larger photovoltaic gap with respect to the intermolecular gap found for this cell cannot be regarded as an artifact caused by the leakage current. Further note that in order to increase the reliability of the linear extrapolation, the number of data points was significantly increased for the measurements shown in Figure 5.20 (Section 5.2.3) by continuously recording the open circuit voltage and the sample temperature during the cooling process instead of targeting specific temperatures. However, this procedure is not suitable to perform intensity dependent measurements, where a stable temperature is required.

Table 5.3: Subset of parameters extracted from the measurements and fits presented in Section 5.3.1. Within this table E_{PVG} explicitly denotes the photovoltaic gap extracted from the temperature dependence of V_{oc} at the highest illumination intensity. $E_{\mathrm{act}}^{\mathrm{L}}$ and $E_{\mathrm{act}}^{\mathrm{D}}$ denote the photovoltaic gap determined as the activation energy of the dark saturation current extracted from fits to the intensity dependent V_{oc} and the dark j-V curves, respectively.

a)

	measured			
	Cell temperature T (K)	equivalent intensity (suns)	V_{oc} (V)	j_{sc} (mA/cm^2)
DIP/C_{60}	296	0.53	0.90	1.93
6T(RT)/C_{60}	298	1.43	0.44	3.58
6T(HT)/C_{60}	298	1.49	0.40	3.68
6T(RT)/DIP	298	1.07	1.23	1.45
6T(HT)/DIP	299	1.22	1.38	0.98
DIP:C_{60} (PMX)	296	0.52	0.88	2.76

b)

	fit results						literature	
	E_{PVG} (eV)	$E_{\mathrm{act}}^{\mathrm{L}}$ (eV)	$n\ln(j_{00})$[a,b]	$E_{\mathrm{act}}^{\mathrm{D}}$ (eV)	j_0[b] (mA/cm^2)	n[b]	$E_{\mathrm{act}}^{\mathrm{D}}$ [67] (eV)	$E_{\mathrm{D/A}}$ [63] (eV)
DIP/C_{60}	1.39	1.43	21.7	1.56	2.1×10^{-12}	1.29	1.46	1.4
6T(RT)/C_{60}	0.96	0.97	22.3	1.08	6.7×10^{-5}	1.57	0.95	0.95
6T(HT)/C_{60}	0.96	0.99	25.0	1.13	2.5×10^{-4}	1.61		0.95
6T(RT)/DIP	1.86	1.82	23.2		7.3×10^{-12}	1.85	2.03	1.8
6T(HT)/DIP	2.07	2.14	29.4		9.6×10^{-11}	2.33	2.1	1.8
DIP:C_{60} (PMX)	1.40	1.46	24.5		1.6×10^{-8}	1.83		

c)

	derived parameters					
	V_{oc} [c] @ 1 sun, T=300 K (V)	n[d]	j_{00} [e] (mA/cm^2)	$E_{\mathrm{PVG}} - qV_{\mathrm{oc}}$ @ 1 sun, T=300 K (eV)	$n\ln(j_{00})$	j_0[f] (mA/cm^2)
DIP/C_{60}	0.91	1.04	1.80×10^{8}	0.48	19.8	3.1×10^{-15}
6T(RT)/C_{60}	0.42	1.55	1.51×10^{6}	0.53	22.1	5.4×10^{-5}
6T(HT)/C_{60}	0.38	1.59	3.71×10^{6}	0.58	24.1	2.0×10^{-4}
6T(RT)/DIP	1.22	1.72	2.25×10^{6}	0.64	25.2	1.1×10^{-12}
6T(HT)/DIP	1.35	1.94	1.25×10^{6}	0.72	27.3	1.4×10^{-12}
DIP:C_{60} (PMX)	0.90	1.62	8.74×10^{5}	0.50	22.2	1.9×10^{-9}

[a]Extracted from the $n\ln(j_0)$ vs. $1/k_{\mathrm{B}}T$ fit. [b]Determined from fits to the intensity dependent open circuit voltage. [c]V_{oc} was calculated by Eq. 2.23 using the parameters from table (c) and linearly scaling j_{sc} to one sun. [d]Differentially determined light ideality factor at the highest measured intensity. [e]Determined from the slope of the temperature dependence of V_{oc} at the highest measured intensity. [f]Calculated with Eq. 2.22 using the parameters from table (c) and E_{PVG} from (b).

5.3.5 Absolute energy loss at V_{oc}

The most important parameters obtained from the above analysis of the different solar cell devices are summarized in Table 5.3. Overall a good agreement was found between the photovoltaic gap determined from the temperature dependence of the open circuit voltage and the photovoltaic gap extracted as the activation energy of the dark saturation current. The latter was obtained from fits of the intensity dependence of V_{oc} for a series of temperatures (E_{act}^{L} in Table 5.3). These quantities have also been found to be in good agreement with the intermolecular energy gap $E_{D/A}$ found by UPS and reported in the literature[63] except for the 6T(HT)/DIP cell, which was discussed in detail in Section 5.2.3. Where available, the photovoltaic gap determined from the temperature dependent analysis of the j-V curve in the dark (E_{act}^{D} in Table 5.3) was slightly larger compared to the other methods. Literature values reported by Dr. Julia Kraus yield a closer match with the other methods.[67] This is ascribed to the extension of the measurement towards higher temperatures where the influence of the series resistance on the separation of the parameters is expected to be less significant.

The consistency of the extracted values shows that all three methods are suitable to extract the energy of the photovoltaic gap directly from respective device as long as the influence of the parasitic resistances is negligible. For the linear extrapolation of the temperature dependence of V_{oc} this means that the light intensity has to be large enough to outrange the influence of the parallel resistance. This was achieved for all investigated solar cells but cannot necessarily *a priori* be taken for granted, especially if the device yields a low short circuit current.

In accordance with what was pointed out by Kirchartz *et al.*,[187] a reasonable interpretation of the ideality factor was only possible if n was determined differentially from the intensity dependence of the open circuit voltage. Fits across a voltage range yield average values for the ideality factor and are not suitable to identify the prevailing recombination mechanism. Even for the differential ideality factor a value that seems reliable could only be obtained for the highest illumination intensities. With decreasing intensity a slight, and possibly reasonable increase of n was observed for some cells, while a severe impact of the leakage current has been observed for others. An attempt was made to remove this effect by deriving the ideality factor from the slope of the temperature dependence of the open circuit voltage. The result of this procedure seems to be plausible in most cases but can only be regarded as a trend. In order to get a decent picture of the charge recombination a more direct method has to be chosen to study the internal processes. This can for example be achieved by different types of transient current methods.[198–200]

Even if the exact details of the recombination mechanisms in the presented cells cannot be revealed, deeper insight on the energy loss can be gained from the obtained results. As presented in Section 2.5.3 the open circuit voltage is ultimately limited by the respective photovoltaic gap E_{PVG} but reduced by recombination losses at finite temperature. This was expressed by Eq. 2.23 which can be written in the form

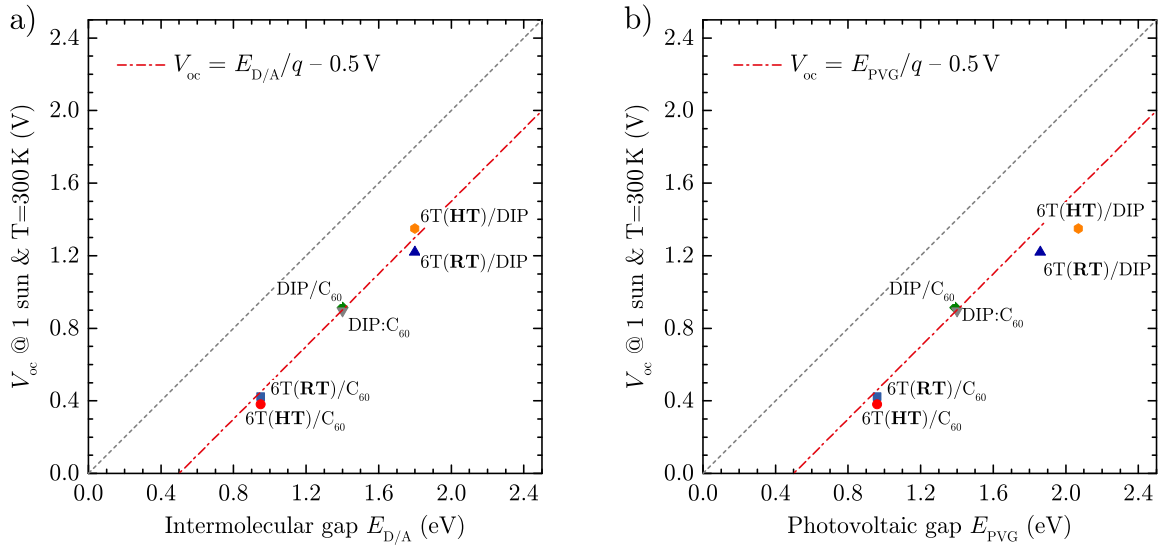

Figure 5.53: Open circuit voltage of the investigated solar cells in relation to the intermolecular donor/acceptor gap determined by UPS[63] (a) and to the photovoltaic gap extracted from the temperature dependence of the open circuit voltage (b). The red line indicates an energy loss of 0.5 eV typically reported in the literature, the gray line marks a one to one correspondence. Both are provided as a guide to the eye. For better comparability the open circuit voltage was adjusted to correspond to an illumination intensity of one sun and a cell temperature of 300 K.

$$qV_{oc} = E_{PVG} - \underbrace{nk_BT\ln(j_{00})}_{\text{loss}} + \underbrace{nk_BT\ln(j_{sc})}_{\text{compensation}}. \tag{5.8}$$

For further quantification of the energy losses in the investigated devices the open circuit voltage has been scaled to equal conditions for all solar cells. By applying Eq. 2.23 and the experimentally determined parameters, V_{oc} values corresponding to an illumination intensity of one sun and a cell temperature of 300 K have been derived (cf. Table 5.3 (c)).

In Figure 5.53 (a) this adjusted open circuit voltage is plotted against the intermolecular donor/acceptor gap $E_{D/A}$ determined by PES.[63] The empirically found rule of thumb that at V_{oc} about half a volt is lost compared to $E_{D/A}/q$ is clearly confirmed as indicated by the red line.[59,63,64]

Figure 5.53 (b) shows the same V_{oc} data plotted against the photovoltaic gap E_{PVG} extracted from the linear extrapolation of the temperature dependent V_{oc} measurement. Here a distinctly larger loss is found for both 6T/DIP solar cells which is attributed to recombination via the DIP singlet, which provides an additional loss channel as described in detail in Section 5.2.3.

The absolute loss with respect to the photovoltaic gap E_{PVG} is shown in Figure 5.54. The energy loss term $nk_BT\ln(j_{00})$, derived from the linear slope of the $V_{oc}(T)$ dependence, and its individual components n and j_{00} are plotted against the absolute energy loss $E_{PVG} - qV_{oc}$ at $T = 300$ K and one sun. The discrepancy between the loss term and

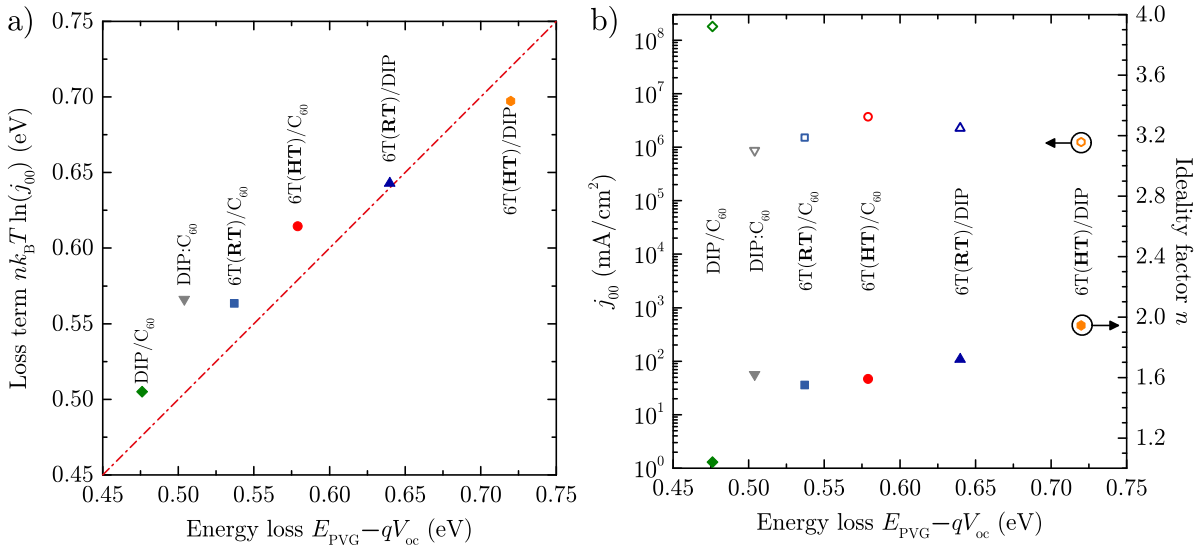

Figure 5.54: Experimentally determined energy loss term $nk_BT\ln(j_{00})$ (a) and its individual components (b) plotted versus the observed energy loss at V_{oc} at an intensity of one sun and a cell temperature of 300 K.

the actual energy loss in Figure 5.54 (a) is due to photocurrent current, which compensates a part of the loss but is not accounted for in the graph (cf. Eq. 5.8). The loss term $nk_BT\ln(j_{00})$ may hence be considered as an intrinsic loss of the cell at a given temperature. This pure loss is smallest for the DIP/C_{60} planar heterojunction and it is clearly visible that, despite their similar open circuit voltages and energy gaps, the intrinsic loss is significantly larger for the DIP:C_{60} planar-mixed heterojunction as expected from the blend morphology. The largest losses are found for the 6T/DIP solar cells. A counter intuitive peculiarity is the observation that the loss term of the 6T(HT)/DIP device falls below the one-to-one correspondence marked by the red line, which would imply that the loss is increased by the photocurrent. It is unclear what causes this effect but it is likely that it is related to the discrepancy between the photovoltaic gap and the intermolecular gap. A tentative guess could be that because of the low intermolecular coupling, the charge generation is bias dependent. In this case, the internal photocurrent in open circuit would be different from the photocurrent under short circuit conditions. Nevertheless, the results of the other devices appear reasonable.

In order to identify the cause of the different intrinsic losses of the investigated cells, it is instructive to consider the individual components n and j_{00} of the loss term. Figure 5.54 (b) indicates that the absolute energy loss follows the trend of the ideality factor but seems inversely to j_{00}. This is counter intuitive since j_{00} is typically expected to be a measure of the coupling and the recombination loss in turn is expected to scale with the coupling.[57,201,202] A possible explanation could be the following scenario: $n > 1$ is a sign of trap assisted recombination which is typically regarded as a non-radiative process.[65] For efficient recombination of free electrons and free holes two requirements are necessary. Free carriers have to be abundant and the direct recombination process needs

to be efficient. An intuitive consequence of the latter could be that the intermolecular coupling has to be sufficiently large to assist direct bimolecular recombination. Hence, insufficient coupling could force alternative recombination mechanisms and thus result in high ideality factors.

A possible pathway out of this dilemma could be a purposeful engineering of the ideality factor towards unity as a first step. This might be achieved through the reduction of disorder (tail states) and deep traps to weaken the competitiveness of the corresponding processes. At the same time it is mandatory to at least maintain the charge carrier density in order to push the dominant recombination mechanism towards direct recombination of free carriers. A material requirement is thus that the absorber (unlike 6T or DIP) may not lose its absorption strength with increased order.

Once an ideality factor of unity is achieved, j_{00} may be adjusted by changing the intermolecular coupling e.g. by morphological changes,[160] by the addition of side groups to the molecules acting as steric spacers[203] or by the introduction of a thin buffer layer at the interface.[204] Obviously, there appears to be an interdependence of the dominating recombination mechanism and the strength of the intermolecular coupling. Hence, one would expect that an optimum situation exists, where the coupling is large enough to allow efficient charge carrier generation and to sustain an ideality factor governed by direct recombination of free charge carriers but low enough to minimize any additional recombination losses.

5.4 Ternary cascading planar heterojunction solar cells

As mentioned above, an attempt can be made to reduce the recombination at the donor/acceptor interface by the deliberate introduction of a thin buffer layer between the two materials. Ideally, a material is chosen that yields an energetic cascade with donor and acceptor. In this case even the benefit of additional and ideally complementary absorption may be exploited if a thicker layer is introduced. This approach was recently demonstrated to enable a remarkable device performance if careful engineering of the energy level alignment and thickness optimization is achieved.[205]

While not complementary in absorption, the materials 6T, DIP and C_{60} discussed throughout this work yield the required energy gradient for both HOMO and LUMO and are thus conceptually suitable for application in a ternary cascading planar heterojunction solar cell (ternary cell). Such devices have been prepared on ITO/PEDOT:PSS, where 6T was deposited at room temperature as the donor, DIP as the intermediate buffer layer and C_{60} was used as the acceptor. As for the other discussed cells the top electrode was BCP/Al. In a variation of the DIP thickness the impact of the interlayer on the device performance has been studied. For this survey the total active layer thickness was held constant at 120 nm and a constant C_{60} thickness of 60 nm was used in order to minimize the impact of internal optical interference effects. Starting from a simple 6T/C_{60} planar heterojunction without DIP, the 6T film thickness was reduced as an increasing amount of DIP was introduced.

The j-V curves of these cells under illumination and in the dark as well as a schematic drawing of the device stack are shown in Figure 5.55; for comparison the j-V curves of a 6T(HT)/C_{60} cell are shown, where the 6T film was deposited at a substrate temperature of 100 °C. The characteristic quantities of the presented cells are summarized in Table 5.4. Clearly, the open circuit voltage increases with increasing amount of DIP. Additionally, the short circuit current increases initially but then saturates. These effects have also been reported in the literature and have been ascribed to reduced recombination losses and increased charge separation efficiency caused by the energy cascade.[204,206] This is in accordance with the continuous reduction of the dark saturation current extracted from the j-V curves in the dark by a fit with the Shockley equation as well as with the increased fill factor.[207,208]

Notably, the open circuit voltage seems to have almost saturated at an interlayer thickness of 5 nm compared to the 2 nm DIP device but then increases again drastically if the DIP thickness is increased to 10 nm. This continues for even thicker DIP films and is shown in the appendix (Figure A.2). A possible explanation is a change in the role of DIP inside the device. Instead of functioning as thin buffer layer that mainly suppresses recombination, the thick DIP layer forms a new heterojunction with either of the other materials and directly contributes to the photo current. This is indicated by the incident photon to current efficiency presented in Figure 5.56: a clear contribution of the DIP film to the photo current is visible around a wavelength of 550 nm for the 10 nm thick interlayer. While there is a slight increase of the IPCE in this region also for the other ternary cells, it is difficult to tell if this can be attributed to charge carriers

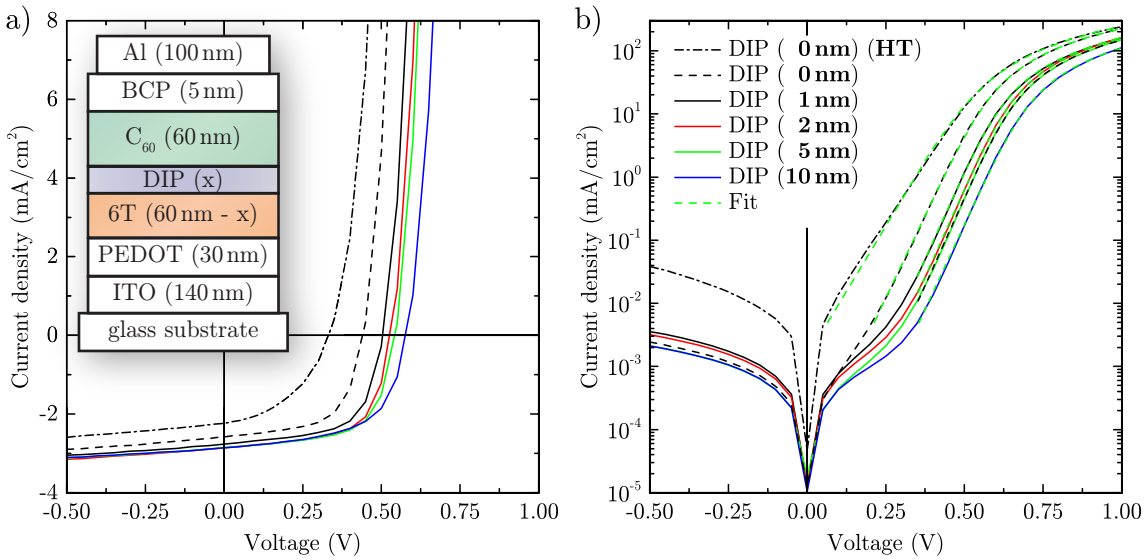

Figure 5.55: Current-voltage characteristics of ternary cascading planar heterojunction solar cell under illumination at approximately one sun (a) and in the dark (b). The layer stack is shown as an inset in (a). The thickness of the DIP buffer layer between the the donor and the acceptor was gradually increased from 0 to 10 nm which is accompanied by an increase of the open circuit voltage.

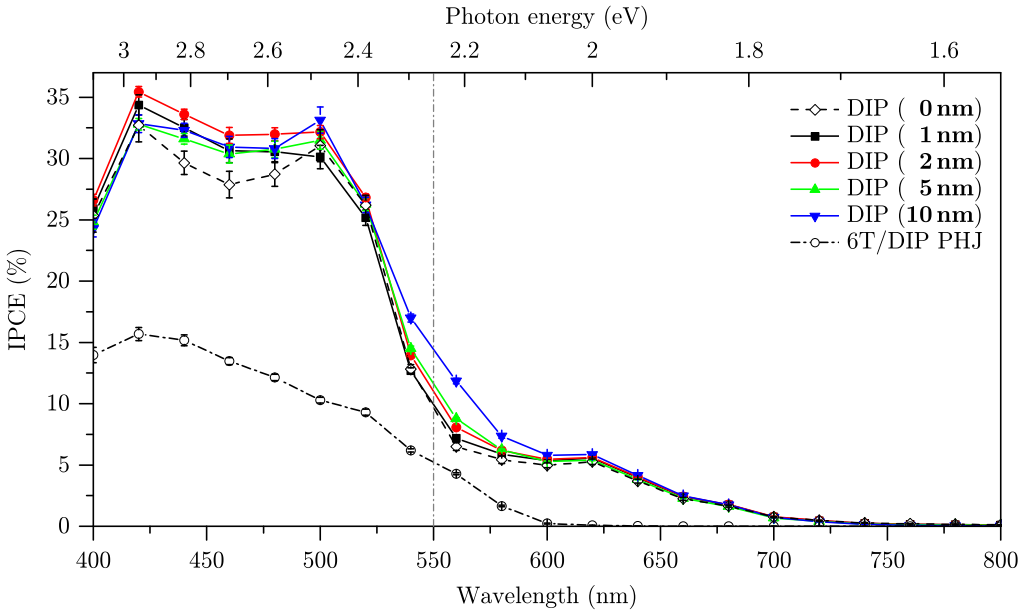

Figure 5.56: Incident photon to current efficiency (IPCE) of the investigated ternary solar cells with increasing DIP interlayer thickness. For comparison the IPCE of a 6T/C_{60} (DIP 0 nm) and a 6T/DIP (without C_{60}) planar heterojunction solar cell are shown. The vertical line at 550 nm indicates the first absorption peak of DIP, which more or less coincides with the absorption onset of 6T (cf. Figure 5.19).

Table 5.4: Characteristic values and fit results of the ternary solar cell devices presented in Figure 5.55. The values of j_{sc}, V_{oc}, the fill factor (FF) and the power conversion efficiency (PCE) are extracted from the j-V characteristics under illumination. Series resistance R_s, ideality factor n and dark saturation current j_0 are extracted by a fit to the dark characteristics with the Shockley equation. V_{oc} (calc) was calculated from j_{sc}, j_0 and n by Eq. 2.8 using $kT = 0.025\,\text{eV}$.

DIP thickness	j_{sc} (mA/cm^2)	V_{oc} (V)	FF (%)	PCE (%)	R_s (Ωcm^2)	n	j_0 (mA/cm^2)	V_{oc} (calc.) (V)
0 nm 6T(HT)	2.23	0.33	43	0.31	1.5	2.14	2.21×10^{-3}	0.37
0 nm	2.58	0.44	61	0.67	1.5	1.61	2.93×10^{-5}	0.46
1 nm	2.76	0.50	63	0.81	1.9	1.51	3.28×10^{-6}	0.52
2 nm	2.86	0.53	63	0.89	1.8	1.51	1.72×10^{-6}	0.54
5 nm	2.85	0.54	63	0.91	1.9	1.50	1.23×10^{-6}	0.55
10 nm	2.86	0.58	60	0.93	2.2	1.56	7.22×10^{-7}	0.59

stemming from absorption inside the thin DIP layer or if this effect has to be attributed to an overall enhanced charge generation efficiency postulated for thin interlayers.[206]

For such a device reduced recombination seems to be an over-simplified explanation for the increased open circuit voltage. As a matter of fact, for thick DIP interlayers, the 6T/C_{60} junction vanishes and hence CT recombination between 6T and C_{60} becomes impossible. Instead this loss channel is expected to be replaced by at least three new, concurring recombination pathways: (1) CT recombination at the 6T/DIP interface, (2) CT recombination at the DIP/C_{60} interface as well as (3) recombination of free electrons stemming from the 6T/DIP heterojunction with free holes stemming from the DIP/C_{60} subcell inside the DIP layer. Since the originally main channel becomes disabled, this implies that the 6T/C_{60} donor-acceptor energy gap loses its relevance as the photovoltaic gap. On the other hand, V_{oc}, defined as the splitting of the electron and hole quasi-Fermi levels, is still expected to be determined by the HOMO and LUMO energies of the embracing 6T and C_{60} layers.

Unfortunately, it seems therefore neither straightforward to understand the physical meaning nor to predict the energy of the photovoltaic gap of a ternary cell. In accordance with the considerations presented earlier in Section 2.5, it appears reasonable that the photovoltaic gap is determined by the dominant recombination process and might change with temperature. The situation becomes significantly more complex if the recombination mechanisms are similarly efficient or if the interlayer is not fully closed. Under such circumstances any of the presented methods to determine E_{PVG} from the device is expected to yield an effective value rather than an energy corresponding to a real physical transition.

Apparently, this effect is indeed observed for the investigated solar cells and the temperature dependence of the open circuit voltage is presented in Figure 5.57 (see even Figure A.3 in the appendix). However, since the intercept of the linear extrapolation of V_{oc} to 0 K depends on the light intensity and does not saturate for any of the investigated cells, there is a remaining doubt if this observation is caused by a change of the effective

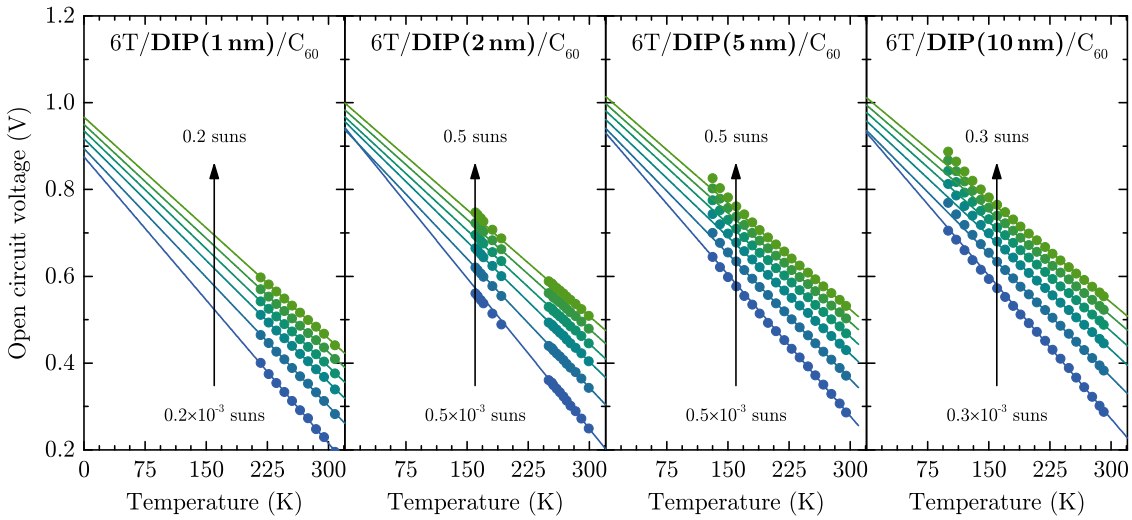

Figure 5.57: Temperature dependent open circuit voltage of ternary solar cells with 1 nm, 2 nm, 5 nm and 10 nm DIP interlayer thickness. Approximate estimates of the highest and lowest equivalent light intensity are given in the respective graphs. A white LED and a stabilized current source have been used as light source for the 1 nm DIP cell. A solar simulator was used in all other cases. For clarity only a subset of intensities is shown.1

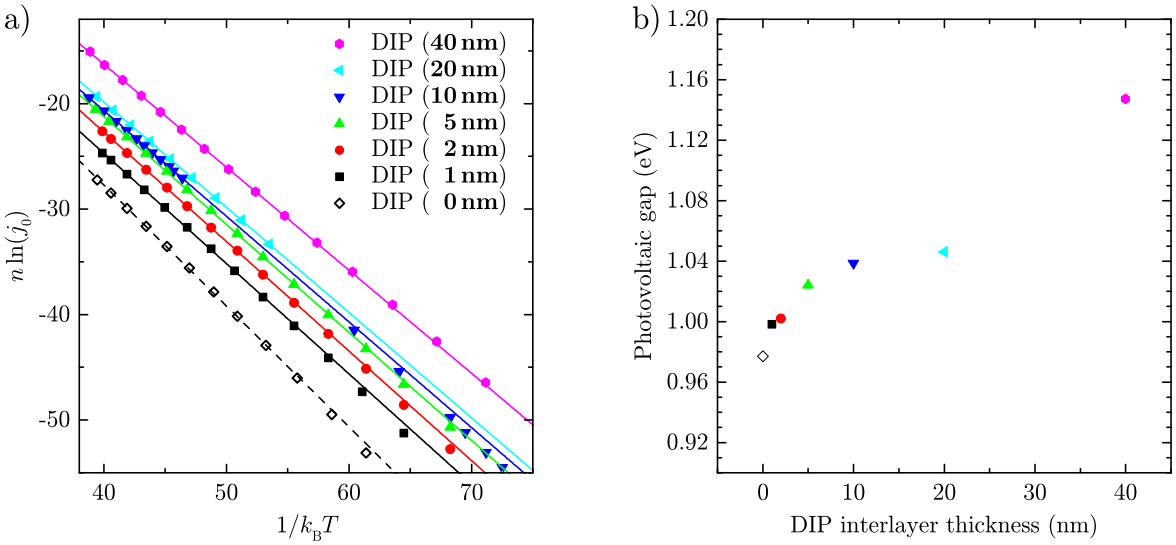

Figure 5.58: Dependence of the photovoltaic gap on the DIP interlayer thickness extracted from the $n\ln(j_0)$ vs. $1/k_\mathrm{B}T$ slope. The corresponding fits to the intensity dependence of the open circuit voltage can be found in the appendix.

photovoltaic gap as postulated above or if it is an artifact caused by the presence of differently filled band tails.

It might thus be helpful to extract E_{PVG} as the activation energy of the dark saturation current. The required n and j_0 values are extracted from a fit of the intensity dependent open circuit voltage and may thus be considered as an average over different light intensities. The result of this procedure is presented in Figure 5.58 and seems to confirm the presence of a changing effective photovoltaic gap with increasing DIP thickness. While a trend is present, the absolute change is small and within the estimated error of the method of about $\pm 0.03\,\mathrm{eV}$. Only for a DIP thickness of 40 nm the result is clear and a significant change of the effective gap is observed. (For this cell also the temperature dependent V_{oc} yields a significantly increased E_{PVG}. For details see Appendix A.2.)

These findings confirm that the increase of the open circuit voltage observed in ternary cells, compared to their planar heterojunction counterpart cannot solely be attributed to reduced recombination losses but are, at least for thick interlayers, partially caused by an increased effective photovoltaic gap. A similar observation has recently been reported for ternary blends in bulk heterojunction solar cells.[209]

An expected consequence of the proposed change of the recombination pathways would be an effective photovoltaic gap, that depends on the spectrum of the light source. A spectrum that favors the generation of charge carriers in one subcell but not in the other would obviously change the relative contribution of the two junctions at V_{oc} and strengthen the role of the corresponding energy gap. An interesting way to further test this hypothesis would be to determine E_{PVG}, if only a single material is excited by the incident light. In the present case this is only possible with C_{60} at the long wavelength end of the IPCE because of the spectral overlap of all three materials at higher energies. Under such circumstances, it is anticipated that only the DIP/C_{60} junction generates charge carriers, while the 6T/DIP subcell is inactive. The photovoltaic gap would then be expected to coincide with that of the simple DIP/C_{60} planar heterojunction. Deeper insight on the physics of ternary solar cells could be gained if suitable materials with mutually exclusive absorption spectra were available.

A side effect of the introduction of thin DIP interlayers between 6T and C_{60} is a significant increase of the device stability. Interestingly, however, this is only the case for very thin interlayers. Figure 5.59 shows j-V curves of a 6T/C_{60} planar heterojunction and ternary cells with DIP thicknesses of 1 nm, 2 nm, 5 nm and 10 nm recorded for the fresh devices and after several month of storage in inert gas (N_2) atmosphere. Both the planar heterojunction and the devices with 5 nm and 10 nm are heavily degraded after eight and ten months, respectively and the dark curves indicate that the series resistance has significantly increased.[‡] For very thin interlayers of 1 nm or 2 nm, only, the cells are in perfect shape even after more than one year of storage.

Unless systematic investigations of this phenomenon are carried out, it can only be speculated what might cause this effect. Amongst others, potential degradation

[‡]The actual degradation time is expected to be significantly shorter and on the order of a few weeks. However, this was only measured for devices with thinner 6T layers.

mechanisms are based on morphological changes such as recrystallization or internal migration of either the molecules in the active layers or the electrode materials.[210,211] One possible explanation for the stability of ternary cells with thin interlayers could then be that DIP initially forms a diffusion barrier that is seized with increasing thickness. It is imaginable that a very thin DIP film, possibly the first monolayer, grows with its molecules lying on top of the 6T film, possibly because of co-facial π stacking, as observed for other organic molecules.[212] One could then imagine that with increasing thickness the mutual interaction between DIP molecules raises the lying molecules and effectively dissolves the diffusion barrier.

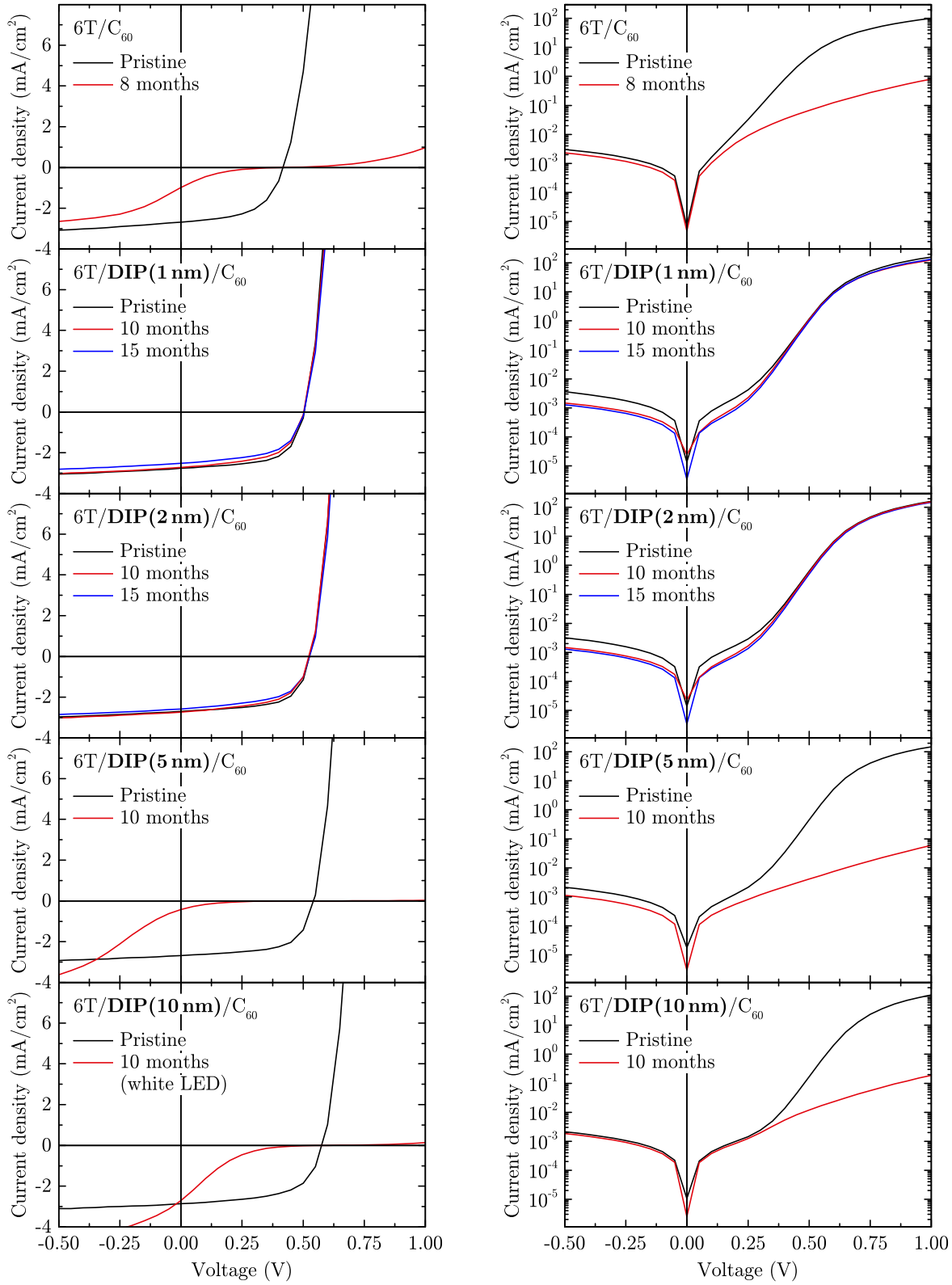

Figure 5.59: Degradation of a $6T/C_{60}$ planar heterojunction and ternary cascading $6T/DIP/C_{60}$ solar cells under storage in inert gas atmosphere. Only a very thin interlayer seems to prevent severe degradation of the device.

Chapter 6

Conclusion and outlook

Organic solar cells are a promising technology in the emerging field of renewable energies and enable potentially cheap harvesting of solar energy. Significant knowledge about the elementary processes in organic photovoltaic cells has been gained in recent years by the collaborative work of researchers around the world. The present work contributes with a special focus on the open circuit voltage of planar heterojunction solar cells and how it is influenced by the film morphology of the active layer materials.

Diindenoperylene (DIP) was introduced as a non-fullerene acceptor in combination with α-sexithiophene (6T) yielding extraordinarily high open circuit voltages for single junctions between 1.2 V and almost 1.4 V and closely approaches what is considered the maximum possible V_{oc} for a material system in combination with poly 3-hexylthiophene (P3HT). While neither these cells nor planar heterojunctions of 6T and the fullerene C_{60} yield particularly high power conversion efficiencies, they are highly interesting academically and well suited to study the effect of morphology on the open circuit voltage. The intrinsically different shape of the rod like DIP molecules and the spherical C_{60} enables insight on the influence of molecular orientation.

Morphological investigations revealed that the crystallinity of 6T grown on PEDOT:PSS is influenced by the growth conditions and in particular by the substrate temperature. While crystallites of both standing and lying 6T domains are present if the film is grown at room temperature, the lying 6T crystallites vanish completely and the size of the standing domains increases if the substrate is heated to 100 °C. These two growth conditions of the 6T film, and only the 6T film, are denoted as room temperature (RT) and high temperature (HT) 6T throughout this work. The different 6T morphologies clearly template the subsequent growth of the acceptor layer: The crystallinity of the C_{60} film becomes remarkably high and the lying DIP virtually vanishes.

From a device perspective the different morphologies result in distinct changes of the open circuit voltage. In the case of 6T/C_{60} heterojunctions a significant reduction of V_{oc} was observed if 6T is grown at a substrate temperature of 100 °C. While this

can unambiguously be attributed to increased recombination losses their exact cause is less clear. Different possible arguments have been proposed, including the oppositely directed interface dipoles found by UPS for the two heterojunctions as well as increased electronic coupling at the donor/acceptor interface, which may potentially be caused by the reduction of structural disorder. Even a combination of effects seems reasonable but unfortunately this remains an open question.

For the 6T/DIP devices the V_{oc} shift is in the opposite direction and the open circuit voltage is increased by the morphology that is induced by the high temperature 6T growth. Strikingly, it was found that the absolute loss becomes even larger for this solar cell. Instead, temperature dependent device characterization indicates different photovoltaic energy gaps E_{PVG} for the room temperature and the high temperature prepared device. Opposed to these findings, the intermolecular donor/acceptor energy gap remains unchanged as was shown by UPS measurements. It was hence concluded that the optical gap of DIP is extracted as the photovoltaic gap of the 6T(HT)/DIP device.

In order to explain this unprecedented observation, a modification of the Shockley-Queisser theory for organic heterojunctions, which was previously reported in the literature,[53] has been reconsidered with a special focus on constellations where a linear extrapolation of the predicted open circuit voltage would indeed result in the optical gap of the absorber rather than in the intermolecular charge transfer energy gap. A temperature dependent competition between the recombination via the CT gap and the optical gap of the absorber has been identified as the culprit. The concept of a transition temperature T_{tr} was introduced above which recombination is dominated by the optical gap and below which CT recombination prevails. It was shown that this transition temperature scales with the energy offset between optical and charge transfer gap $\Delta E = E_{opt} - E_{CT}$ and the absorption strength of the CT state. In non-ideal devices T_{tr} is additionally expected to be strongly influenced by the ideality factor. Noteworthy, activation of singlet emission from polymer blends for low energy offsets ΔE has recently been reported in the literature.[170]

Within this framework the extraction of the intermolecular gap ($E_{PVG} = E_{D/A}$) for the room temperature prepared 6T(RT)/DIP solar cell but the optical gap of DIP ($E_{PVG} = E_{opt}$) for 6T(HT)/DIP from the temperature dependence of the open circuit voltage can be explained by a strongly reduced transition temperature for the HT device, below the operating temperature of the solar cell. This was attributed to significantly reduced intermolecular electronic coupling of 6T and DIP in standing/standing configuration in addition to the already small offset ΔE for this system. A remarkable result, considering that usually T_{tr} is higher than the operating temperature of the solar cell as implied by the identification of the photovoltaic gap with the CT energy for virtually all organic solar cells reported in the literature. This demonstrates that recombination via the optical gap of the absorber, which has only been predicted for extreme parameters affecting the electronic coupling, may actually become relevant in real world devices.

Additionally, a combined temperature and intensity dependent analysis of these 6T based cells and DIP/C_{60} devices was carried out. Methodologically, it was confirmed

that both the linear extrapolation of the temperature dependent open circuit voltage to 0 K as well as the slope of the temperature dependence of the dark saturation current are suitable to extract the photovoltaic gap directly from the device. For the latter it is principally irrelevant if the necessary parameters were extracted from the intensity dependence of the open circuit voltage or form the j-V curve of the device in the dark, as long as the measurement extends far enough into the high temperature range. Similarly, the linear extrapolation of the open circuit voltage was found to yield reliable results only, if the illumination intensity is large enough to outweigh the influence of a finite shunt resistance which may result in over- or underestimated values, depending on how severe its influence is. While this aspect appears to be generally ignored, it was found to be relevant for solar cells with low dark saturation current and is thus expected to affect solar cells with large photovoltaic gaps. It is hence advisable to cross-check the result at more than a single intensity.

More drastically, the influence of the parallel resistance on the ideality factor was confirmed to be severe and the extraction of reliable values for the ideality factor was found to be non-trivial. Opposed to the, at least until recently, widespread habit to interpret the ideality factor as extracted from a fit to dark j-V curve or to the intensity dependence of V_{oc} in terms of the prevailing recombination mechanism, it was clearly confirmed that this quantity has to be regarded as an average over a wide voltage range and does not allow such conclusions. Only a careful consideration of the differentially determined light ideality factor may potentially be regarded as a sign of the recombination mechanism at the respective voltage, if a residual contribution stemming from the leakage current can be excluded. Judging from this method, direct, bimolecular recombination of free charge carriers was only found to be the dominating recombination mechanism in the DIP/C_{60} planar heterojunction cell. For all other investigated cells a significant amount of trap assisted recombination seems to be present. Nevertheless, a more direct investigation of the recombination processes in these cells would be enlightening.

For 6T/C_{60} solar cells the photovoltaic gap extracted from the temperature dependence of the open circuit voltage was found to depend on the light intensity. This behavior was reconstructed by accounting for recombination of mobile charges with oppositely charged carriers trapped at the quasi-Fermi level within the band tail. In agreement with the extracted ideality factor this particular kind of trap assisted recombination via tail states is thus identified as a possible cause for an intensity dependent photovoltaic gap and corresponds to a gradual filling of the tail states with increasing light intensity.

The absolute energy loss at V_{oc} with respect to the intermolecular donor/acceptor gap determined by means of photoelectron spectroscopy was found to be in agreement with the typically reported value of half an electron volt at room temperature. However, with respect to the photovoltaic gap extracted directly from the device, the loss is larger for most cells. This is especially indicated by the raw loss term $n \ln(j_{00})$ that is not compensated by the photo current. Further analysis of its components n and j_{00} has shown that the observed additional loss is mostly governed by the ideality factor and

not by j_{00}, which is usually considered to account for the intermolecular coupling. A reduction of the ideality factor by reducing the amount of disorder and avoiding traps was thus suggested as a first goal to minimize non-radiative recombination losses. It was furthermore proposed that the ideality factor and j_{00} are not fully independent of each other but that insufficient intermolecular coupling will force alternative recombination channels such as trap assisted recombination and hence potentially lead to an increased ideality factor.

Finally, ternary cascading planar heterojunction solar cells, comprising 6T, DIP and C_{60} in the active layer have been analyzed. A continuous increase of the open circuit voltage with increasing amount of DIP was found and a reduction of the recombination losses upon the introduction of thin DIP layers between 6T and C_{60} was confirmed. Yet, it was proposed that the effective photovoltaic energy gap increases with thicker interlayers as the role of DIP changes and forms new heterojunctions with the surrounding materials. This seems to be confirmed by comparison of the results of combined intensity and temperature dependent analysis measurements of these cells. The exact physical meaning of the extracted values, however, poses an open question. An interesting observation is the impact of the DIP interlayer on the device stability, which is significantly enhanced by thin DIP films of less than 5 nm but not for larger thicknesses. A morphological cause was tentatively suggested, where a thin layer of lying molecules might act as a diffusion barrier and hinder degradation. However, a detailed investigation of the degradation mechanism of these cells has not yet been performed but is inevitable in order to answer this question. This should include detailed morphological investigation of solar cells at various stages of degradation.

Future investigation should further include electro- and photoluminescence spectroscopy of 6T/DIP solar cells in order to obtain clear evidence for the proposed role of recombination via the optical gap in these devices. Furthermore, the presented considerations are expected to be relevant for other material systems in a similar manner. Examples might include heterojunctions of 6T and tetraphenyldibenzoperiflanthene (DBP), which is similar to DIP, or even DIP/DBP heterojunctions.[213,214] A similar effect may possibly also be relevant for DIP/pentacene solar cells.[67]

Also a more direct investigation of the recombination mechanisms of the investigated solar cells would be feasible in order to verify the interpretation of the differentially determined ideality factor. Working setups for charge extraction by linearly increasing voltage (CELIV) and open circuit corrected charge carrier extraction (OTRACE) have already been built in the organic semiconductors group and first field tests have successfully been performed.[215,216] In combination with the cryostat setup temperature and pump intensity dependent transient current measurements are a powerful tool to gain in-depth understanding of charge carrier recombination processes.

Additionally, full featured numerical drift-diffusion simulations would be helpful to better understand the observed intensity dependence of the 6T/C_{60} devices. While the presented naive extension of the analytical model employed could successfully reproduce the measured data, verification is necessary and the impact of other parameters should be studied. A good starting point might be the "organic photovoltaic device model" by

Roderick MacKenzie, University of Nottingham, which is available free of charge.[217,218] First simulation attempts with this software have been made but more work is required.

The results obtained in the present work yield substantial insight into the physics determining the open circuit voltage of organic heterojunction solar cells and their energy losses. New aspects are revealed and ideas presented. The careful review of established experimental methods for device characterization and the extended theoretical considerations of this work provide a solid basis and a decent framework for further investigation of recombination processes in organic solar cells. Only a conclusive, in-depth understanding of the elementary processes in organic solar cell devices gained by further research will be able to lead this promising technology to success.

Appendix A

Appendix

A.1 Indexing of X-ray scattering spectra

For elastic scattering, the scattering vector $\boldsymbol{q}$ needs to be equal to a reciprocal lattice vector $\boldsymbol{G}$.[114] A reciprocal lattice vector has the form

$$\boldsymbol{G} = h\boldsymbol{a}^* + k\boldsymbol{b}^* + l\boldsymbol{c}^*, \tag{A.1}$$

where h, k, l are the Miller indices of the corresponding lattice plane and $\boldsymbol{a}^*$, $\boldsymbol{b}^*$ and $\boldsymbol{c}^*$ are the axis vectors of the reciprocal lattice correlated with the crystal axis vectors $\boldsymbol{a}$, $\boldsymbol{b}$ and $\boldsymbol{c}$ in real space by[114]

$$\boldsymbol{a}^* = 2\pi\frac{\boldsymbol{b}\times\boldsymbol{c}}{\boldsymbol{a}\cdot\boldsymbol{b}\times\boldsymbol{c}}; \qquad \boldsymbol{b}^* = 2\pi\frac{\boldsymbol{c}\times\boldsymbol{a}}{\boldsymbol{a}\cdot\boldsymbol{b}\times\boldsymbol{c}}; \qquad \boldsymbol{c}^* = 2\pi\frac{\boldsymbol{a}\times\boldsymbol{b}}{\boldsymbol{a}\cdot\boldsymbol{b}\times\boldsymbol{c}} \tag{A.2}$$

If the unit cell parameters a, b, c and α, β, γ are known, the magnitude of the total momentum transfer can simply be calculated as the norm of the respective reciprocal lattice vector $|\boldsymbol{q}| = |\boldsymbol{G}|$. The out-of-plane momentum transfer q_z is then the z-component of $\boldsymbol{q}$ and the in-plane component of the momentum transfer is given by

$$q_{xy} = \sqrt{q_x^2 + q_y^2} \tag{A.3}$$

For the actual calculation, however, the axis vectors given by the unit cell parameters need to be transformed to the orthonormal basis of the laboratory system. A schematic drawing of the lattice axes and the laboratory coordinate system is shown in Figure A.1. Note that by choice the c-axis coincides with the x-axis and the cb-plane lies in the xy-plane. This choice directly yields

$$\boldsymbol{c} = c\hat{\boldsymbol{x}} \tag{A.4}$$

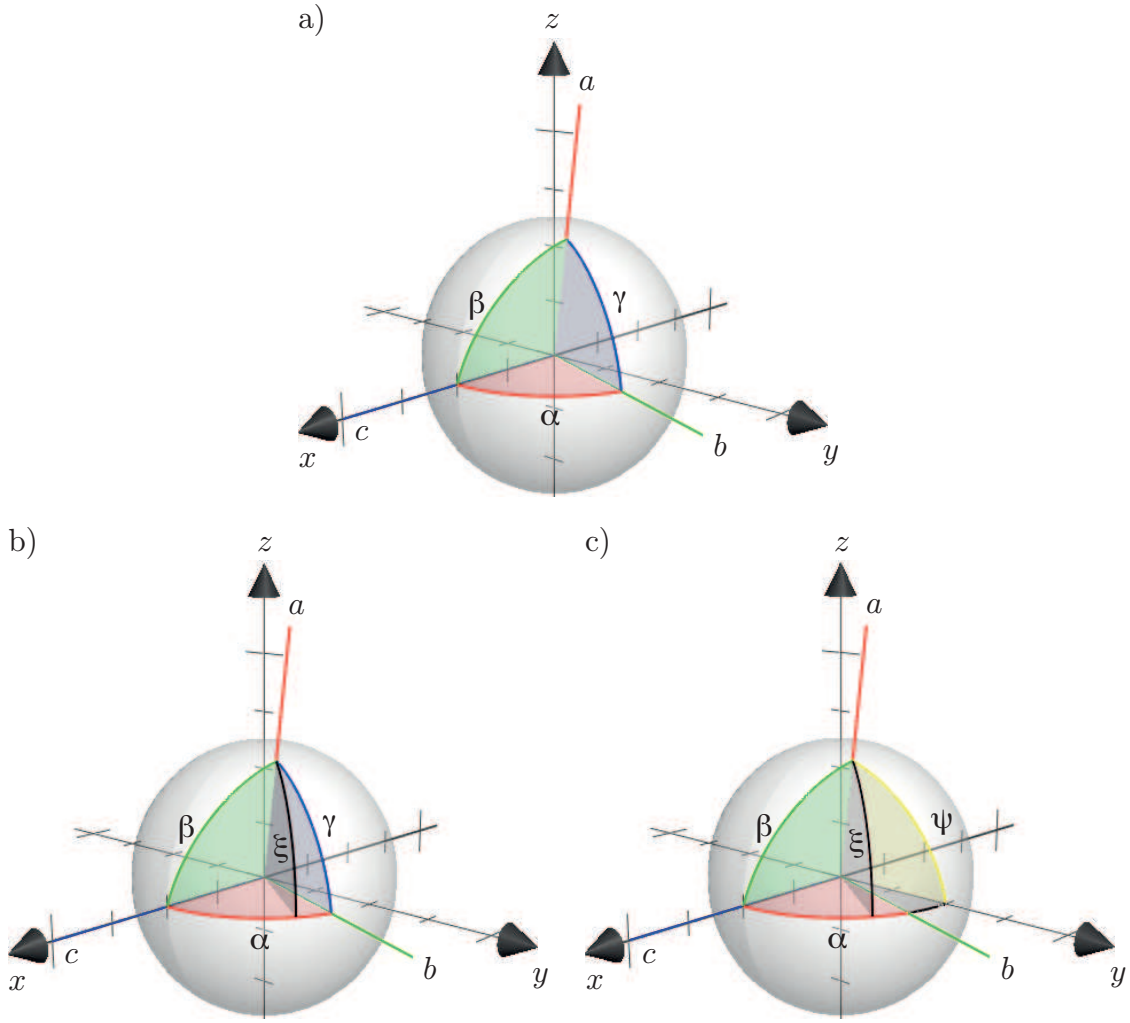

Figure A.1: Schematic drawing of the relevant angles and axes for basis transformation from the crystal to the laboratory coordinate system.

and

$$\boldsymbol{b} = b\,(\cos(\alpha)\hat{\boldsymbol{x}} + \sin(\alpha)\hat{\boldsymbol{y}}) \tag{A.5}$$

From Figure A.1 (c) it is obvious that $\boldsymbol{a}$ is given by

$$\boldsymbol{a} = a\,(\cos(\beta)\hat{\boldsymbol{x}} + \cos(\psi)\hat{\boldsymbol{y}} + \sin(\xi)\hat{\boldsymbol{z}})\,, \tag{A.6}$$

where $\hat{\boldsymbol{x}}$, $\hat{\boldsymbol{y}}$ and $\hat{\boldsymbol{z}}$ are the basis vectors in x, y and z direction. The angles ξ and ψ can be calculated by applying spherical trigonometry. Let C denote the angle between β and α on the unit sphere (cf. Figure A.1 (a)). Then with the cosine rule for spherical triangles[219] $\cos(C)$ can be expressed as

$$\cos(C) = \frac{\cos(\gamma) - \cos(\alpha)\cos(\beta)}{\sin(\alpha)\sin(\beta)} \tag{A.7}$$

Hence, with the sine rule for spherical triangles[219] and an angle of 90° between ξ and α (i.e. the xy-plane) we receive

$$\begin{aligned}\sin(\xi) &= \sin(\beta)\sin(C) = \sin(\beta)\sqrt{1-\cos^2(C)} \\ &= \frac{1}{\sin(\alpha)}\sqrt{\sin^2(\alpha)-\cos^2(\beta)-\cos^2(\gamma)+2\cos(\alpha)\cos(\beta)\cos(\gamma)}\end{aligned} \tag{A.8}$$

Similarly, with an angle of 90° between the c and the y axis (see Figure A.1 (c)) and Eq. A.7 we get

$$\begin{aligned}\cos(\psi) &= \cos(\beta)\cos(90)+\sin(\beta)\sin(90)\cos(C) = \sin(\beta)\cos(C) \\ &= \frac{\cos(\gamma)-\cos(\beta)\cos(\alpha)}{\sin(\alpha)}\end{aligned} \tag{A.9}$$

Note that this method of calculating the momentum transfer does not account for structure or form factor forbidden peaks in the X-ray scattering data.

A.2 Ternary solar cells

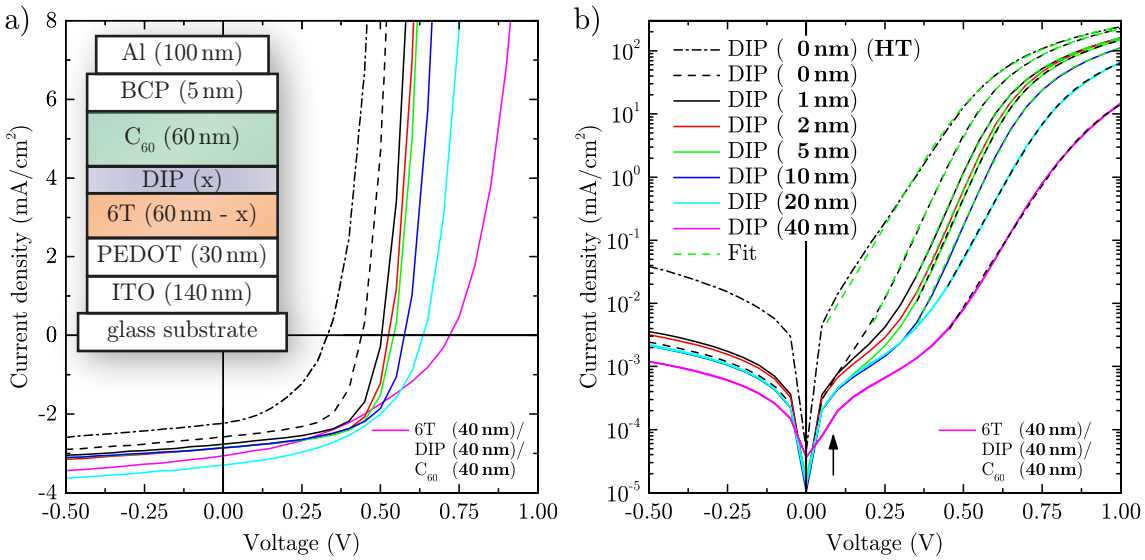

Figure A.2: Current-voltage characteristics of ternary cascading planar heterojunction solar cell under illumination at approximately one sun (a) and in the dark (b). The layer stack is shown as an inset in (a). The thickness of the DIP buffer layer between the the donor and the acceptor was gradually increased from 0 to 40 nm which is accompanied by an increase of the open circuit voltage. In the case of the 40 nm interlayer, all layers are 40 nm thick in order to keep the total thickness at 120 nm and prevent malfunctioning caused by a too thin 6T layer.

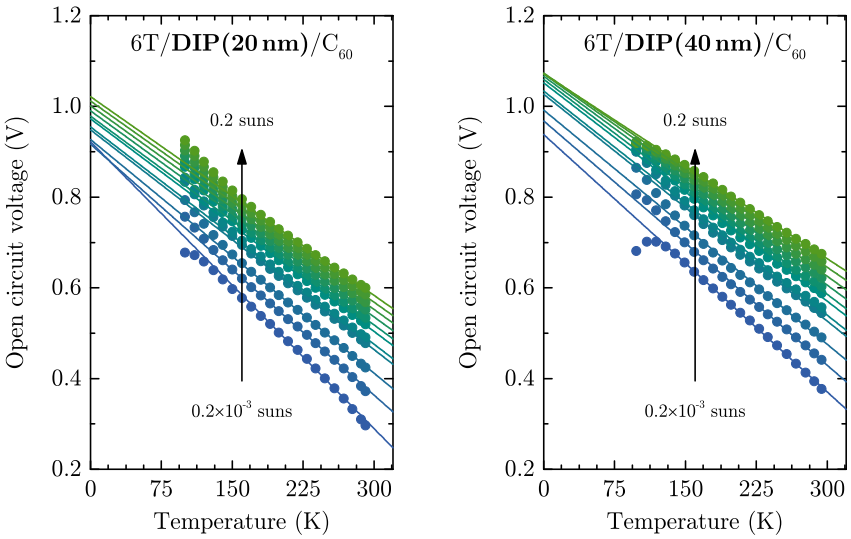

Figure A.3: Temperature dependent open circuit voltage of ternary solar cells with 20 nm and 40 nm DIP interlayer thickness. Approximate estimates of the highest and lowest equivalent light intensity are given in the respective graphs. A solar simulator was used as light source. In the case of the 40 nm interlayer, all layers are 40 nm thick in order to keep the total thickness at 120 nm and prevent malfunctioning caused by a too thin 6T layer.

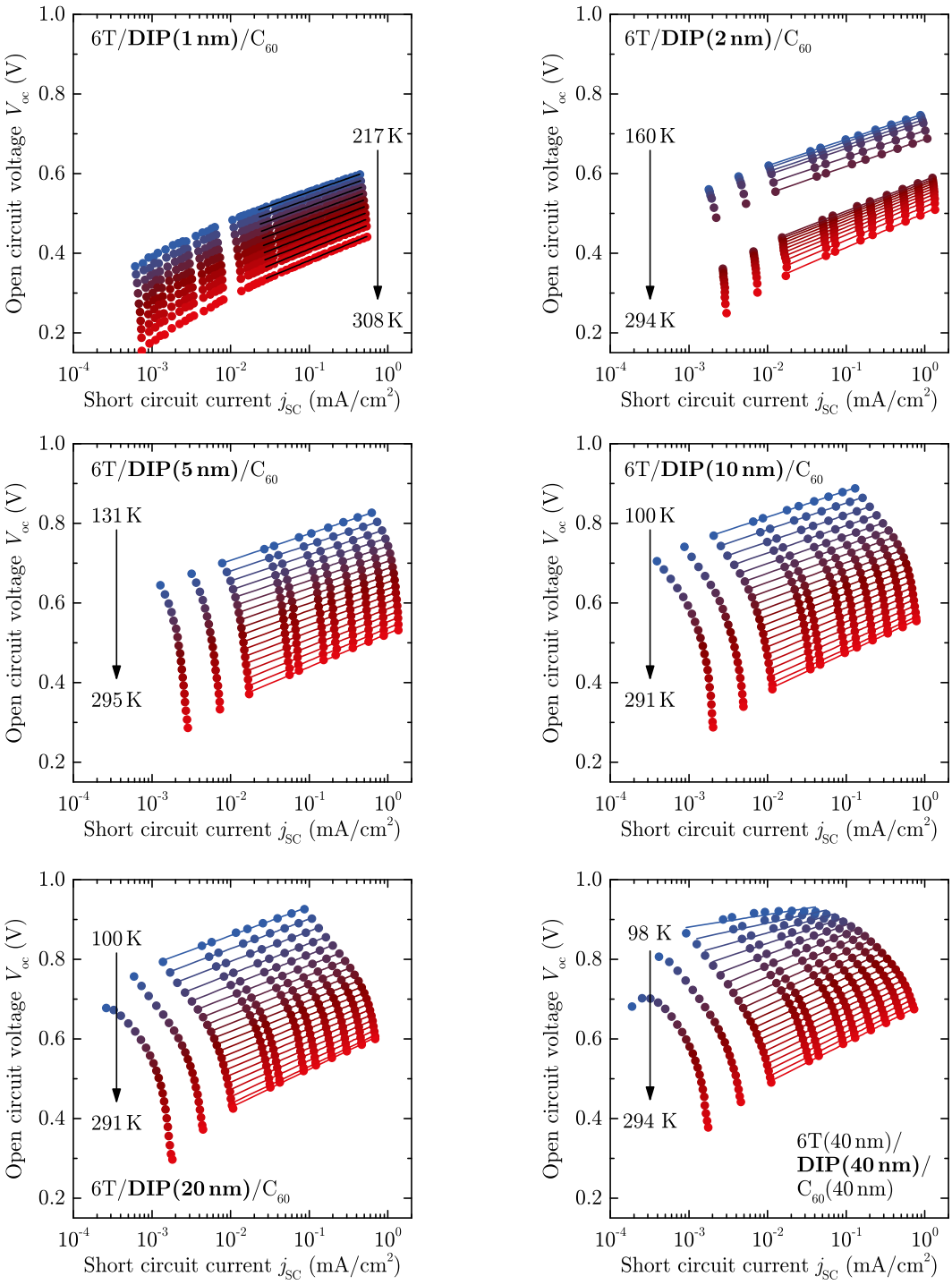

Figure A.4: Open circuit voltage plotted against the short circuit current of ternary solar cells for various temperatures and intensities. Fits with Eq. 5.1 are shown as the solid lines.

Bibliography

[1] L. Jan Anton Koster, V.D. Mihailetchi, M. Lenes, and Paul W. M. Blom. Performance improvement of polymer: Fullerene solar cells due to balanced charge transport. In Christoph Brabec, Vladimir Dyakonov, and Ulrich Scherf, editors, *Organic Photovoltaics: Materials, Device Physics and Manufacturing Technologies*, chapter 10, pages 283–297. Wiley-VCH, Weinheim, 2008.

[2] W. Hermann. Quantifying global exergy resources. *Energy*, 31(12):1685–1702, 2006.

[3] D. M. Chapin, C. S. Fuller, and G. L. Pearson. A new silicon p-n junction photocell for converting solar radiation into electrical power. *Journal of Applied Physics*, 25(5):676–677, 1954.

[4] US Energy Information Administration EIA. International energy outlook 2013 (www.eia.gov/forecasts/archive/ieo13/). Accessed December 12, 2014.

[5] International energy agency. World energy outlook 2014 factsheet (www.worldenergyoutlook.org). Accessed December 12, 2014.

[6] IEEE Spectrum. Fukushima accident upgraded to severity level 7 (spectrum.ieee.org/tech-talk/energy/nuclear/fukushima-accident-upgraded-to-severity-level-7). Accessed December 12, 2014.

[7] Bundesministerium für Wirtschaft und Energie. Eckpunkte für ein energiepolitisches Konzept (www.bmwi.de/DE/Themen/energie,did=405004.html). Accessed 2014-12-12.

[8] Frauenhofer-Institut für Solare Energiesysteme. Aktuelle Fakten zur Photovoltaik in Deutschland (www.pv-fakten.de). Accessed December 12, 2014.

[9] M. A. Green, K. Emery, Y. Hishikawa, W. Warta, and E. D. Dunlop. Solar cell efficiency tables (version 44). *Progress in Photovoltaics: Research and Applications*, 22(7):701–710, 2014.

[10] C. W. Tang. Two-layer organic photovoltaic cell. *Applied Physics Letters*, 48(2):183, 1986.

[11] S. Morita, A. Zakhidov, and K. Yoshino. Doping effect of buckminsterfullerene in conducting polymer: Change of absorption spectrum and quenching of luminescene. *Solid State Communications*, 82(4):249–252, 1992.

[12] N. S. Sariciftci, L. Smilowitz, A. J. Heeger, and F. Wudl. Photoinduced electron transfer from a conducting polymer to buckminsterfullerene. *Science*, 258(5087):1474–1476, 1992.

[13] G. Yu, J. Gao, J. C. Hummelen, F. Wudl, and A. J. Heeger. Polymer photovoltaic cells: Enhanced efficiencies via a network of internal donor-acceptor heterojunctions. *Science*, 270(5243):1789–1791, 1995.

[14] Heliatek GmbH. Heliatek reaches efficiency record with 40 % transparent organic solar cells (Press release March 24, 2014). (www.heliatek.com/newscenter/latest_news/heliatek-erzielt-effizienzrekord-mit-40-transparenten-organischen-solarzellen).

[15] BELECTRIC OPV GmbH. Schmidhuber and BELECTRIC OPV bring energy into the German pavilion (Press release June 26, 2014). (http://www.solarte.de).

[16] B. Azzopardi, C. J. M. Emmott, A. Urbina, F. C. Krebs, J. Mutale, and J. Nelson. Economic assessment of solar electricity production from organic-based photovoltaic modules in a domestic environment. *Energy & Environmental Science*, 4(10):3741–3753, 2011.

[17] M. Grätzel. The light and shade of perovskite solar cells. *Nature Materials*, 13(9):838–842, 2014.

[18] T. Erb, U. Zhokhavets, G. Gobsch, S. Raleva, B. Stühn, P. Schilinsky, C. Waldauf, and C. J. Brabec. Correlation between structural and optical properties of composite polymer/fullerene films for organic solar cells. *Advanced Functional Materials*, 15(7):1193–1196, 2005.

[19] C. M. Björström Svanström, J. Rysz, A. Bernasik, A. Budkowski, F. Zhang, O. Inganäs, M. R. Andersson, K. O. Magnusson, J. J. Benson-Smith, J. Nelson, and E. Moons. Device performance of APFO-3/PCBM solar cells with controlled morphology. *Advanced Materials*, 21(43):4398–4403, 2009.

[20] B. Ray, M. S. Lundstrom, and M. A. Alam. Can morphology tailoring improve the open circuit voltage of organic solar cells? *Applied Physics Letters*, 100(1):013307, 2012.

[21] M. Gruber, M. Rawolle, J. Wagner, D. Magerl, U. Hörmann, J. Perlich, S. V. Roth, A. Opitz, F. Schreiber, P. Müller-Buschbaum, and W. Brütting. Correlating structure and morphology to device performance of molecular organic donor-acceptor photovoltaic cells based on diindenoperylene (DIP) and C_{60}. *Advanced Energy Materials*, 3:1075–1083, 2013.

[22] Ulrich Hörmann. *Characterization of planar and diffuse heterojunction solar cells based on poly (3-hexylthiophene) and fullerenes*. Diploma thesis, University of Augsburg, 2009.

[23] Wolfgang Brütting. *Physics of Organic Semiconductors*. Wiley-VCH, Weinheim, 2005.

[24] W. Brütting and W. Rieß. Grundlagen der organischen halbleiter. *Physik Journal*, 7(5):33–38, 2008.

[25] Markus Schwoerer and Hans Christoph Wolf. *Organische Molekulare Halbleiter, Einführung in die Physik von π-Systemen*. Wiley-VCH Verlag, Weinheim, 2005.

[26] H. Bässler. Charge transport in disordered organic photoconductors. *physica status solidi (b)*, 175:15–56, 1993.

[27] D. Hertel and H. Bässler. Photoleitung in polymeren. *Physik Journal*, 5(11):39–45, 2006.

[28] P. Blom, V. Mihailetchi, L. Koster, and D. Markov. Device physics of polymer:fullerene bulk heterojunction solar cells. *Advanced Materials*, 19(12):1551–1566, 2007.

[29] S.M. Sze and Kwok K. Ng. *Physics of Semiconductor Devices*. Wiley Interscience, New Jersey, third edition, 2007.

[30] G. Dennler, M. C. Scharber, and C. J. Brabec. Polymer-fullerene bulk-heterojunction solar cells. *Advanced Materials*, 21(13):1323–1338, 2009.

[31] J.-L. Brédas, D. Beljonne, V. Coropceanu, and J. Cornil. Charge-transfer and energy-transfer processes in π-conjugated oligomers and polymers: a molecular picture. *Chemical Reviews*, 104(11):4971–5004, 2004.

[32] J. Kniepert, I. Lange, N. J. van der Kaap, L. J. A. Koster, and D. Neher. A conclusive view on charge generation, recombination, and extraction in as-prepared and annealed P3HT:PCBM blends: Combined experimental and simulation work. *Advanced Energy Materials*, 4(7), 2014 (doi:10.1002/aenm.201301401).

[33] S. Albrecht, K. Vandewal, J. R. Tumbleston, F. S. U. Fischer, J. D. Douglas, J. M. J. Fréchet, S. Ludwigs, H. Ade, A. Salleo, and D. Neher. On the efficiency of charge transfer state splitting in polymer:fullerene solar cells. *Advanced Materials*, 26(16):2533–2539, 2014.

[34] K. Vandewal, S. Albrecht, E. T. Hoke, K. R. Graham, J. Widmer, J. D. Douglas, M. Schubert, W. R. Mateker, J. T. Bloking, G. F. Burkhard, A. Sellinger, J. M. J. Fréchet, A. Amassian, M. K. Riede, M. D. McGehee, D. Neher, and A. Salleo. Efficient charge generation by relaxed charge-transfer states at organic interfaces. *Nature Materials*, 13(1):63–68, 2014.

[35] T. Stübinger and W. Brütting. Exciton diffusion and optical interference in organic donor-acceptor photovoltaic cells. *Journal of Applied Physics*, 90(7):3632–3641, 2001.

[36] C. M. Proctor, M. Kuik, and T.-Q. Nguyen. Charge carrier recombination in organic solar cells. *Progress in Polymer Science*, 38(12):1941–1960, 2013.

[37] Peter Würfel. *Physics of Solar Cells: From Basic Principles to Advanced Concepts*. Wiley-VCH Verlag, Weinheim, 2nd edition, 2009.

[38] T. Kirchartz, B. Pieters, K. Taretto, and U. Rau. Mobility dependent efficiencies of organic bulk heterojunction solar cells: Surface recombination and charge transfer state distribution. *Physical Review B*, 80(3):035334, 2009.

[39] H. Hoppe and N. S. Sariciftci. Organic solar cells: An overview. *Journal of Materials Research*, 19(07):1924–1945, 2004.

[40] C. J. Brabec, N. S. Sariciftci, and J. C. Hummelen. Plastic solar cells. *Advanced Functional Materials*, 11(1):15–26, 2001.

[41] J. Xue, B. P. Rand, S. Uchida, and S. R. Forrest. A hybrid planar-mixed molecular heterojunction photovoltaic cell. *Advanced Materials*, 17(1):66–71, 2005.

[42] C. van Berkel, M. J. Powell, A. R. Franklin, and I. D. French. Quality factor in a-Si:H nip and pin diodes. *Journal of Applied Physics*, 73(10):5264–5268, 1993.

[43] C. Waldauf, M. C. Scharber, P. Schilinsky, J. A. Hauch, and C. J. Brabec. Physics of organic bulk heterojunction devices for photovoltaic applications. *Journal of Applied Physics*, 99(10):104503, 2006.

[44] W. Tress, K. Leo, and M. Riede. Influence of hole-transport layers and donor materials on open-circuit voltage and shape of I-V curves of organic solar cells. *Advanced Functional Materials*, 21(11):2140–2149, 2011.

[45] M. G. Harrison, J. Grüner, and G. C. W. Spencer. Analysis of the photocurrent action spectra of MEH-PPV polymer photodiodes. *Physical Review B*, 55(12):7831–7849, 1997.

[46] V. Shrotriya, G. Li, Y. Yao, T. Moriarty, K. Emery, and Y. Yang. Accurate measurement and characterization of organic solar cells. *Advanced Functional Materials*, 16(15):2016–2023, 2006.

[47] Standard IEC 60904-3. Measurement principles for terrestrial photovoltaic solar devices with reference spectral irradiance data. International Electrotechnical Commission, Geneva, Switzerland.

[48] W. Shockley and H. J. Queisser. Detailed balance limit of efficiency of p-n junction solar cells. *Journal of Applied Physics*, 32(3):510–519, 1961.

[49] T. Kirchartz, J. Mattheis, and U. Rau. Detailed balance theory of excitonic and bulk heterojunction solar cells. *Physical Review B*, 78(23):235320, 2008.

[50] T. Kirchartz, K. Taretto, and U. Rau. Efficiency limits of organic bulk heterojunction solar cells. *The Journal of Physical Chemistry C*, 113(41):17958–17966, 2009.

[51] N. C. Giebink, G. P. Wiederrecht, M. R. Wasielewski, and S. R. Forrest. Thermodynamic efficiency limit of excitonic solar cells. *Physical Review B*, 83(19):195326, 2011.

[52] L. J. A. Koster, S. E. Shaheen, and J. C. Hummelen. Pathways to a new efficiency regime for organic solar cells. *Advanced Energy Materials*, 2(10):1246–1253, 2012.

[53] M. Gruber, J. Wagner, K. Klein, U. Hörmann, A. Opitz, M. Stutzmann, and W. Brütting. Thermodynamic efficiency limit of molecular donor-acceptor solar cells and its application to diindenoperylene/C_{60}-based planar heterojunction devices. *Advanced Energy Materials*, 2(9):1100–1108, 2012.

[54] G. Kirchhoff. Ueber das Verhältniss zwischen dem Emissionsvermögen und dem Absorptionsvermögen der Körper für Wärme und Licht. *Annalen der Physik*, 185(2):275–301, 1860.

[55] R. T. Ross. Some thermodynamics of photochemical systems. *The Journal of Chemical Physics*, 46(12):4590–4593, 1967.

[56] W. J. Potscavage, S. Yoo, and B. Kippelen. Origin of the open-circuit voltage in multilayer heterojunction organic solar cells. *Applied Physics Letters*, 93(19):193308, 2008.

[57] M. D. Perez, C. Borek, S. R. Forrest, and M. E. Thompson. Molecular and morphological influences on the open circuit voltages of organic photovoltaic devices. *Journal of the American Chemical Society*, 131(26):9281–9286, 2009.

[58] K. R. Graham, P. Erwin, D. Nordlund, K. Vandewal, R. Li, G. O. Ngongang Ndjawa, E. T. Hoke, A. Salleo, M. E. Thompson, M. D. McGehee, and A. Amassian. Re-evaluating the role of sterics and electronic coupling in determining the open-circuit voltage of organic solar cells. *Advanced Materials*, 25(42):6076–6082, 2013.

[59] U. Hörmann, J. Kraus, M. Gruber, C. Schuhmair, T. Linderl, S. Grob, S. Kapfinger, K. Klein, M. Stutzman, H. Krenner, and W. Brütting. Quantification of energy losses in organic solar cells from temperature-dependent device characteristics. *Physical Review B*, 88(23):235307, 2013.

[60] K. Vandewal, K. Tvingstedt, A. Gadisa, O. Inganäs, and J. V. Manca. Relating the open-circuit voltage to interface molecular properties of donor:acceptor bulk heterojunction solar cells. *Physical Review B*, 81(12):125204, 2010.

[61] J. Widmer, M. Tietze, K. Leo, and M. Riede. Open-circuit voltage and effective gap of organic solar cells. *Advanced Functional Materials*, 23(46):5814–5821, 2013.

[62] B. Rand, D. Burk, and S. Forrest. Offset energies at organic semiconductor heterojunctions and their influence on the open-circuit voltage of thin-film solar cells. *Physical Review B*, 75(11):115327, 2007.

[63] A. Wilke, J. Endres, U. Hörmann, J. Niederhausen, R. Schlesinger, J. Frisch, P. Amsalem, J. Wagner, M. Gruber, A. Opitz, A. Vollmer, W. Brütting, A. Kahn, and N. Koch. Correlation between interface energetics and open circuit voltage in organic photovoltaic cells. *Applied Physics Letters*, 101(23):233301, 2012.

[64] D. Veldman, S. C. J. Meskers, and R. A. J. Janssen. The energy of charge-transfer states in electron donor-acceptor blends: Insight into the energy losses in organic solar cells. *Advanced Functional Materials*, 19(12):1939–1948, 2009.

[65] T. Kirchartz, B. E. Pieters, J. Kirkpatrick, U. Rau, and J. Nelson. Recombination via tail states in polythiophene:fullerene solar cells. *Physical Review B*, 83(11):115209, 2011.

[66] U. Hörmann, J. Wagner, M. Gruber, A. Opitz, and W. Brütting. Approaching the ultimate open circuit voltage in thiophene based single junction solar cells by applying diindenoperylene as acceptor. *physica status solidi (RRL) - Rapid Research Letters*, 5(7):241–243, 2011.

[67] Julia Katharina Kraus. *Physics of Molecular Donor-Acceptor Solar Cells*. Ph.D. thesis, University of Augsburg, 2013.

[68] K. Vandewal, K. Tvingstedt, A. Gadisa, O. Inganäs, and J. V. Manca. On the origin of the open-circuit voltage of polymer-fullerene solar cells. *Nature materials*, 8(11):904–909, 2009.

[69] M. A. Green. Radiative efficiency of state-of-the-art photovoltaic cells. *Progress in Photovoltaics: Research and Applications*, 20(4):472–476, 2012.

[70] H. Ishii, K. Sugiyama, E. Ito, and K. Seki. Energy level alignment and interfacial electronic structures at organic/metal and organic/organic interfaces. *Advanced Materials*, 11(8):605–625, 1999.

[71] A. Opitz, J. Frisch, R. Schlesinger, A. Wilke, and N. Koch. Energy level alignment at interfaces in organic photovoltaic devices. *Journal of Electron Spectroscopy and Related Phenomena*, 190(Part A):12–24, 2013.

[72] J. Wagner, M. Gruber, A. Hinderhofer, A. Wilke, B. Bröker, J. Frisch, P. Amsalem, A. Vollmer, A. Opitz, N. Koch, F. Schreiber, and W. Brütting. High fill factor and open circuit voltage in organic photovoltaic cells with diindenoperylene as donor material. *Advanced Functional Materials*, 20(24):4295–4303, 2010.

[73] W. Osikowicz, M. P. de Jong, and W. R. Salaneck. Formation of the interfacial dipole at organic-organic interfaces: C_{60}/polymer interfaces. *Advanced Materials*, 19(23):4213–4217, 2007.

[74] B. P. Rand, J. Li, J. Xue, R. J. Holmes, M. E. Thompson, and S. R. Forrest. Organic double-heterostructure photovoltaic cells employing thick tris(acetylacetonato)ruthenium(iii) exciton-blocking layers. *Advanced Materials*, 17(22):2714–2718, 2005.

[75] P. I. Djurovich, E. I. Mayo, S. R. Forrest, and M. E. Thompson. Measurement of the lowest unoccupied molecular orbital energies of molecular organic semiconductors. *Organic Electronics*, 10(3):515–520, 2009.

[76] M. Kiel, K. Duncker, C. Hagendorf, and W. Widdra. Molecular structure and chiral separation in α-sexithiophene ultrathin films on Au(111): Low-energy electron diffraction and scanning tunneling microscopy. *Physical Review B*, 75(19):195439, 2007.

[77] G. Horowitz, D. Fichou, X. Peng, Z. Xu, and F. Garnier. A field-effect transistor based on conjugated alpha-sexithienyl. *Solid State Communications*, 72(4):381–384, 1989.

[78] G. Horowitz, B. Bachet, A. Yassar, P. Lang, F. Demanze, J.-L. Fave, and F. Garnier. Growth and characterization of sexithiophene single crystals. *Chemistry of Materials*, 7(7):1337–1341, 1995.

[79] B. Servet, G. Horowitz, S. Ries, O. Lagorsse, P. Alnot, A. Yassar, F. Deloffre, P. Srivastava, R. Hajlaoui, P. Lang, and F. Garnier. Polymorphism and charge transport in vacuum-evaporated sexithiophene films. *Chemistry of Materials*, (6):1809–1815, 1994.

[80] A. Moser, I. Salzmann, M. Oehzelt, A. Neuhold, H.-G. Flesch, J. Ivanco, S. Pop, T. Toader, D. R. Zahn, D.-M. Smilgies, and R. Resel. A disordered layered phase in thin films of sexithiophene. *Chemical Physics Letters*, 574:51–55, 2013.

[81] C. Aruta, P. D'Angelo, M. Barra, G. Ausanio, and A. Cassinese. Improved structural ordering in sexithiophene thick films grown on single crystal oxide substrates. *Applied Physics A: Materials Science & Processing*, 97(2):387–394, 2009.

[82] C. Simbrunner. Epitaxial growth of sexi-thiophene and para-hexaphenyl and its implications for the fabrication of self-assembled lasing nano-fibres. *Semiconductor Science and Technology*, 28(5):053001, 2013.

[83] R. N. Marks, M. Muccini, E. Lunedi, R. H. Michel, M. Murgia, R. Zamboni, C. Taliani, G. Horowitz, F. Gamier, M. Hopmeier, M. Oestreich, and R. F. Mahrt. Disorder influenced optical properties of α-sexithiophene single crystals and thin evaporated films. *Chemical Physics*, 227:49–56, 1998.

[84] S. Duhm, G. Heimel, I. Salzmann, H. Glowatzki, R. L. Johnson, A. Vollmer, J. P. Rabe, and N. Koch. Orientation-dependent ionization energies and interface dipoles in ordered molecular assemblies. *Nature Materials*, 7(4):326–332, 2008.

[85] H. Sirringhaus, N. Tessler, and R. H. Friend. Integrated optoelectronic devices based on conjugated polymers. *Science*, 280(5370):1741, 1998.

[86] B. Xu and S. Holdcroft. Molecular control of luminescence from poly(3-hexylthiophenes). *Macromolecules*, 26(17):4457–4460, 1993.

[87] Silviu-Cosmin Grecu. *Charge transport in polymeric field-effect devices*. Phd Thesis, University of Augsburg, 2008.

[88] M. Al-Ibrahim, H. Roth, M. Schroedner, A. Konkin, U. Zhokhavets, G. Gobsch, P. Scharff, and S. Sensfuss. The influence of the optoelectronic properties of poly(3-alkylthiophenes) on the device parameters in flexible polymer solar cells. *Organic Electronics*, 6:65–77, 2005.

[89] A. C. Dürr, F. Schreiber, M. Münch, N. Karl, B. Krause, V. Kruppa, and H. Dosch. High structural order in thin films of the organic semiconductor diindenoperylene. *Applied Physics Letters*, 81(12):2276–2278, 2002.

[90] A. K. Tripathi and J. Pflaum. Correlation between ambipolar transport and structural phase transition in diindenoperylene single crystals. *Applied Physics Letters*, 89(8):082103, 2006.

[91] M. Heinrich, J. Pflaum, A. Tripathi, W. Frey, M. Steigerwald, and T. Siegrist. Enantiotropic polymorphism in di-indenoperylene. *Journal of Physical Chemistry C*, 111(51):18878–18881, 2007.

[92] S. Kowarik, A. Gerlach, S. Sellner, L. Cavalcanti, O. Konovalov, and F. Schreiber. Real-time X-ray diffraction measurements of structural dynamics and polymorphism in diindenoperylene growth. *Applied Physics A*, 95(1):233–239, 2009.

[93] A. Dürr, N. Koch, M. Kelsch, A. Rühm, J. Ghijsen, R. Johnson, J.-J. Pireaux, J. Schwartz, F. Schreiber, H. Dosch, and A. Kahn. Interplay between morphology, structure, and electronic properties at diindenoperylene-gold interfaces. *Physical Review B*, 68(11):115428, 2003.

[94] M. Horlet, M. Kraus, W. Brütting, and A. Opitz. Diindenoperylene as ambipolar semiconductor: Influence of electrode materials and mobility asymmetry in organic field-effect transistors. *Applied Physics Letters*, 98(23):233304, 2011.

[95] U. Heinemeyer, R. Scholz, L. Gisslén, M. Alonso, J. Ossó, M. Garriga, A. Hinderhofer, M. Kytka, S. Kowarik, A. Gerlach, and F. Schreiber. Exciton-phonon coupling in diindenoperylene thin films. *Physical Review B*, 78(8):085210, 2008.

[96] P. A. Heiney, J. E. Fischer, A. R. McGhie, W. J. Romanow, A. M. Denenstein, J. P. McCauley Jr., A. B. Smith, and D. E. Cox. Orientational ordering transition in solid C_{60}. *Physical Review Letters*, 66(22):2911–2914, 1991.

[97] M. K. Kelly, P. Etchegoin, D. Fuchs, W. Krätschmer, and K. Fostiropoulos. Optical transitions of C_{60} films in the visible and ultraviolet from spectroscopic ellipsometry. *Physical Review B*, 46(8):4963–4968, 1992.

[98] R. Lof, M. van Veenendaal, B. Koopmans, H. T. Jonkman, and G. A. Sawatzky. Band gap, excitons, and coulomb interaction in solid C_{60}. *Physical Review Letters*, 68(26):3924–3927, 1992.

[99] B. Kraabel, D. McBranch, N. S. Sariciftci, D. Moses, and A. J. Heeger. Ultrafast spectroscopic studies of photoinduced electron transfer from semiconducting polymers to C_{60}. *Physical Review B*, 50(24):18543–18552, 1994.

[100] A. F. Hebard, R. C. Haddon, R. M. Fleming, and A. R. Kortan. Deposition and characterization of fullerene films. *Applied Physics Letters*, 59(17):2109–2111, 1991.

[101] David F. Kronholm and Jan C. Hummelen. Fullerene-based acceptor materials. In Christoph Brabec, Vladimir Dyakonov, and Ulrich Scherf, editors, *Organic Photovoltaics: Materials, Device Physics and Manufacturing Technologies*, chapter 5, pages 155–178. Wiley-VCH, Weinheim, 2008.

[102] L. Li, H. Tang, H. Wu, G. Lu, and X. Yang. Effects of fullerene solubility on the crystallization of poly(3-hexylthiophene) and performance of photovoltaic devices. *Organic Electronics*, 10(7):1334–1344, 2009.

[103] P. Peumans and S. R. Forrest. Very-high-efficiency double-heterostructure copper phthalocyanine/C_{60} photovoltaic cells. *Applied Physics Letters*, 79(1):126–128, 2001.

[104] A. Steindamm, M. Brendel, A. K. Topczak, and J. Pflaum. Thickness dependent effects of an intermediate molecular blocking layer on the optoelectronic characteristics of organic bilayer photovoltaic cells. *Applied Physics Letters*, 101(14):143302, 2012.

[105] A. Kahn, N. Koch, and W. Gao. Electronic structure and electrical properties of interfaces between metals and π-conjugated molecular films. *Journal of Polymer Science Part B: Polymer Physics*, 41(21):2529–2548, 2003.

[106] Andreas Elschner and Stephan Kirchmeyer. PEDOT-type materials in organic solar cells. In Christoph Brabec, Vladimir Dyakonov, and Ulrich Scherf, editors, *Organic Photovoltaics: Materials, Device Physics and Manufacturing Technologies*, chapter 7, pages 213–242. Wiley-VCH, Weinheim, 2008.

[107] N. Koch, A. Vollmer, and A. Elschner. Influence of water on the work function of conducting poly(3,4-ethylenedioxythiophene)/poly(styrenesulfonate). *Applied Physics Letters*, 90(4):043512, 2007.

[108] J. Wagner, M. Gruber, A. Wilke, Y. Tanaka, K. Topczak, A. Steindamm, U. Hörmann, A. Opitz, Y. Nakayama, H. Ishii, J. Pflaum, N. Koch, and W. Brütting. Identification of different origins for s-shaped current voltage characteristics in planar heterojunction organic solar cells. *Journal of Applied Physics*, 111(5):054509, 2012.

[109] C. J. Lawrence. The mechanics of spin coating of polymer films. *Physics of Fluids*, 31(10):2786–2795, 1988.

[110] C.-C. Chang, C.-L. Pai, W.-C. Chen, and S. A. Jenekhe. Spin coating of conjugated polymers for electronic and optoelectronic applications. *Thin Solid Films*, 479(1-2):254–260, 2005.

[111] W. W. Flack, D. S. Soong, A. T. Bell, and D. W. Hess. A mathematical model for spin coating of polymer resists. *Journal of Applied Physics*, 56(4):1199–1206, 1984.

[112] C.-S. Lu and O. Lewis. Investigation of film-thickness determination by oscillating quartz resonators with large mass load. *Journal of Applied Physics*, 43(11):4385–4390, 1972.

[113] Paul Peter Ewald. *Fifty years of X-ray diffraction.* For the international union of crytallography by N. V. A. Oosthoek's uitgeversmaatschappij, Utrecht, The Netherlands, 1962.

[114] Charles Kittel. *Einführung in die Festkörperphysik.* Oldenburg Wissenschaftsverlag, München, 14. Auflage, 2006.

[115] P. Scherrer. Bestimmung der Grösse und der inneren Struktur von Kolloidteilchen mittels Röntgenstrahlen. *Nachrichten von der Gesellschaft der Wissenschaften zu Göttingen, Mathematisch-Physikalische Klasse*, 1918:98–100, 1918.

[116] J. Stöhr and R. Jaeger. Absorption-edge resonances, core-hole screening, and orientation of chemisorbed molecules: Co, no, and n_2 on ni(100). *Physical Review B*, 26(8):4111–4131, 1982.

[117] D. M. DeLongchamp, E. K. Lin, and D. A. Fischer. Organic semiconductor structure and chemistry from NEXAFS. *Proceedings of SPIE*, 5940:59400A, 2005.

[118] B. Watts, L. Thomsen, and P. Dastoor. Methods in carbon K-edge NEXAFS: Experiment and analysis. *Journal of Electron Spectroscopy and Related Phenomena*, 151(2):105–120, 2006.

[119] J. Stöhr and D. A. Outka. Determination of molecular orientations on surfaces from the angular dependence of near-edge X-ray-absorption fine-structure spectra. *Physical Review B*, 36(15):7891–7905, 1987.

[120] MAX-Lab (www.maxlab.lu.se/node/458). Accessed on July 21, 2014.

[121] Y. L. Huang, W. Chen, H. Huang, D. C. Qi, S. Chen, X. Y. Gao, J. Pflaum, and A. T. S. Wee. Ultrathin films of diindenoperylene on graphite and SiO_2. *The Journal of Physical Chemistry C*, 113(21):9251–9255, 2009.

[122] J. Q. Zhong, H. Y. Mao, R. Wang, D. C. Qi, L. Cao, Y. Z. Wang, and W. Chen. Effect of gap states on the orientation-dependent energy level alignment at the DIP/F_{16}CuPc donor-acceptor heterojunction interfaces. *The Journal of Physical Chemistry C*, 115(48):23922–23928, 2011.

[123] A. S. Anselmo, A. Dzwilewski, K. Svensson, and E. Moons. Molecular orientation and composition at the surface of spin-coated polyfluorene:fullerene blend films. *Journal of Polymer Science Part B: Polymer Physics*, 51(3):176–182, 2013.

[124] A. S. Anselmo, L. Lindgren, J. Rysz, A. Bernasik, A. Budkowski, M. R. Andersson, K. Svensson, J. van Stam, and E. Moons. Tuning the vertical phase separation in polyfluorene:fullerene blend films by polymer functionalization. *Chemistry of Materials*, 23(9):2295–2302, 2011.

[125] J. Genzer, E. J. Kramer, and D. A. Fischer. Accounting for auger yield energy loss for improved determination of molecular orientation using soft X-ray absorption spectroscopy. *Journal of Applied Physics*, 92(12):7070–7079, 2002.

[126] F. Reinert and S. Hüfner. Photoemission spectroscopy – from early days to recent applications. *New Journal of Physics*, 7:97, 2005.

[127] Rudy Schlaf. Calibration of Photoemission Spectra and Work Function Determination (http://rsl.eng.usf.edu/Documents/Tutorials/PEScalibration.pdf). Accessed August 14, 2014.

[128] S. Krause, M. B. Casu, A. Schöll, and E. Umbach. Determination of transport levels of organic semiconductors by UPS and IPS. *New Journal of Physics*, 10(8):085001, 2008.

[129] N. Koch and A. Vollmer. Electrode-molecular semiconductor contacts: Work-function-dependent hole injection barriers versus fermi-level pinning. *Applied Physics Letters*, 89(16):162107, 2006.

[130] G. Binnig, C. F. Quate, and C. Gerber. Atomic force microscope. *Physical Review Letters*, 56(9):930–933, 1986.

[131] Q. Zhong, D. Inniss, K. Kjoller, and V. B. Elings. Fractured polymer/silica fiber surface studied by tapping mode atomic force microscopy. *Surface Science*, 290(1-2):L688 – L692, 1993.

[132] S. N. Magonov, V. Elings, and M.-H. Whangbo. Phase imaging and stiffness in tapping-mode atomic force microscopy. *Surface Science*, 375(2-3):L385–L391, 1997.

[133] OMT Instruments (http://www.mut-group.com/sensors/omtsys-tfa/thin-film-analysis.html). Accessed December 16, 2014.

[134] W. Theiss Hard- and Software SCOUT (http://www.wtheiss.com).

[135] A. Opitz, J. Wagner, W. Brütting, A. Hinderhofer, and F. Schreiber. Molecular semiconductor blends: Microstructure, charge carrier transport, and application in photovoltaic cells. *physica status solidi (a)*, 2694(12):2683–2694, 2009.

[136] A. Opitz, M. Horlet, M. Kiwull, J. Wagner, M. Kraus, and W. Brütting. Bipolar charge transport in organic field-effect transistors: Enabling high mobilities and transport of photo-generated charge carriers by a molecular passivation layer. *Organic Electronics*, 13(9):1614–1622, 2012.

[137] P. E. Shaw, A. Ruseckas, and I. D. W. Samuel. Exciton diffusion measurements in poly(3-hexylthiophene). *Advanced Materials*, 20(18):3516–3520, 2008.

[138] FLUXiM Setfos (evaluation version) Material data base – www.fluxim.com.

[139] U. Hörmann, C. Lorch, A. Hinderhofer, A. Gerlach, M. Gruber, J. Kraus, B. Sykora, S. Grob, T. Linderl, A. Wilke, A. Opitz, R. Hansson, A. S. Anselmo, Y. Ozawa, Y. Nakayama, H. Ishii, N. Koch, E. Moons, F. Schreiber, and W. Brütting. V_{oc} from a morphology point of view: The influence of molecular orientation on the open circuit voltage of organic planar heterojunction solar cells. *Journal of Physical Chemistry C*, 118(46):26462–26470, 2014.

[140] B. Servet, S. Ries, M. Trotel, P. Alnot, G. Horowitz, and F. Garnier. X-ray determination of the crystal structure and orientation of vacuum evaporated sexithiophene films. *Advanced Materials*, 5(6):461–464, 1993.

[141] H. J. Egelhaaf, P. Bäuerle, K. Rauer, V. Hoffmann, and D. Oelkrug. UV/Vis and IR spectroscopic studies on molecular orientation in ultrathin films of polythiophene model compounds. *Journal of Molecular Sructure*, 293:249–252, 1993.

[142] K. Momma and F. Izumi. Vesta 3 for three-dimensional visualization of crystal, volumetric and morphology data. *Journal of Applied Crystallography*, 44(6):1272–1276, 2011.

[143] S. Kowarik, A. Gerlach, S. Sellner, F. Schreiber, L. Cavalcanti, and O. Konovalov. Real-time observation of structural and orientational transitions during growth of organic thin films. *Physical Review Letters*, 96(12):125504, 2006.

[144] J. L. de Boer, S. van Smaalen, V. Petricek, M. Dusek, M. A. Verheijen, and G. Meijer. Hexagonal close-packed C_{60}. *Chemical Physics Letters*, 219:469–472, 1994.

[145] A. Hinderhofer, A. Gerlach, K. Broch, T. Hosokai, K. Yonezawa, K. Kato, S. Kera, N. Ueno, and F. Schreiber. Geometric and electronic structure of templated C_{60} on diindenoperylene thin films. *The Journal of Physical Chemistry C*, 117(2):1053–1058, 2013.

[146] A. Dürr, B. Nickel, V. Sharma, U. Täffner, and H. Dosch. Observation of competing modes in the growth of diindenoperylene on sio_2. *Thin Solid Films*, 503(1-2):127–132, 2006.

[147] G. Koller, S. Berkebile, J. R. Krenn, F. P. Netzer, M. Oehzelt, T. Haber, R. Resel, and M. G. Ramsey. Heteroepitaxy of organic-organic nanostructures. *Nano Letters*, 6(6):1207–1212, 2006.

[148] H. Sitter, R. Resel, G. Koller, M.G. Ramsey, A. Andreev, and C. Teichert. Fundamentals of organic film growth and characterisation. In Katharina Al-Shamery, Horst-Günter Rubahn, and Helmut Sitter, editors, *Organic Nanostructures for Next Generation Devices*, pages 3–19. Springer Berlin / Heidelberg, 2008.

[149] A. Yassar, G. Horowitz, P. Valat, V. Wintgens, M. Hmyene, F. Deloffre, P. Srivastava, P. Lang, F. Garnier, and F. Gamier. Exciton coupling effects in the absorption and photoluminescence of sexithiophene derivatives. *The Journal of Physical Chemistry*, 99(22):9155–9159, 1995.

[150] J.-L. Brédas, J. E. Norton, J. Cornil, and V. Coropceanu. Molecular understanding of organic solar cells: the challenges. *Accounts of Chemical Research*, 42(11):1691–1699, 2009.

[151] W. N. Han, K. Yonezawa, R. Makino, K. Kato, A. Hinderhofer, R. Murdey, R. Shiraishi, H. Yoshida, N. Sato, N. Ueno, and S. Kera. Quantitatively identical orientation-dependent ionization energy and electron affinity of diindenoperylene. *Applied Physics Letters*, 103(25):253301, 2013.

[152] N. Koch. Organic electronic devices and their functional interfaces. *ChemPhysChem: A European journal of chemical physics and physical chemistry*, 8(10):1438–55, 2007.

[153] R. W. Munn, M. Andrzejak, P. Petelenz, A. D. Esposti, and C. Taliani. Calculation of refractive indices and local electric field tensors in α-sexithiophene crystal. *Chemical Physics Letters*, 336:357–363, 2001.

[154] S. Verlaak, D. Beljonne, D. Cheyns, C. Rolin, M. Linares, F. A. A. Castet, J. A. A. Cornil, and P. Heremans. Electronic structure and geminate pair energetics at organic-organic interfaces: The case of pentacene/C_{60} heterojunctions. *Advanced Functional Materials*, 19(23):3809–3814, 2009.

[155] N. Koch. Electronic structure of interfaces with conjugated organic materials. *physica status solidi (RRL) - Rapid Research Letters*, 6(7):277–293, 2012.

[156] A. Wilke, P. Amsalem, J. Frisch, B. Bröker, A. Vollmer, and N. Koch. Electric fields induced by energy level pinning at organic heterojunctions. *Applied Physics Letters*, 98(12):123304, 2011.

[157] C. J. Brabec, A. Cravino, D. Meissner, N. S. Sariciftci, T. Fromherz, M. T. Rispens, L. Sanchez, and J. C. Hummelen. Origin of the open circuit voltage of plastic solar cells. *Advanced Functional Materials*, 11(5):374–380, 2001.

[158] L. Sims, U. Hörmann, R. Hanfland, R. C. MacKenzie, F. R. Kogler, R. Steim, W. Brütting, and P. Schilinsky. Investigation of the s-shape caused by the hole selective layer in bulk heterojunction solar cells. *Organic Electronics*, 15(11):2862–2867, 2014.

[159] W. Tress, A. Petrich, M. Hummert, M. Hein, K. Leo, and M. Riede. Imbalanced mobilities causing s-shaped IV curves in planar heterojunction organic solar cells. *Applied Physics Letters*, 98(6):063301, 2011.

[160] Y. Yi, V. Coropceanu, and J.-L. Brédas. Exciton-dissociation and charge-recombination processes in pentacene/C_{60} solar cells: Theoretical insight into the impact of interface geometry. *Journal of the American Chemical Society*, 131(43):15777–15783, 2009.

[161] Y. Yi, V. Coropceanu, and J.-L. Brédas. A comparative theoretical study of exciton-dissociation and charge-recombination processes in oligothiophene/fullerene and oligothiophene/perylenediimide complexes for organic solar cells. *Journal of Materials Chemistry*, 21(5):1479–1486, 2011.

[162] Y.-T. Fu, D. A. da Silva Filho, G. Sini, A. M. Asiri, S. G. Aziz, C. Risko, and J.-L. Brédas. Structure and disorder in squaraine-C_{60} organic solar cells: A theoretical description of molecular packing and electronic coupling at the donor-acceptor interface. *Advanced Functional Materials*, 24(24):3790–3798, 2014.

[163] J. D. Zimmerman, X. Xiao, C. K. Renshaw, S. Wang, V. V. Diev, M. E. Thompson, and S. R. Forrest. Independent control of bulk and interfacial morphologies of small molecular weight organic heterojunction solar cells. *Nano Letters*, 12(8):4366–4371, 2012.

[164] Y.-T. Fu, C. Risko, and J.-L. Brédas. Intermixing at the pentacene-fullerene bilayer interface: A molecular dynamics study. *Advanced Materials*, 25(6):878–882, 2013.

[165] R. A. Cantrell, C. James, and P. Clancy. Computationally derived rules for persistence of C_{60} nanowires on recumbent pentacene bilayers. *Langmuir: the ACS journal of surfaces and colloids*, 27(16):9944–9954, 2011.

[166] N. Sai, R. Gearba, A. Dolocan, J. R. Tritsch, W.-L. Chan, J. R. Chelikowsky, K. Leung, and X. Zhu. Understanding the interface dipole of copper phthalocyanine (CuPc)/C_{60} : Theory and experiment. *The Journal of Physical Chemistry Letters*, 3(16):2173–2177, 2012.

[167] K. S. Nalwa, H. K. Kodali, B. Ganapathysubramanian, and S. Chaudhary. Dependence of recombination mechanisms and strength on processing conditions in polymer solar cells. *Applied Physics Letters*, 99(26):263301, 2011.

[168] A. Foertig, A. Wagenpfahl, T. Gerbich, D. Cheyns, V. Dyakonov, and C. Deibel. Nongeminate recombination in planar and bulk heterojunction organic solar cells. *Advanced Energy Materials*, 2(12):1483–1489, 2012.

[169] J. Nelson, J. Kirkpatrick, and P. Ravirajan. Factors limiting the efficiency of molecular photovoltaic devices. *Physical Review B*, 69(3):035337, 2004.

[170] M. A. Faist, T. Kirchartz, W. Gong, R. S. Ashraf, I. McCulloch, J. C. de Mello, N. J. Ekins-Daukes, D. D. C. Bradley, and J. Nelson. Competition between the charge transfer state and the singlet states of donor or acceptor limiting the efficiency in polymer:fullerene solar cells. *Journal of the American Chemical Society*, 134(1):685–692, 2012.

[171] N. A. Ran, M. Kuik, J. A. Love, C. M. Proctor, I. Nagao, G. C. Bazan, and T.-Q. Nguyen. Understanding the charge-transfer state and singlet exciton emission from solution-processed small-molecule organic solar cells. *Advanced Materials*, 26(43):7405–7412, 2014.

[172] Theresa Linderl. University of augsburg, unpublished.

[173] R. R. Hung and J. J. Grabowski. A preclse determination of the triplet energy of C_{60} by photoacoustlc calorimetry. *Journal of Physical Chemistry*, 95(16):6073–6075, 1991.

[174] P. Lane, X. Wei, and Z. Vardeny. Absorption spectroscopy of charged excitations in α-sexithiophene: evidence for charge conjugation symmetry breaking. *Chemical physics*, 210:229–234, 1996.

[175] X. Wei, P. Lane, M. Liess, and Z. Vardeny. Triplet excitations in sexithiophene films. *Synthetic Metals*, 84(1-3):565–566, 1997.

[176] P. Lane, X. Wei, Z. Vardeny, J. Poplawski, E. Ehrenfreund, M. Ibrahim, and A. J. Frank. Spin signature of photoexcitations in sexithiophene. *Synthetic Metals*, 76(1-3):57–60, 1996.

[177] J. Poplawski, E. Ehrenfreund, J. Cornil, J.-L. Brédas, R. Pugh, M. Ibrahim, and A. J. Frank. Photogeneration of polarons in sexithiophene oligomers. *Synthetic Metals*, 69(1-3):401–402, 1995.

[178] R. Capelli, C. Taliani, and M. Muccini. Modeling of the photophysical properties of α-sexithiophene thin films. *Synthetic Metals*, 139(3):691–693, 2003.

[179] Z. Sun and S. Stafström. Bipolaron recombination in conjugated polymers. *The Journal of Chemical Physics*, 135(7):074902, 2011.

[180] G. A. H. Wetzelaer, M. Kuik, M. Lenes, and P. W. M. Blom. Origin of the dark-current ideality factor in polymer:fullerene bulk heterojunction solar cells. *Applied Physics Letters*, 99(15):153506, 2011.

[181] L. J. A. Koster, V. D. Mihailetchi, R. Ramaker, and P. W. M. Blom. Light intensity dependence of open-circuit voltage of polymer:fullerene solar cells. *Applied Physics Letters*, 86(12):123509, 2005.

[182] M. M. Mandoc, F. B. Kooistra, J. C. Hummelen, B. de Boer, and P. W. M. Blom. Effect of traps on the performance of bulk heterojunction organic solar cells. *Applied Physics Letters*, 91(26):263505, 2007.

[183] K. S. Nalwa, R. C. Mahadevapuram, and S. Chaudhary. Growth rate dependent trap density in polythiophene-fullerene solar cells and its implications. *Applied Physics Letters*, 98(9):093306, 2011.

[184] K. Harada, M. Riede, K. Leo, O. Hild, and C. Elliott. Pentacene homojunctions: Electron and hole transport properties and related photovoltaic responses. *Physical Review B*, 77(19):195212, 2008.

[185] G. A. H. Wetzelaer, L. J. A. Koster, and P. W. M. Blom. Validity of the einstein relation in disordered organic semiconductors. *Physical Review Letters*, 107(6):066605, 2011.

[186] N. C. Giebink, G. P. Wiederrecht, M. R. Wasielewski, and S. R. Forrest. Ideal diode equation for organic heterojunctions. I. Derivation and application. *Physical Review B*, 82(15):155305, 2010.

[187] T. Kirchartz, F. Deledalle, P. S. Tuladhar, J. R. Durrant, and J. Nelson. On the differences between dark and light ideality factor in polymer:fullerene solar cells. *The Journal of Physical Chemistry Letters*, 4(14):2371–2376, 2013.

[188] W. Huynh, J. Dittmer, N. Teclemariam, D. Milliron, A. Alivisatos, and K. Barnham. Charge transport in hybrid nanorod-polymer composite photovoltaic cells. *Physical Review B*, 67(11):115326, 2003.

[189] S. Yoo, B. Domercq, and B. Kippelen. Intensity-dependent equivalent circuit parameters of organic solar cells based on pentacene and C_{60}. *Journal of Applied Physics*, 97(10):103706, 2005.

[190] C. H. Henry. Limiting efficiencies of ideal single and multiple energy gap terrestrial solar cells. *Journal of Applied Physics*, 51(8):4494, 1980.

[191] A. Maurano, R. Hamilton, C. G. Shuttle, A. M. Ballantyne, J. Nelson, B. O'Regan, W. Zhang, I. McCulloch, H. Azimi, M. Morana, C. J. Brabec, and J. R. Durrant. Recombination dynamics as a key determinant of open circuit voltage in organic bulk heterojunction solar cells: a comparison of four different donor polymers. *Advanced Materials*, 22(44):4987–4992, 2010.

[192] T. Kirchartz and J. Nelson. Meaning of reaction orders in polymer:fullerene solar cells. *Physical Review B*, 86(16):165201, 2012.

[193] G. Juška, K. Genevičius, N. Nekrašas, G. Sliaužys, and G. Dennler. Trimolecular recombination in polythiophene: fullerene bulk heterojunction solar cells. *Applied Physics Letters*, 93(14):143303, 2008.

[194] J. C. Blakesley and D. Neher. Relationship between energetic disorder and open-circuit voltage in bulk heterojunction organic solar cells. *Physical Review B*, 84(7):075210, 2011.

[195] S. A. Hawks, G. Li, Y. Yang, and R. A. Street. Band tail recombination in polymer:fullerene organic solar cells. *Journal of Applied Physics*, 116(7):074503, 2014.

[196] G. Garcia-Belmonte. Temperature dependence of open-circuit voltage in organic solar cells from generation-recombination kinetic balance. *Solar Energy Materials and Solar Cells*, 94(12):2166–2169, 2010.

[197] R. A. Street, A. Krakaris, and S. R. Cowan. Recombination through different types of localized states in organic solar cells. *Advanced Functional Materials*, 22(21):4608–4619, 2012.

[198] B. Homa, M. Andersson, and O. Inganäs. Photogenerated charge carrier transport and recombination in polyfluorene/fullerene bilayer and blend photovoltaic devices. *Organic Electronics*, 10(3):501–505, 2009.

[199] J. Kniepert, M. Schubert, J. C. Blakesley, and D. Neher. Photogeneration and recombination in P3HT/PCBM solar cells probed by time-delayed collection field experiments. *The Journal of Physical Chemistry Letters*, 2(7):700–705, 2011.

[200] A. Baumann, J. Lorrmann, D. Rauh, C. Deibel, and V. Dyakonov. A new approach for probing the mobility and lifetime of photogenerated charge carriers in organic solar cells under real operating conditions. *Advanced Materials*, 24(32):4381–4386, 2012.

[201] S. Yamamoto, A. Orimo, H. Ohkita, H. Benten, and S. Ito. Molecular understanding of the open-circuit voltage of polymer:fullerene solar cells. *Advanced Energy Materials*, 2(2):229–237, 2012.

[202] C. W. Schlenker and M. E. Thompson. The molecular nature of photovoltage losses in organic solar cells. *Chemical Communications*, 47(13):3702–3716, 2011.

[203] P. Erwin and M. E. Thompson. Elucidating the interplay between dark current coupling and open circuit voltage in organic photovoltaics. *Applied Physics Letters*, 98(22):223305, 2011.

[204] K. Cnops, B. P. Rand, D. Cheyns, and P. Heremans. Enhanced photocurrent and open-circuit voltage in a 3-layer cascade organic solar cell. *Applied Physics Letters*, 101(14):143301, 2012.

[205] K. Cnops, B. P. Rand, D. Cheyns, B. Verreet, M. A. Empl, and P. Heremans. 8.4 % efficient fullerene-free organic solar cells exploiting long-range exciton energy transfer. *Nature Communications*, 5:3406, 2014.

[206] T. D. Heidel, D. Hochbaum, J. M. Sussman, V. Singh, M. E. Bahlke, I. Hiromi, J. Lee, and M. A. Baldo. Reducing recombination losses in planar organic photovoltaic cells using multiple step charge separation. *Journal of Applied Physics*, 109(10):104502, 2011.

[207] R. Mauer, I. A. Howard, and F. Laquai. Effect of nongeminate recombination on fill factor in polythiophene/methanofullerene organic solar cells. *The Journal of Physical Chemistry Letters*, 1(24):3500–3505, 2010.

[208] Y. Zhang, X.-D. Dang, C. Kim, and T.-Q. Nguyen. Effect of charge recombination on the fill factor of small molecule bulk heterojunction solar cells. *Advanced Energy Materials*, 1(4):610–617, 2011.

[209] R. A. Street, D. Davies, P. P. Khlyabich, B. Burkhart, and B. C. Thompson. Origin of the tunable open-circuit voltage in ternary blend bulk heterojunction organic solar cells. *Journal of the American Chemical Society*, 135(3):986–989, 2013.

[210] M. Jørgensen, K. Norrman, and F. C. Krebs. Stability/degradation of polymer solar cells. *Solar Energy Materials and Solar Cells*, 92(7):686–714, 2008.

[211] R. R. Lunt, T. P. Osedach, P. R. Brown, J. A. Rowehl, and V. Bulović. Practical roadmap and limits to nanostructured photovoltaics. *Advanced Materials*, 23(48):5712–5727, 2011.

[212] A. Opitz, A. Wilke, T. Mizokuro, R.-P. Blum, J. Rabe, U. Hörmann, P. Amsalem, R. Hansson, E. Moons, and N. Koch. Study of the interface between hydrogen- and fluorine-terminated phthalocyanines in planar and bulk heterojunctions by photoemission and X-ray absorption. *In preparation.*

[213] D. Fujishima, H. Kanno, T. Kinoshita, E. Maruyama, M. Tanaka, M. Shirakawa, and K. Shibata. Organic thin-film solar cell employing a novel electron-donor material. *Solar Energy Materials and Solar Cells*, 93(6-7):1029–1032, 2009.

[214] S. Grob, M. Gruber, A. N. Bartynski, U. Hörmann, T. Linderl, M. E. Thompson, and W. Brütting. Amorphous vs crystalline exciton blocking layers at the anode interface in planar and planar-mixed heterojunction organic solar cells. *Applied Physics Letters*, 104(21):213304, 2014.

[215] Lena Reichardt. *Charakterisierung der Transport- und Injektionseigenschaften von organischen Solarzellen mittels Transientenstrommethoden.* Master's thesis, University of Augsburg, 2012.

[216] Alexander Hofmann. *Transient electrical measurements on organic solar cells.* Master's thesis, University of Augsburg, 2014.

[217] R. C. I. MacKenzie, T. Kirchartz, G. F. A. Dibb, and J. Nelson. Modeling nongeminate recombination in P3HT:PCBM solar cells. *The Journal of Physical Chemistry C*, 115(19):9806–9813, 2011.

[218] Roderick C.I. MacKenzie. Organic photovoltaic device model (www.opvdm.com).

[219] I. N. Bronstein, K. A. Semendjajew, G. Musiol, and H. Mühlig. *Taschenbuch der Mathematik.* Verlag Harri Deutsch, Thun und Frankfurt am Main, 5. Auflage, 2001.

Acknowledgement – Danksagung – Författarens Tack

Ich möchte mich bei all denjenigen bedanken, die mich während der letzten Jahre begleitet und unterstützt haben, sei es durch wissenschaftliche Diskussion, hilfreiche Ratschläge, technische Hilfestellung oder dadurch, dass sie mein Leben fernab der Wissenschaft bereichern. Ohne euch wäre diese Arbeit nicht möglich gewesen, auch wenn ihr euren Namen vielleicht nicht hier finden mögt.

- Insbesondere bedanke ich mich bei **Prof. Dr. Wolfgang Brütting** für die Ermöglichung meiner Promotion in seiner Arbeitsgruppe und unter seiner ausgezeichneten Betreuung sowie für die uneingeschränkte Unterstützung, das stets offene Ohr und das Vertrauen während meiner Arbeit. Auch meine Auslandsaufenthalte und Konferenzreisen wären ohne seine bereitwillige Förderung nicht denkbar gewesen.

- Jag tackar dessutom **Prof. Dr. Ellen Moons** vid Karlstads Universitet i Sverige för granskning av denna avhandling, för att få forska i hennes grupp under den tid jag vistades i Sverige och för möjliggörandet av NEXAFS mätningarna. Jag är också tacksam för all stöd, råd och den uppmuntring jag fått var ända gång vi möttes.

- Des Weiteren möchte ich den Herrn **Prof. Dr. Bernd Stritzker** sowie **Prof. Dr. Manfred Albrecht** für die Aufnahme am Lehrstuhl Experimentalphysik IV danken.

- In besonderer Weise unterstützt hat mich **PD Dr. Andreas Opitz**, Humboldt Universität zu Berlin, der mir stets mit Rat und Tat zur Seite stand. Insbesondere bedanke ich mich für die Simulation optischer Konstanten und die Unterstützung bei der Messung und Auswertung von NEXAFS Spektren sowie für die tolle Zeit in Augsburg, Karlstad und Lund.

- Diese Arbeit wäre außerdem nicht möglich gewesen ohne die entsprechende finanzielle Unterstützung durch ein Promotionsstipendium der **Bayerischen Forschungsstiftung** während der ersten drei Jahre und die darüberhinausgehende Förderung durch die **Deutsche Forschungsgemeinschaft** im Rahmen des

Schwerpunktprogramms SPP 1355 „Elementarprozesse der organischen Photovoltaik“. Mein Dank gebührt deshalb diesen großzügigen Organisationen.

- Ich bedanke mich herzlich bei unseren Projektpartnern im Rahmen des Schwerpunktprogramms für die ausgezeichnete, fruchtbare und bereichernde Kooperation. Mein besonderer Dank gilt **Prof. Dr. Frank Schreiber**, **Dr. Alexander Hinderhofer** und **Christopher Lorch** der Universität Tübingen, **Prof. Dr. Norbert Koch** und **Dr. Andreas Wilke** der Humboldt Universität zu Berlin sowie **Prof. Dr. Jens Pflaum**, **Katharina Topczak** und **Andreas Steindamm** der Universität Würzburg. Vielen Dank für die wertvollen Diskussionen, zahlreiche Messungen und die geduldigen Erklärungen dazu.

- I am grateful to the **Japan Society for the Promotion of Science** for a fellowship within their JSPS Summer Program 2011. This enabled the unique opportunity of a research stay at the Ishii laboratory for organic electronics at Chiba University in Japan. My sincere thanks are given to **Prof. Dr. Hisao Ishii**, **Prof. Dr. Yutaka Noguchi**, **Prof. Dr. Yasuo Nakayama**, **Dr. Yuya Tanaka**, **Dr. Machida Shin-ichi**, **Mr. Taiki Yamada**, **Mr. Shunhikari Tamura**, **Mr. Yusuke Ozawa** and **Ms Kuniko Ito** as well as all members of the Ishii lab. I am deeply indebted and want to express my gratitude to my host family **Mrs. Yuko Ichikawa**, **Dr. Kazuyoshi Ichikawa** and their daughters **Chiharu** and **Mayo**. The people I met, the places I've seen and the things I've learned have made this summer in Japan an invaluable enrichment both personally and scientifically.

- Jag vill också säga tack till **Prof. Dr. Jan van Stam**, **Dr. Ana Sofia Anselmo** och **Rikard Hansson** vid Karlstads Universitet samt **Dr. Alexei Preobrajenski** vid MAX-lab för all hjälp, stöd och den underbara tiden i Karlstad, Lund och annanstans.

- Ich danke auch **PD Dr. Giuseppe Scarpa** und **Robin Nagel**, TU München, für Versuche zur Nanoimprint-Lithographie.

- Zudem bedanke ich mich herzlich bei **Prof. Dr. Hubert Krenner** für die hilfreiche Diskussion und die fruchtbare Zusammenarbeit.

- Auch meinen Schützlingen **Benedikt Sykora**, **Ferdinand Sedlmair**, **Ljubomir Barbic**, **Lena Reichardt**, **Alexander Hofmann** und **Jonas Nekrasovas** die ich während ihrer Praktika, Bachelor- oder Masterarbeiten betreuen durfte, möchte ich für die gemeinsame Arbeit, die Diskussion, die Unterstützung bei und mit Experimenten und die schöne Zeit danken.

- Den hilfsbereiten Mitarbeitern der **feinmechanischen und der Elektronik-Werkstatt** danke ich für die unkomplizierte Hilfe und die zügige Anfertigung maßgeschneiderter Laborausrüstung.

- Ganz besonders Danken möchte ich auch meinen Bürokollegen **Dr. Tobias D. Schmidt** (auch für das Korrekturlesen in letzter Minute), **Lars Jäger**, **Christian Stehl** und **Björn Gallheber** für den fachlichen Rat, die hervorragende Kollegialität und die tolle Zeit in 456.

- Mein Dank gilt auch meinen Organik-Kollegen **Stefan Grob**, **Theresa Linderl**, **Alexander Hofmann** und **Lothar Sims**, **Bert Scholz**, **Sebastian Wehrmeister**, **Eduard Meister** und **Christian Mayr**. Besonders hervorzuheben sind dabei **Dr. Julia Kraus** und **Dr. Mark Gruber,** meine OPV-Mitstreiter von Anfang an, ohne die einfach gar nichts geht.

- Herzlich danken möchte ich außerdem allen früheren Kollegen der Arbeitsgruppe „Organische Halbleiter“, die mich während der letzten Jahre auf Abschnitten begleitet haben, stets hilfsbereit waren und von denen ich die Grundlagen der experimentellen Arbeit gelernt habe: **Dr. Michael Kraus**, **Dr. Jörg Frischeisen**, **Dr. Stefan Nowy** und **Dr. Thomas Wehlus**.

- Ebenso richtet sich mein Dank an alle anderen Mitglieder des **Lehrstuhls Experimentalphysik IV**. Die arbeitsgruppenübergreifende Hilfsbereitschaft und die freundlich-kollegiale Arbeitsatmosphäre bereichern die Arbeit jeden Tag aufs Neue. Besonders bedanke ich mich für die direkte Unterstützung labor-, EDV- oder verwaltungstechnischer Art bei **Wolfgang Reiber**, **Birgit Knoblich**, **Sybille Heidemeyer**, **Michael Weinl**, **Maria Fuso**, **Bettina Schestak** und **Christine Schäfer**.

- Ein besonderes Dankeschön sende ich an das Büro-Team der **DPSG Augsburg** für die herzliche Aufnahme während des Verfassens dieser Arbeit.

- Schließlich Danke ich meinen **Eltern** und **Brüdern** für die uneingeschränkte, nieenden-wollende Unterstützung von Anfang an, ohne die alles ganz anders gekommen wäre. Und meiner Freundin **Yvonne**, für die Geduld, den Rückhalt und das Glück – Danke!